جمهورية العراق

وزارة التعليم العالي والبحث العلمي

جامعة بابل / كلية العلوم

قسم الفيزياء

استخدام تقنيات متعددة لمعالجة الصور لكشف وعزل الشذوذ في الصور الطبية

رسالة مقدمة الى
قسم الفيزياء /كلية العلوم /جامعة بابل
كجزء من متطلبات نيل درجة الماجستير في علوم الفيزياء

من قبل

اصيل علي حسين علوان

بكالوريوس في علوم الفيزياء (2018)

بأشراف

أ. د. رباب سعدون عبدون

١٤٤٤هـ ٢٠٢٣ م

Republic of Iraq
Ministry of Higher Education and Scientific Research
University of Babylon / College of Science
Department of Physics

Utilizing Multi Image Processing Techniques to Detect and Isolate Abnormalities in Medical Images

A Thesis

Submitted to the Physics Department, College of Science, University of Babylon in Partial Fulfillment of the Requirements for the Degree of Master of Science in Physics

By

Aseel Ali Hussein Alwan

B.Sc. in Physics (2018)

Supervised by

Prof. Dr. Rabab Saadoon Abdoon

2023 A.D. **1444 A.H.**

بِسْمِ اللّٰهِ الرَّحْمَنِ الرَّحِيمِ

إِنَّ فِي خَلْقِ السَّمَاوَاتِ وَالْأَرْضِ وَاخْتِلَافِ اللَّيْلِ
وَالنَّهَارِ لَآيَاتٍ لِأُولِي الْأَلْبَابِ

صدق اللّٰه العلي العظيم

(سورة آل عمران/آية ١٩٠)

Supervisor Certificatio

I certify that this thesis entitled (**Utilizing Multi Image Processing Techniques to Detect and Isolate Abnormalities in Medical Images**) was prepared by (**Aseel Ali Hussein Alwan**) under my supervision at Department of Physics, College of Sciences, University of Babylon, as a partial fulfillment of the requirements for the degree of master in science of physics.

Signature :

Supervised: Dr. Rabab Saadoon Abdoon

Title : Professor

Address: Department of Physics – College of Science - University of Babylon

Date : / /2023

Certication of the Head of the Department

In view of the available recommendation, I forward this proposal for debate by the examination committee.

Signature:

Name: Dr. Samira Adnan Mahdi

Title: Assistant Professor

Address: Head of the Department of Physics - College of Science-
University of Babylon

Date: / / 2023

Acknowledgments

Foremost, I am highly grateful to Allah (God) for his unlimited blessings that continue to flow into my life, and because of You, I made this through against all odds.

I would like to express my appreciation to my supervisor Prof. Dr. Rabab Saadoon Abdoon who has given me great support, encouragement, and valuable advices during the progress of the work.

Many thanks go to the College of Sciences at Babylon University and the Department of Physics for offering me the opportunity to complete my Thesis.

I would like to express my thanks to Dr. Ruaa Falah al- Jubawi, Mr. Raed Mahdy, Mr. Mohammed Abdul Karim, worked in Zaid Al-Khafaji Clinic Center for their consultation and reviewing the quality of the extracted infected regions. As well as, Iam grateful to Dr. Zaid Hadi Al-Khafaji Center, Ashur Clinic and Fadak Clinic for providing the Covid-19 images and other abnormal CT scac image.

Aseel

Dedication

This work is dedicated to…

The Iraqi martyrs of all sects and nationalities who gave their lives so that we could live in peace, whether on the battlefield or in nonviolent marches, to seek rights.

My father, My mother, My husband, To my daughter, My beloved brothers and sisters, To all who love me sincerely and sincerely.

Aseel
2022

الخلاصة:

هناك العديد من الاورام والامراض المستجدة (مثل جائحة كوفيد-19) التي قد تسبب الوفاة بين البشر لذا يعتبر الكشف المبكر عن هذه الامراض ضرورة ملحة لزيادة فرص الحياة والنجاة من هذه الامراض. ان انتشار "مرض فيروس كورونا الجديد 2019 (Covid-19)" بسرعة كبيرة في جميع أنحاء العالم تسبب بوفاة نسبة عالية من الاشخاص حول العالم بسبب قلة عدد مجموعات اختبار Covid-19 المتاحة في المستشفيات حيث كانت محدود مقارنة بالعدد المتزايد للحالات كل يوم. لذا فمن الضروري إدخال نظام الكشف التلقائي كطريقة تشخيص بديلة سريعة للمساعدة في تجنب انتشار Covid-19 بين الناس عن طريق استخدام تقنيات التصوير الطبي (ومنها المفراس).

في هذه الدراسة ، تم استخدام الشبكات العصبية الاصطناعية على مرحلتين: المرحلة الأولى وفيها تم اقتراح طريقة آلية تعتمد على نهج التعلم الآلي الهجين الشبكة العصبية التلافيفية (CNN) لتشخيص حالات كوفيد -19 والأورام والحالات الطبيعية. حيث دربت الشبكة باستخدام صور عددها 5000 لصنف حالات الكوفيد-19 و الاورام ايضا 5000 صورة و 5000 صورة تمثل حالات طبيعية. كانت دقة الشبكة في التصنيف 99.82% ولخطوة الاختبار كانت مقاييس أداء الاختبار (الحساسية, النوعية والدقة) هي (99.99, 99.99 و99.99)% لحالات الكوفيد و (99.98, 99.98 و99.98) % لحالات الاورام على التوالي.

المرحلة الثانية من الدراسة قسمت الصور التي تم تصنيفها في المرحلة الأولى على أنها حالات شاذة (كوفيد -19 وأورام) لغرض كشف وعزل واستخراج المناطق غير الطبيعية ، وذلك باستخدام الشبكات العصبية الاصطناعية (غير الخاضعة للأشراف) و طريقتان لتجميع (K-Means و Fuzzy C-mean (FCM)) بالإضافة إلى اقتراح طريقة هجينة لتقليل وقت التنفيذ المطلوب لخريطة ميزات التنظيم الذاتي للرسم البياني (HSOFM). تم تنفيذ هذه التقنيات باستخدام عدد من العناقيد وعدد من العقد (3,4 و 5). أظهرت النتائج أن الطرق المطبقة كانت كفوءه للكشف عن وعزل واستخراج المناطق المصابة بـ Covid-19 بدقة (95, 95, 94 و 94)٪ لتقنية k-mean وFCM وHSOFM و hybrid على التوالي.

أدى تطبيق الطريقة الهجينة إلى تقليل وقت التنفيذ المطلوب لـ HSOFM مع تخفيض النسبة المئوية تراوحت بين (18.99 - 49.62) ٪ لـ Covid-19 وتراوحت القيمة النسبية للنسبة من (13.05 - 52.2) ٪ للورم.

تم حساب نسبة الإصابة النسبية وتراوحت نسبة الإصابة بين (0.01279-0.06694)٪ لكوفيد-19و(0.79 - 28.15) ٪ لحالات الاورام.

وأظهرت النتائج أن التقنيات الأربع المقترحة كانت كفؤة ونجحت في عزل واستخراج مناطق غير طبيعية بناءً على استشارة أخصائي الأشعة ، وكانت النتائج متوافقة مع تحديد أخصائي الأشعة للمناطق غير الطبيعية لـ Covid-19 والأورام.

Summary:

There are many emerging tumors and diseases (such as the Covid-19 pandemic) that may cause death in humans, so early detection of these diseases is an urgent necessity to increase the chances of life and survival from these diseases. The spread of “novel coronavirus disease 2019 (Covid-19)” very quickly around the world caused a high proportion of people to die around the world due to the limited number of Covid-19 test kits available in hospitals, which were limited compared to the increasing number of cases every day. It is therefore necessary to introduce an automatic detection system as a rapid alternative diagnostic method to help avoid the spread of Covid-19 among people by using medical imaging technologies (CT scans).

In this study, artificial neural networks are used in two phases: the first phase in which an automated method based on a hybrid machine learning approach Convolutional Neural Network (CNN) is proposed to diagnose COVID-19 cases, tumors and normal cases. Where the network was trained using 5,000 images to classify Covid-19 cases and 5,000 tumors, as well as 5,000 images representing natural cases. The accuracy of the network in classification was 99.82% and for the test step the test performance measures (Sensitivity, Specificity and Accuracy)% were (99.99, 99.99 and 99.99) % for Covid-19 cases and (99.98, 99.98 and 99.98) % for tumor cases, respectively.

The second stage of the study divides the images that are classified in the first stage as anomalies (Covid-19 and tumors) for the purpose of detecting, isolating and extracting abnormal regions, using (unsupervised, Hierarchical self-organizing feature map (HSOFM)) artificial neural networks. Two methods for clustering (K-Means and Fuzzy C-mean (FCM)) as well as proposing a hybrid method to reduce the execution time required for the HSOFM. These techniques were implemented using a number of clusters and a number of nodes (3, 4 and 5) The results showed that the applied methods were sufficient to detect, isolate and extract areas affected by Covid-19 with accuracy (95, 95, 94 and (94%) for k-mean, FCM, HSOFM and hybrid technology, respectively.

The application of the hybrid method reduced the execution time required for HSOFM with the percentage reduction ranged between (18.99 - 49.62)% for Covid-19 and the relative value of the percentage ranged from (13.05 - 52.2) % for the tumor.

The relative incidence rate is calculated and the incidence rate ranged between (0.01279-0.06694)% for Covid-19 and (0.79-28.15%) for tumor cases.

The results showed that the four proposed techniques were sufficient and succeeded in isolating and extracting abnormal areas according to the advice of the radiologist, and the results are consistent with the radiologist's identification of the abnormal areas of Covid-19 and tumors.

Contents

Chapter One: General Introduction

Chapter Two: Medical Imaging Techniques and Lung Abnormality Types

Chapter Five: Conclusion and Future Studies

References

Appendix1

K-means Clustering Method

1- K-means Clustering with (3, 4 and 5) Clusters for Covid-19 Infected Lung CT Images:

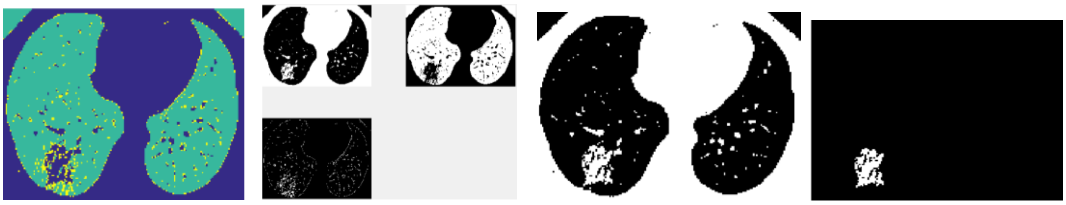

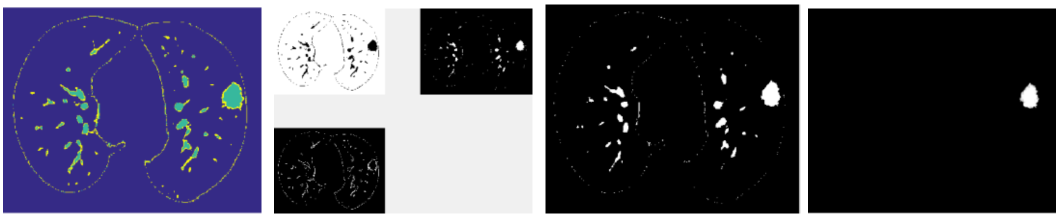

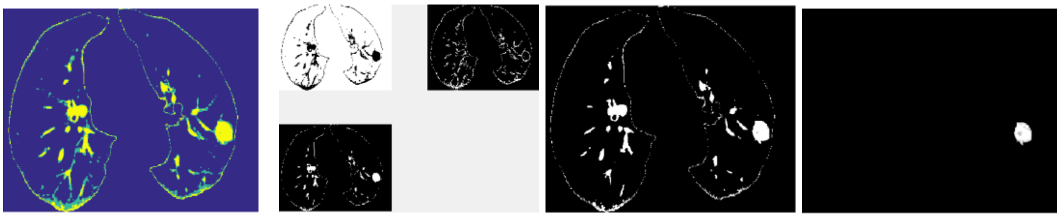

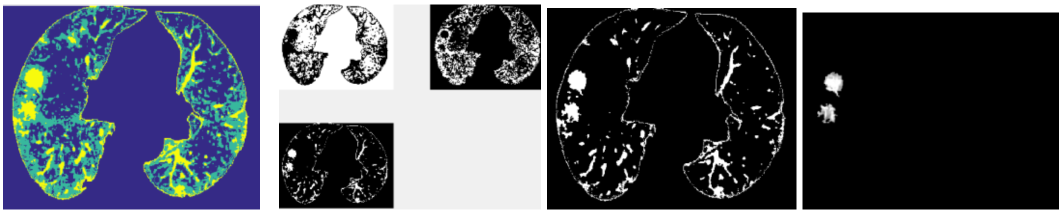

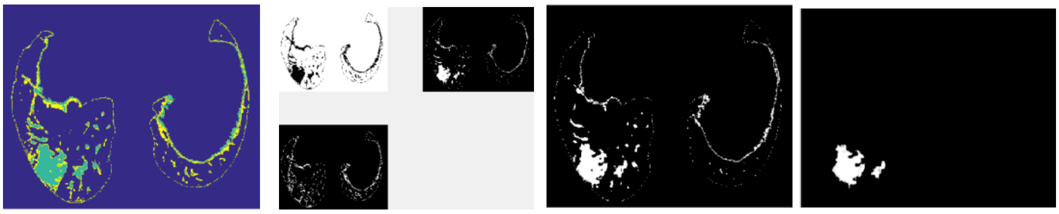

a **b** **c** **d**

Figure (1): Results of implementing K-means Clustering with three clusters. (a) segmented image, (b) the discrete clusters, (c) the cluster of the infected region and (d) the final extracted infected region.

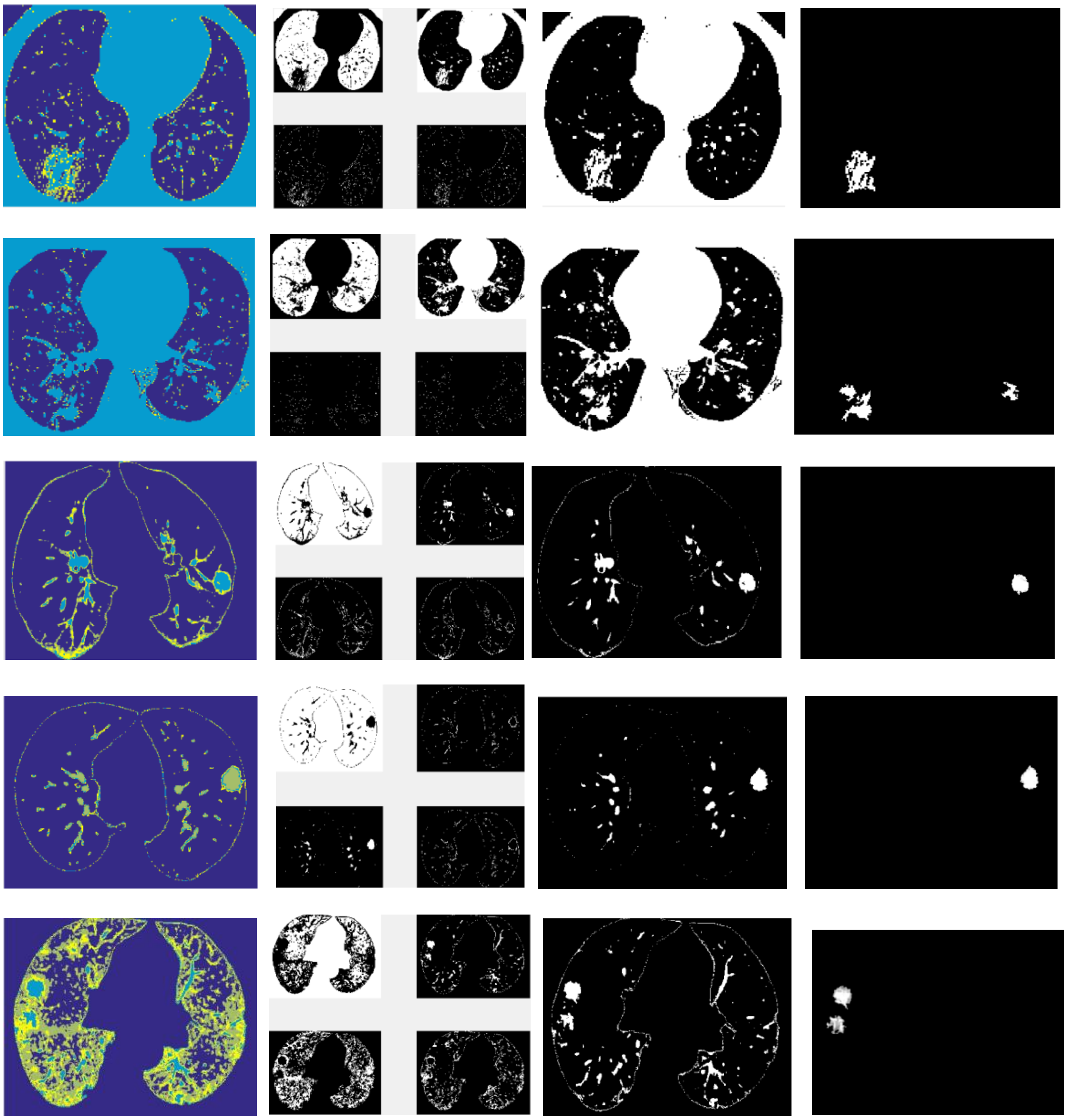

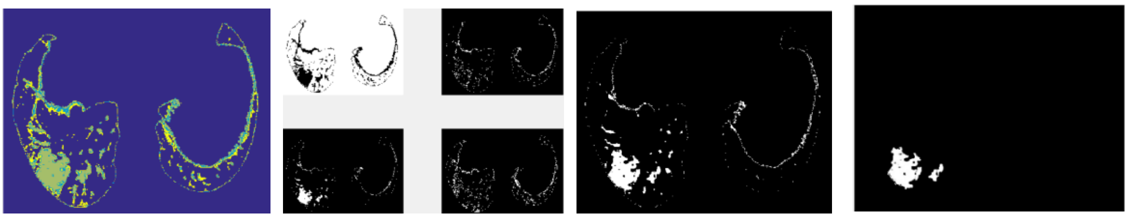

a **b** **c** **d**

Figure (2): Results of implementing K-means Clustering with four clusters. (a) segmented image, (b) the discrete clusters, (c) the cluster of the infected region and (d) the final extracted infected region.

.

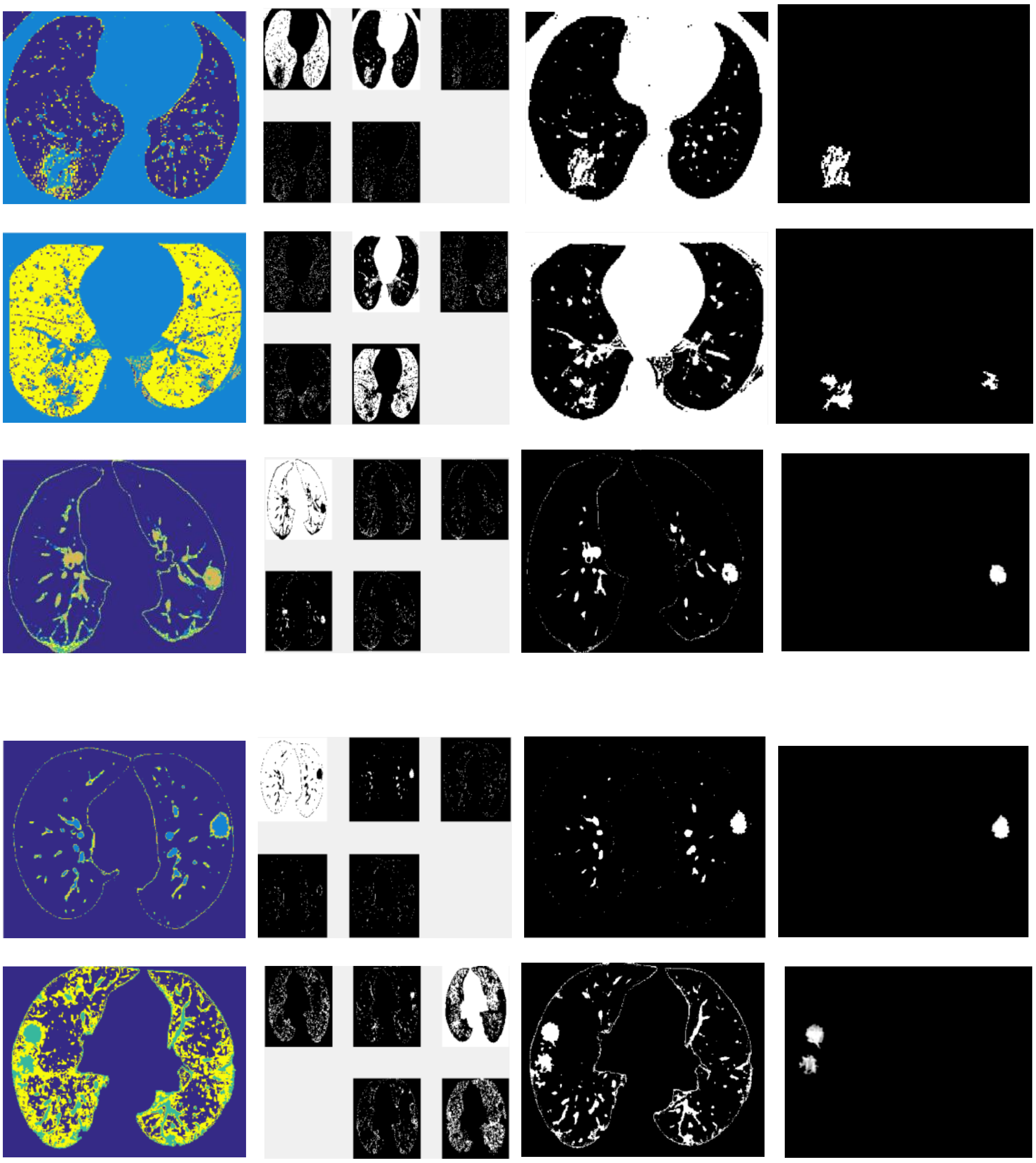

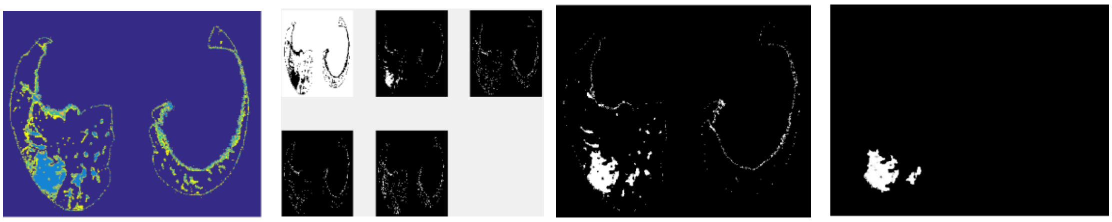

a **b** **c** **d**

Figure (3): Results of implementing K-means Clustering with five clusters. (a) segmented image, (b) the discrete clusters, (c) the cluster of the infected region and (d) the final extracted infected region.

2- K-means Clustering with (3, 4 and 5) Clusters for Tumors Infected Lung CT Images:

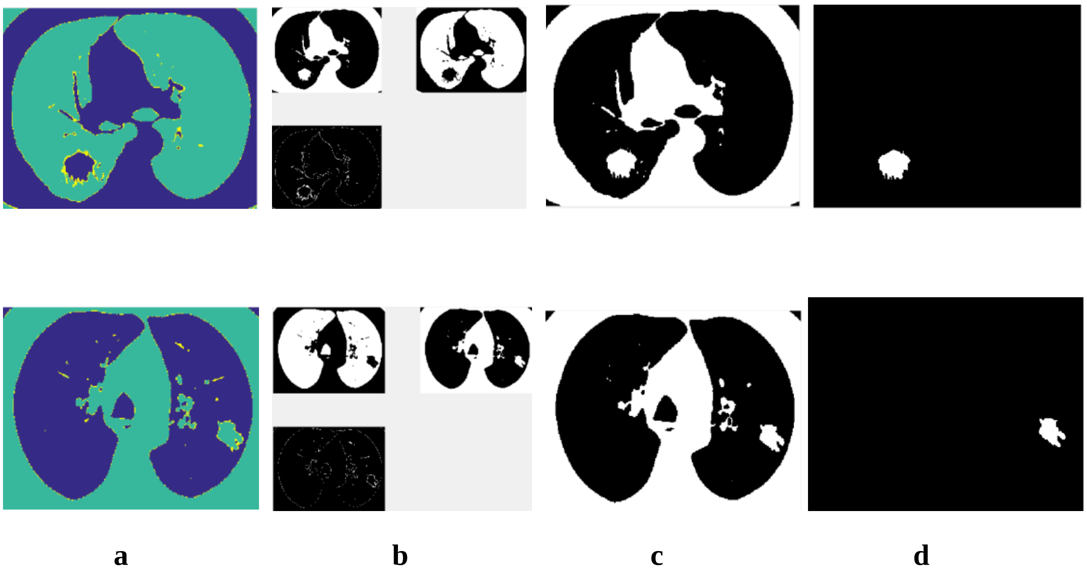

Figure (4): Results of implementing K-means Clustering with three clusters. (a) segmented image, (b) the discrete clusters, (c) the cluster of the infected region and (d) the final extracted infected region.

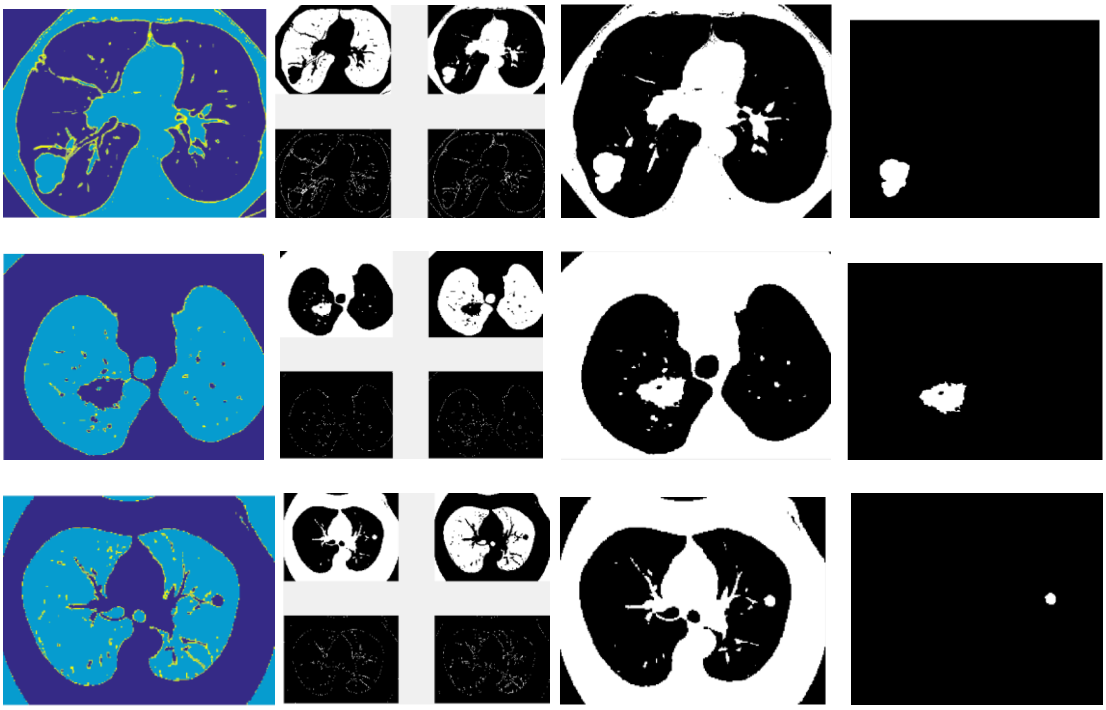

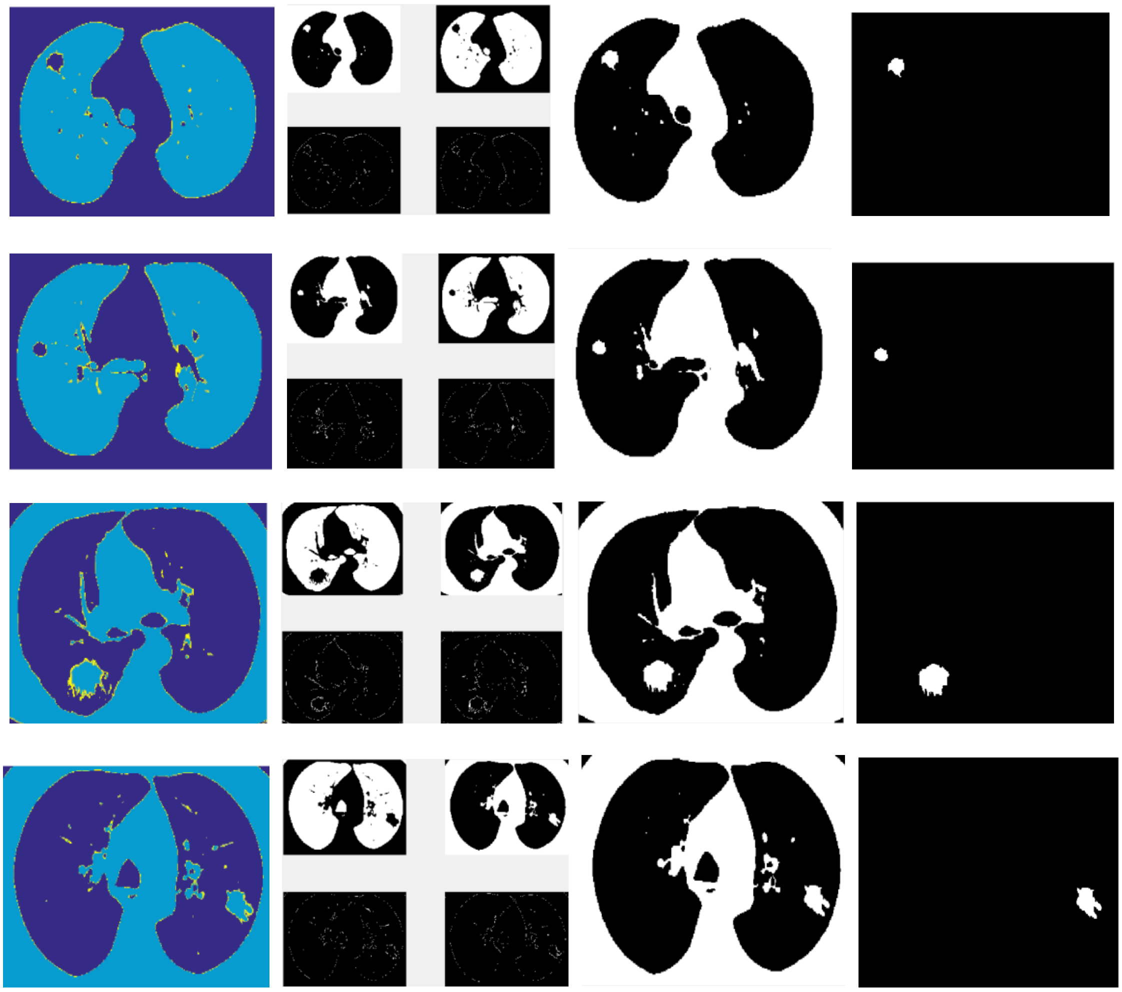

a **b** **c** **d**

Figure (5): Results of implementing K-means Clustering with four clusters. (a) segmented image, (b) the discrete clusters, (c) the cluster of the infected region and (d) the final extracted infected region.

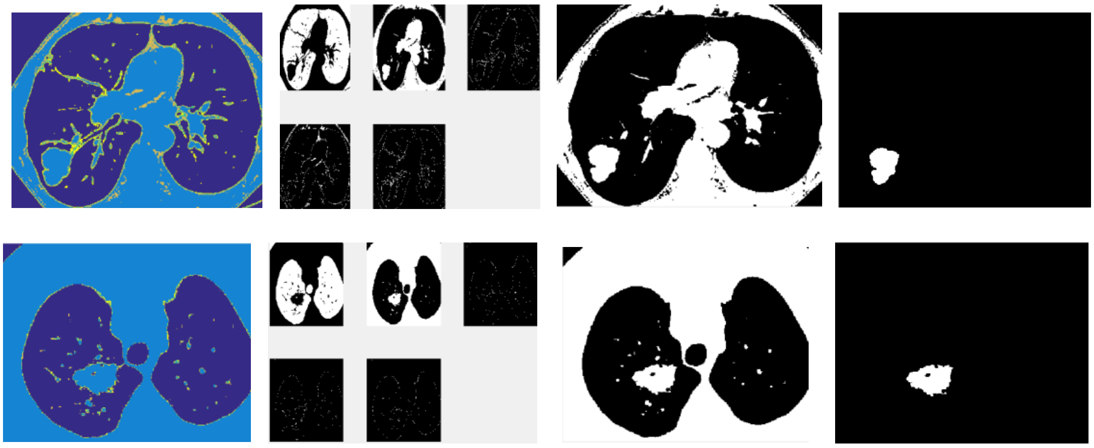

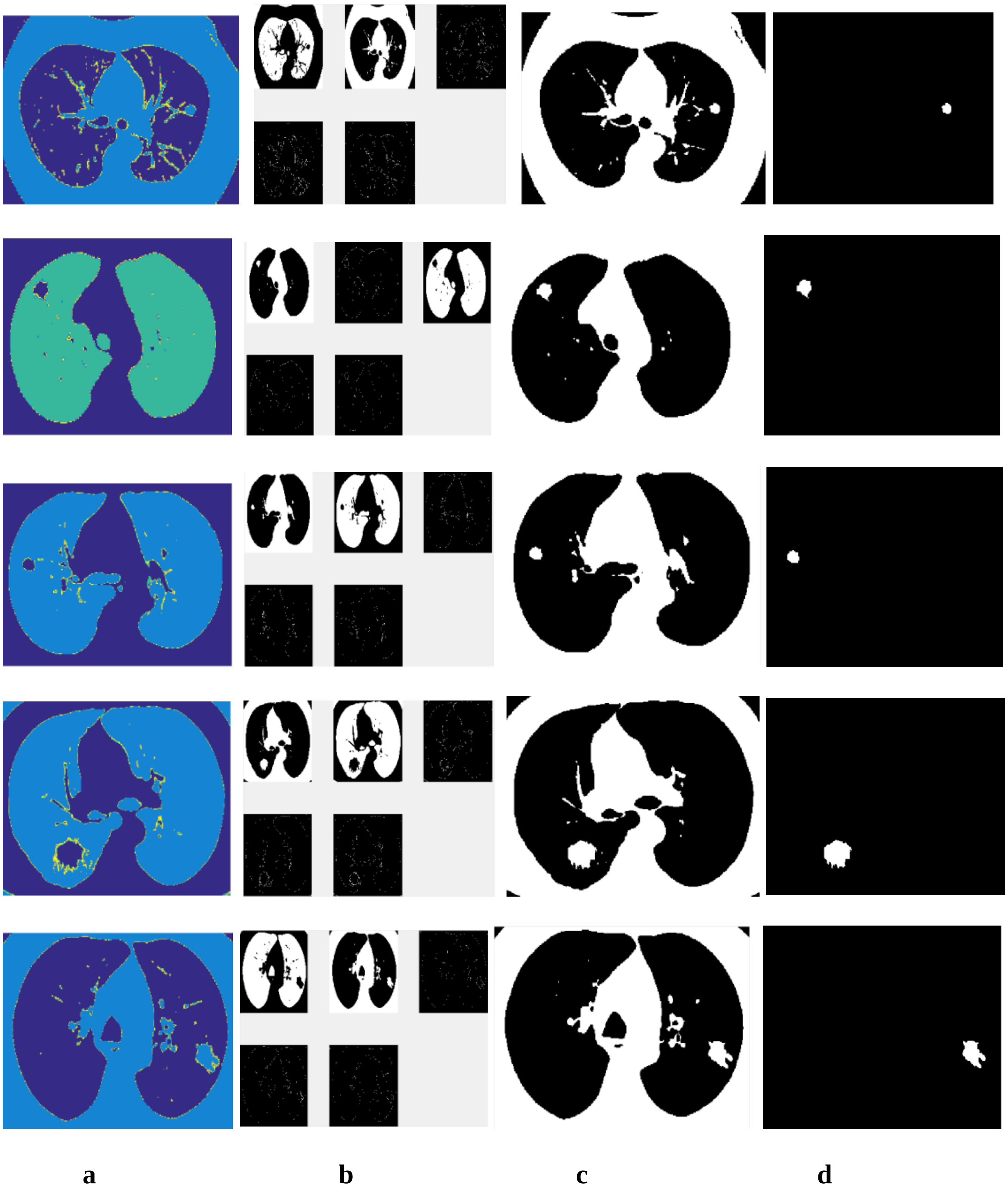

Figure (6): Results of implementing K-means Clustering with five clusters. (a) segmented image, (b) the discrete clusters, (c) the cluster of the infected region and (d) the final extracted infected region.

Appendix2

HSOFM Unsupervised ANN

1- HSOFM Unsupervised ANN with (3, 4 and 5) Nodes for Covid-19 Infected Lung CT Images:

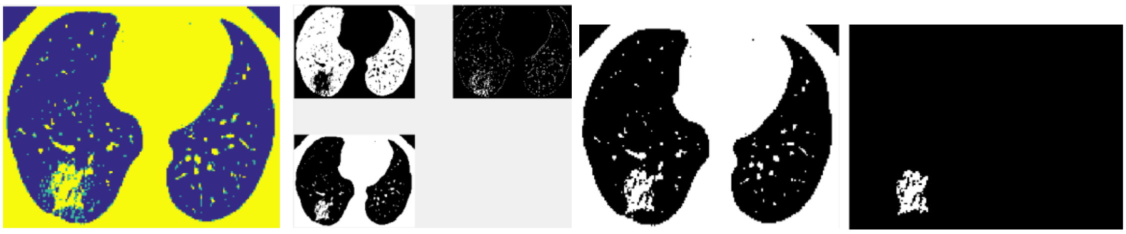

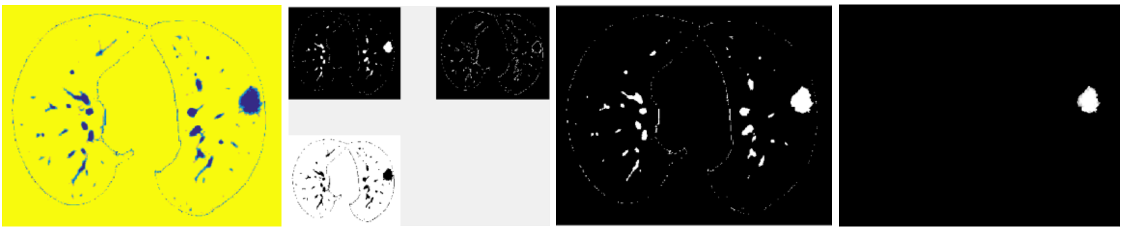

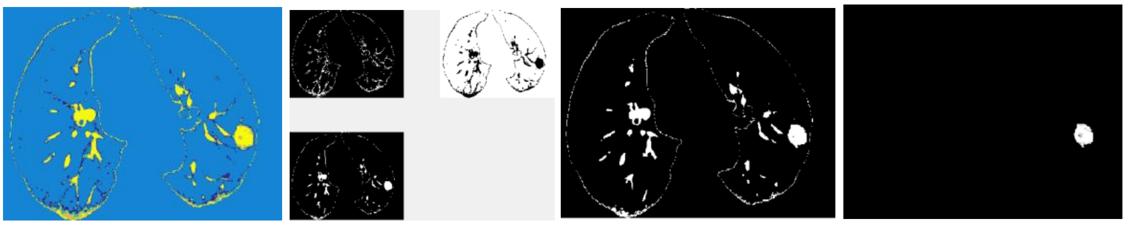

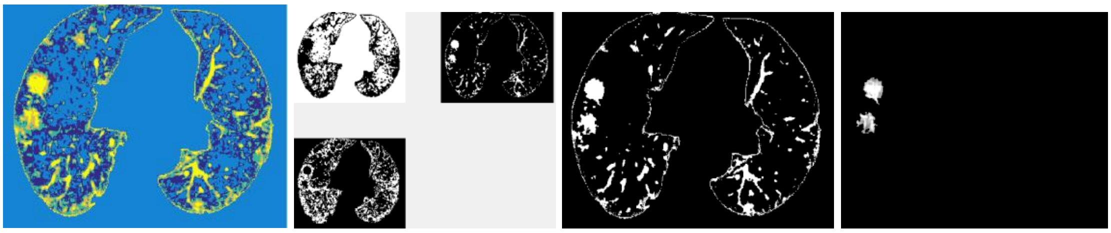

a b c d

Figure (7): Results of implementing HSOFM clustering with three nodes. (a) segmented image, (b) the discrete clusters, (c) the cluster of the infected region and (d) the final extracted infected region.

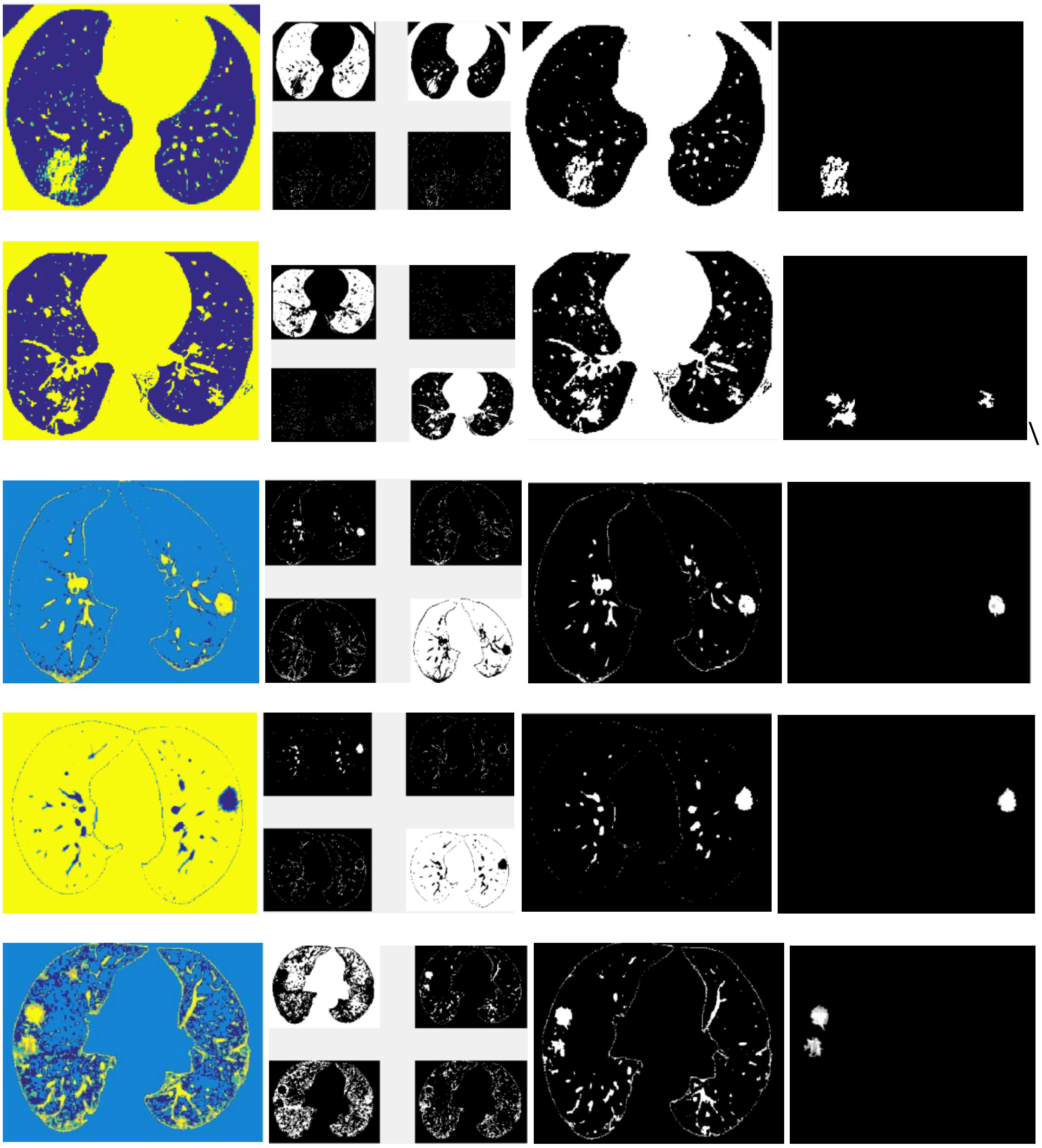

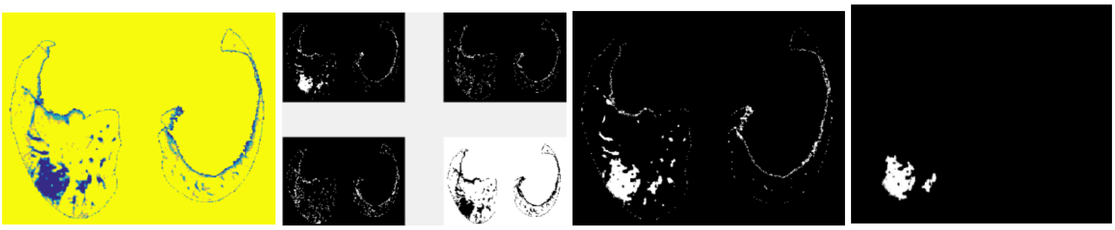

a **b** **c** **d**

Figure (8): Results of implementing HSOFM Clustering with four nodes. (a) segmented image, (b) the discrete nodes, (c) the cluster of the infected region and (d) the final extracted infected region.

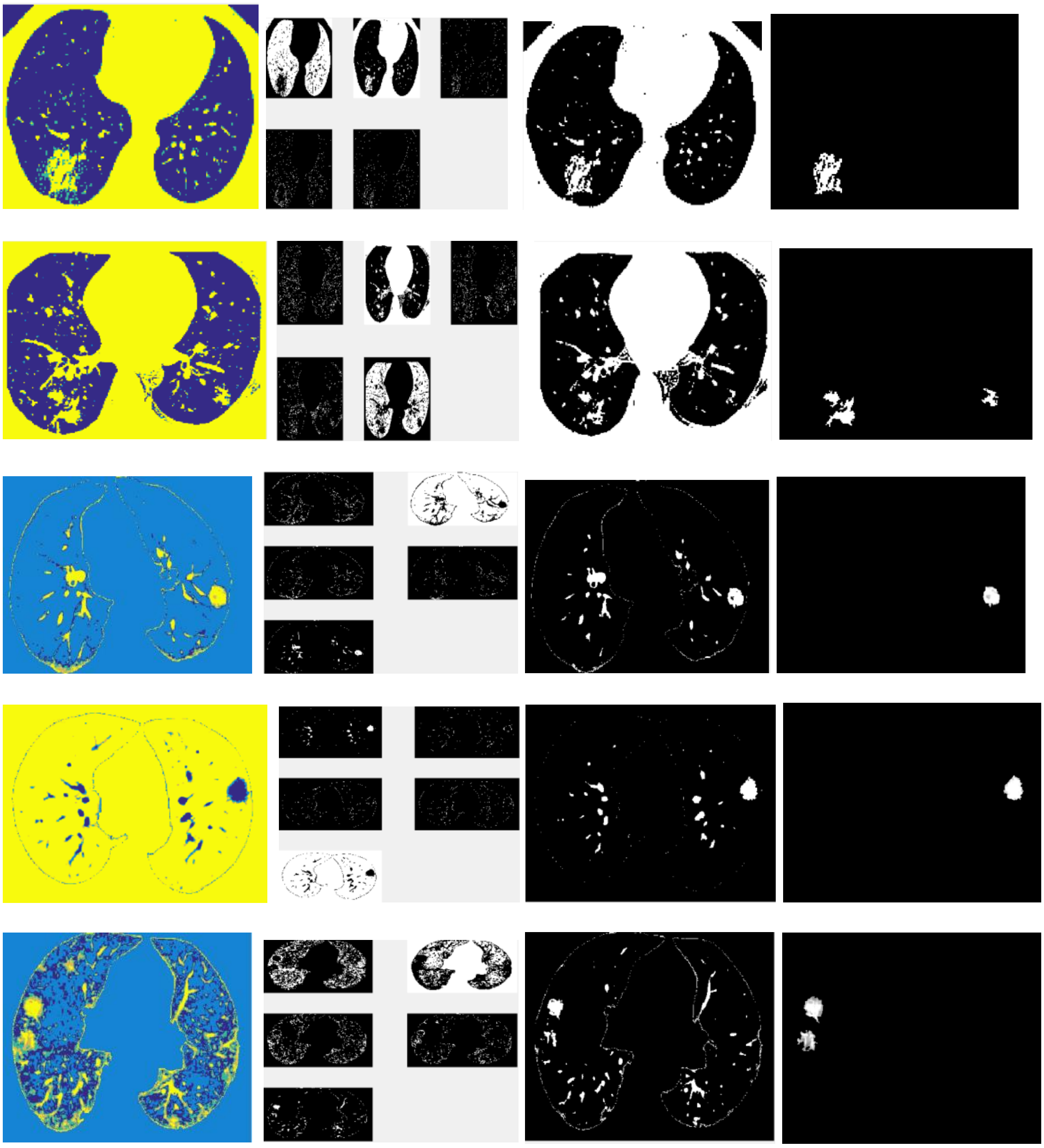

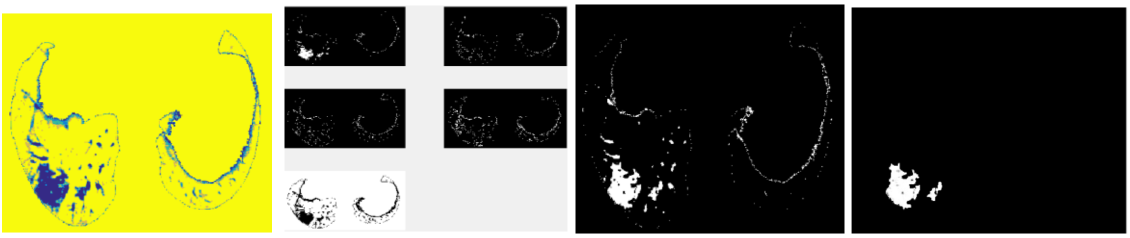

a b c d

Figure (9): Results of implementing HSOFM Clustering with five nodes. (a) segmented image, (b) the discrete nodes, (c) the cluster of the infected region and (d) the final extracted infected region.

2- HSOFM Unsupervised ANN with (3, 4 and 5) Nodes for Tumor Infected Lung CT Images:

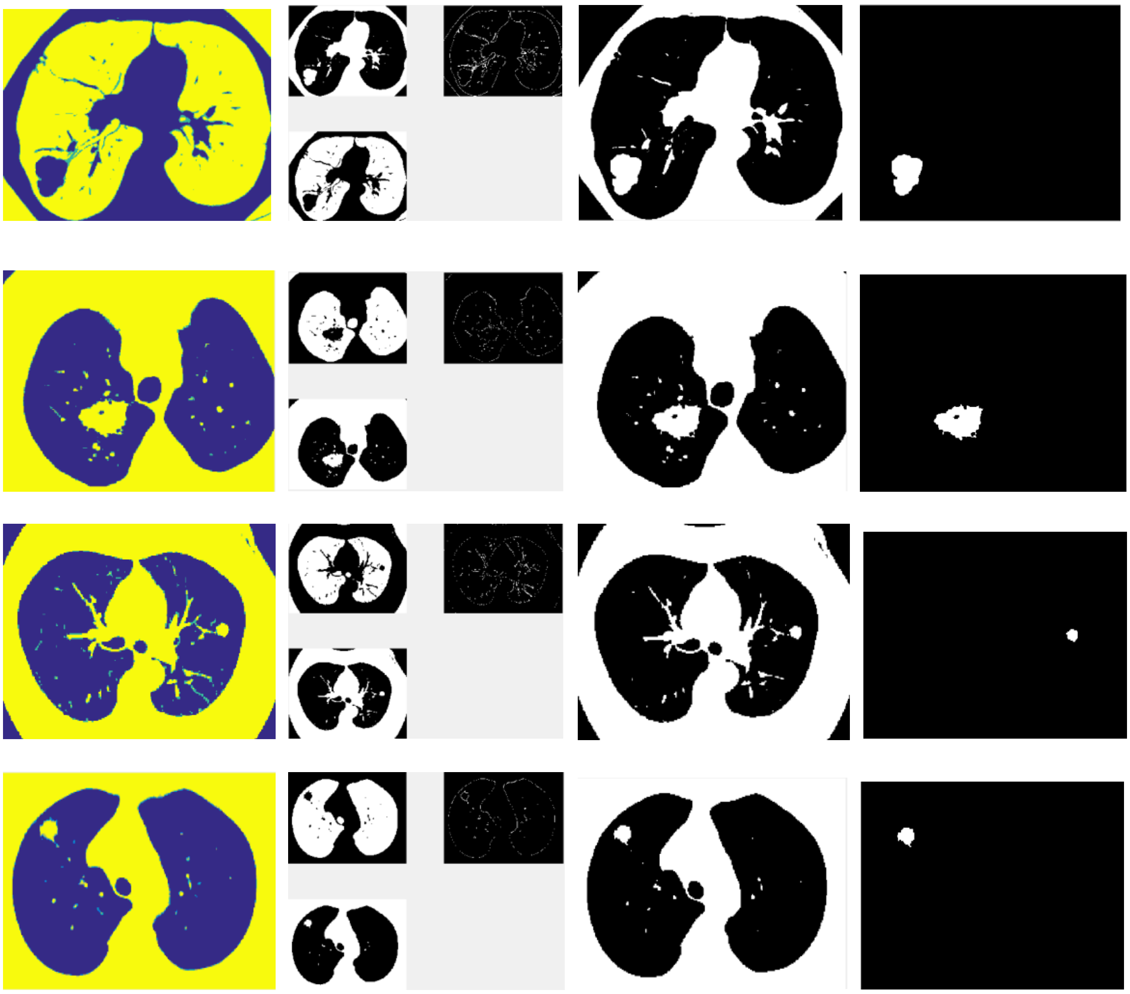

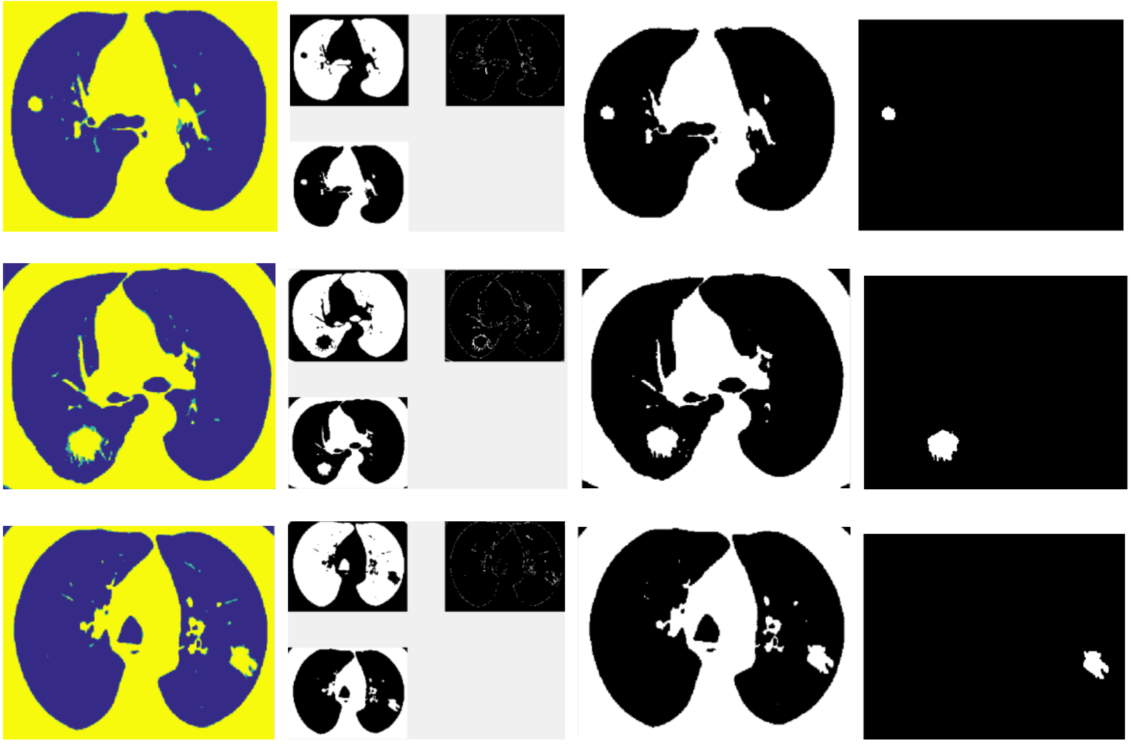

a **b** **c** **d**

Figure (10): Results of implementing HSOFM Clustering with three nodes. (a) segmented image, (b) the discrete nodes, (c) the cluster of the infected region and (d) the final extracted infected region.

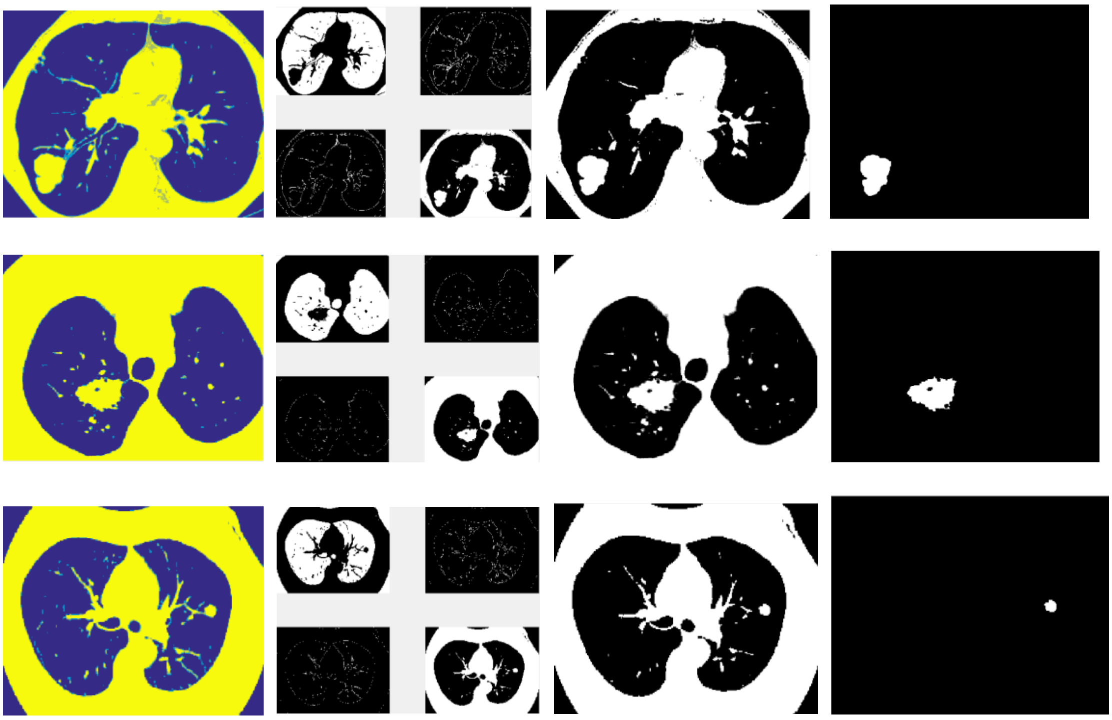

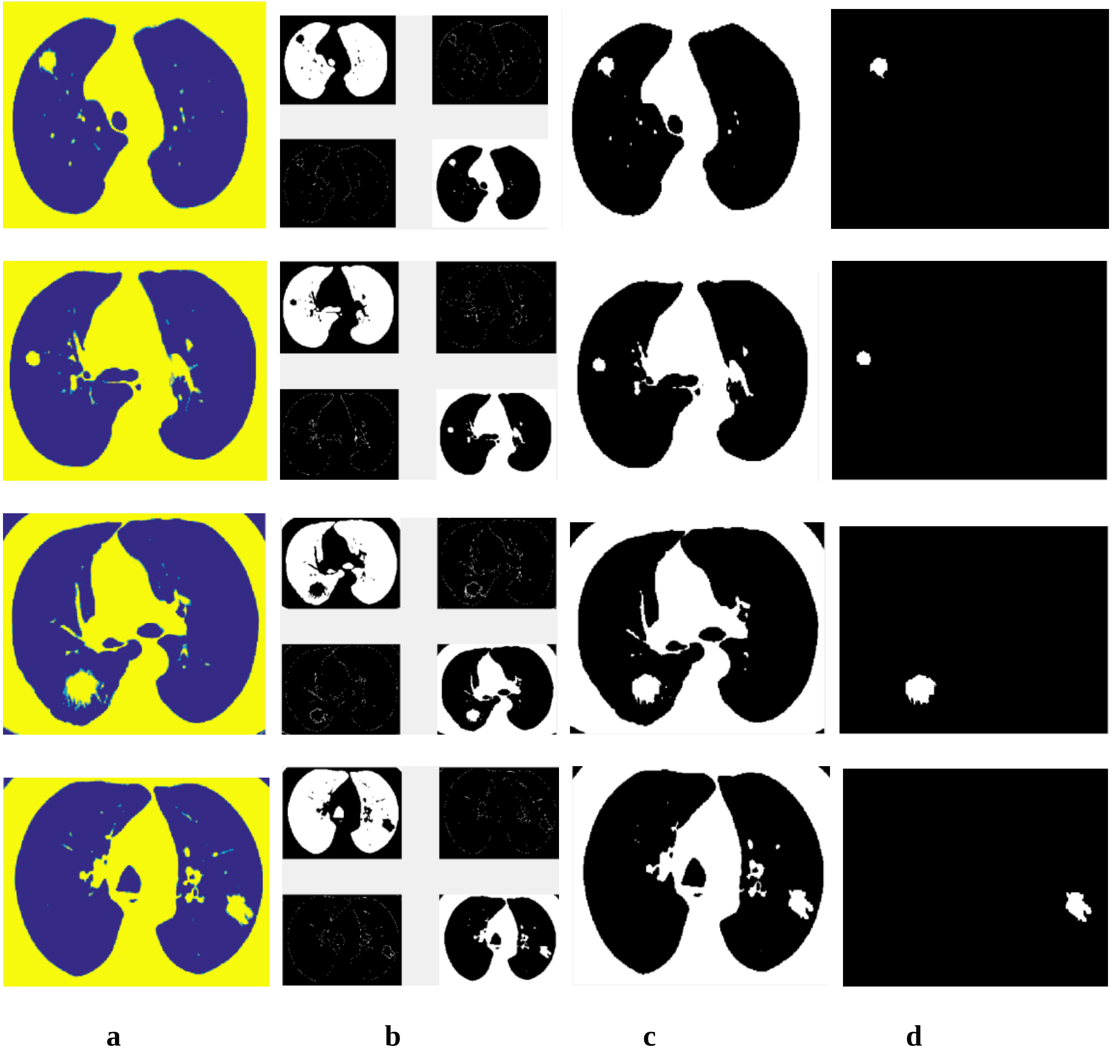

Figure (11): Results of implementing HSOFM Clustering with four nodes. (a) segmented image, (b) the discrete nodes, (c) the cluster of the infected region and (d) the final extracted infected region.

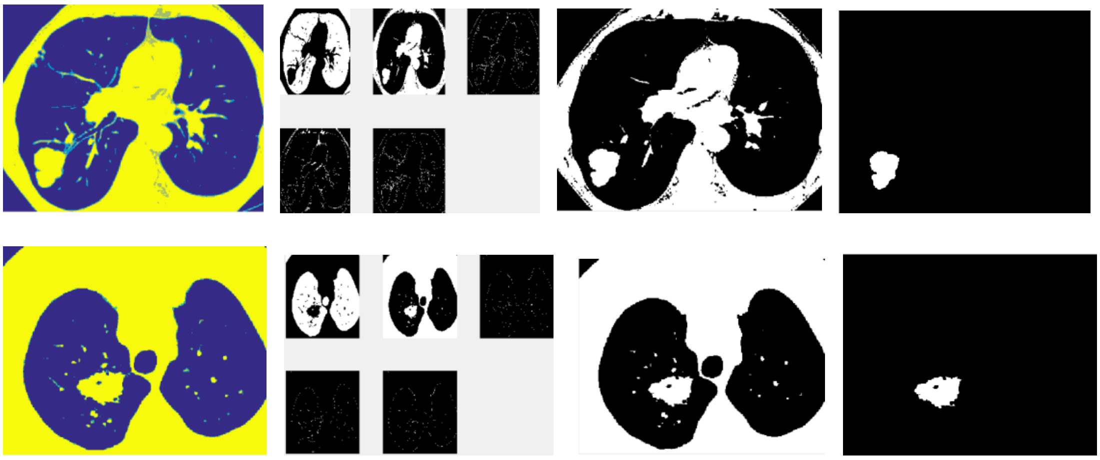

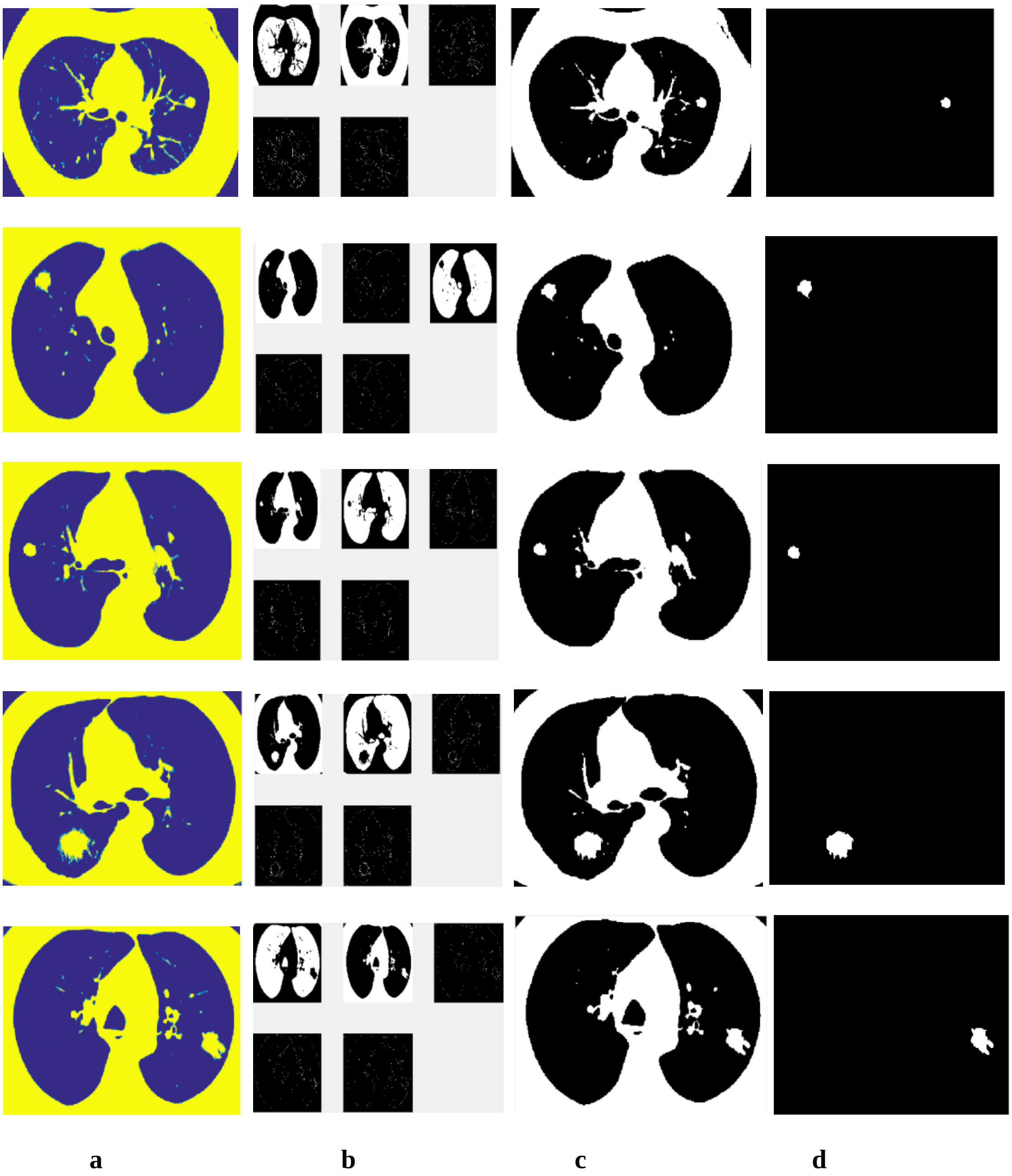

Figure (12): Results of implementing HSOFM Clustering with five nodes. (a) segmented image, (b) the discrete nodes, (c) the cluster of the infected region and (d) the final extracted infected region.

Appendix3

FCM Clustering

1- FCM Clustering with (3, 4 and 5) Clusters for Covid-19 Infected Lung CT Images:

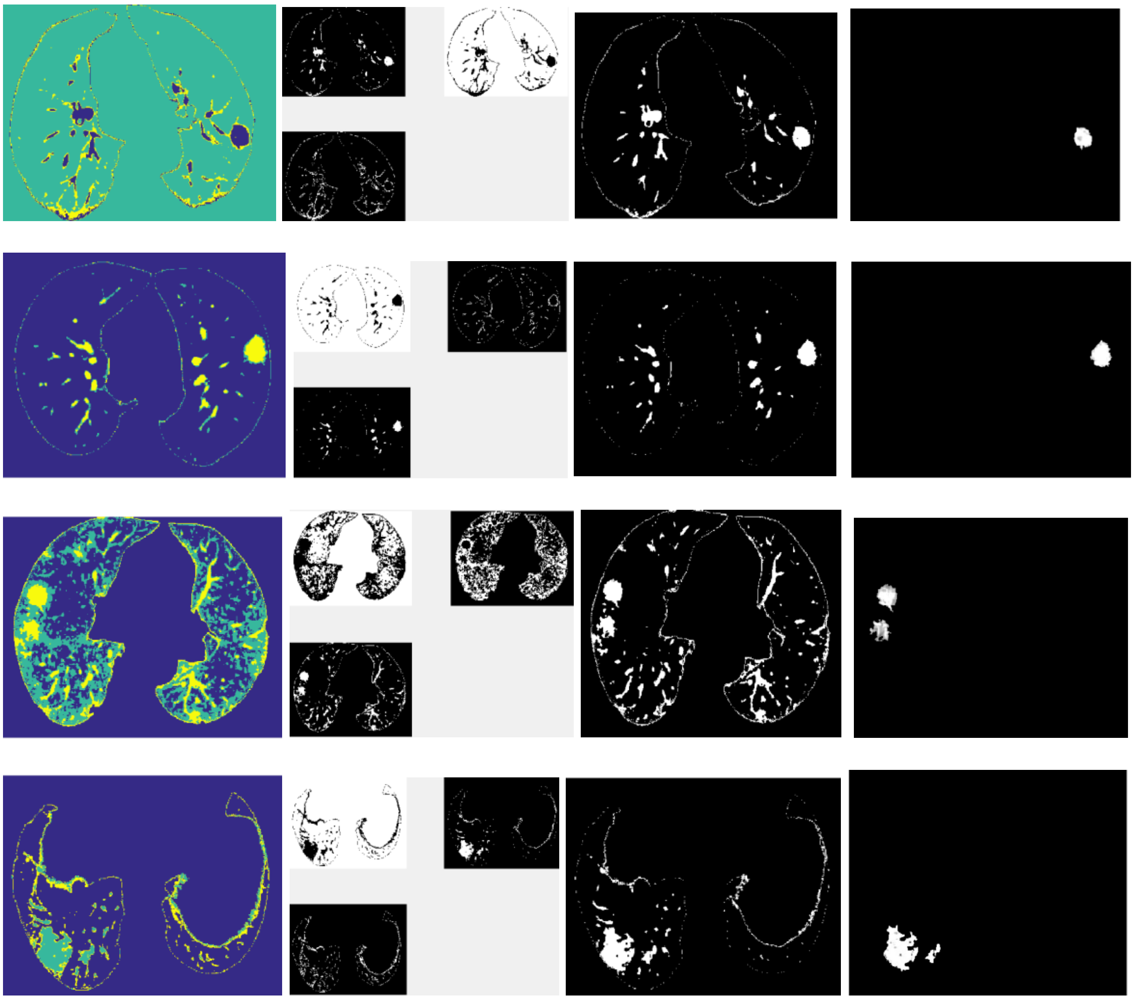

a b c d

Figure (13): Results of implementing FCM Clustering with three clusters. (a) segmented image, (b) the discrete clusters, (c) the cluster of the infected region and (d) the final extracted infected region.

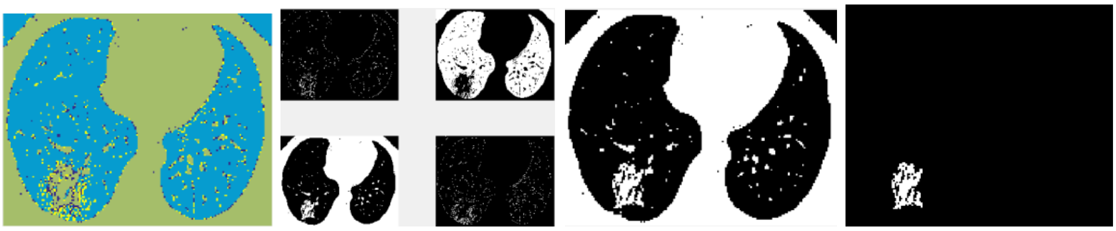

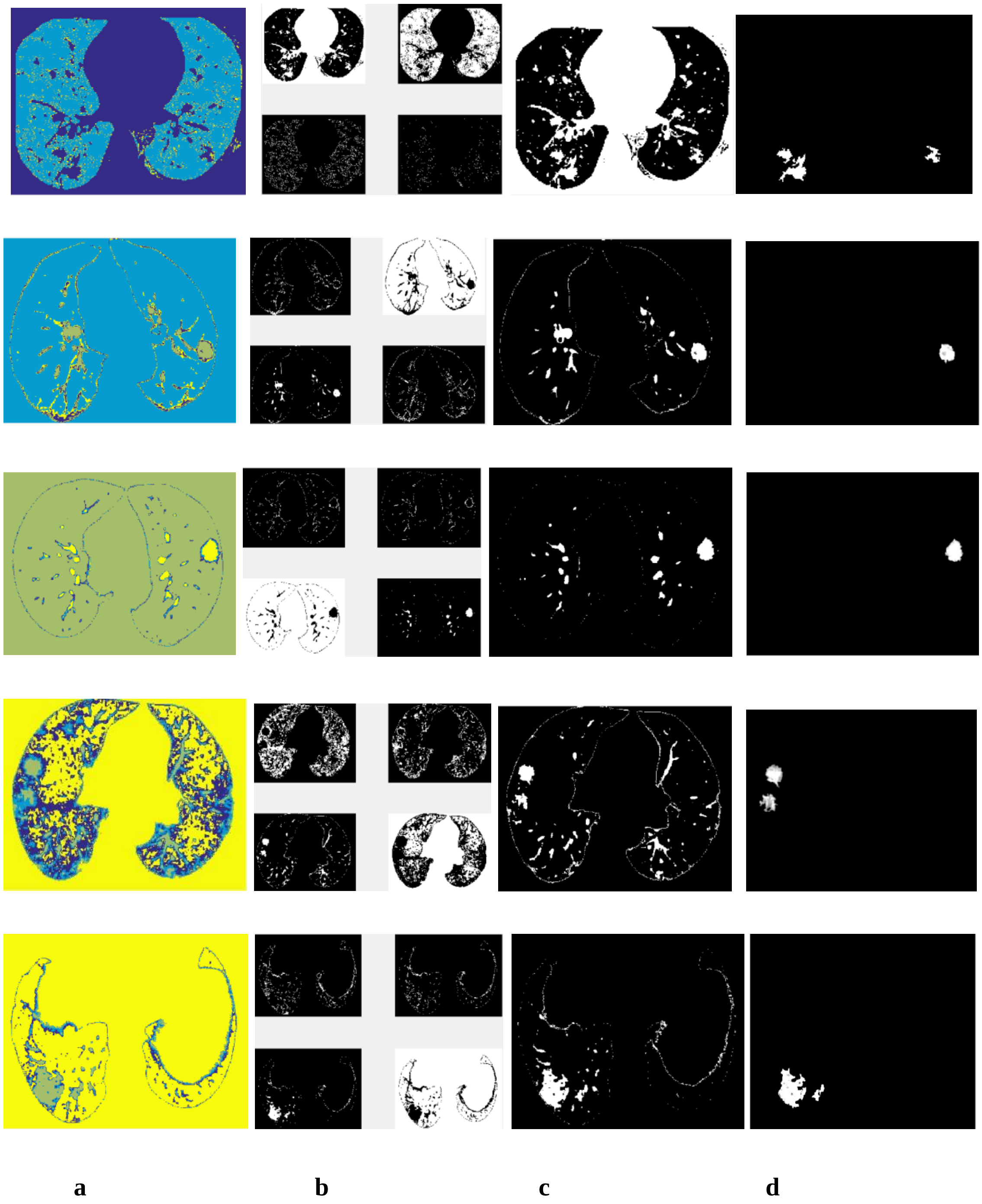

Figure (14): Results of implementing FCM Clustering with four clusters. (a) segmented image, (b) the discrete clusters, (c) the cluster of the infected region and (d) the final extracted infected region.

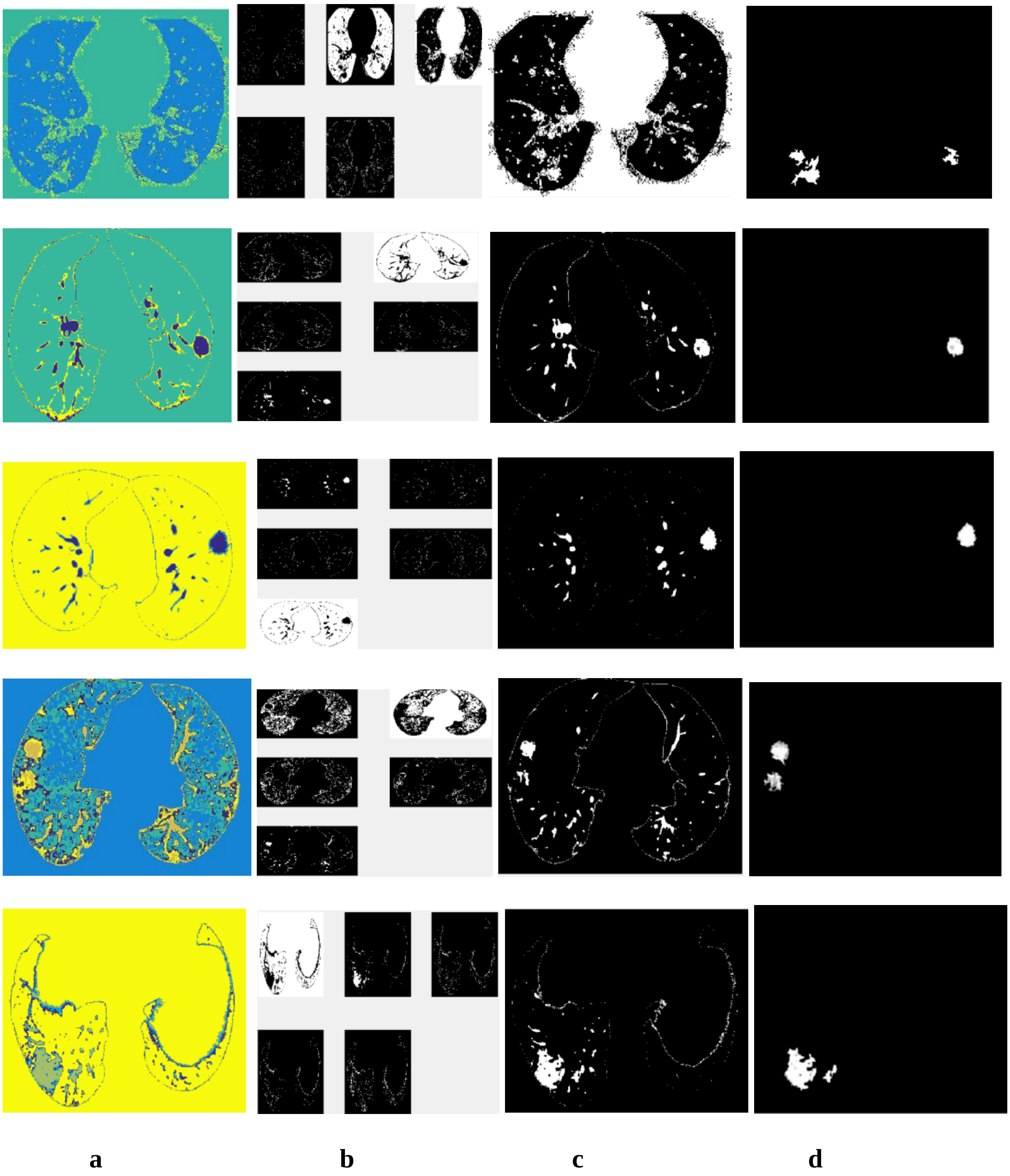

Figure (15): Results of implementing FCM Clustering with five clusters. (a) segmented image, (b) the discrete clusters, (c) the cluster of the infected region and (d) the final extracted infected region.

2- FCM Clustering with (3, 4 and 5) Clusters for Tumors Infected Lung CT Images:

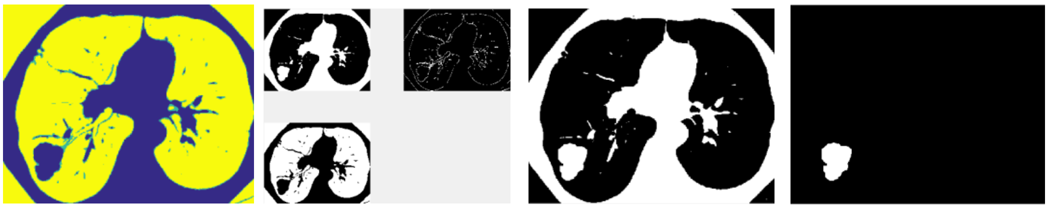

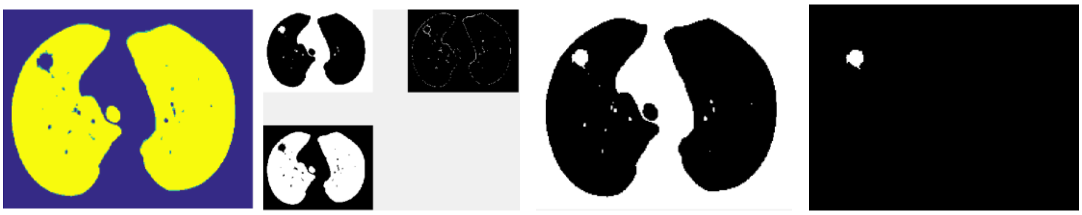

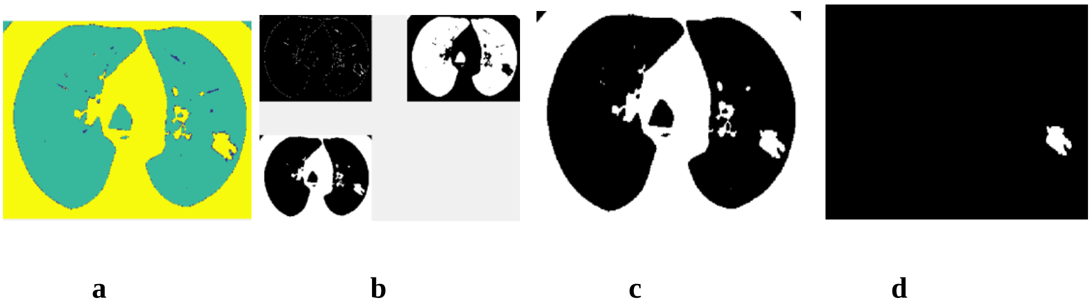

Figure (16): Results of implementing FCM Clustering with three clusters. (a) segmented image, (b) the discrete clusters, (c) the cluster of the infected region and (d) the final extracted infected region.

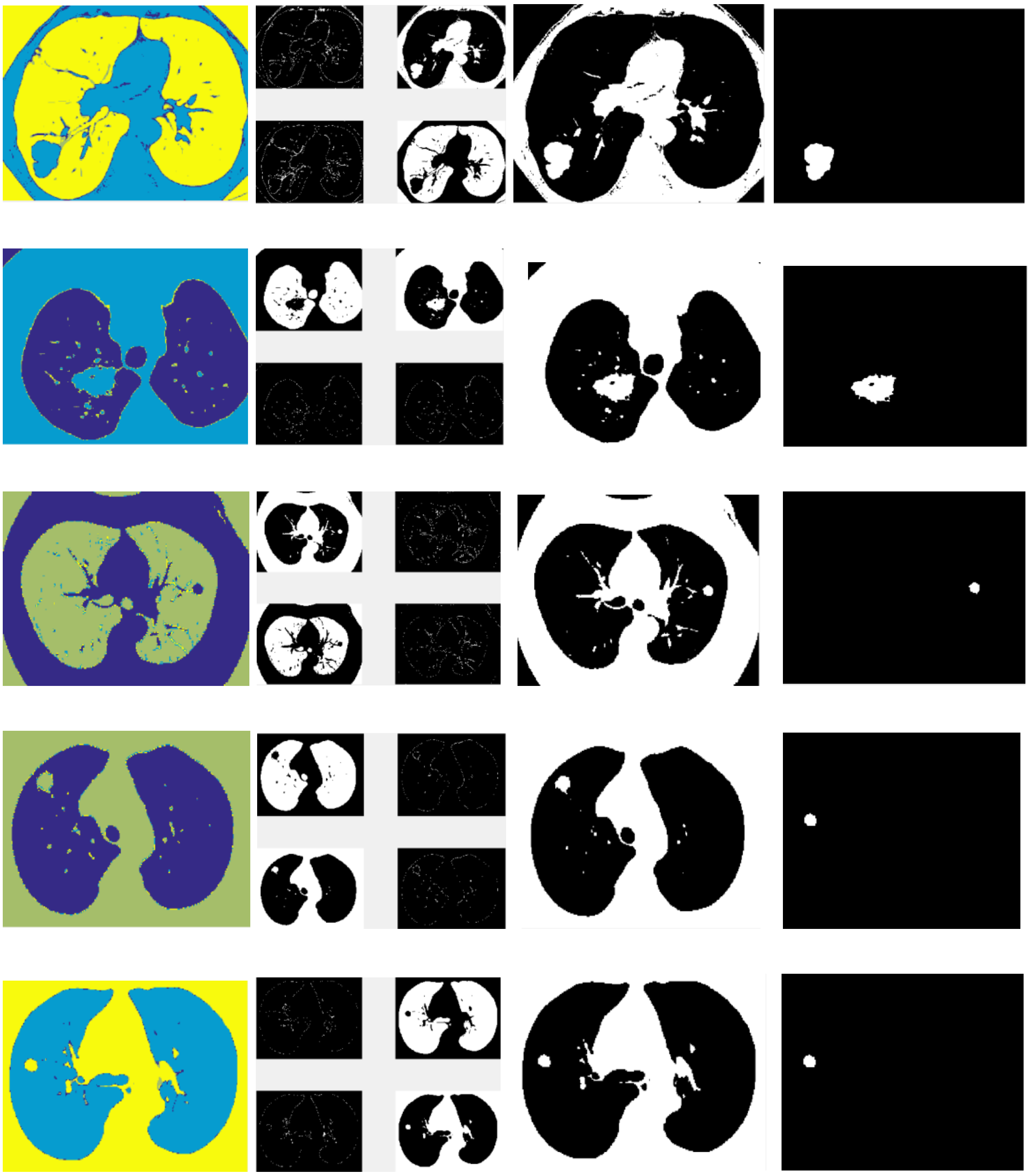

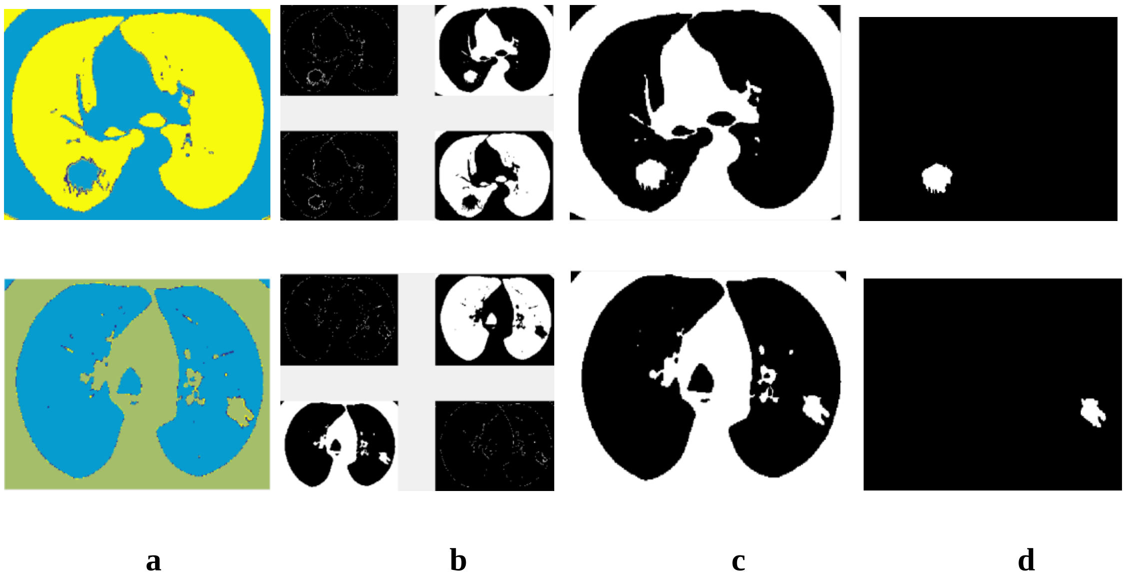

Figure (17): Results of implementing FCM Clustering with four clusters. (a) segmented image, (b) the discrete clusters, (c) the cluster of the infected region and (d) the final extracted infected region.

.

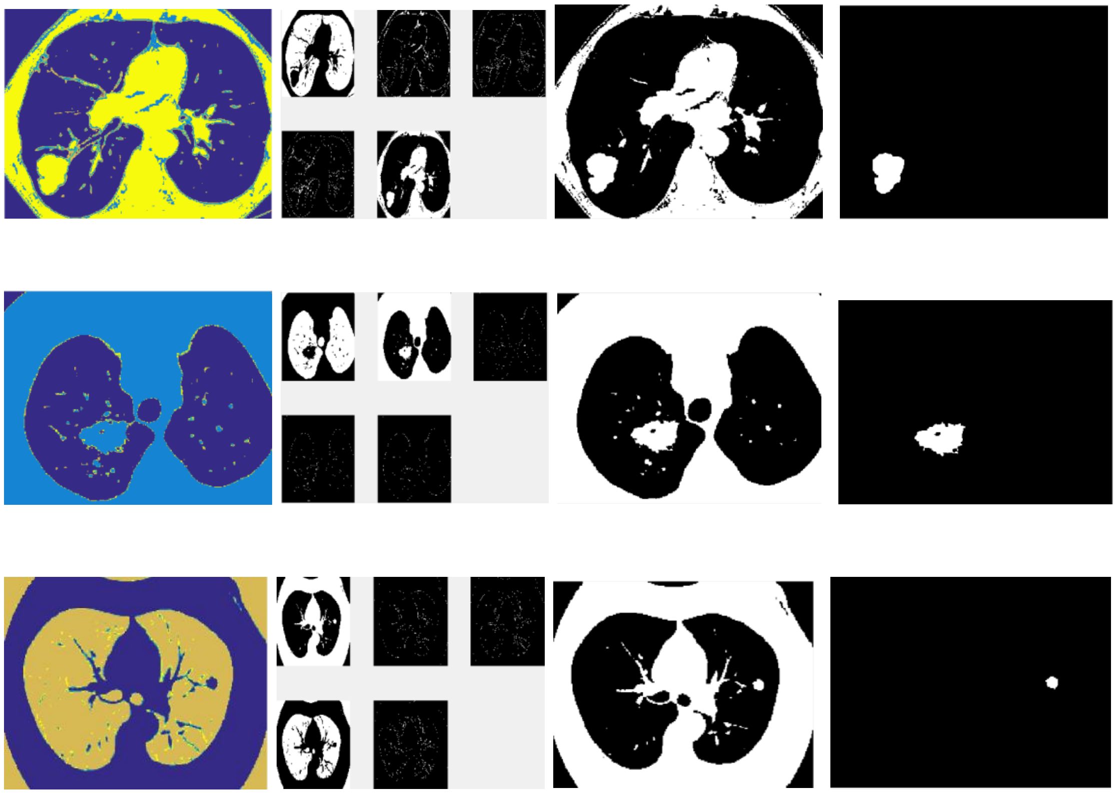

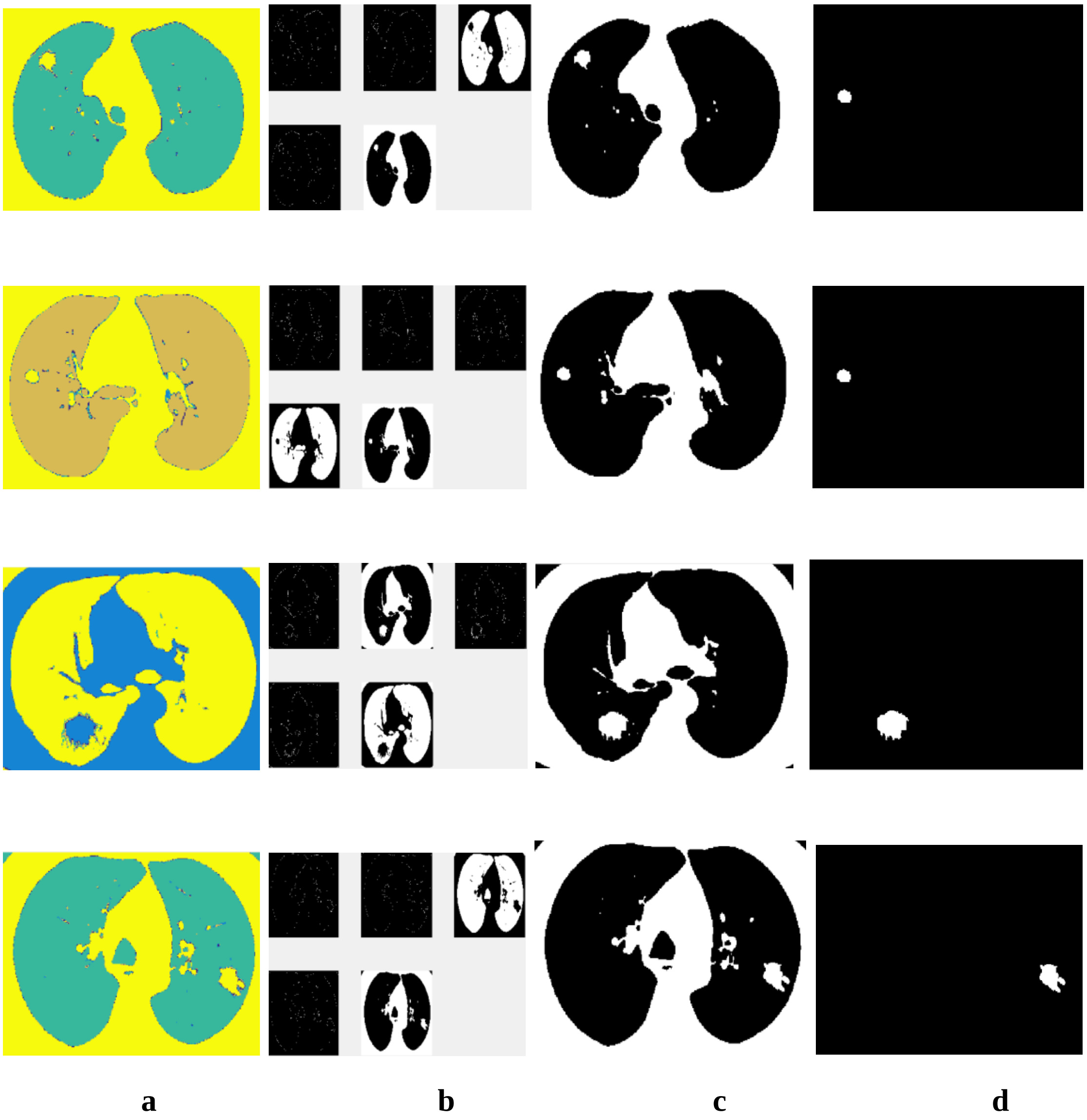

Figure (18): Results of implementing FCM Clustering with five clusters. (a) segmented image, (b) the discrete clusters, (c) the cluster of the infected region and (d) the final extracted infected region.

Appendix4

HSOFM Hybrid Technique

1- HSOFM Hybrid Technique with (3, 4 and 5) Nodes for Tumors Infected Lung CT Images:

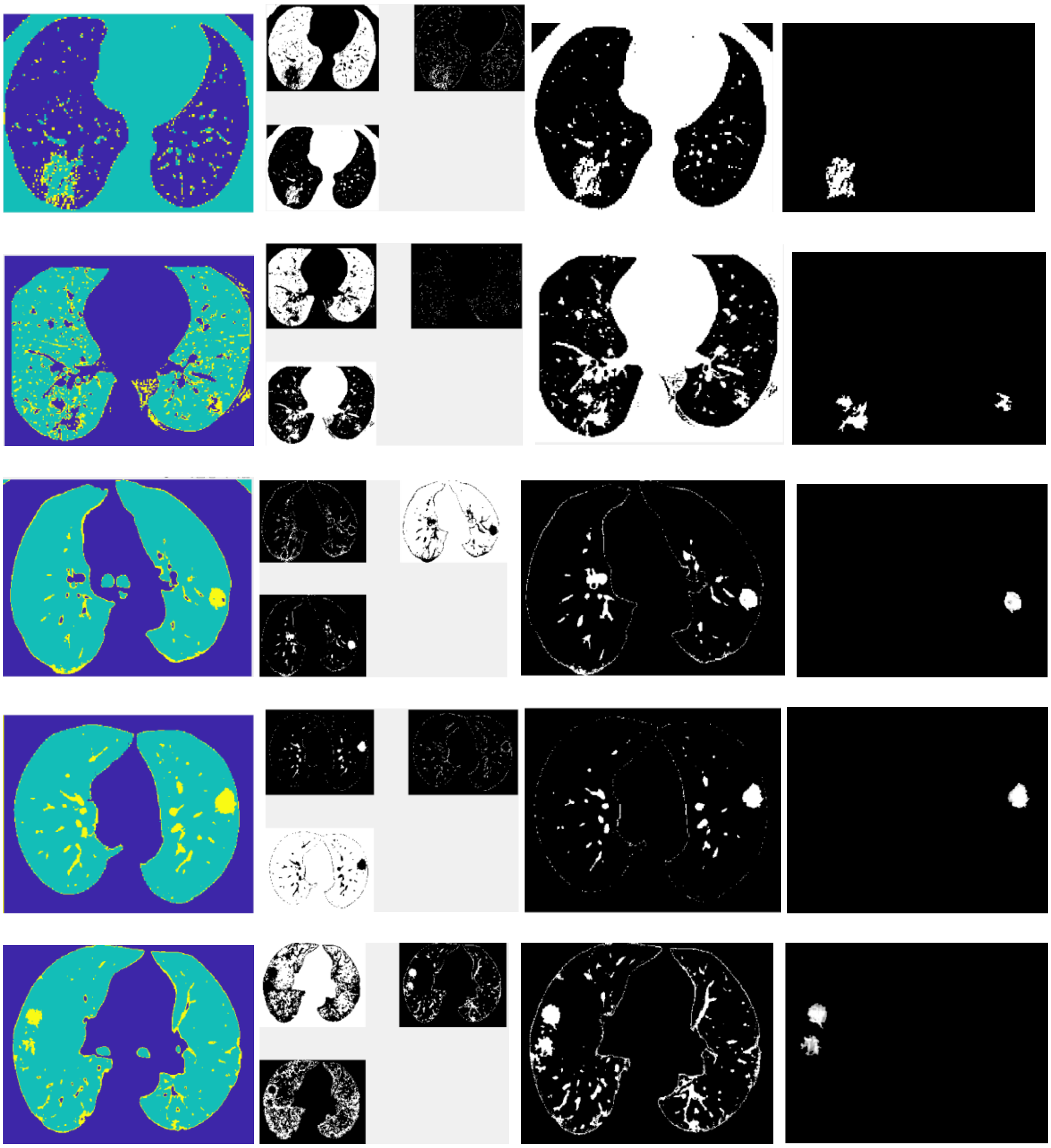

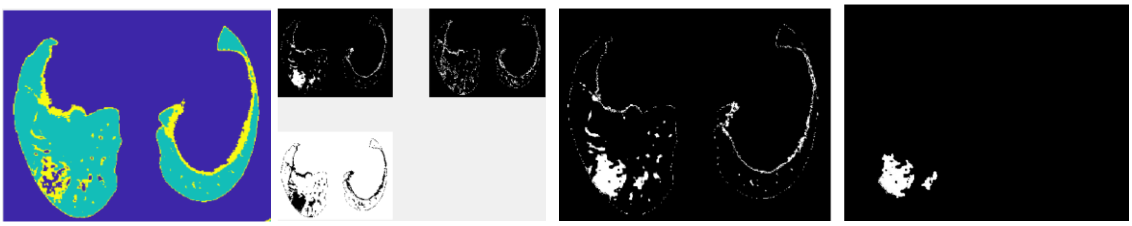

a **b** **c** **d**

Figure (19): Results of implementing the hybrid clustering technique with three clusters. (a) segmented image, (b) the discrete clusters, (c) the cluster of the infected region and (d) the final extracted infected region.

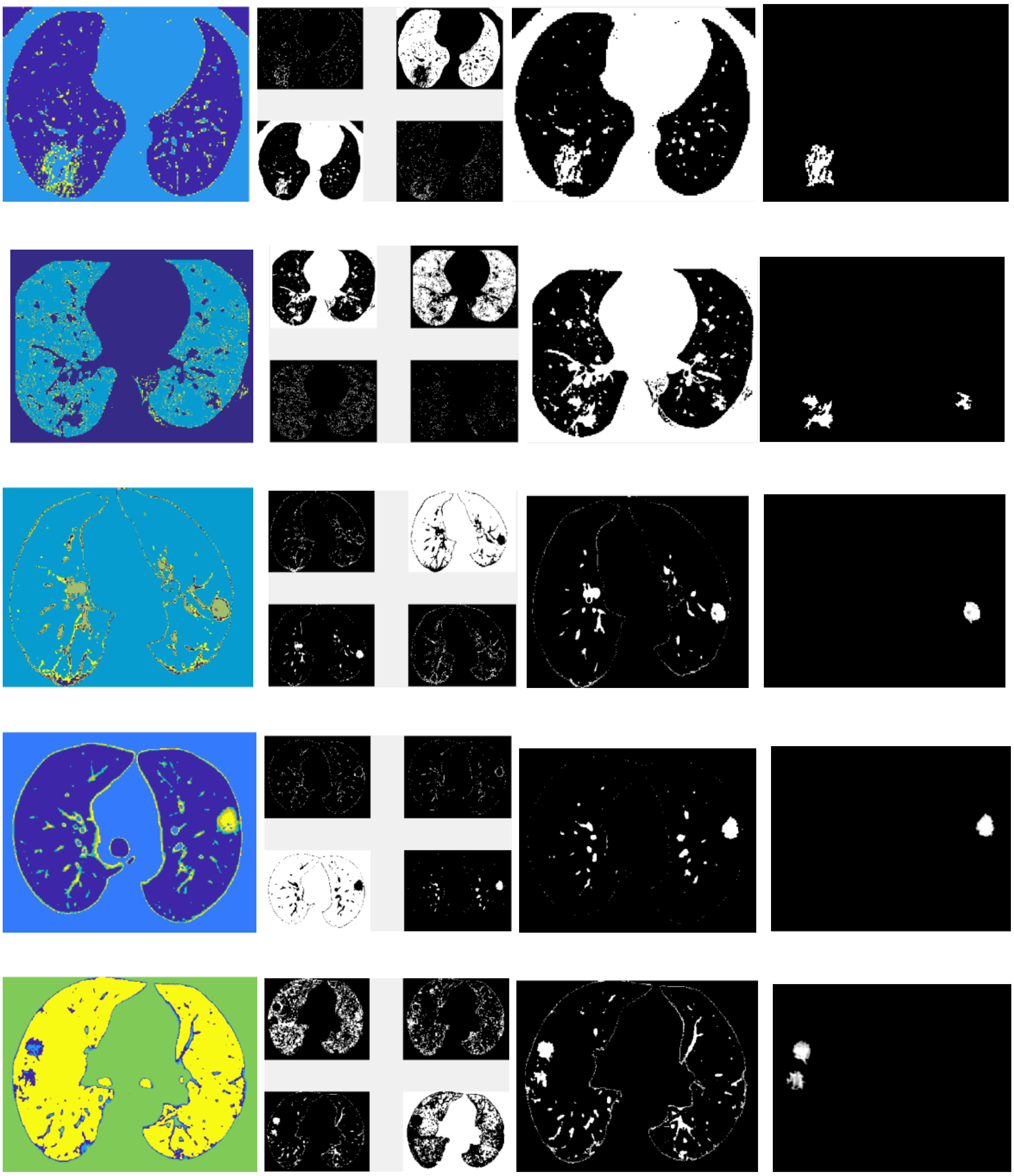

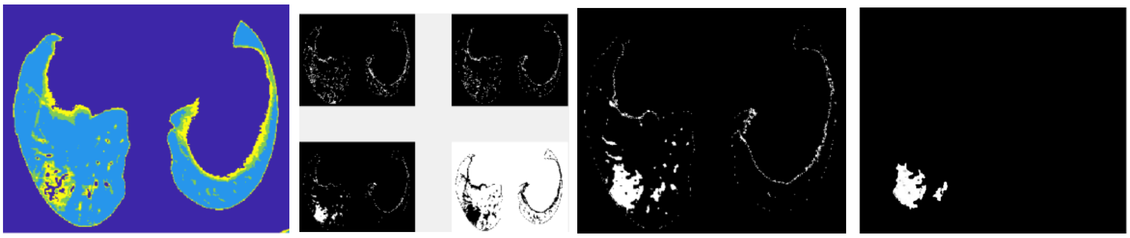

a b c d

Figure (20): Results of implementing the hybrid clustering technique with four clusters. (a) segmented image, (b) the discrete clusters, (c) the cluster of the infected region and (d) the final extracted infected region.

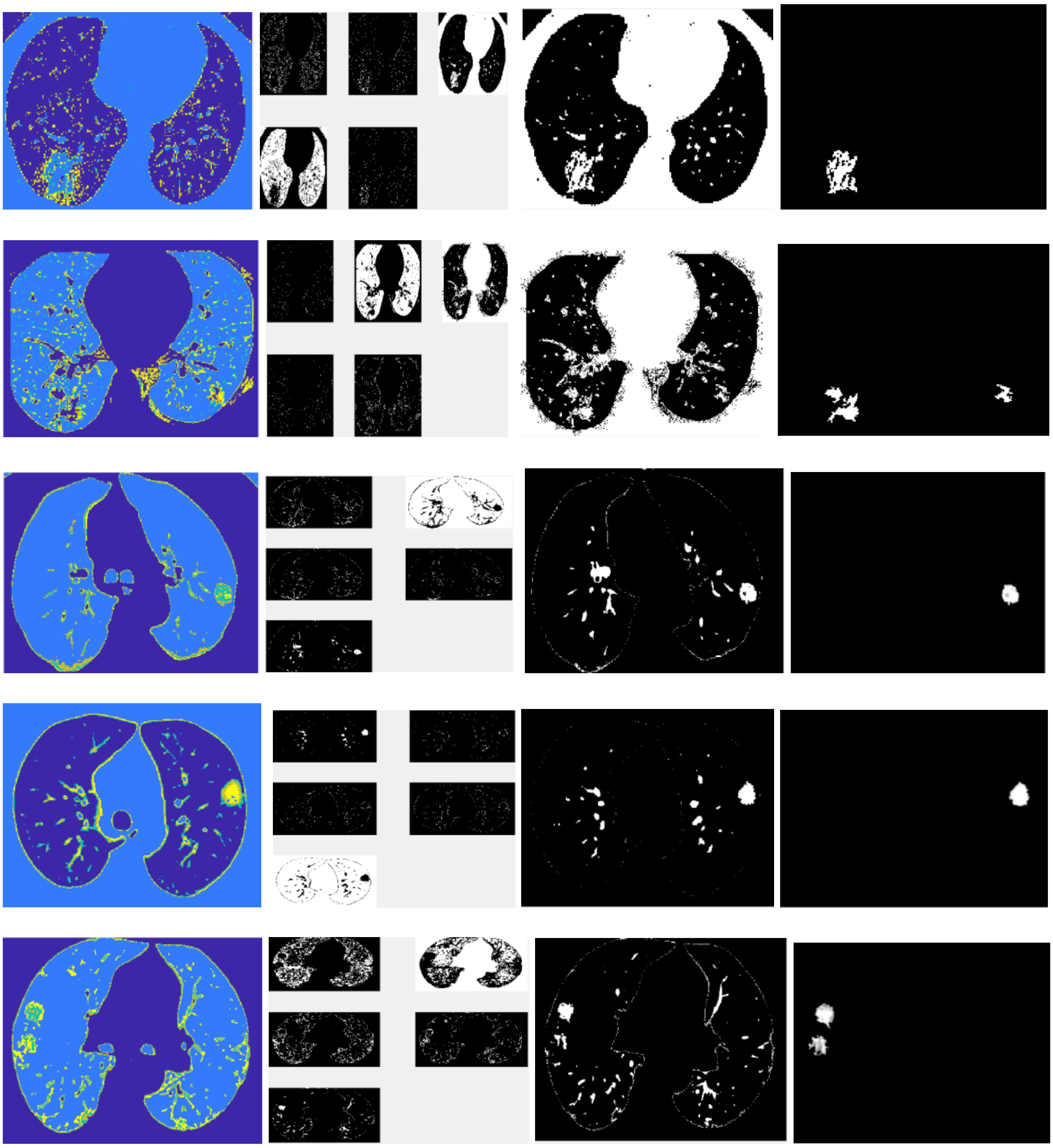

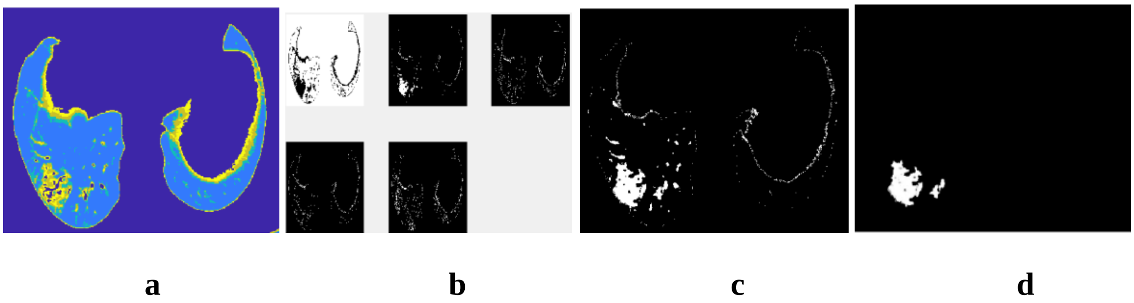

Figure (21): Results of implementing the hybrid clustering technique with five clusters. (a) segmented image, (b) the discrete clusters, (c) the cluster of the infected region and (d) the final extracted infected region

2- HSOFM Hybrid Technique with (3, 4 and 5) Nodes for Tumors Infected Lung CT Images:

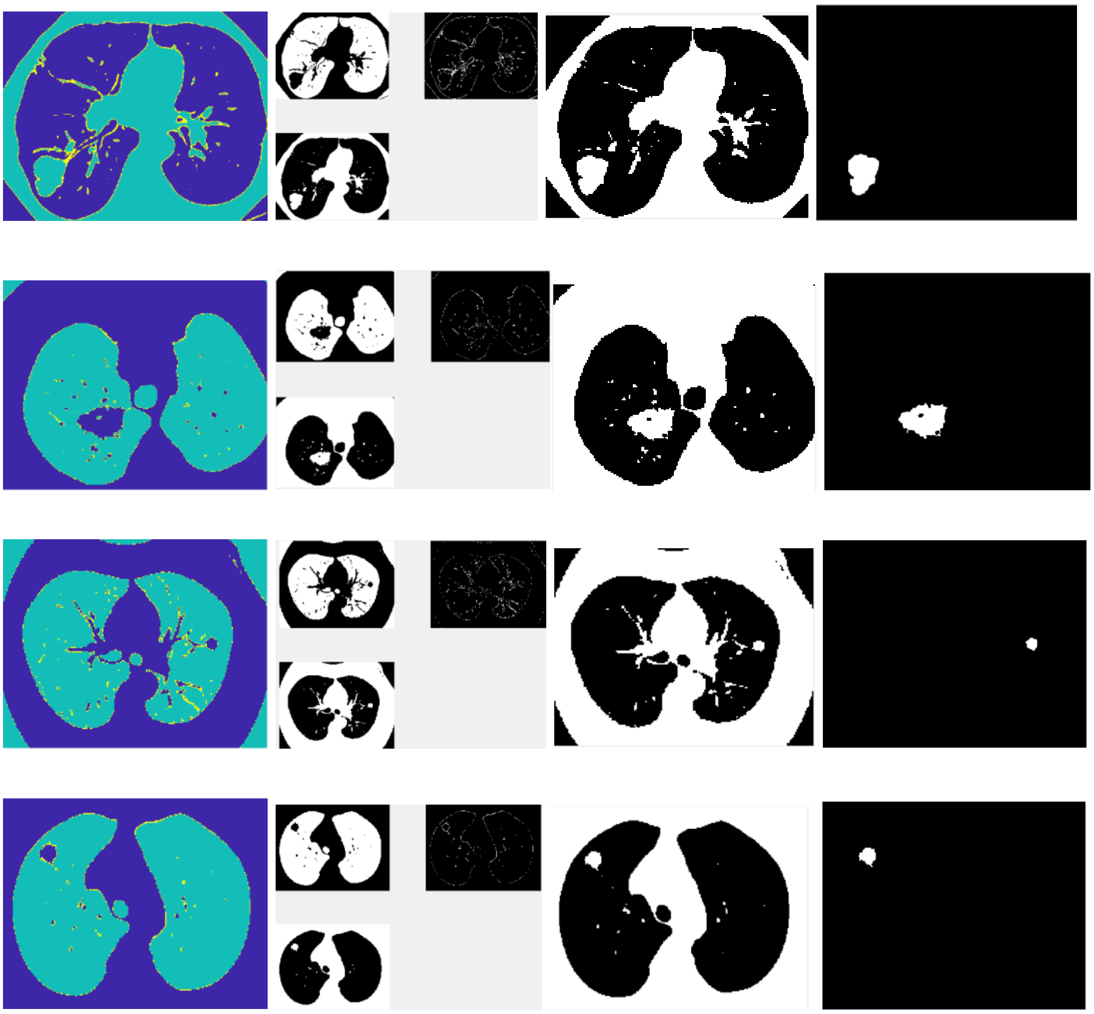

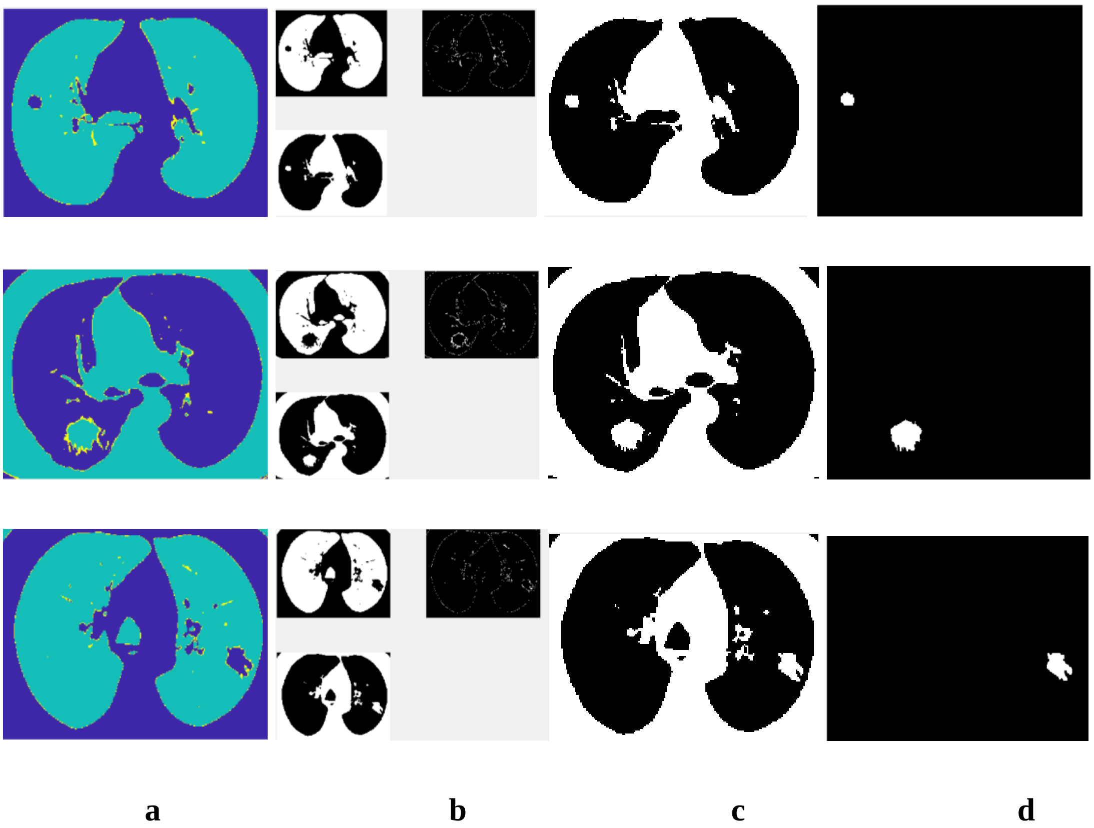

Figure (22): Results of implementing hybrid clustering technique with three nodes. (a) segmented image, (b) the discrete nodes, (c) the cluster of the infected region and (d) the final extracted infected region.

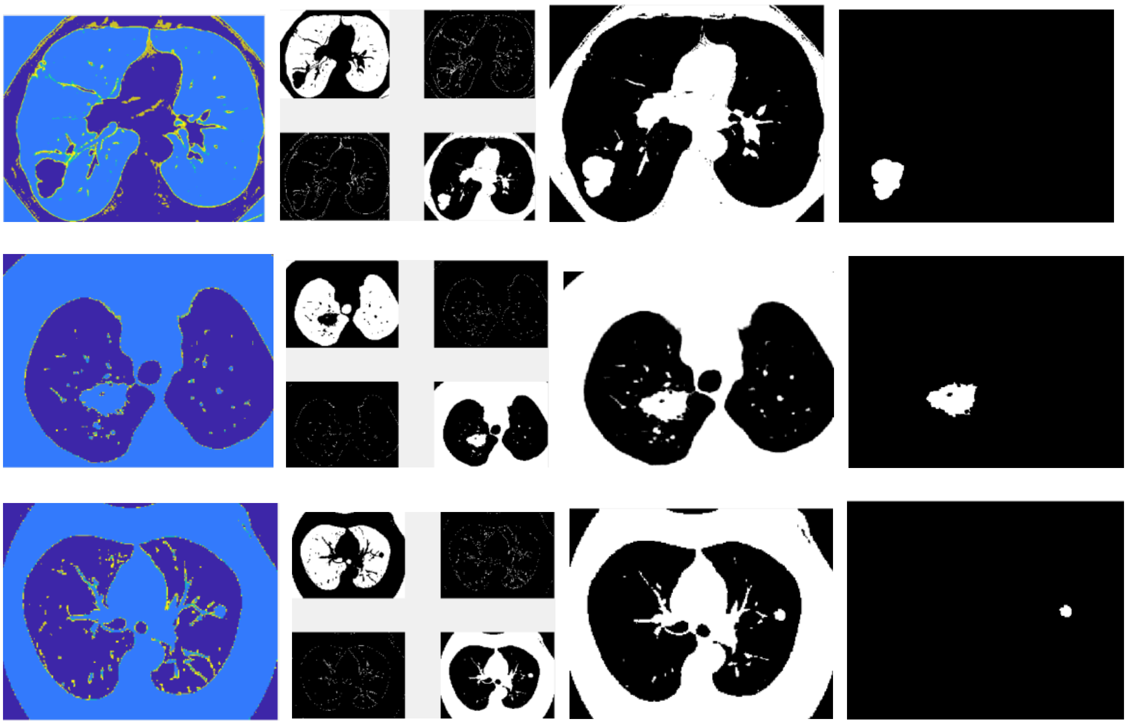

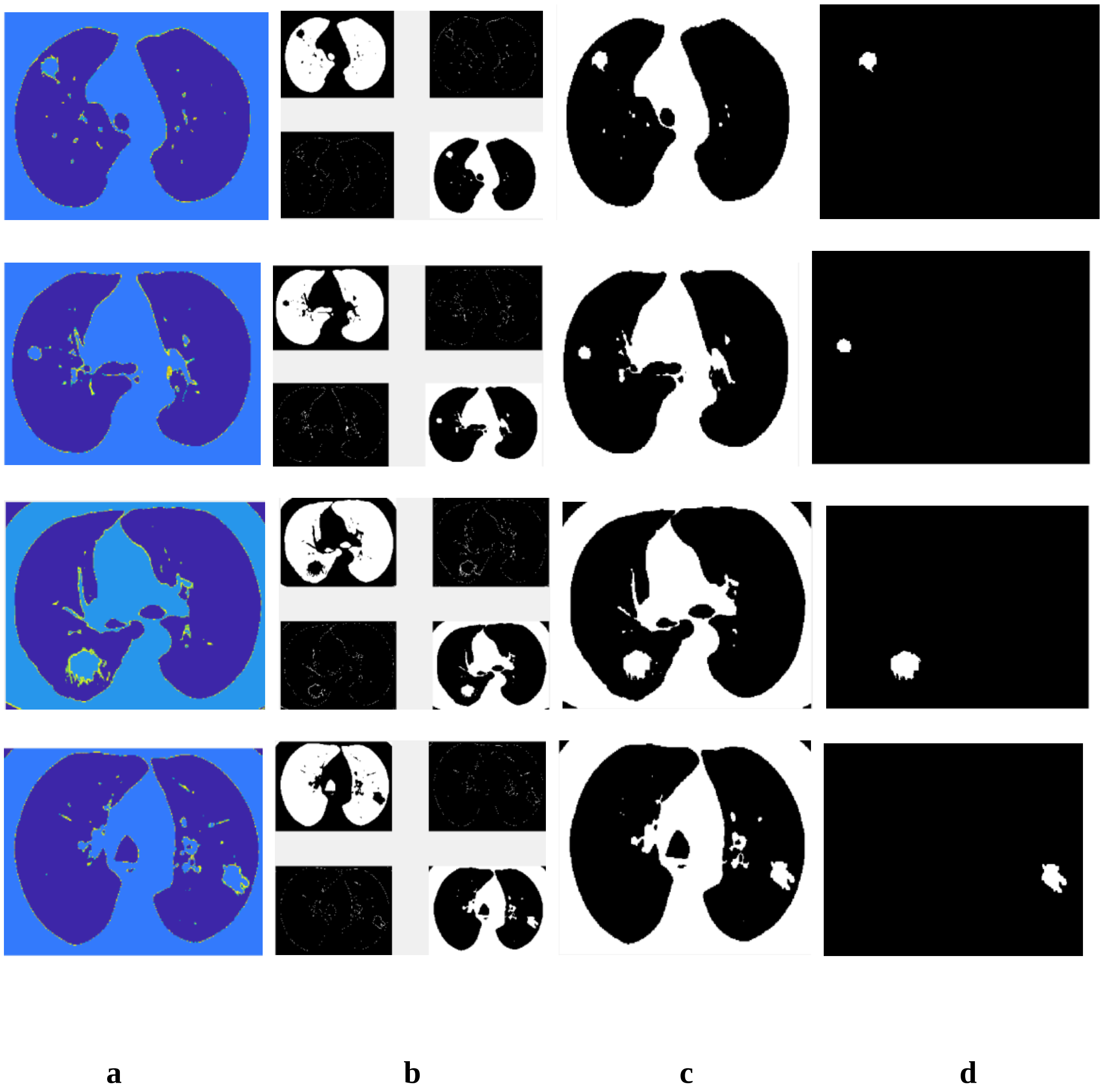

Figure (23): Results of implementing the hybrid clustering technique with four nodes. (a) segmented image, (b) the discrete nodes, (c) the cluster of the infected region and (d) the final extracted infected region.

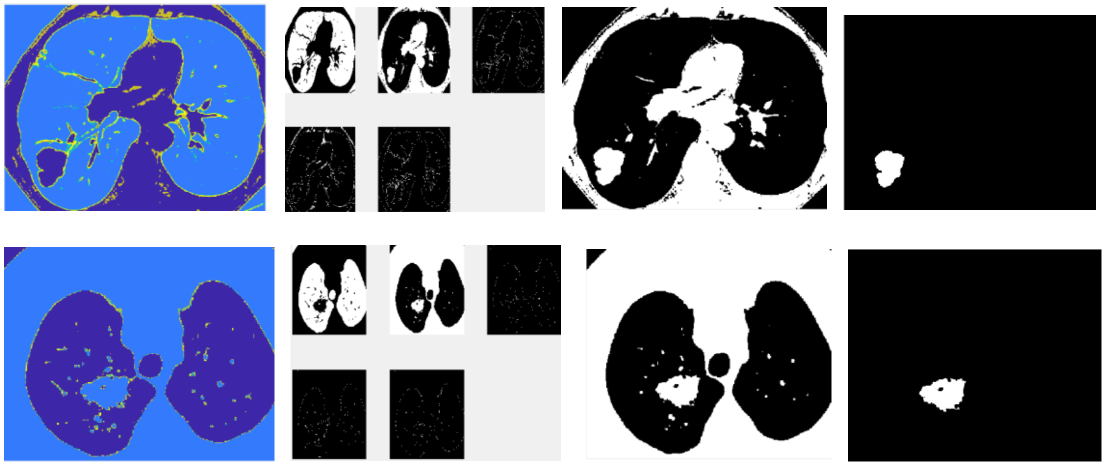

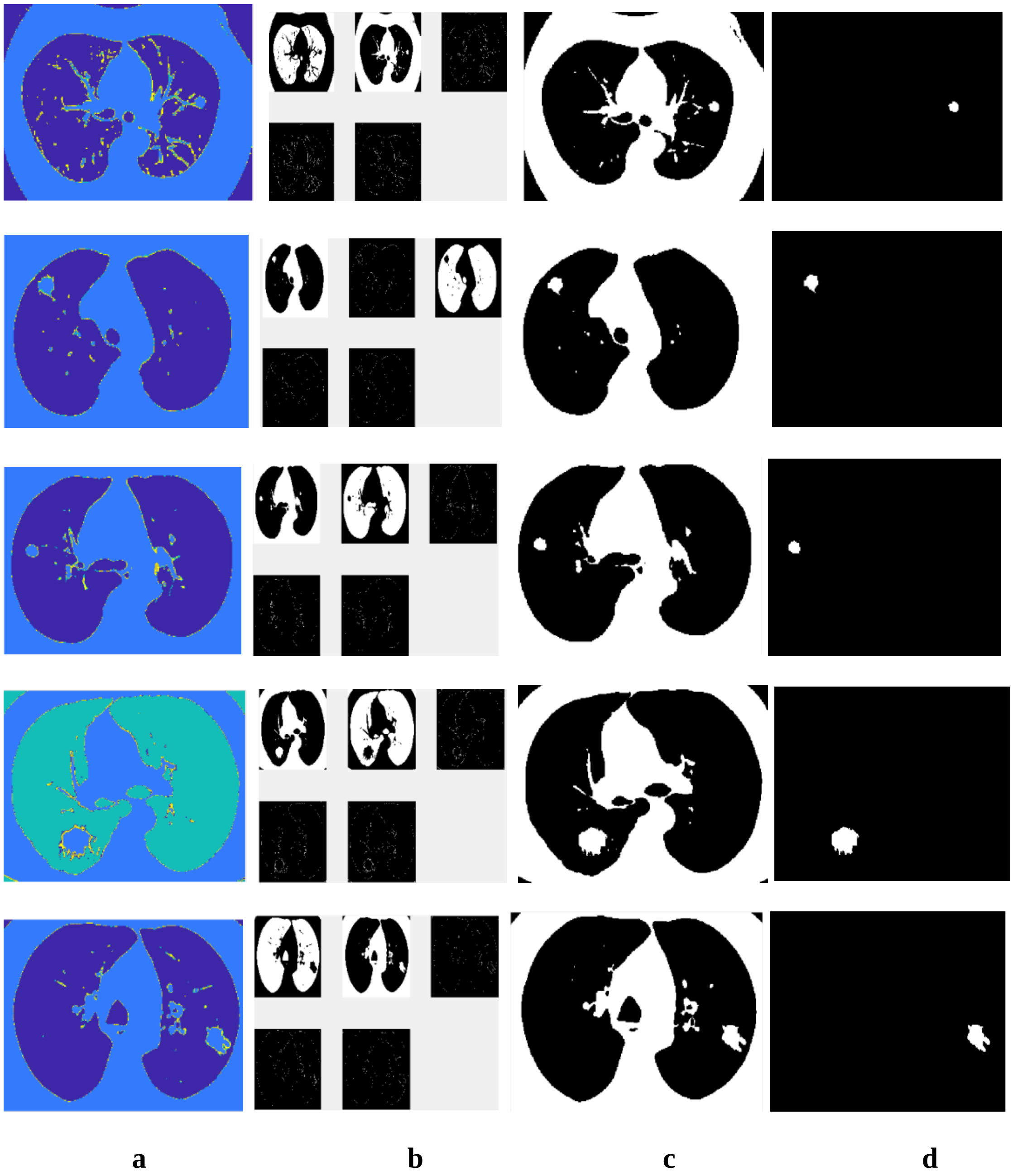

Figure (24): Results of implementing the hybrid clustering technique with five nodes. (a) segmented image, (b) the discrete nodes, (c) the cluster of the infected region and (d) the final extracted infected region.

Appendix5

Test Image Under Study by CNN

The images under study for Covid-19 and tumors, were tested The test result are shown in the Figures (25) and (26) for Covid-19 and tumors images respectively.

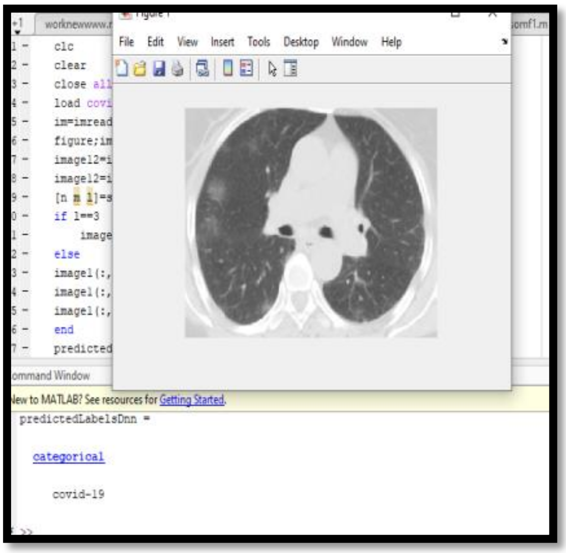

```
clc
clear
close all
load covi
im=imread
figure;im
image12=i
image12=i
[n m l]=s
if l==3
    image
else
image1(:,
image1(:,
image1(:,
end
predicted
```

```
Command Window
New to MATLAB? See resources for Getting Started.
 predictedLabelsDnn =

   categorical

     covid-19

>>
```

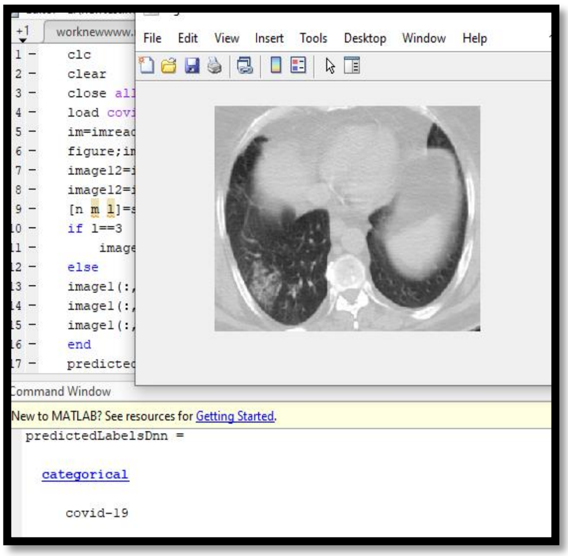

```
clc
clear
close all
load covi
im=imread
figure;im
image12=i
image12=i
[n m l]=s
if l==3
    image
else
image1(:,
image1(:,
image1(:,
end
predicted
```

```
Command Window
New to MATLAB? See resources for Getting Started.
 predictedLabelsDnn =

   categorical

     covid-19
```

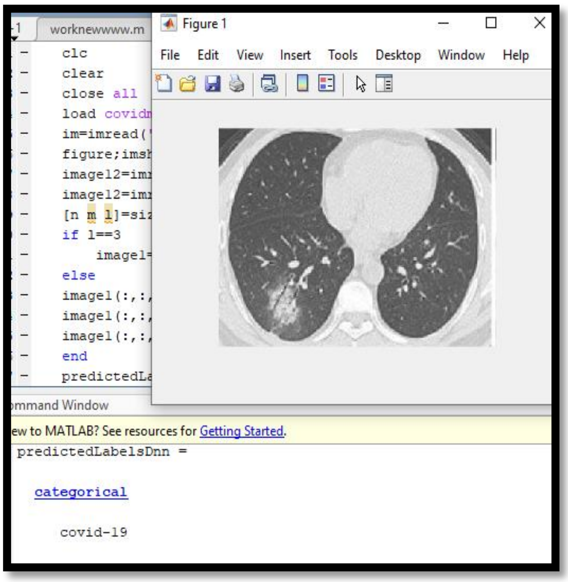

```
clc
clear
close all
load covidm
im=imread('
figure;imsh
image12=imr
image12=imr
[n m l]=siz
if l==3
    image1=
else
image1(:,:,
image1(:,:,
image1(:,:,
end
predictedLa
```

```
Command Window
New to MATLAB? See resources for Getting Started.
 predictedLabelsDnn =

   categorical

     covid-19
```

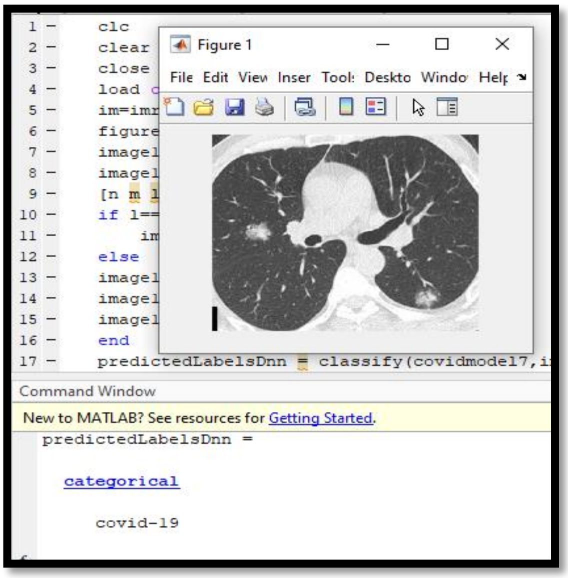

```
clc
clear
close
load c
im=imr
figure
image1
image1
[n m l
if l==
    im
else
image1
image1
image1
end
predictedLabelsDnn = classify(covidmodel7,i
```

```
Command Window
New to MATLAB? See resources for Getting Started.
 predictedLabelsDnn =

   categorical

     covid-19
```

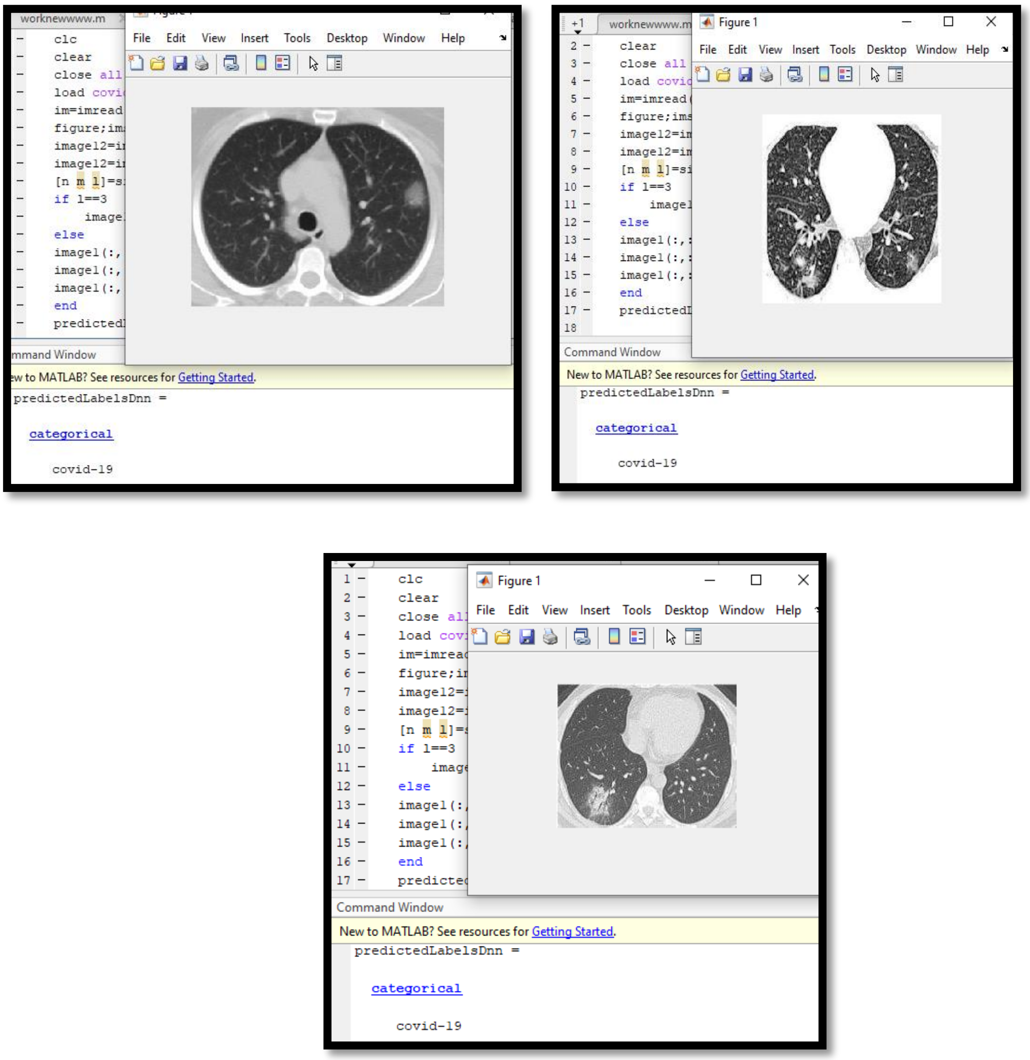

```
clc
clear
close all
load covi
im=imread
figure;im
image12=i
image12=i
[n m l]=s
if l==3
    image
else
image1(:,
image1(:,
image1(:,
end
predicted
```

ew to MATLAB? See resources for Getting Started.

```
predictedLabelsDnn =

  categorical

     covid-19
```

```
clear
close all
load covic
im=imread(
figure;ims
image12=im
image12=im
[n m l]=si
if l==3
    image1
else
image1(:,:
image1(:,:
image1(:,:
end
predictedL
```

New to MATLAB? See resources for Getting Started.

```
predictedLabelsDnn =

  categorical

     covid-19
```

```
clc
clear
close all
load cov
im=imread
figure;im
image12=i
image12=i
[n m l]=s
if l==3
    imag
else
image1(:,
image1(:,
image1(:,
end
predicte
```

New to MATLAB? See resources for Getting Started.

```
predictedLabelsDnn =

  categorical

     covid-19
```

Figure (25): Test result for Covid-19.

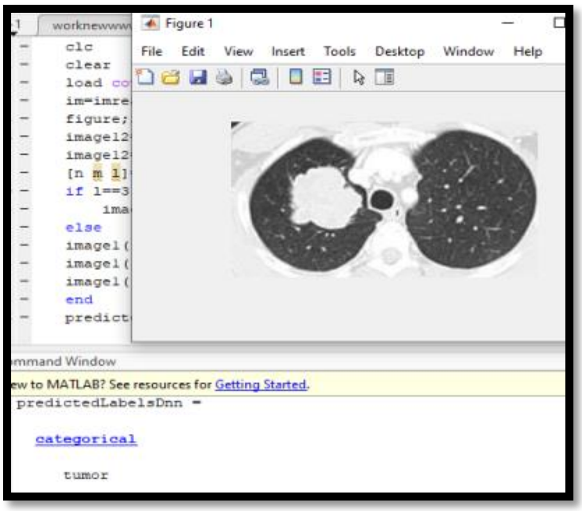

```
clc
clear
load co
im=imre
figure;
image12
image12
[n m l]
if l==3
    ima
else
image1(
image1(
image1(
end
predict
```

```
mmand Window
ew to MATLAB? See resources for Getting Started.
predictedLabelsDnn =

  categorical

    tumor
```

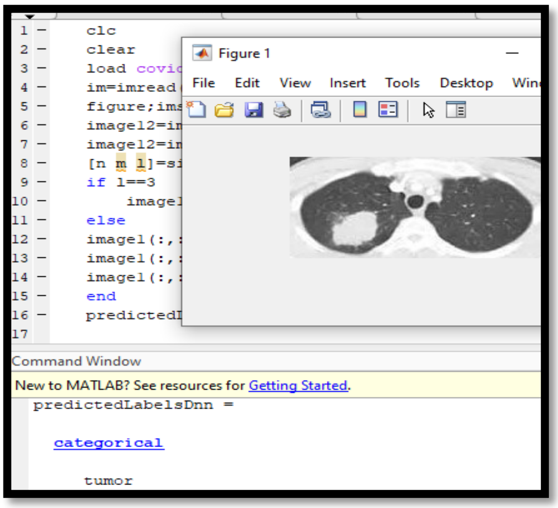

```
clc
clear
load covic
im=imread
figure;ims
image12=in
image12=in
[n m l]=si
if l==3
    imagel
else
image1(:,:
image1(:,:
image1(:,:
end
predictedI
```

```
Command Window
New to MATLAB? See resources for Getting Started.
  predictedLabelsDnn =

    categorical

      tumor
```

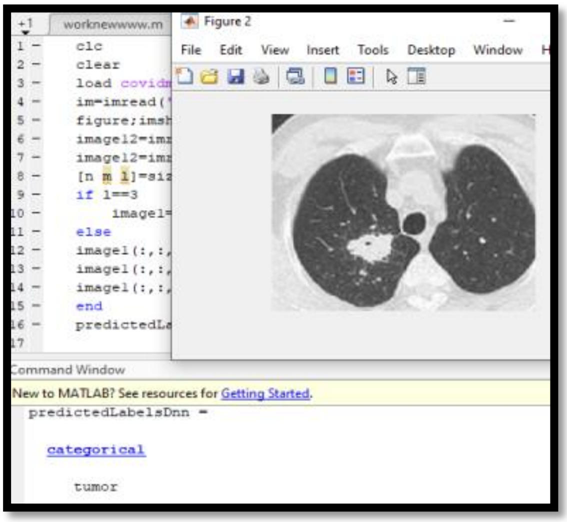

```
clc
clear
load covidn
im=imread('
figure;imsh
image12=imr
image12=imr
[n m l]=siz
if l==3
    image1=
else
image1(:,:,
image1(:,:,
image1(:,:,
end
predictedLa
```

```
Command Window
New to MATLAB? See resources for Getting Started.
  predictedLabelsDnn =

    categorical

      tumor
```

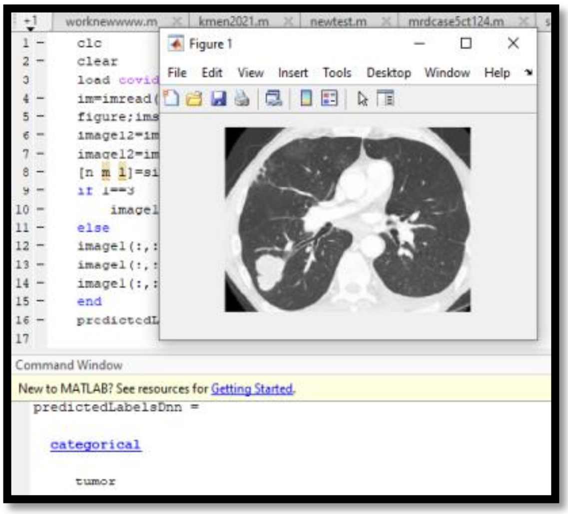

```
clc
clear
load covid
im=imread(
figure;ims
image12=im
image12=im
[n m l]=si
if l==3
    image1
else
image1(:,:
image1(:,:
image1(:,:
end
predictedL
```

```
Command Window
New to MATLAB? See resources for Getting Started.
  predictedLabelsDnn =

    categorical

      tumor
```

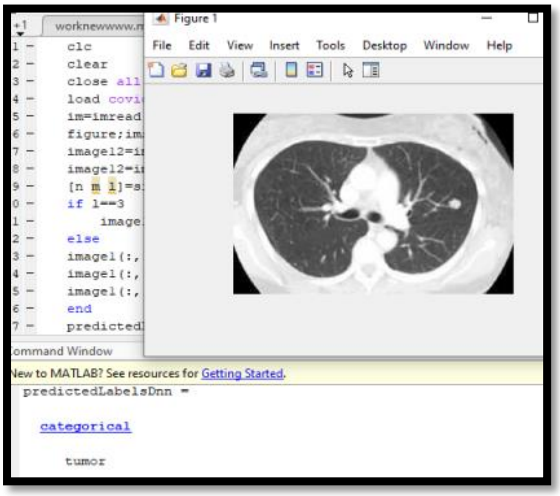

```
clc
clear
close all
load covi
im=imread
figure;im
image12=i
image12=i
[n m l]=s
if l==3
    image
else
image1(:,
image1(:,
image1(:,
end
predicted
```

```
ommand Window
lew to MATLAB? See resources for Getting Started.
  predictedLabelsDnn =

    categorical

      tumor
```

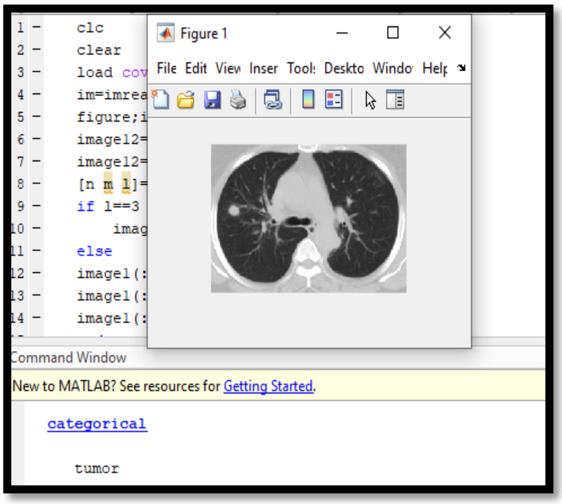

```
clc
clear
load cov
im=imrea
figure;i
image12=
image12=
[n m l]=
if l==3
    imag
else
image1(:
image1(:
image1(:
```

```
Command Window
New to MATLAB? See resources for Getting Started.

  categorical

    tumor
```

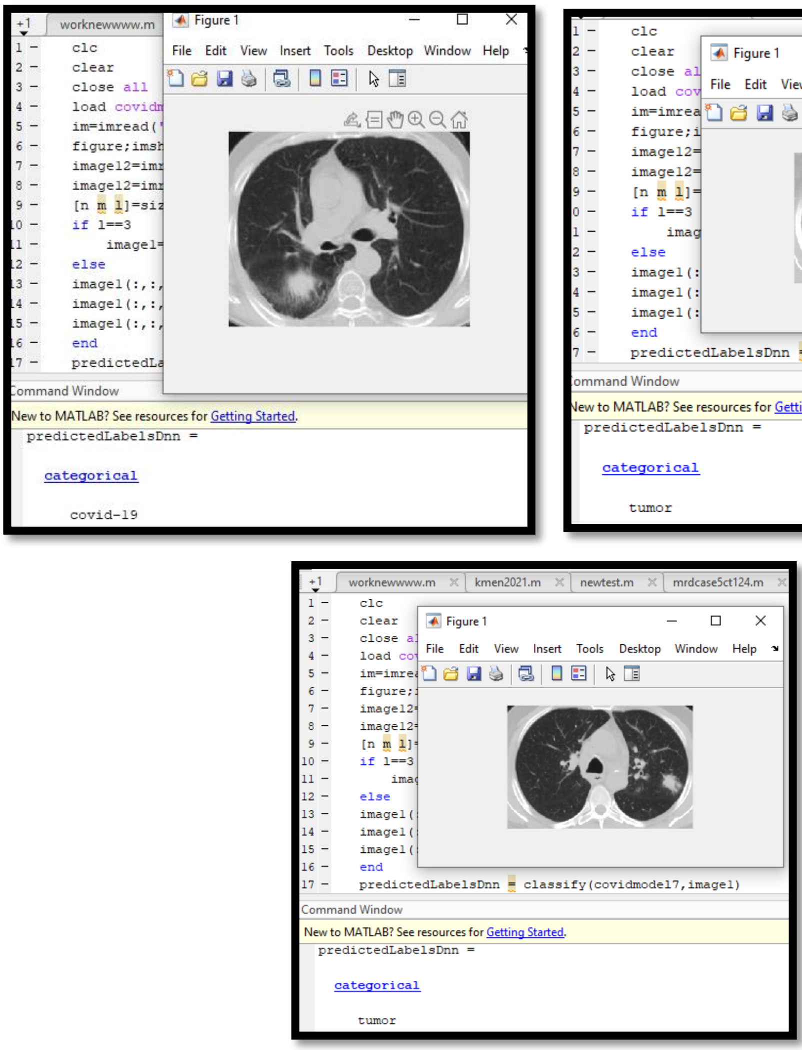

```
clc
clear
close all
load covidm
im=imread('
figure;imsh
image12=imr
image12=imr
[n m l]=siz
if l==3
    image1=
else
image1(:,:,
image1(:,:,
image1(:,:,
end
predictedLa
```

```
predictedLabelsDnn =

  categorical

     covid-19
```

```
clc
clear
close al
load cov
im=imrea
figure;i
image12=
image12=
[n m l]=
if l==3
    imag
else
image1(:
image1(:
image1(:
end
predictedLabelsDnn = classify(covidmodel7,image1)
```

```
predictedLabelsDnn =

  categorical

     tumor
```

```
clc
clear
close a
load co
im=imre
figure;
image12
image12
[n m l]
if l==3
    ima
else
image1(
image1(
image1(
end
predictedLabelsDnn = classify(covidmodel7,image1)
```

```
predictedLabelsDnn =

  categorical

     tumor
```

Figure (26): Test result for Tumor.

General Introduction

1.1 Introduction

The technology of digital image processing is the use of a number of computer algorithms to process digital images. This process can lead to either images or a set of characteristics or properties that are representative of the original images. Digital image processing is often used in robotics and other intelligent systems, medical imaging, remote sensing, photography, and forensics. The main goal of digital image processing is to make it possible for people to get a high-quality image or one that describes the original image. Also, unlike the human visual system, which can adapt to different situations, imaging or sensory machines aren't quick to automatically pick up "meaningful" targets [1]. Digital images have a huge effect on modern society, so image processing is now an important part of both science and technology. With the rapid advancements in computerized medical image reconstruction, analysis methodologies, and computer-aided diagnosis, medical imaging has become an important subfield of scientific imaging [2].

The production of new pieces of machinery is capable of high-speed image acquisition and of greater resolutions calls for a large amount of work to be put toward the development of methods that process photos in a more time-effective manner. In addition, medical applications make use of new image modalities and require algorithms for the interpretation of these images as well as for the registration and fusion of the various image modalities; consequently, image processing is a fruitful area for the development of applications that span multiple disciplines [3].

1.2 Medical Image Processing

Medical imaging become a commonplace and necessary aspect of everyday practice. Rather than relying on symptoms to make a diagnosis, doctors might look for specific pathologies [4]. Medical image analysis and processing are very important, especially for non-invasive treatments and clinical research. Many illnesses may now be detected and diagnosed with it, making it a vital diagnostic tool. Using this technology, doctors and radiologists can have a better understanding of specific diagnoses. In addition, imaging aids doctors in visualizing and analyzing images to better comprehend internal structural anomalies [5].

Since X-rays were discovered more than 100 years ago, several imaging methods have been created to show the human body's anatomy, the shape of its tissues, and how its muscles, bones, and nerves work. Most people have heard of computed tomography (CT), magnetic resonance imaging (MRI), and ultrasound (US). However, magnetic resonance spectroscopy imaging (MRSI), fluorescence endoscopy, CT angiography, and optical surface scanning (OSS) are also used in clinical practice [6].

1.3 Image Enhancement

Image enhancement aims to process an image so that the resulting image is of more enhanced quality as compared to original image [7]. Image enhancement is essentially perception improvement of information in likeness for human viewers and ensuring the provision of improved input for different image processing approaches that are automated. Modification of one or more characteristics of the image is done with the selection of characteristics including the modification process being particular to specific work because of the availability of many techniques for digital image enhancement without alteration. The classification of the enhancement method entails two class's spatial domain methods and frequency domain methods [8]

1.4 Image Segmentation

Image segmentation is usually the first step of most analysis procedures [9]. Segmentation of an image entails the division or separation of the image into regions of similar attribute represented by the grouping of a set of pixels that share similar characteristics, such as intensity and texture. The most basic attribute for segmentation is image luminance amplitude for a monochrome image and color components for a color image. Image edges and texture are also useful attributes for segmentation [10].

Identification of the boundaries of objects in images, is one of the most important problems in computer vision and image processing. The applications of segmentation techniques range from medicine (i.e., locating an injury) to industry (i.e., robotic vision) and the military (i.e., target detection). Medical imaging plays an increasingly important role in the diagnosis and handling of disease, segmentation techniques have been applied to extract clinically useful information about anatomic structures through techniques such as x-ray, CT, MRI, PET, ultrasound and other techniques. The segmentation of the images can be performed either manually and medically by using image processing and computer vision techniques [11]. Automated image segmentation aims to extract object boundary features and it plays a fundamental role in understanding image content [12].

1.6 Literature Review

Many researchers have implemented ANN, and many other methods for training and testing as well for segmenting purpose. In the following a review of some of their studies:

- **Kiran S. Darne and Suja S. Panicker, (2013)[13]** utilized two different methods: FCM and Fuzzy Min-Max Neural Network (FMNN) for lung images (plain X-ray and CT scan). Both FCM and FMNN have implemented the independent results of FMNN and FCM on the standard datasets to detect lung cancer. The algorithms are tested on standard datasets, like the lung cancer dataset from the metadata repository. This dataset was then normalized using the Min-Max method, which was also used to make the training and testing datasets.

- **Ada and Rajneet Kaur, (2013)[14]** proposed a way to improve lung CT scan images that was a hybrid method that used both factor extraction and Principal Component Analysis (PCA). In their work, feature extraction and PCA for lung extraction were utilized. For the pre-processing step of the images, most of the features were taken out using component analysis and histogram equalization. The system produced capable results for lung tumor detection.

- **Wafaa Abdul Ameer Abbas, (2014)[15]** proposed four ways to divide up lung CT scan images: K-mean clustering, Multi threshold, region growing, and FCM clustering. The first step was to get rid of the background, make the contrast better, and isolate the lung area to make the image easier to work with. In the second step, four segmentation methods were used, and each one was done separately so that they could be compared**.** The results of segmentation were utilized to extract the lung abnormal regions and to calculate the surface area. All the methods utilized gave good results when implemented on an image after lung region isolation, and the best method was FCM, according to the researcher.

- **Rabab Saadoon Abdoon *et. al.*, (2015)[16]** in this study, many methods are applied; Contour based segmentation utilizing contour and contour filling methods, K-Means, Fuzzy C-Mean (FCM), K-Means and FCM based on GLCM features, Possibility Fuzzy C-Mean based on image histogram. Untraditional methods like hierarchical self-organization feature map, and hierarchical self-organization feature map based on FCM were implemented. As well as, supervised neural networks based on image intensity and standard deviation once, and based on GLCM features another is also used to modify the overall efficiency suitable for the work configuration, which is a very hard case of segmentation due to the overlapping spectrum fingerprint of tissue.
- **Sanjeev N. Jain and Bhagyashri G. Patil, (2015)[17]** proposed two modalities of segmentation which are thresholding and watershed utilized to detect the cancer cell in lung CT scan images, and find out which is better. To obtain more accurate results three steps were utilized: Image enhancement step, image segmentation step, and features extraction step. The marker-controlled watershed segmentation viewpoint takes more accuracy (85.27%) and quality in comparison to the thresholding method (81.24%). The tumor showed in only one image.
- **Badrul Alam Miah and Mohammad Abu Yousuf, (2015)[18]** proposed an image segmentation procedure based on the thresholding method for lung CT scan images, which included two stages, the first stage consisted several processes: pre-processing, binearization, and thresholding method. In the second one, the segmentation technique is utilized to isolate the lung CT scan image. The completion of the suggested system displays acceptable results and the suggested technique is 96.67% accurate. There is some distortion in the lungs form when the lungs are isolated from one another.

- **Ezhil E. Nithila and Kumar S.S., (2016)[19]** proposed to advance a region-based active contour technique for segmenting lung nodule on lung CT scan images. The recommended methodology emphasizes on, acquiring lung CT scan images, reconstructing lung parenchyma and segmentation by employing the utilization of specific Selected binary and Gaussian filtering with new signed pressure force (SBGF-new SPF) and clustering algorithm (FCM) were used for nodule segmentation with binary and Gaussian filtering.

- **Xenia Fave *et al.,* (2016)[20]** proposed a method for pre-processing lung CT scan images. Radionics characteristics have been utilized in many different works to predict patient case or provide detection of large cell lung cancer. The objective of their work is the evaluation of how image pre-processing methods can be significant to volume dependence and prognostic potential for the characteristics in univariate analyses. On the contrary, there lacks the existence of procedures for the best ways to perform the characteristic calculation for maximization of prognostic potential.
- **Prionjit Sarker *et. al.,* (2017)[21]** have applied presented K- means clustering of lung CT scan images to extract the lung abnormal regions. In this research, many morphological operations were utilized to extract the image background, noises, and airways on the lung CT image. Utilizing K-means clustering algorithms was to detect lung abnormalities using MATLAB workspace. Calculation of the volumes and average diameters of 3-D lung nodules is done and the highest diameters of each nodule for each CT slice were executed.
- **Ola Saad Khudhair Abboud , (2017)[22]** in this study , presents techniques for image processing and image segmentation of three different modalities are: mammography, Magnetic Resonance Imaging (MRI) and

Computed Tomography (CT) images, and images of three different organs that studies here are: breast, brain and liver. To achieve the tumors and abnormalities detection task, seven segmentation techniques are presented in this work: clustering hard scheme (K-means); clustering soft scheme (Fuzzy c-means, FCM); Gray level co-occurrence matrix (GLCM) and Histogram equalization which is one of the pixel-based enhancement methods. As well as three proposed hybrid methods: K-means and GLCM; K-means and FCM and K-means and histogram equalization. applying hybrid methods (K-means and FCM) with two passes segmentation can reduced the long elapsed time to be very small, and the relative percent reduction of time became (0.03-0.16). From the results of all the proposed technique, these techniques succeed to detect, isolate and extract the tumor and abnormalities regions according to the consultation of three radiologist, and they are in good agreement with the delineation of radiologists.

- **Anjali Sevani and Hardik Modi, (2018)[23]** utilized median filter and morphological operations to facilitate detection of lung tumor in CT scan images, extraction and calculation the tumor surface area. Morphological operations were used in this study via dilation and erosion of an image, then a median filter was used in a sharpening process to reduce noise without altering the tumor's boundaries. However, researchers did not explain how to extract a tumor from an image of a lung using this method.

- **Alex Chang and Abhishek Moturu, (2019)[24]** applied a neural network approach to lung image segmentation. A neural network utilizing patches from synthetically generated frontal chest X-rays (CXR) utilizing Beer's Law on chest (CT) scan. Bone removal to obtain soft tissue, isolate lungs within CT scan and randomize nodule placement, nodule generation to grow nodules of various shapes and sizes. The results of the neural network utilizing to improve the accuracy while reducing the space and the time complexity. Experimental results were helped to detect lung cancer at an early stage.

- **Sema Candemir and Sameer Antani, (2019)[25]** proposed hybrid methods to isolate and extract infected lung from chest plain X-ray images, especially the lungs of children. These methods exhibit operation training that consumes more time and present computations that are very complex. The difficulty was the development of interference robust lung boundary detection algorithms where a deeper exploration of lung region detection algorithms would have an impact on automated detection field researchers' detection.

- **Hussein Saadi Kareem Rasool, (2020)[26]** in this study presents efficient techniques that are capable of segmenting medical images depended on X-rays of three modalities which are: plain X-ray, CT scan and mammography images for two organs (lung and breast). Five segmentation techniques are proposed in this work: enhancement contrast based technique which is one of the enhancement methods, mean shift clustering method and K-means clustering method, as well as, two proposed hybrid methods: mean shift based on K- means and K-means based on mean shift. The results of the five proposed techniques were succeeding to isolate and extract abnormal regions according to the consultation of four radiologists.

- **Kadhim, Widad Dhahir, and Rabab Saadoon Abdoon, (2020)[27]** In this study, the K-mean algorithm is used on six MRI and CT scans of different numbers of groups. Also, many morphological operations such as opening and dilating after excision of small tumor areas were effectively applied. The results and computed surface areas of discrete tumor areas were compared with radiologist demarcation and the results of this study indicate the high-quality performance of the clustering-based segmentation method.

- **Bhansali, Rahul and Duke, (2020)[28]** introduced an automated Covid-19 detection system using the novel deep CNN structure on CT dataset. They also applied data augmentation and the Laplace filter on CT images to increase the number of training data and to significantly increase CNN performance Covid-19 diagnosis. The highest accuracy achieved was 92%.

- **Mishra *et al.*, (2020)[29]** used different Deep CNN-based approaches to detect the presence of Covid-19 on CT images. A decision fusion-based system is also proposed, which joins predictions from multiple individual models (DenseNet201, DenseNet121, InceptionV3, ResNet50, and VGG16) by majority voting method to produce a final prediction. Results showed the best classification efficiency in the decision fusion-based approach with testing accuracy of 86%.

- **Jim *et al.*, (2020)[30]** introduced a sequential Convolutional Neural Network (CNN)- based model to identify COVID-19 through analyzing Computed Tomography (CT) scan images. The model is capable of identifying the disease with an Accuracy, Specificity, Sensitivity, F1 score, and Precision of this model are 92%, 89%, 94%, 94%, and 93% respectively

- **Anwar and Seemab, (2020)[31]** adopted deep learning technology to distinguish between Covid-19 CT images and healthy CT images. Efficient Net deep learning architecture is used for timely and accurate detection of Covid-19 with an accuracy of 0.89, AUC of 0.89, and F1 score of 0.89. Three various learning rate strategies were applied; cyclic learning rate, constant learning rate, and decreasing the learning rate when model performance stops increasing (reduce on the plateau).

- **Loey, Gunasekaran and Nour, (2020)[32]** used five different deep CNN-based models (ResNet50, Google Net, VGGNet19, VGGNet16, and Alex Net) for the diagnosis of Covid-19 pneumonia infected patients. In this study, data augmentation techniques along and Conditional Generative Adversarial Nets (CGAN) based on a deep transfer learning model for Covid-19 diagnosis in chest CT images were introduced. Results showed the best classification efficiency in the ResNet50 model with testing specificity of 87.62%, sensitivity of 77.66%, and accuracy of 82.91%.

- **Zhao *et al.*, (2020)[33]** has built an open-source dataset for CT images of Covid-19 patients, which consists of 746 CT scan images (349 Covid-19 CT images and 397 Non-Covid-19 CT images). In this dataset, some information regarding the patients was presented such as gender of the patients, age of the patients, and certain characteristic manifestations of Covid-19. They also used this dataset to develop disease diagnostic methods based on self-supervised learning and multitasking learning, which achieve an accuracy of 89%, an Area Under Curve of 98%, and an F1 of 90%.

- **Purohit *et al.*, (2020)[34]** introduce a Covid-19 detection system using CNN based multi-data Augmentation technique from X-ray and CT images. Multi-data augmentation employs discontinuity data collected in the filtered images to increase the number of training examples the (CNN) model and improve the model's efficiency. The highest accuracy in CT classification and X-ray images with Multi-Data Augmentation is (95.38%) and (98.97%) respectively.

- **Ouyang *et al.*, (2020)[35]** has suggested a Covid-19 detection system by a new 3D CNN with a dual sampling attention network to concentrate the disease locations in lungs while making diagnostic decisions and to train two 3D Residual Net34 models. 2186 CT scan images of training samples for (1588) patients were used, and for the test sample, using a different independent data set consisting of 2796 CT scan images for 2057 patients. Results indicated that CT image diagnosis accuracy was 87.5.

- **Narin, Ceren and Ziynet, (2020)[36]** used three various CNN-based models (ResidualNet50, InceptionV3, and Inception Residual NetV2) for the diagnosis of Covid-19 pneumonia infected patients. The transfer learning method was applied to overcome training time and achieve higher precision in predicting inadequate X-ray images. Results represent the best classification efficiency in the retrained ResNet50 model. Experiments based on the 100 X-ray images (50 of a healthy and 50 of Covid patients). The highest accuracy achieved was 87%.

- **Zheng *et al.*, (2020)[37]** introduced a Covid-19 detection system by DeCoVNet (3D deep CNN) from CT scanning. DeCoVNet has been split into three phases. The first phase was comprised of 3D convolution, batch norm layer, and pooling layer. Two (3D) residual blocks were used in the second phase (3D convolution layer and batch normalization layer). Third thase was a gradual classification, which chiefly comprised of three layers of 3D convolution, Fully Connected (FC), and Soft Max function. Data augmentation technique was used on a training set to decrease over fitting problems. This method has experimented on CT scanning, and 3D lung mask that pre-trained. The accuracy of CT image diagnosis was 90.1%.

- **Hu *et al.*, (2020)[38]** suggested a Covid-19 classification method by applying CNN with Shuffle Net V2 on CT scan images to identify Covid -19 patients from persons not infected or infected via other pneumonia effectively. They adopted five types of data augmentation methods consisting of 16 operations practiced for the training sample to improve model performance. A 1042 chest CT-scan is entered into the shuffle net V2 structure (composed of 521 Covid-19, 397 heavyduty scans, 76 pneumonia, and 48 SARS) after doing a random cropping process. The output from shuffle net V2 structure will then be supplied to a linear layer to produce a diagnostic response. The accuracy of CT scan diagnosis was 91.21%.

- **Yang *et al.*, (2020)[39]** convolutional Neural Network CNN (Dense Net) is used to offer an automatic way to find Covid-19 on High-Resolution Computed Tomography (HRCT) dataset, which is composed of 295. The Dense net has been trained and validated to diagnose (HRCT) images as Covid-19 or normal. It minimizes the detection rate since the dense network focuses on the image components in which the infection resides. The highest accuracy achieved was 95%.

- **Xu *et al.*, (2020)[40]** has employed two 3D CNN models (traditional resent 18) to segment various candidate areas in CT image and classified CT image datasets (candidate area) into Covid-19, viral-pneumonia, and normal. Bayesian function was applied to compute a whole confidence score and the disease type. This method has been experimented on 1710 CT image pieces collected from (90) CT samples. The highest accuracy that has been achieved was 86.7%.

- **Amyar *et al.*, (2020)[41]** has suggested a diagnosis and segmentation structure for covid-19 via an encoder and two decoders of CT image restoration, and disease segmentation, Multi-task learning (MTL) was used for feature extraction and diagnostic of Covid-19 and non-Covid-19 from CT scan images. The approach has experimented on CT scan images of 1044 patients (this comprises 449 Covid-19 cases, 100 normal cases, 98 lung cancer cases, and 397 cases with various diseases). The highest accuracy achieved was 86% for the classification.

- **Singh, Vijay and Manjit, (2020)[42]** has introduced a way of classification of Covid-19 infected cases from CT images into Covid 19+ and Covid 19- classes by applying "multi-objective differential evolution (MODE) – based on CNN" The primary CNN parameters had been tuned with multi-objective differential evolution (MODE) because hyper parameter fixing problems influence CNN. Therefore, they carry out mutation operation, crossover operation, and selection operation to optimize the problem using Differential evolution. The accuracy of CT scan diagnosis was 92%.

- **Santa Cruz, (2021)[43]** proposed a multi-stage model for diagnosing Covid-19 through CT scan using six pre-trained models at one stage. and, at another stage, the ensemble strategy was applied to collect the results of six models to predict the outcome. AUC is 90.82 %, an accuracy is 86.70 %, and an F1 score is 85.86 %[13].

- **Garain, Avishek, *et al.*, (2021)[44]** In this study, Covid-19 is found in CT scan images by using a method based on spiking neural networks. Used different deep learning libraries to try to simulate the SNNs. They have used them to divide chest CT scan images into two groups: Covid and non-Covid. Our method has a very high F1 score of 0.99 for the potential-based model and does better than many of the most advanced models.

- **Khan, S. H, *et al.*, (2022)[45]** developed a new CNN architecture STM-RENet to interpret the radiographic patterns from X-ray images. In this regard, suggest proposed a new convolutional block STM that implements the region and edge-based operations separately, The idea of channel boosting is exploited by generating auxiliary channels from the two additional CNNs using Transfer Learning, which are then concatenated to the original channels of the proposed STM-RENet. A significant performance improvement is shown by the proposed CB-STM-RENet in comparison to the standard CNNs on three datasets, especially on the stringent CoV-NonCoV-15k dataset. The good detection rate (97%), accuracy (96.53%), and reasonable F-score (95%) of the proposed technique.

All previous researchers who conducted studies on Covid-19 were merely classification (diagnostic) studies for the presence or absence of Covid-19 and the affected area was not extracted from the approved images of Covid-19. In this study, in addition to the diagnosis of Covid-19 from other anomalies, the infection area was extracted and isolated using several techniques, in addition to the use of a hybrid technique for the purpose of improving extraction and reducing execution time.

1.7 Aim of The Study

The object of the present study is to employ the artificial neural networks to diagnose the presence of Covid-19 infection and tumors in CT-scan lung images and to extract the infected regions. In addition, a hybrid technique was proposed to reduce the implementing required time and to achieve robust extracting of the lung abnormal regions.

Medical Imaging Techniques and lung Abnormality Types

2.1 Introduction

Tumors and other abnormalities can be detected using medical imaging techniques [46]. Medical imaging techniques include X-rays, ultrasounds, MRI, mammograms, PET, SPECT, CT, and a slew of other procedures that can be used to diagnose and treat a wide range of conditions [47,48]. Medical professionals use these approaches to collect essential information and discover anomalies in the body [49]. These techniques it has a substantial impact on patient treatment, and these approaches have been refined and new imaging techniques have been introduced to increase the detection and evaluation of neoplasms dramatically [46].

From many tasks of these techniques they used to detect the infection of lung diseases, such as Covid-19 disease that directly affecting lungs is an acute disease caused death of big number of people around word, so the early detecting of it and asses the relative ratio of the lung infection is a vital need [46]. There are two basic imaging modalities available to clinicians for Covid-19 infections which are: X-ray and CT scan [50]. CT scan is a quick, cheap, good and accurate test for Covid-19 [51].

In this study, many lung CT scan modality images were adopted classify the abnormal case for patient suffer from Covid-19 and other abnormal situations.

2.2 Medical Imaging Methods

In Medicine, doctors can more easily diagnose illnesses by using imaging technologies to view what's going on within the body. It also makes it possible to perform keyhole surgeries in order to reach internal organs without having to open the body all the way [52]. In the next section, we'll talk briefly about the most-used imaging techniques:

2.2.1 X-ray Imaging

One of Conrad Roentgen's discoveries is the discovery of an entirely new type of radiation that could penetrate nearly anything called X-ray. In 1901, he won the Nobel Prize for describing the diagnostic possibilities of X-rays for visualizing the human body. Radiation is sent through the body, and X-rays are collected on film or in an array of detectors. This is the simplest method for medical imaging, and the most commonly used [53].

2.2.2 Ultrasonic Imaging

Ultrasound Imaging is a medical diagnostic technique in which very high frequency sound is directed into the body. The tissue interfaces reflect the sound, and the resulting pattern of sound reflection is processed to produce a photograph or a moving image on a television [54].

2.2.3 Magnetic Resonance Imaging

MRI is an imaging technique used primarily in medical settings to produce high quality images inside the human body [55].

MRI is based on the principles of nuclear magnetic resonance (NMR), a spectroscopic technique used by scientists to obtain microscopic chemical and physical information about molecules. This technique referred as MRI rather than NMRI because of the negative connotations associated with the word nuclear in the late 1970's. MRI has advanced beyond a tomographic imaging technique to produce a volume imaging technique [56].

2.2.4 Mammography

Mammography is the main test used to check for breast cancer and find it early, Usually by looking for specific masses and/or tiny calcifications [57].

2.2.5 Positron Emission Tomography Imaging

Positron Emission Tomography (PET) is an imaging system that detects two annihilation photons or gamma rays originating from the tracer compounds labeled with positron emitting radionuclides, which are injected or administered into the subject Many proton-rich radioisotopes may decay via positron β+-decay, in which a proton in the nucleus decays to a neutron by emission of a positron and a neutrino [58].

2.2.6Single-Photon Emission Computed Tomography Imaging

SPECT stands for Single-Photon Emission Computed Tomography powerful way to measure how a radioactive compound (called a "radiotracer") moves around in people. When a SPECT radioisotope breaks down, gamma radiation of various energy is discharged in random directions by the device.. Living tissue does a good job of reducing the energy of SPECT photons [59].

2.2.7 Optical Imaging

When light photons interact with living tissue, they can either be absorbed or dispersed. Thus, the two primary types of optical imaging are based on absorption and scattering [60].

2.2.8 Computed Tomography Scanning (CT)

Computed Tomography CT or Computed Axial Tomography CAT scan, is a diagnostic medical test that produces multiple images of the inside of the body. The cross-sectional images generated during CT scan can be reformatted in multiple planes, and can even generate three-dimensional images. These images can be viewed on a computer monitor, printed on film or transferred to a Compacted Disk (CD) or Digital Video Disk (DVD)[61].

Using specialized equipment and expertise to create and interpret CT scans of the body, radiologists can more easily diagnose problems such as cancer, cardiovascular disease, infectious disease, appendicitis, trauma and musculoskeletal disorders [61]. Figure (2.1) shows CT Scanner.

Figure (2.1): CT Scanner [62].

CT scan images give better details of internal organs, bones, and blood vessels than traditional X-rays, as shown in Figure (2.2). CT scan is often used for imaging, spin, skull, lung, liver and bones as well as it is used to view the inner ear and sinuses because these areas are made of very fine bones and many other organs in the human body[63].

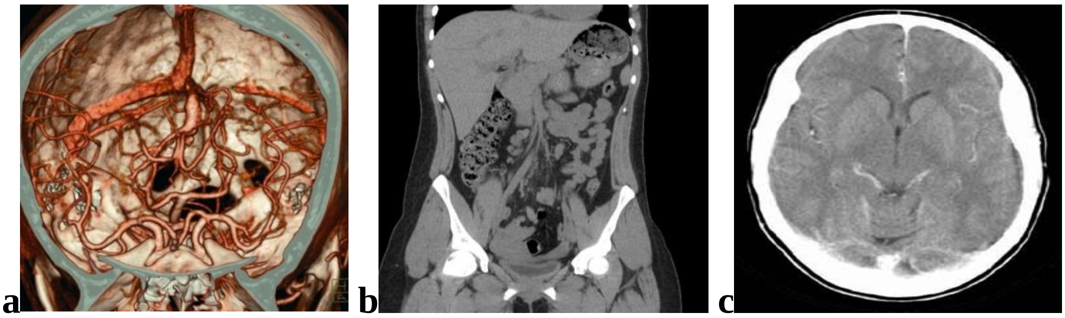

Figure (2.2): CT of (a) Angiography (CTA) [64], (b) Abdomen and pelvis [65] and (c) brain [66].

2.2.8.1 Basic Principles of CT

The basic principles of CT scan system are as follows [67,68]:

- CT imaging system moves around the body part at a fixed location, as illustrated in Figure (2.3).
- Attenuation information obtained in multiple planes.
- Reconstruct of this attenuation information into a simple grid.
- Each body section divided into 3 dimensional boxes – voxel.
- 2 dimension grid of pixels .
- Calculate attenuation in each direction.
- Add up all attenuations in each pixel.
- Density of each pixel varies resulting in a pictorial representation of the density of structures within that section.
- Repeat for each subsequent slice.
- The higher resolution, the smaller the pixel.

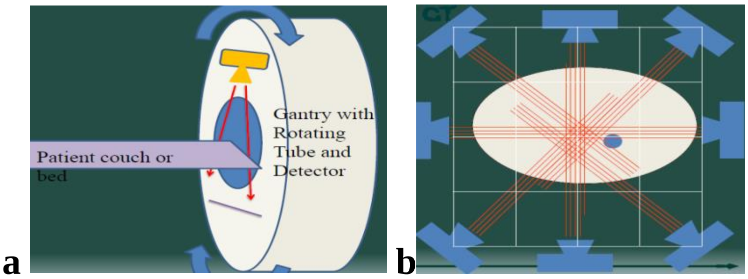

Figure (2.3): (a) CT Scan and (b) CT system moves around The scanning body part [69].

2.3 Anatomy of Lungs

The lungs are the major organs of the respiratory system and are responsible for performing gas exchange [70]. The top, cone shaped part of the lung that fits under the collarbone is called the apex. The broad, bottom part of the lung that rests on the diaphragm is called the base. Unlike some other paired organs in the body, the two lungs are not identical (see Figure 2.4). The right lung is normally larger than the left [71].

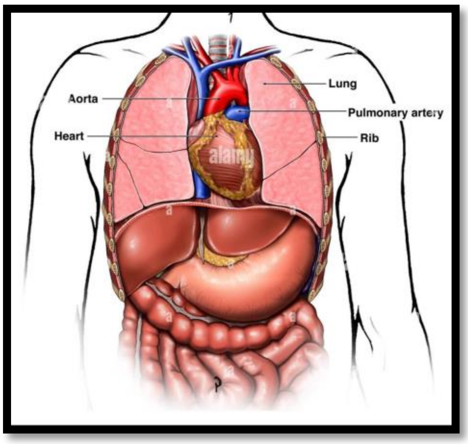

Figure (2.4): Organs of the Chest in the body[71].

lungs are located on either sides of the heart in the chest cavity and protected by the rib cage [72]. The size and age of a person change how much air they can take in. People who are shorter have smaller lungs than people who are taller. There is also a decrease in lung capacity and a loss of lung elastic as we grow older [73].

2.4 Tumors Types

Tumors are groups of abnormal cells that form lumps or growths. Healthy cells in our bodies divide and replace themselves during a controlled pattern. Cancer starts when a cell is somehow altered in order that it multiplies out of control. Most cancers form tumors, but not all tumors are cancerous. Benign, or noncancerous, tumors do not spread to other parts of the body, and do not create new tumors. Malignant or cancerous, tumors displace healthy cells, interfere with body functions, and draw nutrients from body tissues. Cancers still grow and spread by direct extension or through a process called metastasis, whereby the malignant cells travel through the lymphatic or blood vessels eventually forming new tumors in other parts of the body [74].

2.4.1 Benign Lung Tumors

Benign tumors have the advantage of having benign masses that do not turn to cancer; they fail to spread to the organs and occupy close tissues or other tangible areas, just like cancer tumors. Benign tumors are usually not harmful, and their growth is unhurried, but they may cause some symptoms and signs build on its site; for example, if close to the nerves they may cause symptoms that lead to the need to remove them [75].

2.4.2 Malignant Tumors

Malignant tumors exhibit cancer signs; they unroll to several organs and areas via lymph ducts and blood vessels, and they capture adjacent tissues [76]. Indicators malignant tumors are: endless fatigue even amidst rest, the presentation is important as the tumor grows, uncertain weight loss, this may be the early signs of cancer in the victims of certain cancers in particular, Coughing with blood coming out, which may be a symptom of breast cancer. The majority of cancer patients develop high temperatures, especially as the impact of the disease on their immune system or the impact of treatment on them; it may weaken the ability of the body to fight infections [77].

2.5 Types of Lung Cancer

In existence are two major groupings of lung cancer; Non-Small Cell Lung Cancer (NSCLC) and Small Cell Lung Cancer (SCLC). Their distinguishing factor is in how cancerous their cell of origin is. Moreover, cell appearance and how fast they escalate to other body parts and their response to indicators are also distinguishing factors. However, there is no relationship with the breathing of the lungs. The spread of lung cancer or other body parts is attributed to late diagnosis. With respect to where cancer has escalated to, features can include headaches, coughing up blood (hemoptysis), weakness, and lack of appetite, weight drop, bone dislocations, or blood clots [78]. NSCLC is a composition of 80-85% of all lung cancers with three major subcategories: Adenocarcinoma (bronchioloalveolar carcinoma), squamous cell carcinoma (formerly called epidermis carcinoma) and big cell carcinoma. However, SCLC is a composition of 15–20% of all lung cancers [78]. Figure (2.5) shows the tumor shape in the right lung.

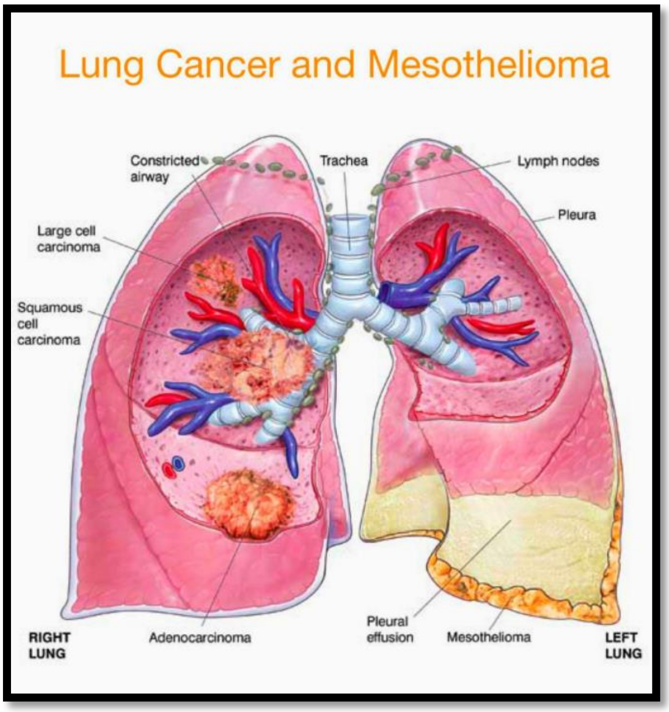

Figure (2.5): Lung tumor [79].

2.6 Coronavirus Disease (Covid-19)

Coronavirus-2019 (Covid-19) is a new strain of virus; It was detected in Wuhan region China in December (2019). It is an acute infectious disease that has compromised the health of many people around the world, by directly impacting the lungs [80]. The virus enters the lung through the respiratory system and can infect the entire system until it reaches the alveoli and disrupts these vesicles' function. Once it binds to a specific receptor, it will cause an overreaction in the immune system because it cannot recognize this virus. Thus, many immune cells are pushed into the lung, causing more chaos than repair. This attack from the virus and the immune system's strong response makes the virus vital. In the worst cases, the alveoli collapse, and when this happens, the lung begins to fill with cells and fluids, and thus the bloodstream does not get enough oxygen, and the patient's breathing becomes difficult [81].

2.7 Detection of Covid-19 CT-scan Manifestations

Viruses are essentially a group of genetic instructions that are protected by a layer of fat and protein. Their main and only purpose is a reproduction since they can enter living cells through the protrusion of the surface of this virus. These viruses are active inside an organism because they depend on the cellular components to reproduce and are weak outside the organism. Figure (2.6) illustrates the COVID-19 virus [81].

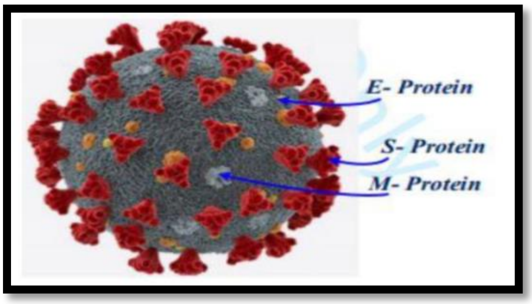

Figure (2.6) illustrates the structure of the Covid-19 virus [81].

Usually, the lungs appear black, but images of the lungs in Coronavirus patients are white; this is because the virus causes cells to leak into the lungs, which causes the lungs to appear white on the scan. Figure

(2.7) displays CT scan images for a normal healthy person and Covid-19 patient [82].

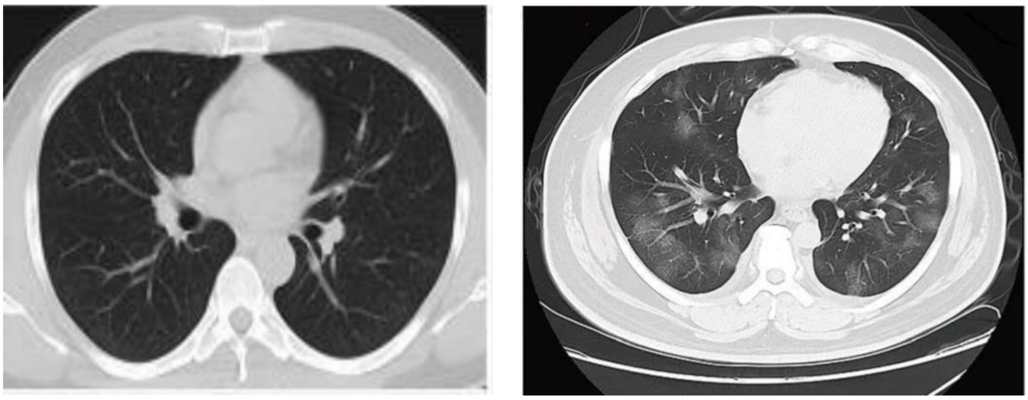

Figure (2.7): (a) normal healthy person (b) Covid-19 patient [82].

Image Segmentation Techniques

3.1 Introduction

Even though biomedical imaging techniques have improved over the past few years, there are still some things that can make it hard to see contrast in images [83]. The information obtained by different imaging methods can be used in many ways to see the tissues being looked at and helps doctors learn more about the diseases. This task requires knowing where different parts of the body are on the image and drawing lines between them. Although the extracted data from medical images can be converted into useful information for diagnosis purposes, they require classification and labeling, using segmentation operation. In image segmentation, it is important to divide an image into meaningful parts and label them so that they can be used for further analysis [84].

During the segmentation process, an image is broken up into its parts [85]. Depending on the problem being looked at, the level of detail in the segmentation process will vary. When an application's objects or regions of interest are discovered, segmentation should come to an end. Segmenting complex images is one of the hardest things to do in image processing, and its accuracy determines whether computerized analysis procedures will work or not in the end. Because of this, care must be taken to increase the chances of correct segmentation.. Most of the existent approaches of segmentation rely primarily on the features of the processed image; like color, gray level, texture uniformity of an image's areas, as well as the smoothness and continuity of areas where contours meet; or a combination of these features [86].

There are different methods for segmenting images; it can be done by comparing the image with standard ones, or delineating the boundaries of the segmented region. It can be performed manually by professionals who having enough expertise in image analysis and image regions differentiation. Computerized picture segmentation can also benefit from methods based on knowledge. An image's final objective is to be segmented in order to find areas of similarity; homogeneity may be referred to texture, color, distribution of intensities, motion field, etc. Segmentation produces one of two outcomes: either an image with labels identifying all parts that are similar [87].

3.2 Segmentation Methods

Generally, classical segmentation techniques, like thresholding, boundary-based segmentation, and region-based segmentation, can be put into two groups: statistically based segmentation techniques and classical segmentation techniques. Segmentation can be manual, semiautomatic, or automatic [88, 89]. A brief description of the segmentation methods which were proposed in literature will be discussed in this chapter.

I- Single Contrast Methods

These methods are classified as follows [90]:

- **Threshold-Based Segmentation:** This is the most straightforward way to divide things into groups. The user sets the upper and lower thresholds. This type of segmentation has its limits, and the fact that anatomy and image artifacts can be different makes it hard to use in clinical settings.
- **Edge-Based Segmentation:** Edges are usually found by looking for sudden changes in the values of the intensity of pixels as you move through a set of pixels. In edge detection, operators like the first and second derivatives are very important. Most of the time, these techniques have problems like not enough intensity gradients, noise or artifacts, or a bad guess of the threshold, which can lead to too much or too little segmentation**.**

- **Boundary Tracing**: In this method, the user chooses a pixel on the edge of the region to use as a starting point, then follows the edge from that point. This method works well in situations where the edge boundary is clear. But this method can be hard to use with images that show differences in tissue.
- **Seeded Growing Segmentation:** The user chooses a seed or several seeds to segment the growing population, and then they choose a threshold value. The approach then looks at the pixels that are adjacent to the selected seed(s) and incorporates them into the region if the pixels in those adjacent regions also meet the requirements.

II- Multi Spectral Segmentation

There are two types of these methods: supervised and unsupervised [90].

- **Supervised Types** segmentation needs input from the user. To do this, training pixels or training regions are chosen from the images.
- **Unsupervised Types**, This is also known as "clustering," and it is a technique for discovering patterns in data. Clustering and computing time are significant, but initialization is critical. It is possible to replicate clustering methods, however this does not always lead to a meaningful segmentation and may need a lot of computing time.

3.3 Medical Image Segmentation

Image segmentation performs a key task in several medical imaging executions by automating or helping in the representation of anatomical and other areas of attention [87]. Research labors are committed to procedures and analyzing medical images in order to detect important information like area and form to isolate and extract abnormal regions. Automated image segmentation has a goal to detect object boundary features, and this plays a significant part in perceiving image contents. A taxing issue is segmentation areas without boundaries, (i.e. background, missing edges or lack of texture contrast between areas of interest). Many segmentation procedures were suggested in the literature to address this difficulty, and several of them providing good outcomes [91]. In this chapter, the methodologies implemented to segment CT scan based lung medical images.

3.4 Artificial Neural Network (ANN)

The "biological nervous systems" is simulated that produced "Neural Networks" (NNs). The neural net can be supposed to be a system of processing data, containing of an enormous number of straightforward, extremely interconnected processing components "artificial neurons", in a structural design (architecture) stimulated by the cerebral cortex structure of the brain. The interrelated neural calculating components have the ability to teach and in that way obtain awareness and make it accessible for usage. An ANNs have establish wide-ranging applications in areas likes' processing of pattern image, control systems, optimization and forecasting [92] .

The fundamental components of a brain in human named "neurons" are the objects, which do calculations such as perception, logical inference, and recognition of patterns and so on. Subsequently the machinery that has been constructed on a simplified simulated of calculating by neurons of the human brain that named "Artificial Neural Systems" (ANS) technology or Artificial Neural Networks (ANN) or just neural networks, Figure (3.1) and (3.2) show the biological and mathematical model of the neuron respectively.

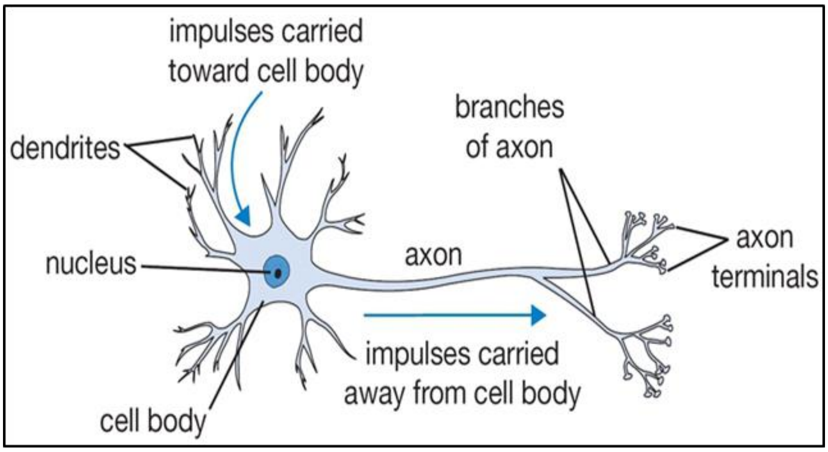

Figure (3.1) Drawing of a biological neuron [92].

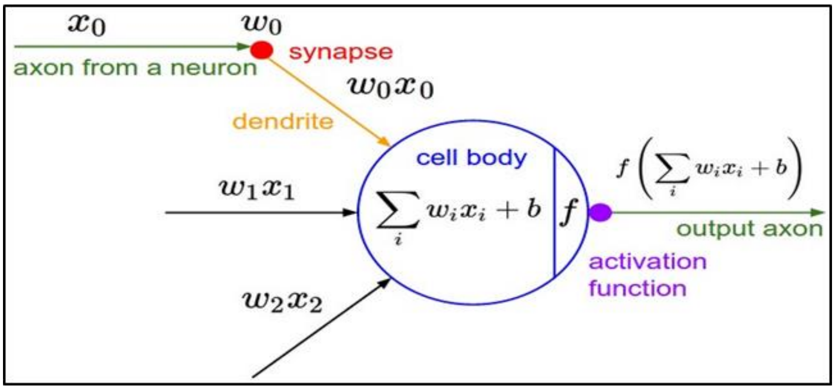

Figure (3.2) Drawing of a mathematical model of the neuron [92].

3.4.1 Properties of Neural Networks:

The main proprieties of an ANN are [93]:

1. ANNs display mapping abilities, i.e., they are able to map patterns of input to their related patterns of output.
2. ANNs teach by samples/examples. Therefore, ANN architectures can be learned with well-known instances of a problem before they are verified for their inference ability on unidentified examples of the problem. They can, for that reason, classify new objects earlier unlearned.
3. ANNs keep the ability to generalize/oversimplify. Thus, they can forecast new results from the previous trends.

4. ANNs are strong systems and are "fault tolerant", than remember complete patterns from partial or noisy and incomplete patterns.
5. ANNs can handle process information in parallel, at fast speed, and in a distributed way.

3.4.2 Characteristics of Neural Networks

To define the Features of an ANN, need the following three characteristics [94]:

1. The number of layers and nodes in every net layers called "the architecture".
2. The teaching learning method that has been useful to update "the net connections weights".
3. The activation functions which is used in different net layers.

3.5 Artificial Neural Networks Training Schemes

Two schemes of training: supervised and unsupervised schemes. In the following subsection the explanation for ANN each of them. In this study using back- propagation of ANN Supervised and using one of types Convolutional Neural Network (CNN) to train Covid-19, normal, tumors.

3.5.1 Artificial Neural Networks of Supervised Training Scheme

Neural networks are composed of simple elements (neurons or nodes) operating in parallel. The network function is determined largely by the connections between these elements. The neural network can be trained to perform a particular function (job) by adjusting the values of the connections (weights) between elements [95]. Commonly neural networks are adjusted, or trained, so that a particular input leads to a specific target output (Supervised fashion). Such a situation is shown in Figure (3-3). In this fashion, the network is adjusted based on a comparison of the output and the target until the network output matches the target. Typically, many such input/target pairs are used, in this supervised learning, to train a network [95].

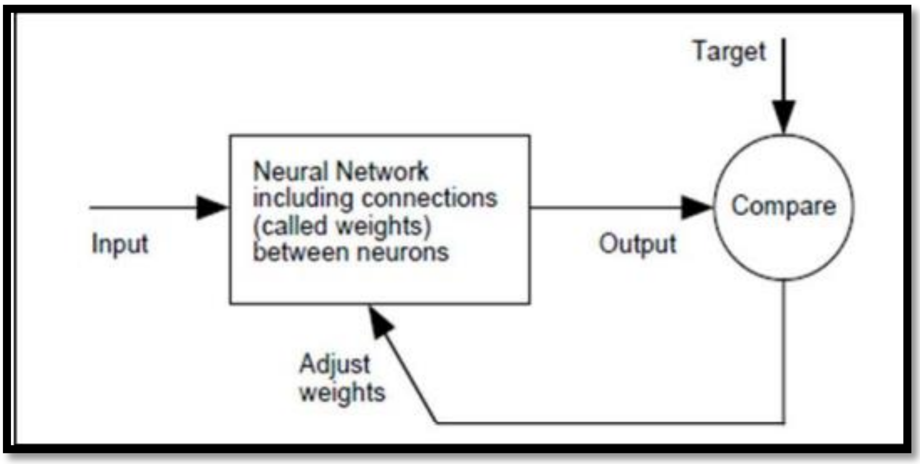

Figure (3.3): Supervised training of the neural network [95].

3.5.1.1 Feed-forward Artificial Neural Networks

Artificial neural network with feed-forward topology is called FeedForward artificial neural network and as such has only one condition which is, the information must flow from input to output in only one direction with no back-loops. There are no limitations on number of layers, type of transfer function used in individual artificial neuron or number of connections between individual artificial neurons. The simplest feed-forward artificial neural network is a single perceptron that is only capable of learning linear problems [96]. Figure (3-4) shows a simple multi-layer feed-forward artificial neural network for purpose of analytical description that listed in the sets of Eqs. (3-1) - (3-3) as following[96]:

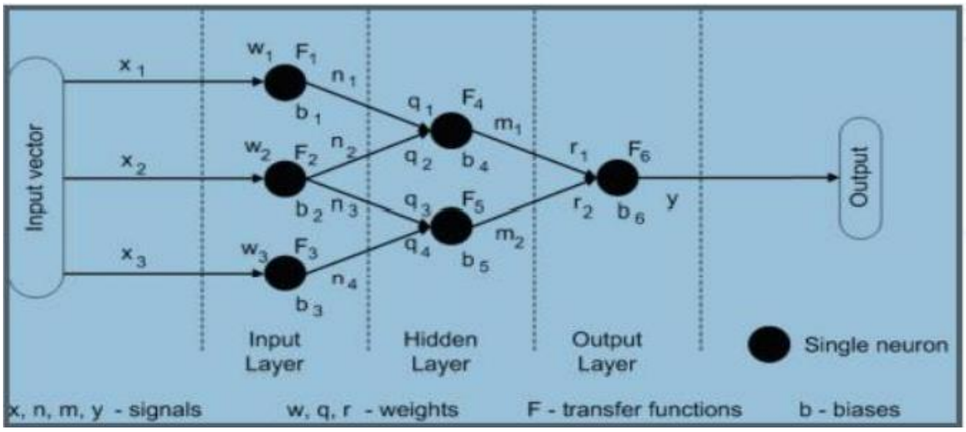

Figure (3.4): Feed-forward artificial neural network [96].

$$\left.\begin{aligned}
&\boldsymbol{n_1 = F_1(w_1x_1 + b_1)}\\
&\boldsymbol{n_2 = F_{12}(w_2x_2 + b_{12})}\\
&\boldsymbol{n_3 = F_4(w_3x_3 + b_{13})}\\
&\boldsymbol{n_4 = F_4(w_4x_4 + b_4)}
\end{aligned}\right\} \qquad \text{......(3.1)}$$

$$\left.\begin{aligned}
&\boldsymbol{m_1 = F_4(q_1n_1 + q_2n_2 + b_4\ )}\\
&\boldsymbol{m_2 = F_5(q_3n_3 + q_4n_4 + b_5\ )}\\
&\boldsymbol{y = F_6(r_1m_1 + r_2m_2 + b_6\ )}
\end{aligned}\right\} \qquad \text{.......(3.2)}$$

$$\boldsymbol{y = F_6}\begin{bmatrix} \boldsymbol{r_1\,(F_4[q_1\,F_1[w_1x_1 + b_1] + q_2F_2[w_2x_2 + b_2]] + b_4 +} & \dots \\ \boldsymbol{\dots + r_2\,(F_5[q_3\,F_2[w_2x_2 + b_2] + q_4F_3[w_3x_3 + b_3]] + b_5} & \end{bmatrix} \quad \text{...(3.3)}$$

Where x_1, x_2 and x_3 represent the inputs; w_1, w_2, w_3, q_1, q_2, q_3, r_1 and r_2 represent the weights; b_1, b_2, b_3, b_4, b_5 and b_6 represent the biases and y represents the output of the network.

3.5.1.2 Back- propagation (Back propagation)

Back propagation is an abbreviation for "backward propagation of errors". It is a common method of training (learning).

● Mathematically Representation for Back-propagation

The Back-propagation algorithm gives a prescription for changing the weights w_{ij} in any feed forward network to learn a training set of input output pairs (x_d, t_d) [97]. For a simple two-layer network that shown in Figure (3.5).

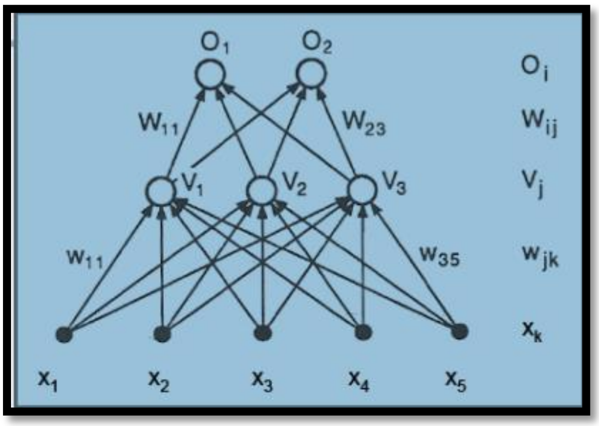

Figure (3.5): Example of a simple two-layer network [97].

Given the pattern x_d the hidden unit j receives a net input as follows [97]:

$$net_j^d = \sum_{k=1}^{5} w_{jk} x_k^d \qquad \text{……..(3.4)}$$

And produces the following output:

$$V_i^d = f\left(net_j^d\right) = f\left(\sum_{k=1}^{5} w_{jk} x_k^d\right) \qquad \text{……. (3.5)}$$

Output unit *i* thus receives:

$$net_j^d = \sum_{j=1}^{3} w_{ij} V_j^d = \sum_{j=1}^{3} \left(W_{ij} \cdot \sum_{k=1}^{5} w_{jk} x_k^d\right) \qquad \text{……. (3.6)}$$

and produces the final output:

$$O_i^d = f\left(net_j^d\right) = f\left(\sum_{j=1}^{3} w_{ij} V_j^d\right) = f\left(\sum_{j=1}^{3} \left(W_{ij} \cdot \sum_{k=1}^{5} w_{jk} x_k^d\right)\right) \quad \text{…. (3.7)}$$

Error value can be calculated as [97]:

$$E(\bar{w}) = \frac{1}{2}\sum_{d \in D} (t_d - O_d)^2 \qquad \text{…….. (3.8)}$$

The factor $\frac{1}{2}$ of is included to cancel the exponent when differentiating. For *l* outputs and input- output pairs $(x_{d\,,}t_d)$:

$$E(\bar{w}) = \frac{1}{2}\sum_{d=1}^{m}\sum_{i=1}^{l}(t_i^d - O_{\,i}^{\,d})^2 \qquad \text{…….. (3.9)}$$

For the previous example becomes:

$$E(\bar{w}) = \frac{1}{2}\sum_{d=1}^{m}\sum_{i=1}^{2}(t_i^d - O_{\,i}^{\,d})^2 \qquad \text{……. (3.10)}$$

$$E(\bar{w}) = \frac{1}{2}\sum_{d=1}^{m}\sum_{i=1}^{l}(t_i^d - f(\sum_{j=1}^{3}(w_{ij} \cdot f(\sum_{k=1}^{5} w_{jk}x_k^d\ )\ ))^2 \qquad \text{……. (3.11)}$$

is differentiable, and the given *f* is differentiable too, Gradient descent can be applied.

For hidden-to-output connections the gradient descent rule gives [97]:

$$\Delta w_{ij} = -\eta\frac{E}{W_{ij}} \qquad \text{…….(3.12)}$$

3.4.3 Convolution Neural Networks (CNN)

Reading the image is in the form of a two-dimensional matrix of pixels, where each pixel location is associated with a numerical value or more, depending on the image is dealing with, whether it is gray or color. The ancient method of handling this rich architecture is unsatisfactory as it ignores the spatial structure of each image so as to flatten it to a one-dimensional vector and feed it through a fully connected Multi-Layer Perceptron MLP. Convolution Neural Networks, CNN aims to be computationally economical since it takes fewer parameters than fully linked structures, which led practitioners to use CNN whenever possible[98,99]. CNN has been used in sound processing and image processing, especially in the medical field, as well as in video processing, by applying a mathematical process based on a matrix called a filter or kernel[100-102]. CNN convulse the inputs into deeper filters to extract powerful features. CNN has two functions, namely feature extraction and classification.

3.4.3.1CNN architecture's fundamental components

The CNN architecture is generally divided into two sections: the feature extractor and the Classification function.

- **Feature extraction function:**

CNN's feature extractor design consists of one or more convolution layers; each one is followed by a nonlinear layer that reflects the activation function of its mission in that layer, allowing it to discriminate between the special signal of valuable features on each hidden layer. CNN uses a convolutional algorithm to extract the feature map when it receives the image. To put it another way, the convolution layer acts as local filters on the input image, using the filter kernel coefficients obtained during the training phase. Edges, lines and other lower-level features, are retrieved from the initial (early) layers, whereas the deeper layers are used to extract higher-level features[101,103].

- **Classification function:**

Finally, one or more hidden layers in a typical neural network can be concatenated, with all of these layers being referred to as Dense or Fully Connected (FC) layers. The model's output layer (the most recent FC layer) is responsible for categorization decision-making[104]. Where the feature extraction function shows the classification function in Figure (3.6).

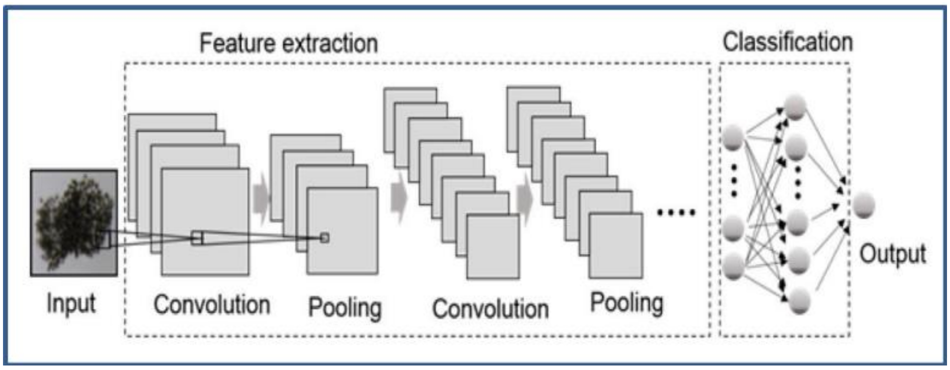

Figure (3.6): CNN architecture with feature extraction and classification functions[105].

3.4.3.2 Two Dimensional Convolution Neural Network (2D-CNN)

2D-CNN consisted of multiple layers, each of which performs a specific function and produces an output using saved weights. Convolution layer, non-linear layer, pooling layer, flatten layer, in addition to a fully connected layer [106], and some layers that can be applied to provide network-wide generalization, such as batch normalization layers and dropout layers [107]. As mentioned earlier, the convolutional layer is part of the CNN layer and the activation function (non-linear), the pooling, and the fully connected layer.

1. Convolution layer

In the two-dimensional tensioner, the cross-correlation operation begins with a convolution window of a specific size on the input tensor on the upper left side and then moves to the right side and from top to bottom. When a convolution window moves to a specific location, the input receptive fields in that window are multiplied element-wise with the kernel tensor, and the resulting feature map is summed to provide a single scalar value. The outcome of this process gives an output tensor at the corresponding location as in Figure (3.7):

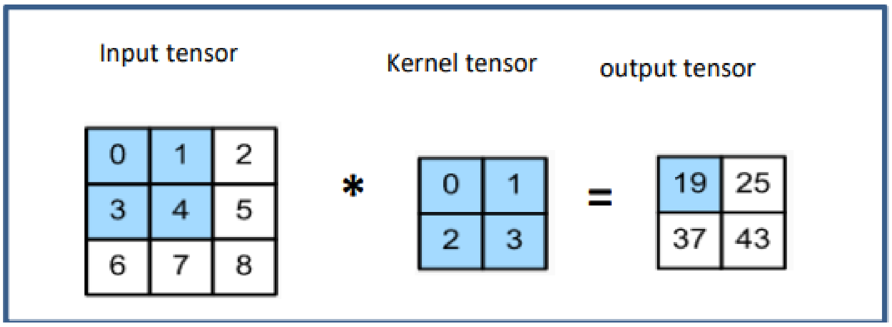

Figure(3.7): Two-dimensional cross-correlation operation[98].

Through the researcher observation of the shape, it is found that the size of the output motor is less than the input's size for the input tensor, and this is the task of the convolutional layers. The size of the insert can give the output size $n_h \times n_w$ minus the size of the convolutional kernel $k_h \times k_w$.

$$feature\ map\ size = (n_h - k_h + 1) \times (n_w - k_w + 1) \quad \ldots(3.13)$$

The convolution layer works by moving many tiny filters used to extract meaningful features from an image[107,108].

2- Activation Functions

The activation function is a mathematical equation that determines the output of a neural network. The function is attached to each neuron in the network and decides whether the neuron should be activated or not, based on whether each neuron's input is relevant for the model's prediction. There are several activation functions available in CNNs like, (Sigmoid, Tanh, ReLU, Leaky ReLU, Maxout, and ELU) as shown in Figure (3.8).

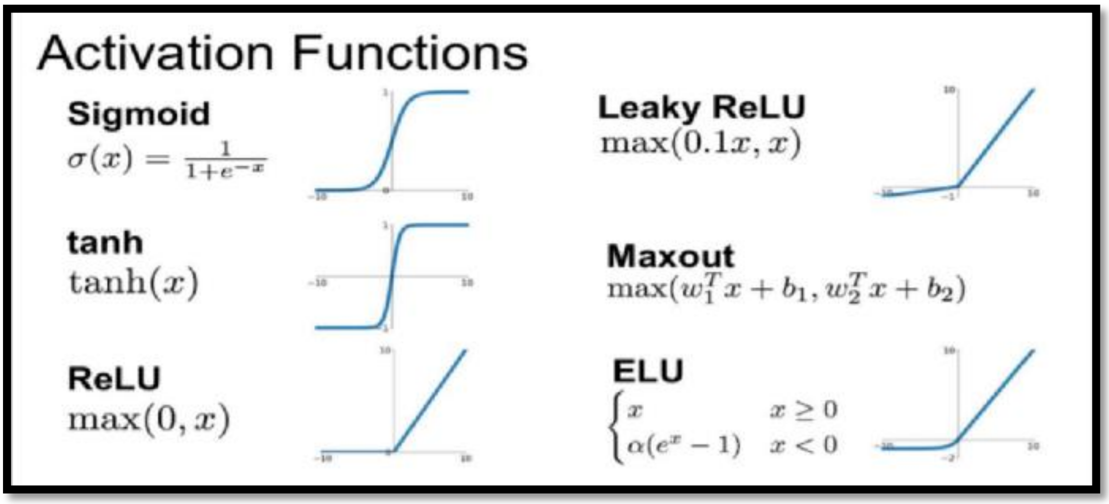

Figure (3.8): Different activation functions (109).

3. Non-Linear Layer (Activation layer)

The activation function that can be denoted as F is a monotonic no decreasing function that represents the weighted sum of the neuron's inputs that determines the characteristics of the neuron such that:

$$f(x) = 0 \; or \; f(x) = 1 \qquad \text{….. (3.14)}$$

There are many activation functions[36], such as the sigmoid function, which are differentiable, and 'Rectified Linear Units (ReLUs) function that convert the linear output into nonlinear [102].

The goal of ReLUs is to adjust the minus value in matrix outputs using the convolution process [110]. Since each function has its own characteristics and is suitable for a specific application, it was used ReLUs with CNN because it speeds up network training several times compared to other linear functions, which implements the same size as the input and output of the layer[31]. The rectifier can be identified as the argument's positive side [111]:

$$f(x) = x^{+} = max\,(0, x) \qquad \text{…….(3.15)}$$

Where x: is the neuron‘s input.

A ReLU function plotted can be illustrated in Figure (3.9)[31].

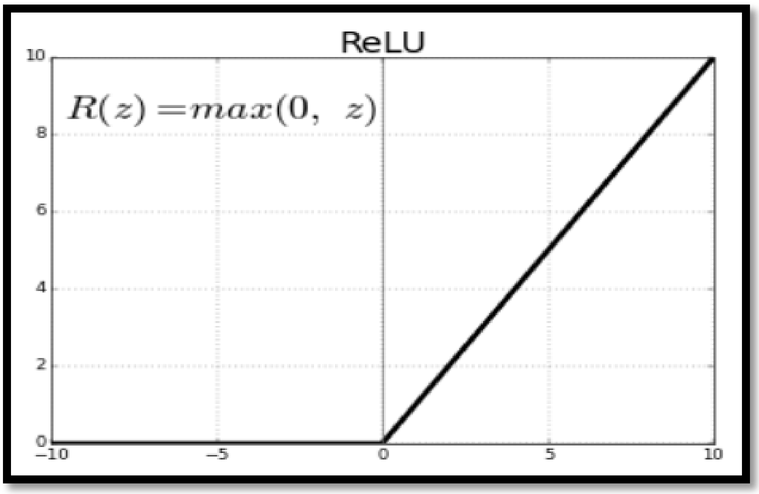

Figure (3.9): ReLU plotted function[112].

4. Fully Connected Layer

It is final layer in CNN that performs the classification task. It comes after convolution and stacking layers. A fully connected layer flattens the output of the preceding layers as the conventional neural network represents its mathematical description by combining the weighting of the previous feature layer. After that, the specific activation function is applied see Figure (3.10).

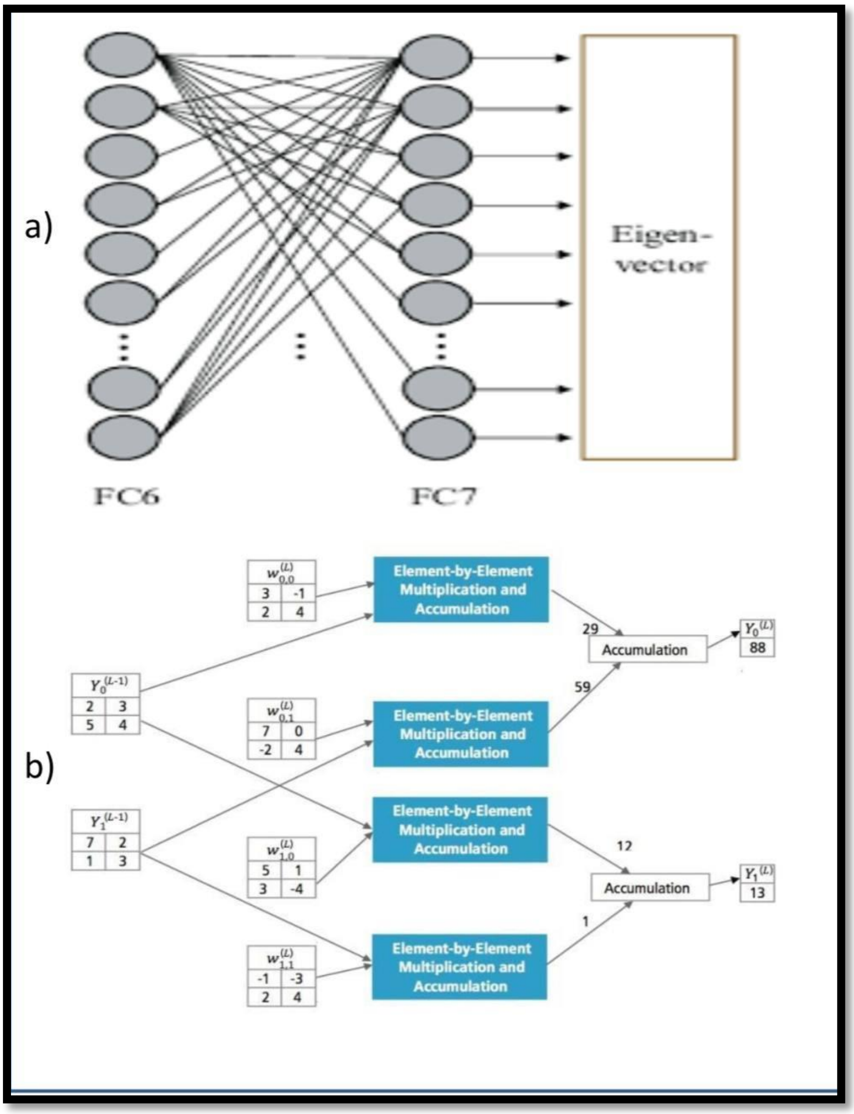

Figure (3.10): The Fully Connected layer (a) The general block diagram of fully connected layer, (b) Processing of fully connected layer[113].

Figure (3.11): the fully connected layer (a) The general block diagram of fully connected layer, (b) Processing of fully connected layer The final fully connected layer is called the output layer, responsible for making decisions and directly producing the class score. The sigmoid function is a more suitable activation function for the output layer with binary classification. With multi-class classification purposes, the softmax function is a more suitable activation function [114].

5. Regularization layers

Over fitting is one of the biggest problems that network models face. It happens in two situations: when the model is complex and when the dataset is weak. Since over fitting makes it difficult to generalize the model to new data, the model's accuracy will be high during the training period but poor during the testing period. To solve the over fitting problem, a dropout layer is used that is one from regularization layers.

- **Dropout layer**

The task of the dropout layer is to reduce the connection between neurons by randomly identifying the neurons (probability P); usually, less than 50%; and dropping their activations during the training procedure, set the weights to a value of 0 (this layer is only active during the training process) and all activations are measured by P during the test. The benefit of this layer is to reduce the over fitting problem [115].

6. Batch-Normalization (BN) Layer

This layer is used to speed up and more stable the training phase and minimize over fitting [116]. The batch normalization layer is often used after convolution layers to reduce the impact of different illumination between the input images and prevent differences in the values that result from the convolution method [117].

The batch normalization process solves the Internal Covariate Shift problem, which is characterized as changes in the distributions of inputs to the current layer as a result of changes in the preceding layer's parameters. As a result, this layer normalizes the performance of the layers before that by setting the mean and standard deviation to zero. Suppose input data x, batch normalization of it is as the following equation(2.8)[118] .

$$x = {}^{(x-\mu)}/_{std} \qquad \text{.......(3.16)}$$

where: std is the standard deviation of (x), and μ is mean of (x).

7. Weight constraints on layers

Large weights in the neural network are evidence of overfitting, while small weights make the model more stable. When predicting new data, it gives better performance, unlike large weights that give a poor prediction. A weight constraint is a network update that examines the weights' size and, if it exceeds a certain threshold, rescales the weights to be between a range of sizes or below the limit[119].

Two keyword arguments are exposed by these layers[120,121]:

- kernel constraint for the matrix of major weights.
- bias constraint for the bias.

There are several types of weight constraints [122]:

- The maximum norm. Restricts the weights of the hidden layers to be less than or equal to the required value.
- The min_max norm. Restricts the weights of the hidden layers so that their value is between the minimum and the maximum.

3.4.3.3 Training of CNN

To train CNN, this demands a big amount of images; this makes it possible for the network to learn different features in still images to get predictions effectively. At first, the images dataset is split into three sets, the training, the validation, and the testing sets. The training dataset is used in the real training stage to adjust weights in various layers and to create the model which will be used for the predictions. The purpose of the validation set is to make adjustments to only the hyper parameters. Whereas, the test set is utilized for the impartial evaluation of the trained model. Through the training phase, the network modifies the filter weights via a back propagation algorithm. The Back propagation operation involves four steps (forward pass, loss function calculation, backward pass, and weights update). At the beginning of the training phase, all weights are randomly initialized. As the primary step of the forward pass, the input image passed across the whole network from the training set is to generate an output. Next, the loss function is computed depend on predicted and actual outputs. Depending on the loss function, it is obvious to know which weights need to be adjusted and how much to decrease this function, this is named the back pass. After this, during the final step of the weights update, all of those weights are updated. It has been updated according to Equation (2.2) shown below:

$$w_{inew} = w_{iold} - \eta \frac{dl}{dwi} \qquad \ldots\ldots(3.17)$$

Where w_{inew} = New weight, w_{iold} = Initial weight

η=Learning rate, $\frac{\mathrm{dl}}{\mathrm{dwi}}$ = Derivative of the loss function,

A learning rate parameter that is an integral part of training operation and is selected via the user. Due to the weights are initially randomly configured, the learning rate is generally maintained higher [123]. This may take little time for the model to converge, i.e. for reducing loss function, a fixed number of learning epochs are applied. Then the resulting model is tested via a test dataset.

3.4.3.4 System Performance Measures

Several criteria have been employed to assess the performance of the classification algorithms:

1. The accuracy checks the number of correctly classified instances, whether positive or negative instances.

$$\boldsymbol{Accuracy(Acc)} = \frac{\boldsymbol{TP+TN}}{\boldsymbol{TP+TN+FP+FN}} \quad \text{……. (3.18)}$$

2. Sensitivity is the rate of identification of positive samples rightly.

$$\textbf{Sensitivity (Sen)} = \frac{\boldsymbol{TP}}{\boldsymbol{TP+FN}} \quad \text{……. (3.19)}$$

3. The precision of the model's performance is determined by testing the true positive from the Expected positives.

$$\textbf{Precision (Pre)} = \frac{\boldsymbol{TP}}{\boldsymbol{TP+FP}} \quad \text{……. (3.20)}$$

4. Specificity is the percentage of identification of negative examples rightly.

$$\textbf{Specificity (Spe)} = \frac{\boldsymbol{TN}}{\boldsymbol{TN+FP}} \quad \text{……. (3.21)}$$

5. F1-score shows a compound of precision and sensitivity for computing a balanced mean output.

$$\boldsymbol{F1 - Score} = \frac{\boldsymbol{2*TP}}{\boldsymbol{2*(TP+FP+FN)}} \quad \text{……. (3.22)}$$

6. Area under the curve

$$\textbf{(AUC)} = \frac{\textbf{(Sensitivity + Specificity)}}{\textbf{2}} \quad \text{……. (3.23)}$$

. Figure (3.11) shows confusion matrix of classifier system.

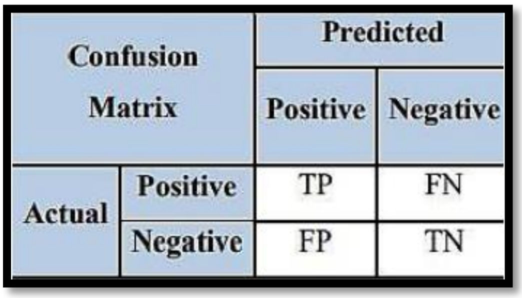

Confusion Matrix		Predicted	
		Positive	Negative
Actual	Positive	TP	FN
	Negative	FP	TN

Figure (3.11): Confusion matrix of classifier system.

The prediction error is recorded by four parameters:

- True Positive (TP) is the positive states that are correctly labeled as positive states.

- False Positive (FP) denotes the negative states that are incorrectly labeled as positive states.
- True Negative (TN) represents the right classification of negative diagnosis.
- False Negative (FN) indicates the positive cases that are incorrectly classified as negative [124].

3.5.2 Artificial Neural Networks of Un-Supervised Training Scheme

In this fashion of training, the network is trained for a specific data set and then adopting this stage to classify the test input data. Clustering operation is achieved by this type of neural networks.

3.5.2.1 Self-Organization Feature Map Artificial Neural Network

In clustering problems, the ANN clusters observations in two main stages. In the first, the learning rule is used to train the network for a specific data set. This is called training or learning stage. In the second, the observations are classified, which is called a recall stage. As mentioned before, the ANNs work into layers. The input layer contains the nodes through which data are input. The output layer generates the output that is interpreted by the user. Between these two layers there can be more layers (hidden layers). The output of each layer is an input of the next layer until the signal reaches the output layers as shown in Figure (3.12) [125].

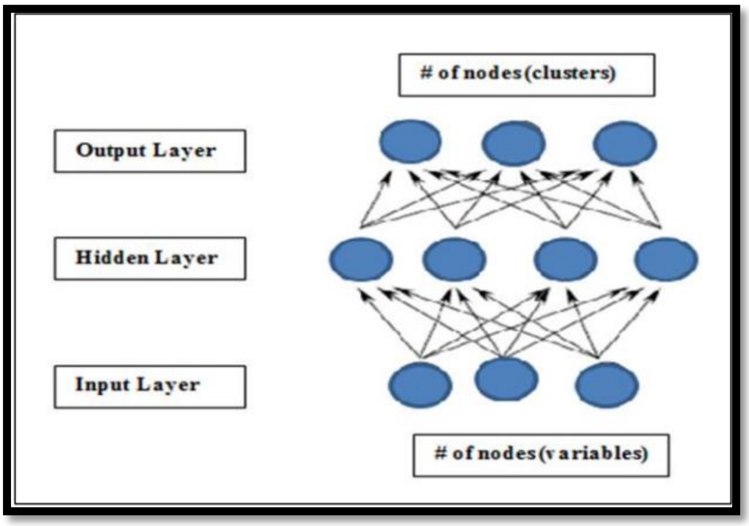

Figure (3.12): Illustration of a neural network for clustering [125].

One of the more important ANN is the Self-Organization Feature Map (SOFM) or SOM that was proposed by Kohonen [126]. It is a feed-forward neural network that has been utilized for medical image segmentation. Sometimes SOFM is called Kohonen map. It projects a high dimensional space (ndimensional input) into a low dimensional space (two dimensional or one). SOFM is basically a competitive network with the characteristic of self-organization providing a topology-preserving mapping from the input space to the clusters [126-128]. Self-organizing map is different in comparison to other artificial neural networks in the sense that they use a neighborhood function to preserve the topological properties of the input space [108]. Mathematically speaking, let $x = (x_1, x_{,2}, \dots., x_p)'$ be the input vector (training case), $w = (w_{l1,} w_{l2,} \dots., w_{\ lp})'$ the weight vector associated with the node *l* where w_{ij} indicates the weight assigned to input x_j to the node ***l***, where is the number of nodes (cluster seeds) and *p* is the number of variables. Each object of the training data set is presented to the network in some random order. Kohonen's learning law is an online algorithm that finds the node closest to each training case and moves that ''winning'' node closer to the training case. The node is moved some proportion of the distance between it and the training case. The proportion is specified by the learning rate. For each object i in the training data set, the distance d_i between the weight vector and the input signal is computed. Then the competition starts and the node with the smallest d_i , is the winner. The weights of the winner node are then updated using some learning rule. The weights of the non-winner nodes are not changed. Usually, the Euclidean distance is used to compare each node with each object although any other metric could be chosen. The Euclidean distance between an object with the observed vector $x = (x_1, x_{,2}, \dots, x_p)'$ and the weight vector $w = (w_{l1,} w_{l2,} \dots, w_{lp})$ is given by [108]:

$$d\,(x, w_I) = [\textstyle\sum_{\boldsymbol{j=1}}^{\boldsymbol{p}} (\boldsymbol{x_j} - \boldsymbol{w_{lj}})^{\boldsymbol{2}}\,]^{\boldsymbol{1/2}} \qquad \dots\dots. (3.24)$$

Let W_L^S, the weight vector for the L^{th} node on the S^{th} step of the algorithm, be the input vector for the i^{th} training case, and α^sbe the learning rate for the S^{th} step. On each step, a training case X$_i$ is selected, and the index q of the winning node (cluster) is determined by [108]:

$$\boldsymbol{q} = ar\,g_l \min \| w\,_s^l - X_i \| \qquad \dots\dots. (3.25)$$

The Kohonen update rule for the winner node is given by [108]:

$$W_q^{s+1} = W_q^s\,(1 - \alpha^s) + X_i\,\alpha^s = W_q^s + \alpha^s\,(X_i - W_q^s\,) \qquad \dots\dots. (3.26)$$

for all non-winning nodes, $W_l^{s+1} = W_l^s$.

A self-organizing map consists of 2-D array of nodes or neurons. Associated with each node is a weight vector i of the same dimension as the input data vectors and a position in the map space. The usual arrangement of nodes is a regular spacing in a hexagonal or rectangular grid. The self-organizing map describes a mapping from a higher dimensional input space to a lower dimensional map space. The procedure for placing a vector from data space onto the map is to find the node with the closest weight vector to the vector taken from data space and to assign the map coordinates of this node to our vector. Euclidean distance to all weight vectors is computed. The neuron with weight vector most similar to the input is called the Best Matching Unit (BMU). The weights of the BMU and neurons close to it in the SOM lattice are adjusted towards the input vector. The magnitude of the change decreases with time and with distance from the BMU. The update formula for a neuron with weight vector [129]:

$$W_i\,(t+1) = W_i\,(t) + \alpha(t) h_{ci}\,(t)\,(x\,(t) - w_i\,(t)) \qquad \ldots\ldots\ (3.27)$$

Where α(t) is a monotonically decreasing learning coefficient, $h_{ci}\,(t)$ is the neighborhood function, typically considered as a Gaussian function. The process repeats for a large number of iterations. SOFM preserves the most important topological and metric relationships of the primary data items. Although a primary application of SOFM is dimension reduction, it has been utilized for medical image segmentation [129,130].

3.6 Clustering Techniques for Segmentation Purpose

Clustering is a process for segmenting and classifying objects or patterns in such a way that samples of the same group are more similar to one another than samples belonging to different groups. Many clustering strategies were introduced used, such as the hard clustering scheme and the fuzzy or soft clustering scheme, each of which has its own special characteristics. The conventional hard clustering method restricts each point of the data set to exclusively just one cluster. As a consequence, with this approach the segmentation results are often very crisp; i.e. each pixel of the image belongs to exactly just one class. But the segmentation utilizing this approach is a difficult task when the images have limited spatial resolution, poor contrast, overlapping intensities, and noise or intensity inhomogeneity variation. To overcome these difficulties the techniques that introduce the idea of partial membership of belonging described by a membership function; fuzzy clustering as a soft segmentation method was widely studied and successfully applied in medical image segmentation by many researchers like [131,132].

3.6.1 K -Means Clustering Algorithm

Hard scheme K-means aims to partition *n* observations into *k* clusters in which each observation belongs to the cluster with the nearest mean, serving as a prototype center of the cluster. This results in a partitioning of the data space into Voronoi cells.

K-means algorithm is a circulating process will continue to change k centers location step by step until no more changes are done and the centers do not move any more. K-means algorithm aims to minimize the objective function that represents the function of squared error which given by [133]:

$$J(V)=\sum_{i=1}^{c}\sum_{j=1}^{c_i}(\|x_i-v_i\|)^2 \qquad \text{.......} \ (3.28)$$

where,

'$\|x_i - v_j\|$' is the Euclidean distance between x_i and v_j.

'c_i' is the number of data points in i^{th} cluster.

'c' is the number of cluster centers [133].

3.6.2 Fuzzy C-Mean Clustering Algorithm

Among the fuzzy (soft) clustering methods, Fuzzy C-Mean (FCM) algorithm is the most popular method used in image segmentation because it has robust characteristics for ambiguity and can retain much more information than hard segmentation methods [134].

Conventional and modified FCM algorithm has been widely studied and successfully applied in medical image segmentation by many researchers such as: [135-136]. As a fuzzy clustering method, FCM algorithm is based on the representation of clusters by their respective centers. The data space $X = \{x1, x2, \ldots, xN\}$ can be clustered by minimizing the objective function with respect to cluster centers and membership matrix by [137]:

$$J = \sum_{j=1}^{N} \sum_{i=1}^{C} U_{ij}^{m} \, d^2(x_j, c_i) \qquad \ldots\ldots(3.29)$$

Based on following constraints:

$$\forall\, i \in [1, N]: \textstyle\sum_{i=1}^{C} U_{ij} \;\; \forall\, j \in [1, N], \forall\, i \in [1, C]: U_{ij} \in [1,0] \qquad \ldots.(3.30)$$

Where U=$[U_{ij}]_{C\times N}$ represents the membership function matrix $d(x_j, c_i)$, the distance between and cluster center is represented by the matric, number of clusters is represented by C, the number of data points in search space is denoted as N and M represents fitness degree where ($m > 1$) [137] .

Using cluster center C_i calculate the membership matric U_{ij} by [138]:

$$U_{ij} = \frac{1}{\sum_{k=1}^{c} \left[\frac{\|x_j - c_i\|}{\|x_j - c_k\|}\right]^{\frac{2}{m-1}}} \qquad \ldots\ldots..(3.31)$$

$$C_i = \frac{\sum_{i=1}^{n} u_{ij}^{m} \cdot x_i}{\sum_{i=1}^{x} x_{ij}^{m}} \qquad \ldots\ldots.(3.32)$$

3.7 Contrast Adjustment based Histogram

- **Histogram**

Thresholding is the simplest and the most commonly used method of segmentation. When an image *f (x, y)* contains an object having homogeneous intensity and a background with different intensity levels, such an image can be segmented into two regions by simple thresholding, the segmented image *g (x, y)* can be expressed as [139]:

$$g(x, y) = \begin{cases} 1 & \text{if } \; f(x, y) > T \\ 0 & \text{otherwise} \end{cases} \qquad \ldots\ldots(3.\,33)$$

Where represents the threshold value. The choice of threshold T can be dependent on the image histogram. If the image has a single object and a background of homogeneous density, it often has a bimodal histogram as shown in the Figure (3.13).

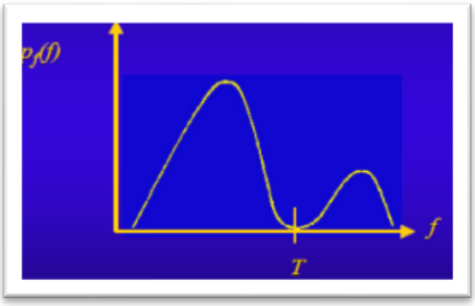

Figure (3.13): Bimodal histogram.

The histogram of pixel values can be denoted by: h_0; h_1;.. h_k …;h_N; where h_k specifies the number of pixels in an image with gray scale value k and N is the maximum pixel intensity value (typically 255). If the histogram is noisy, the calculation of the local histogram minimum is difficult, and in this case, low pass filter is utilized for smoothing to reduce the noise. If the intensity of the object or of the background is slowly varying, the histogram may not contain two clearly distinguished lobes. In this case, a spatially varying threshold can be applied.

In certain cases the region boundary is desired. If the segmented image *g(x, y)* is available, the boundary obtained by finding the transitions from one region to another is:

$$b(x,y) = \begin{cases} 1 \; if \; \{(g(x,y) \in R_i \; and \; g(x,y-1) \in R_j \;, i \; \neq j \\ \; or \; (g(x,y) \in R_i \; and \; g(x-1,y) \in R_j \;, i \neq j \\ 0 \qquad\qquad otherwise \end{cases} \quad \text{……..(3.34)}$$

- **Contrast Adjustment**

The principal objective of enhancement is to process an image so that the result is more suitable than the original image for a specific application. Image enhancement approaches fall into two broad categories spatial domain methods and frequency domain methods. There is no general theory of image enhancement. When an image is processed for visual interpretation, the viewer is the ultimate judge of how well a particular method works. Visual evaluation of images quality is a highly subjective process, thus making the definition of a “good image” an elusive standard by which to compare algorithm performance. However, even in situations when a clear–cut criterion of performance can be imposed on the problem, a certain amount of trial and error usually is required before a particular image enhancement approach is selected [140]. Figure (3.14) shows various pixels based mapping cases that can be used to improve image appearance by utilizing image contrast adjustment process to map range of gray values of the input image to new values depending on gamma parameter, where gamma specifies the shape of the curve describing the relationship between the values in input image and output image. When gamma is less than 1 the mapping would weighted toward higher (brighter) output values. If gamma is greater than 1, the mapping is weighted toward lower (darker) output values. When gamma equals 1, a linear mapping would be achieved.

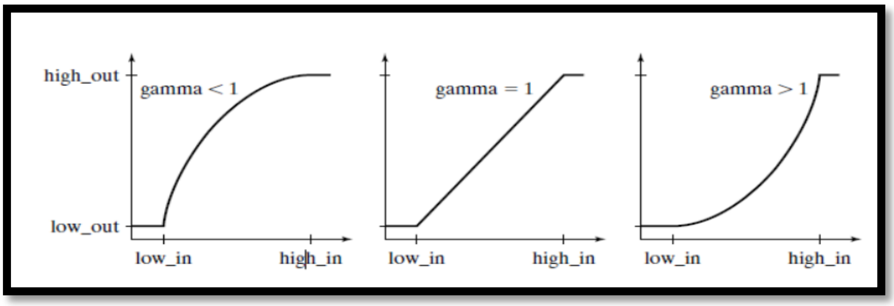

Figure (3.14): Various mappings according to gamma value [141].

In this work, contrast adjustment has been implemented to highlight the intensity of the infected Covid-19 and infected tumor regions.

3.8 HSOFM Hybrid Technique

In this technique the final centers of k-means segments were adopted as initial value of the nodes in HSOFM algorithm in order to reduce the long elapsed times of implementing HSOFM and to improre the clustering process.

3.9 Morphological Operations

Morphological operators are used in image processing due to for their robust performance in preserving the shape of a signal ,while suppressing the noise [142]. There are two basic morphological operators: erosion and dilation, opening and closing are two derived operations in terms of erosion and dilation. Here a brief introduction to the morphological operations [143].

For each morphological operations, there is have a structural element and in is study was used disk-shaped structural element. A structuring element is a matrix consisting of only 0's and 1's that can have any arbitrary shape and size. The pixels with values of 1 define the neighborhood. two-dimensional, or flat, structuring elements are typically much smaller than the image being processed and In mathematical morphology, a structuring element is a shape, used to probe or interact with a given image, with the purpose of drawing conclusions on how this shape fits or misses the shapes in the image.

1- Dilation: Considers the dilation of a binary image by a simple hexagonal structuring element B. This dilation can be expressed as the locus of centers x of the structuring element B_x where the intersection of the image X and B_x is nonempty. This is often referred to as B_x hitting X and, therefore, the name “hit or miss transform” is often applied to this operation. It may be expressed as [142]:

$$X \oplus B = \{x : B_X \cap X \neq \emptyset\} \qquad \ldots\ldots.(3.35)$$

2- Erosion: Duality in mathematical morphology requires that every transformation to a set X also be consistent with operations to its complement X^c . If X dilates then X^c shrinks and vice versa. This shrinking of X^c, termed erosion, is the dual of dilation. Therefore, if the foreground (white region X) of an image is dilated, the background (black region X^c) is eroded. Likewise, if the foreground is eroded, the background is dilated. Again, two interpretations of erosion are possible. Consider first the “hit or miss” transform where the erosion of X by B can be expressed as the set of points x where $\mathrm{B_x}$ can be positioned such that B is completely contained in X [133]:

$$X \ominus \mathrm{B} = \{\mathrm{x} \setminus \mathrm{B_x} \subset \mathrm{X}\} \qquad \ldots\ldots(3.36)$$

3. Opening and Closing: The primitive operations of dilation and erosion are generally applied sequentially using a single structuring element. These combined operations are openings and closings. The opening consists of an erosion followed by a dilation and can be viewed as the union of all points in B everywhere that B is contained in X. This is in contrast to retaining only the origins of B as in the erosion process
described above (3.31).

Opening is denoted in terms of the primitive operations of dilation and erosion as simply [142]:

$$\mathrm{X^{op}} = (\mathrm{X} \ominus \mathrm{B}) \oplus \mathrm{B} \qquad \ldots\ldots(3.37)$$

If isolated portions of X are smaller than the element B, they are removed completely. If X contains peninsulas narrower than B, they are also removed. Closing reverses the order of operations such that X is first dilated and then eroded [142]:

$$\mathrm{X^{cl}} = (\mathrm{X} \oplus \mathrm{B}) \ominus \mathrm{B} \qquad \ldots\ldots(3.38)$$

4.1 Introduction

Artificial neural networks are used to detect and isolate abnormalites in medical images in two stages. The first stage is the stage of diagnosing cases of Covid-19, tumors, and normal cases by training the artificial neural networks on three classes (Covid-19, tumors and normal) . The images under study were tested at this stage, utilizing convolution neural networks (CNN). In the second stage, the images that calassified in the first stage as abnormal cases (Covid-19 and tumors) were examined for the purpose of detecting, isolating and extracting abnormal areas using artificial neural networks (unsupervise Histogram Self-Organization Feature Map (HSOFM)) and two clustering methods (K-Means and Fuzzy C-Mean (FCM)) besides an adapting a hybrid method to reduce the implementation required time for HSOFM algorithm. In this study, Covid-19 infected areas were extracted for the first time.

The specifications of the PC used in this study are (Intel(R) Core i7-8565U @ 1.80GHz CPU, 20GB RAM for Windows 10, 64bit OS). All aspects of the proposed system were implemented using Matlab 2020.

4.2 Traning and Testing CNN Stage

In this stage, images data has been trained the numbers of data 5,000 images of Covid-19-infected lungs, 5,000 images of normal lungs, and 5,000 tumors-infected lungs. These CT scan images were taken via the open-source Kaggle library for this thesis. The training data accounted for 90% of all datasets, the testing data accounted for 10%, and the validation data accounted for 20% of the training data. The statistics of the CT scan division are shown in Table (4.1).

Table (4.1): Shows The data set divided in the second case.

	Covid-19	normal	tumors	Total
Train set	3600	3600	3600	10800
Validation set	900	900	900	2700
Test set	500	500	500	1500

A sample of lung images used in the proposed convolutional neural network is shown in Figure (4.1).

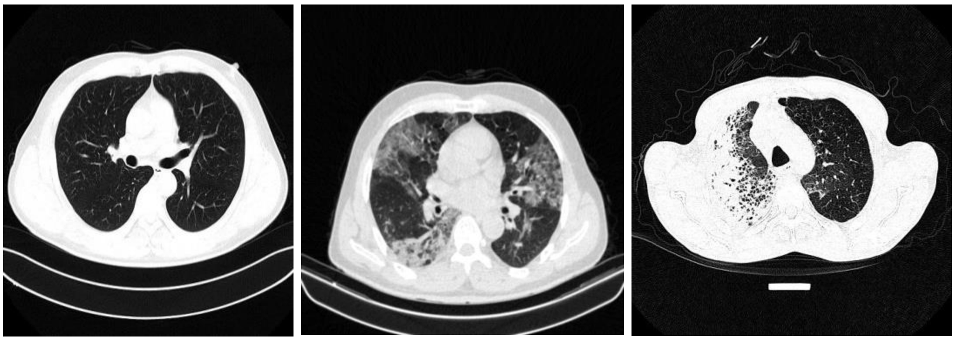

Figure (4.1): Represent samples from the dataset (Normal, Covid, Tumor).

4.2.1 Building and Training CNN Model

CNN networks is created and trained on a database consisting of a group of images (Covid-19, normal and tumors) to obtain the best accuracy and performance. The initial CNN model architecture in Table (4.2) and CNN work diagram show in Figure (4.2).

Table (4.2): The initial CNN model architecture.

Initial CNN Model
Input image size : 200 x 220
Feature extraction:
Layer 1: Convolutional layers with 32 filters, kernel 5x5 ,Relu.
Max pooling layer stride 2x2.
Layer 2: Convolutional layers with 64 filters ,kernel 5x5,Relu.
Max pooling layer stride 2x2.

Layer 3: Convolutional layers with 128 filters ,kernel 3x3,Relu.

Max pooling layer stride 2x2.

Classification:

1 softmax layer.

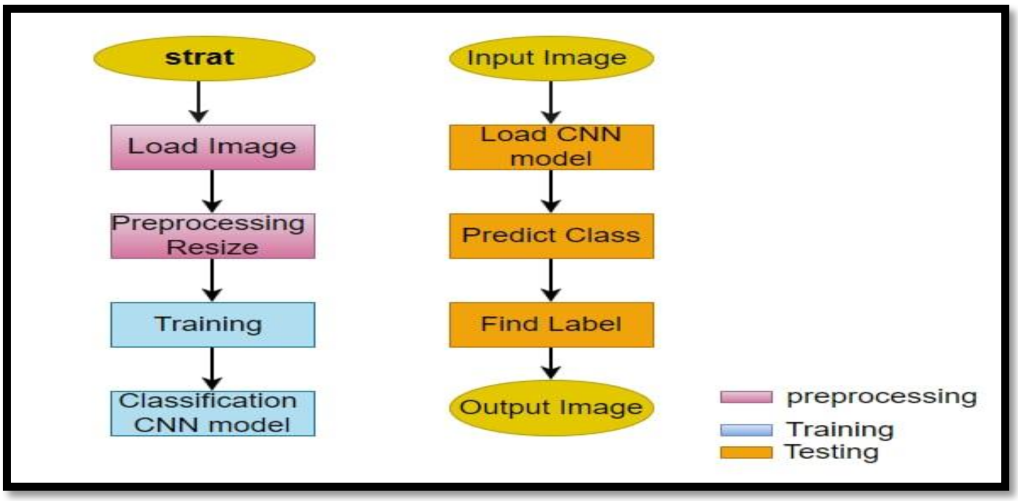

Figure (4.2): CNN work diagram.

The accuracy of the CNN model and losses during training and validation are depicted in Figure (4.3).

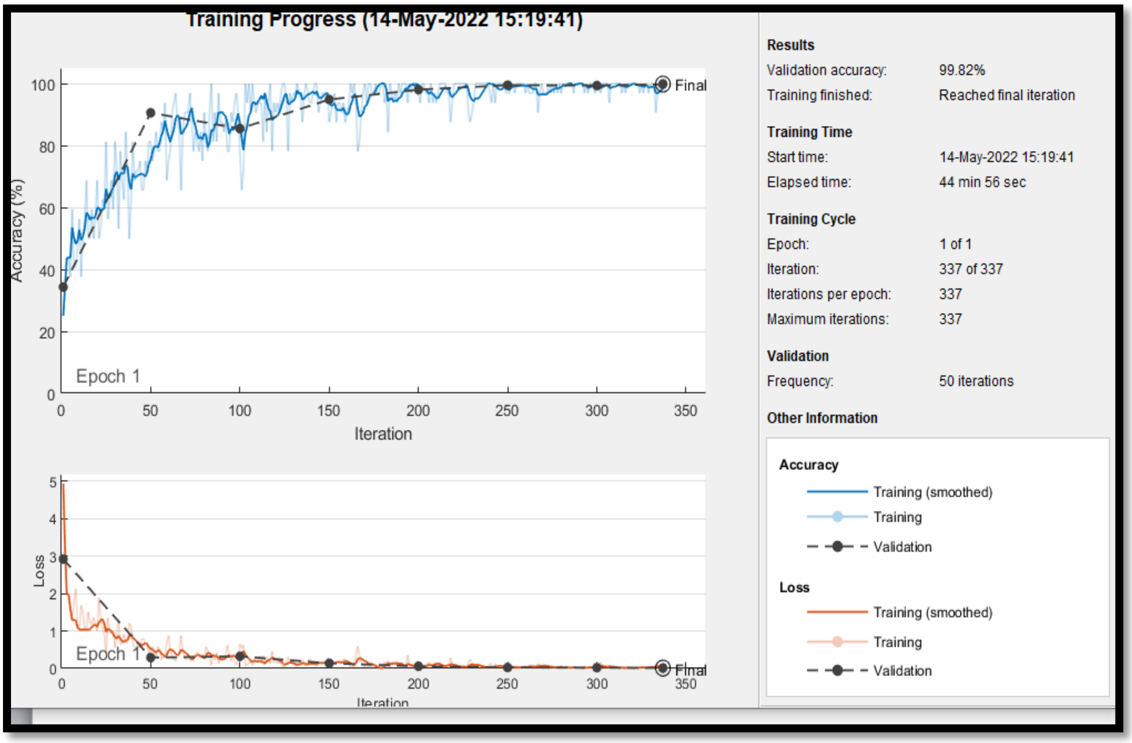
Training Progress (14-May-2022 15:19:41)

Results
Validation accuracy: 99.82%
Training finished: Reached final iteration

Training Time
Start time: 14-May-2022 15:19:41
Elapsed time: 44 min 56 sec

Training Cycle
Epoch: 1 of 1
Iteration: 337 of 337
Iterations per epoch: 337
Maximum iterations: 337

Validation
Frequency: 50 iterations

Other Information

Figure (4.3): CNN (initial model) training accuracy, validation accuracy, training loss, and validation loss.

4.2.2 Fit Parameter of CNN Model

Hyper-parameters must be set correctly to gain the greatest results. Several filters, drop-out, and activation functions. The CNN was trained on three different CNN architectures, and tested for training accuracy as shown in Figure (4.4).

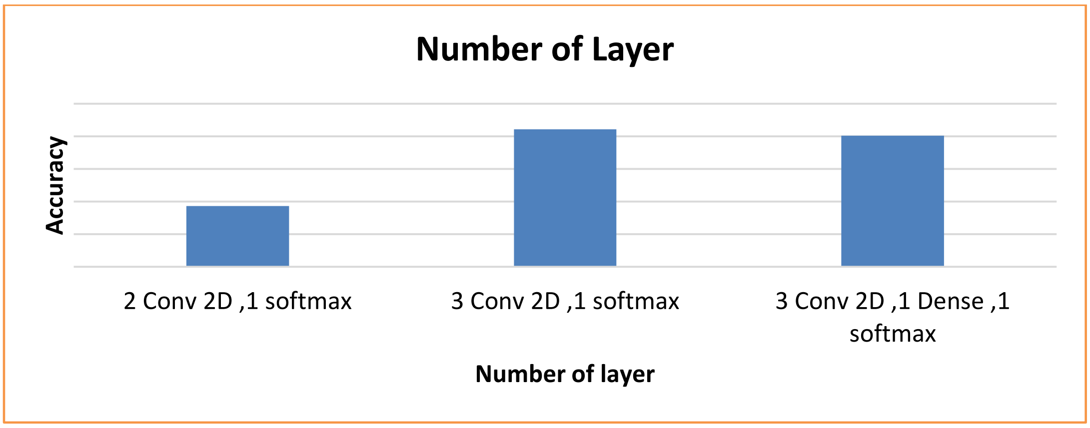

Figure (4.4): Comparison of CNN multi-architectures.

In Figure (4.4), the best CNN is the second (3 Conv 2D, 1 Softmax). 3 Conv 2D, 1 Dense, 1 Softmax) produced nearly the same accuracy, but with a higher number of parameters, which increased execution time.

Filter size affects accuracy by using different number of fillers CNN was tested on different sizes of filters as in Figure (4.5).

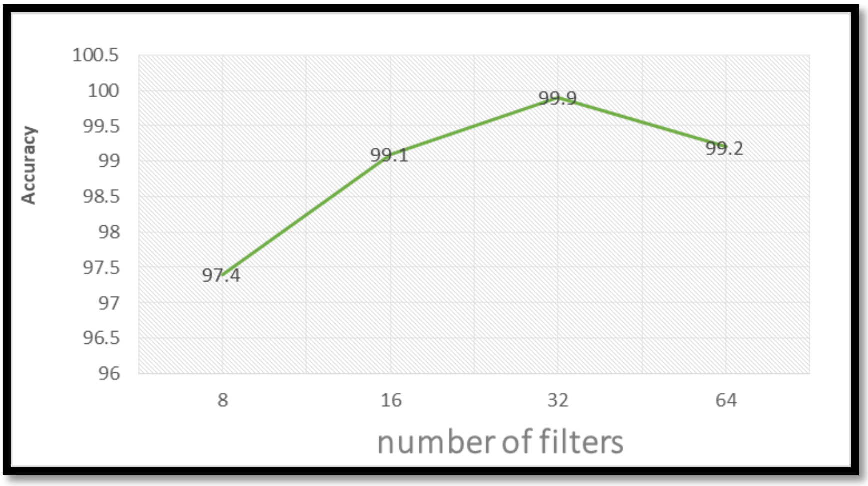

Figure (4.5): Comparison of number of filter.

Figure (4.5) shows the number of filters 32 and it was found the best filter size (5x5).

Different size of the images were tested under training to obtain the best accuracy as in Figure (4.6).

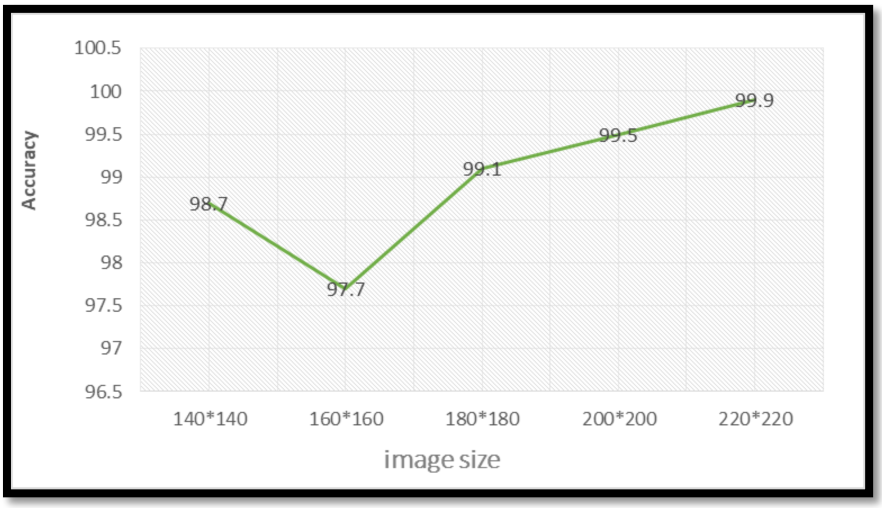

Figure (4.6): Comparison of image input sizes.

Figure (4.6) shows Comparison of image input sizes, and it was (220 * 220) found that is the beast size of image with higher accuracy.

Three different types of activetion function were used to obtain the best accuracy as in Figure (4.7).

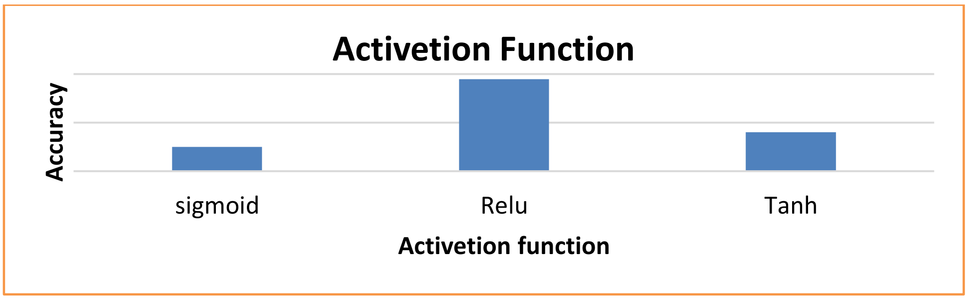

Figure (4.7): A comparison of activation functions.

Figure (4.7) shows Comparison of activation functions, and it was found that (Relu) is the beast activation function with higher accuracy because the relu function is one of the most important activation functions because it converts negative values to zero and positive values remain the same. Thus, complex arithmetic operations will be reduced and training time will decrease because all neurons are not activated at the same time.

A different number of epochs were used in the training process to obtain the highest accuracy as in Figure (4.8).

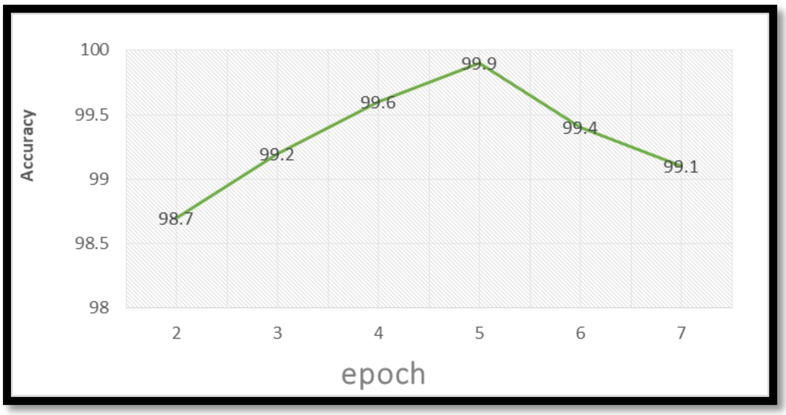

Figure (4.8): Comparison of numbers of epochs.

Figure (4.8) shows comparison of number of epochs, and it was found that the highest accuracy of 99.09% in 5 epochs.

Many types of optimizers can be used in the proposed network. However, each type has its performance. Therefore, three optimizers (Adam, Sgdm, and Rmsprop) were tested, and the best among them was selected in terms of performance. Figure (4.9) shows that the Adam optimizer was the best performer for both models when used in the proposed network.

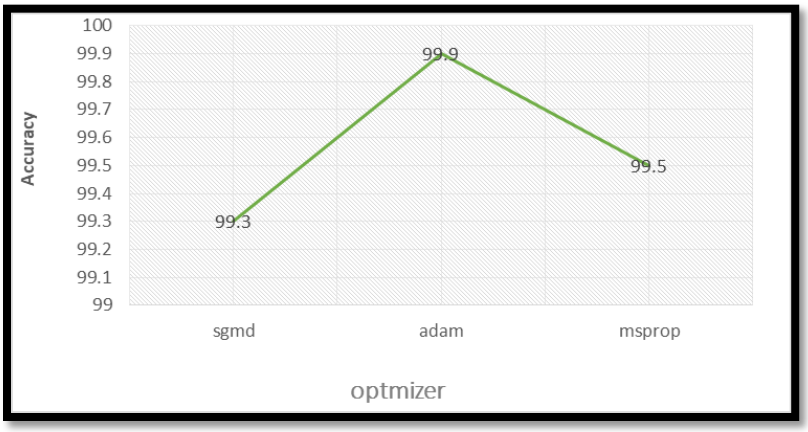

Figure (4.9): Comparison between optimizer and accuracy.

In terms of performance, one of the criteria that significantly impact network performance is the learning rate. The accuracy of the network was tested on different numbers of learning rates, as shown in Figure (4.10). Through the experiment with other numbers, it becomes clear that there is a significant and clear difference in the network's performance. 0.0001 is the best performer in terms of accuracy and other measures.

Figure (4.10): Comparison between learning rate and accuracy.

CNN model has been trained and get the best accuracy by setting hyper parameters correctly to get the best results Many filters, dropout and activation functions as shown in previous comparisons.

Table (4.3) shows the final parameters of CNN.

Table (4.3): The CNN final parameters

Model	CNN Classifier
No. of Epoch	5
Data Augmentation	None
No. of Classes	3
No. of training sample	3600
No. of validating sample	900
Other parameters	Image size: 220x220 Initial learning rate: 0.001 Drop out: 0.3 Filter size : 5x5 No. of layer : 3 Conv2D 1 softmax Activation function : Relu Softmax classifier : 3 class No. of Filter : 32 No. of Epoch: 5

4.3 Performance Measurement

By using the CNN, the training accuracy reached 99% and a validation accuracy of 99%. The accuracy of the CNN model during training, validation, and loss is depicted in Figure (4.3).

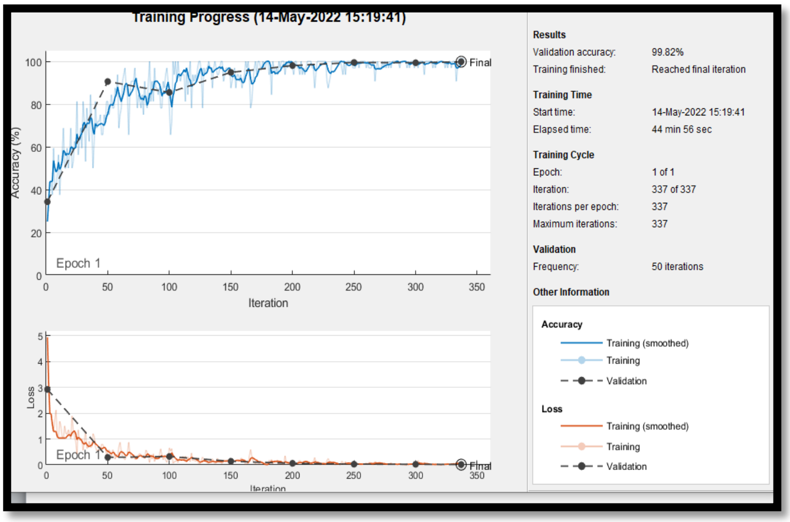

Results
Validation accuracy: 99.82%
Training finished: Reached final iteration
Training Time
Start time: 14-May-2022 15:19:41
Elapsed time: 44 min 56 sec
Training Cycle
Epoch: 1 of 1
Iteration: 337 of 337
Iterations per epoch: 337
Maximum iterations: 337
Validation
Frequency: 50 iterations
Other Information

Figure (4.3): CNN training accuracy, validation accuracy, training loss, and validation loss.

If the result is 100 or near 100 when computing the performance matrix, the model's performance is optimal. A confusion matrix is shown in Figure (4.11), which is made up of a 3x3 array with columns representing true values and rows indicating anticipated values.

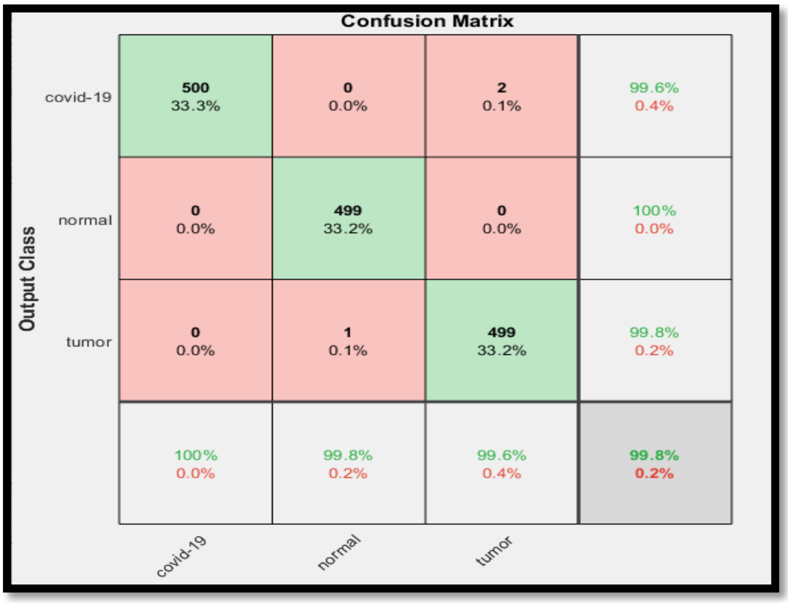

Figure (4. 11): Confusion matrix of CNN model.

Tables (4.4) and (4.5) indicate the number of total tested images, true and false diagnose result, as well as the results of performance measurement for the CNN Model for all 3 classes.

Table (4.4) : Proposed CNN model true and false diagnose result.

Variables in performance	Number of Images
Total Tested Image	1500
True Positive	499
True Negative	499
False Positive	1
False Negative	1

Table (4.5): Performance measurement for the CNN Model.

Performance Matrixes	Result
Accuracy	99.9
Precision	99.9
Recall	99.9
F1-Score	99.9

4.4 Test Image Under Study by CNN Model

The images under study for Covid-19 and tumors, were tested and their Performance Measures was calculated from the equations (3.18), (3.19), (3.21) and (3.23). The test result are shown in the Figure (4.12) for one Covid-19 image and for one tumor image and other results of testing rest experimental images are presented in appendix (5).Test result values for the Performance Measures shown in Table (4.6) for Covid-19 and tumors.

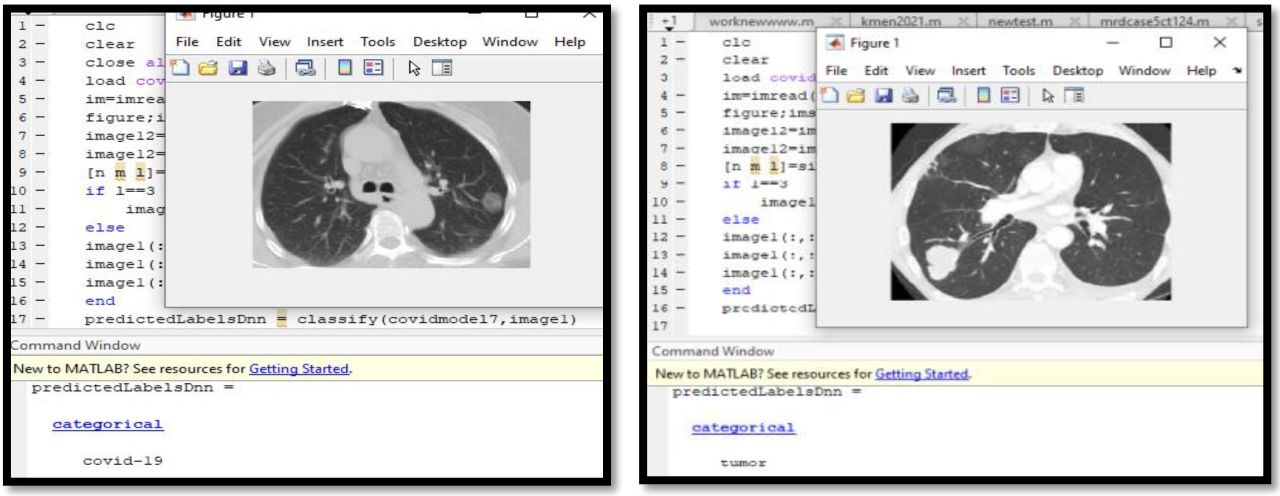

```
clc
clear
close al
load cov
im=imrea
figure;i
image12=
image12=
[n m l]=
if l==3
    imag
else
image1(:
image1(:
image1(:
end
predictedLabelsDnn = classify(covidmodel7,image1)
```

```
predictedLabelsDnn =

  categorical

     covid-19
```

```
clc
clear
load covid
im=imread(
figure;ims
image12=im
image12=im
[n m l]=si
if l==3
    image1
else
image1(:,:
image1(:,:
image1(:,:
end
predictedL
```

```
predictedLabelsDnn =

  categorical

     tumor
```

a **b**

Figure (4.12): Test result for Covid-19 case in (a) and for tumor case in (b).

(4.6): Performance Measures For Covid-19 and Tumor

	Sensitivity%	Specificity%	AUC%	Accuracy%
Covid -19	99.9	99.9	99.90	99.9
Tumors	99.98	99.98	99.98	99.98

4.5 Experimental Images Data

The available information for the images under test, in which utilized to achieve second stage of work (the segmentation stage), is shown in Table (4.7).

Table (4.7): The available information of the Covid-19 infected images.

Images	Name of image	Modality	Size(pixels)	Abnormality and Tumor type	Source
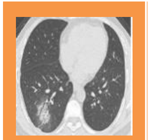	Covid-1	CT Scan	265x357	Covid-19	https://github.com/?fbclid=IwAR2GflDoc2tuiNzfwc7Tkk_aop9AHMxGawytbUIHeBcsQHcmqcx-DrchY4A
	Covid-2		1043x1080	Covid-19	
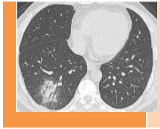	Covid-3		138x175	Covid-19	
	Covid-4		252x331	Covid-19	
	Covid-5		252x331	Covid-19	Dr.Zaid Al-Khafaji Center
	Covid-6		252x331	Covid-19	

	**Covid-7**		**252x331**	**Covid-19**	
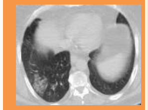	**Covid-8**		**252x331**	**Covid-19**	Ashur Center
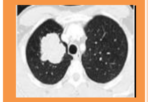	**Tumor1**		**154x264**	**Cancerous**	**https://github.com/?fbclid=IwAR2GflDoc2tuiNzfwc7Tkk_aop9AHMxGawytbUIHeBcsQHcmqcx-DrchY4A**
	**Tumor2**		**96x204**	**Cancerous**	
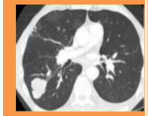	**Tumor3**		**434x570**	**Cancerous**	
	**Tumor4**		**259x320**	**Cancerous**	
	**Tumor5**		**186x271**	**Cancerous**	
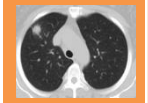	**Tumor6**		**171x262**	**Cancerous**	
	**Tumor7**		**185x268**	**Cancerous**	Fadak Center

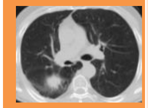	**Tumor8**		**250x317**	**Cancerous**	Dr.Zaid Al-Khafaji Center
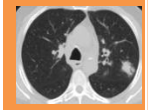	**Tumor9**		**209x315**	**Cancerous**	

4.6 Methodologies of The Segmentation Stage

The implemented techniques in this study can be summarized in the block diagram of Figures (4.13) CT-scan lung for Covid-19 and tumors.

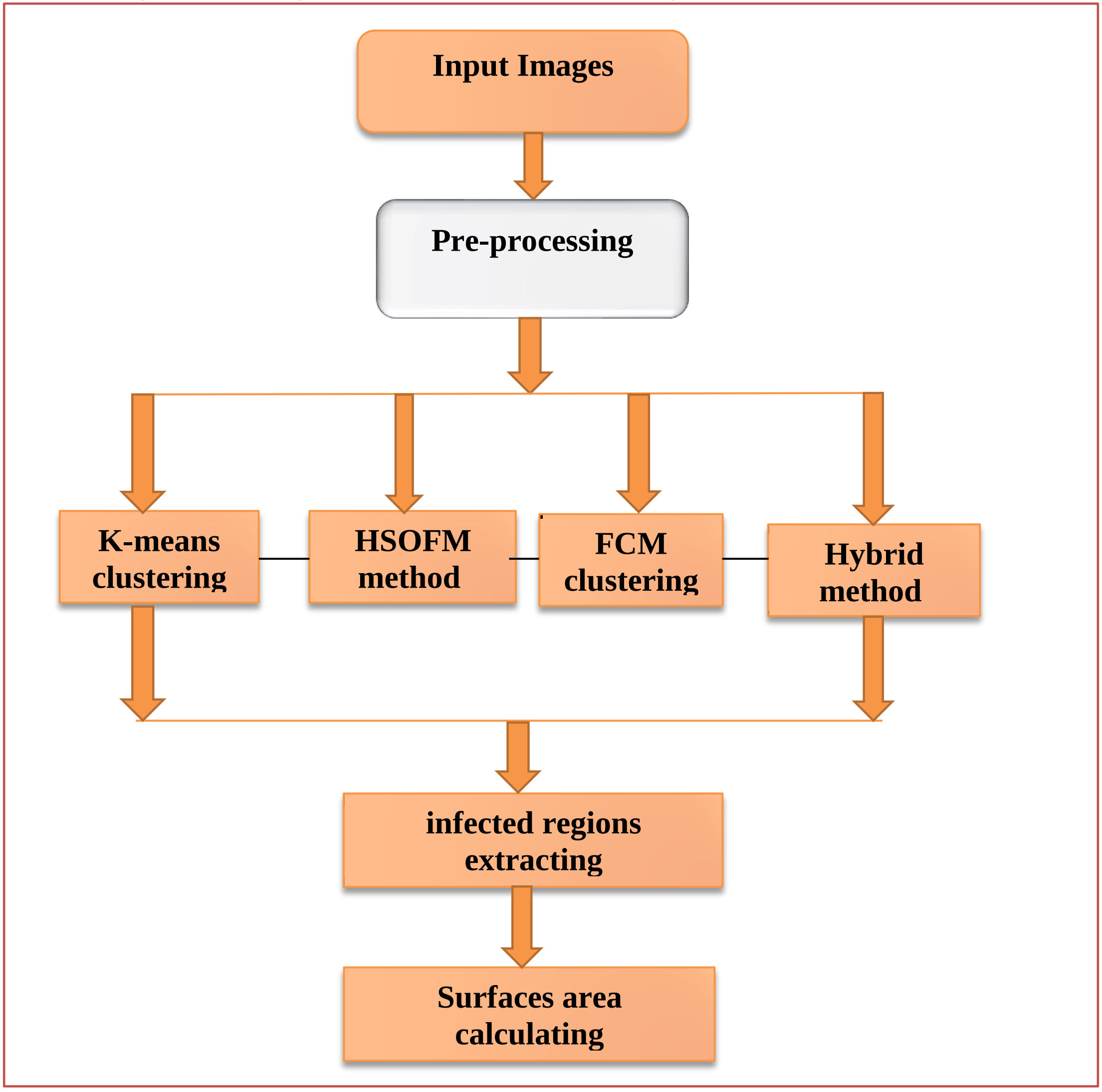

Figure (4.13): Block diagram of the implemented procedure.

4.7 Experiments and Results

Many steps were implemented in this stage, which are presented as follows:

4.7.1 Pre-Processing

The first step of this work is image background cutting and removing any extra part. Figures (4.14) and (4.15) presents the results of this step for the images of the lung (Covid-19 and tumor) respectively.

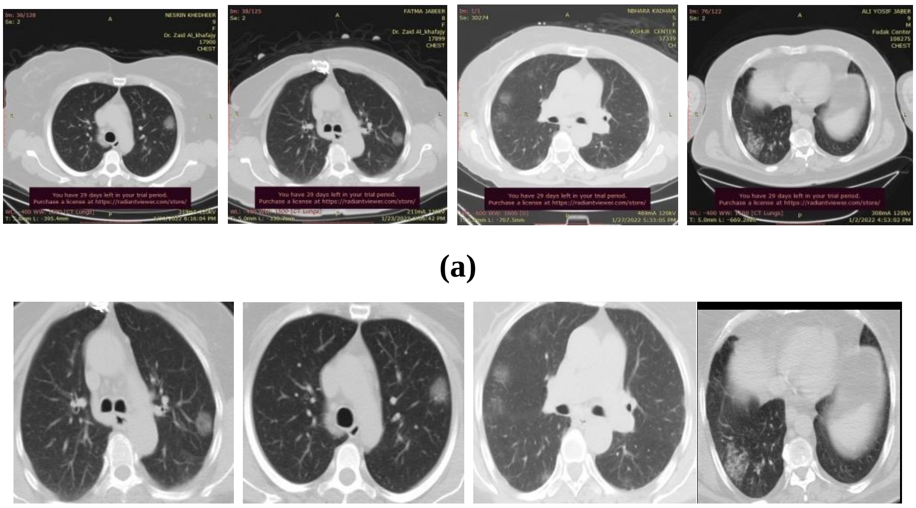

(a)

(b)

Figure (4.14): Input images of lung CT scan: (a) before background cutting (b) after background cutting and removing any extra parts.

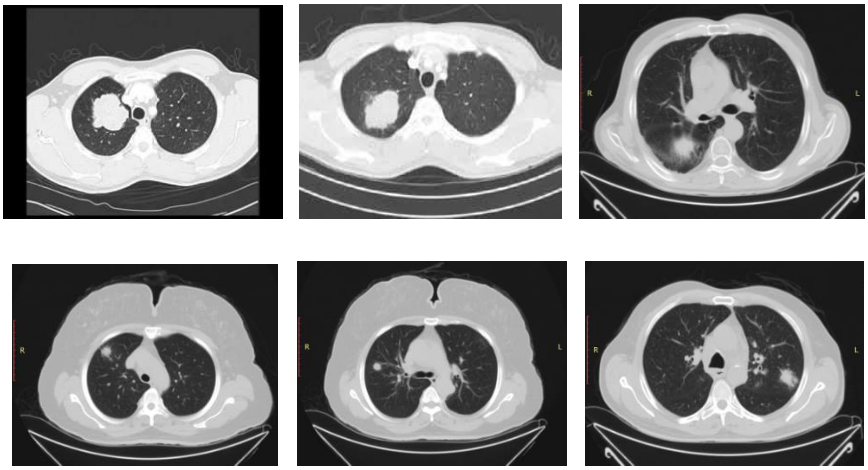

(a)

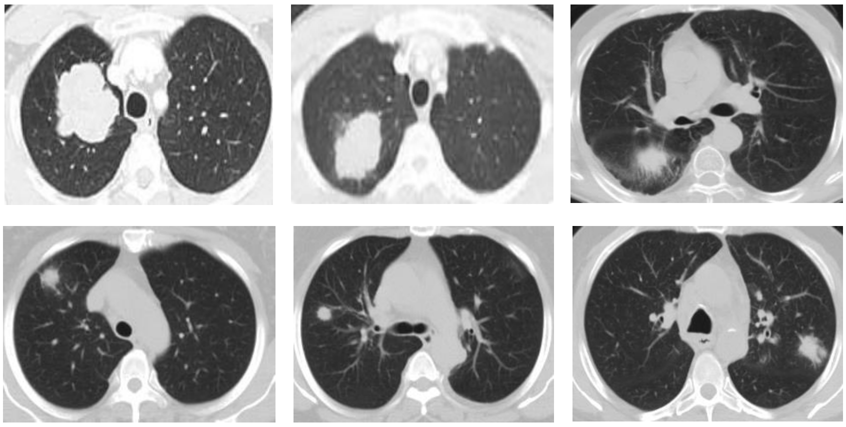

(b)

Figure (4.15): Input images of lung CT scan: (a) before background cutting (b) after background cutting and removing any extra parts.

The second step is to extract the hole lung regions for (Covid-19 and tumor) infecting images after removing any extra portion, this process was achieved by implementing k-means algorithm with two cluster only. Then by using morphological operations using a disk-shaped structural element with different values of radius (2-6) pixels depending on the number of additional pixels. Figures(4-16) and (4-17) present the results of this step for Covid-19 and tumors infected lung image

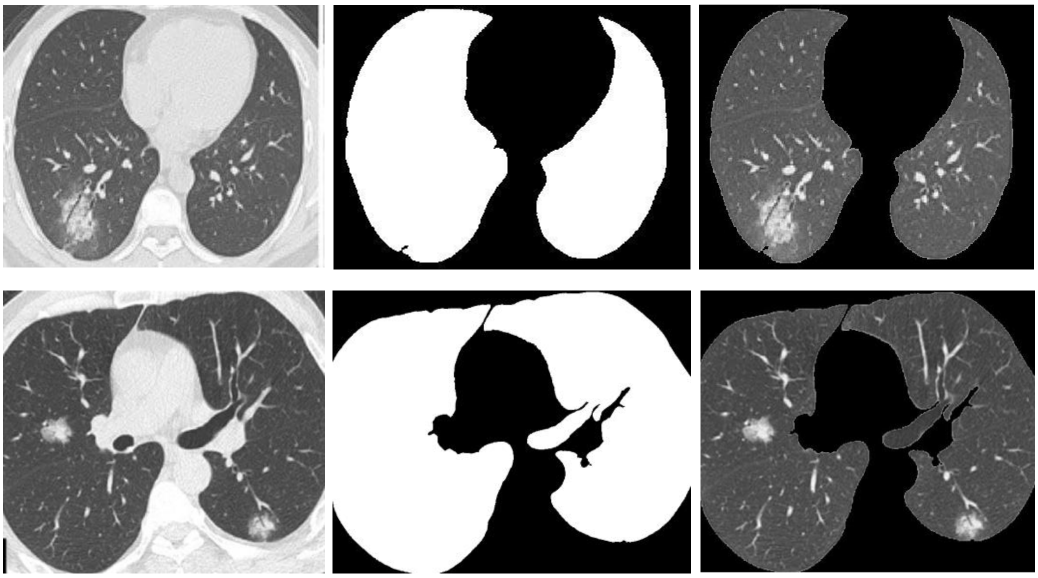

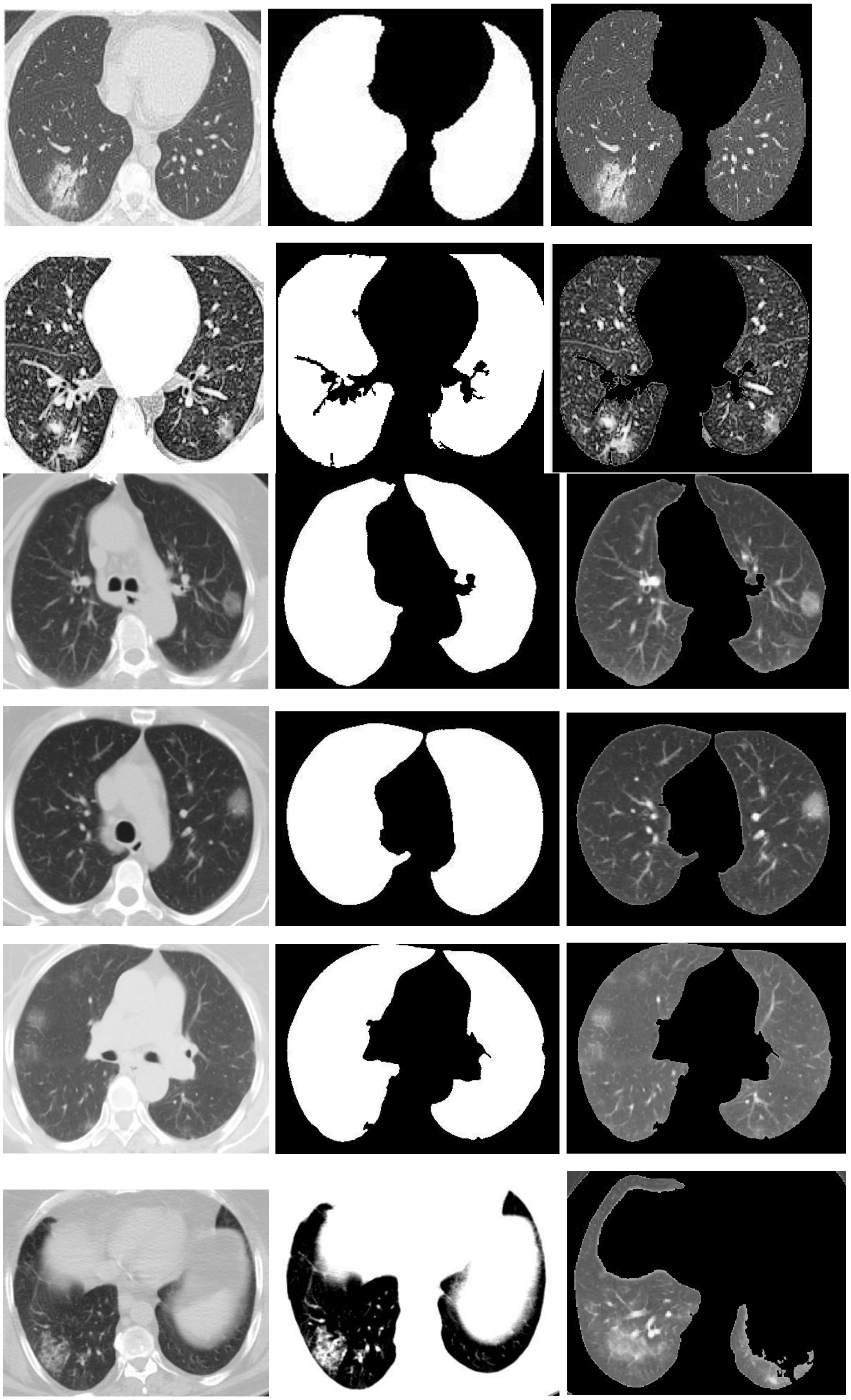

Figure (4.16): Extracting lung regions from CT-scan images for Covid-19.

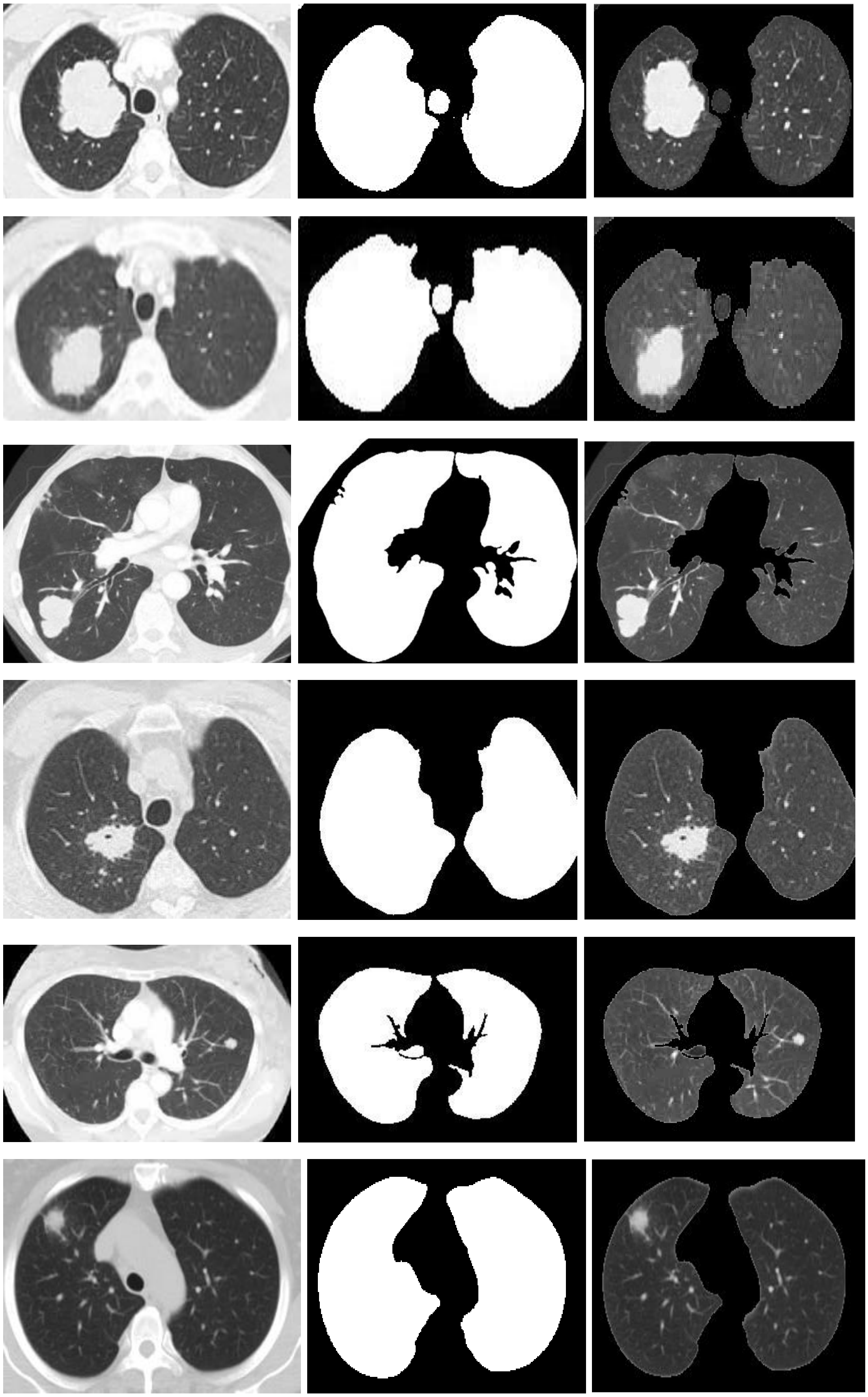

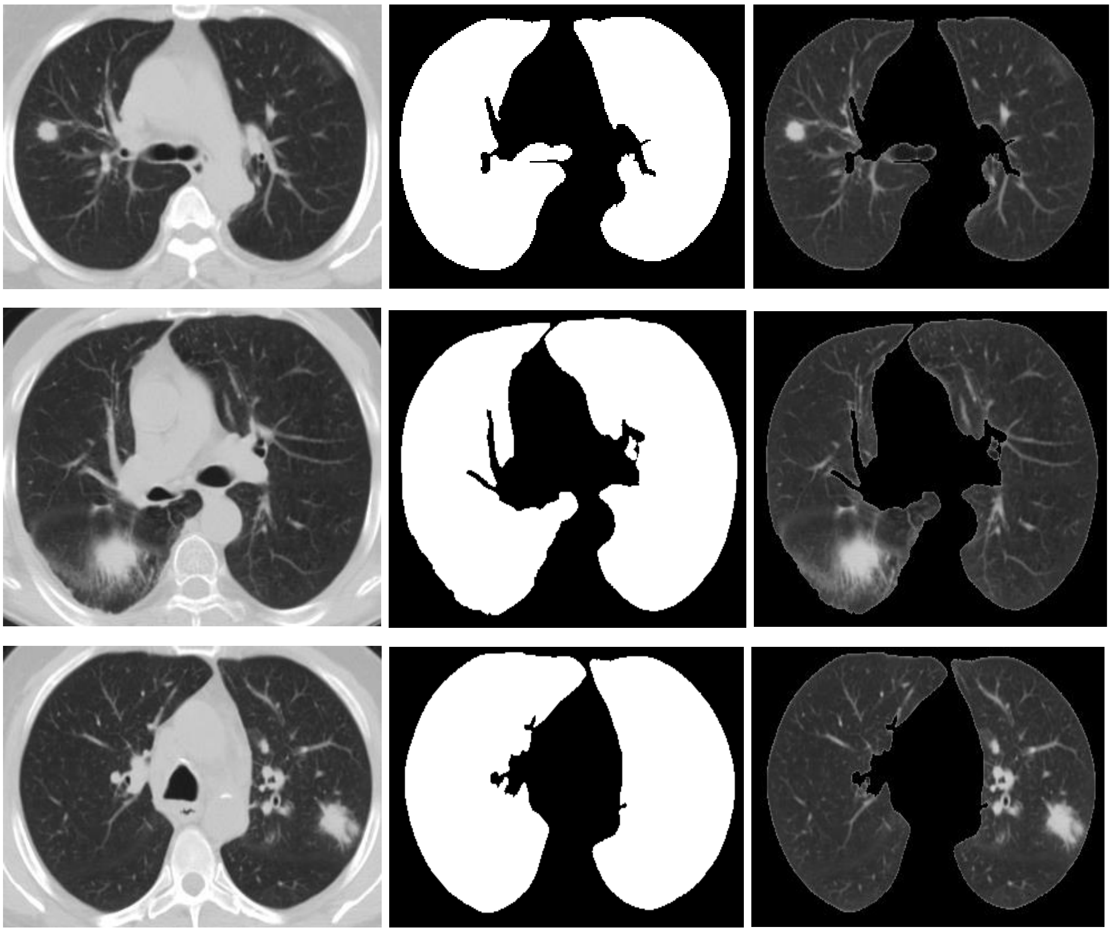

Figure (4.17): Extracting lung regions from CT-scan images for tumors.

In Figures (4.16) and (4.17) the first column represents the input images and the second column represents the lung images, which were resultant by applying k-means algorithm with two classes only, and with the aid of several morphological processes. The third column represents the gray image of the lung region.

4.7.1.1 Histogram

The histogram of the hole images for Covid-19 and tumors lungs and the histogram of samples of their infected regions where plotted as shown in Figures (4-18) and (4.19).

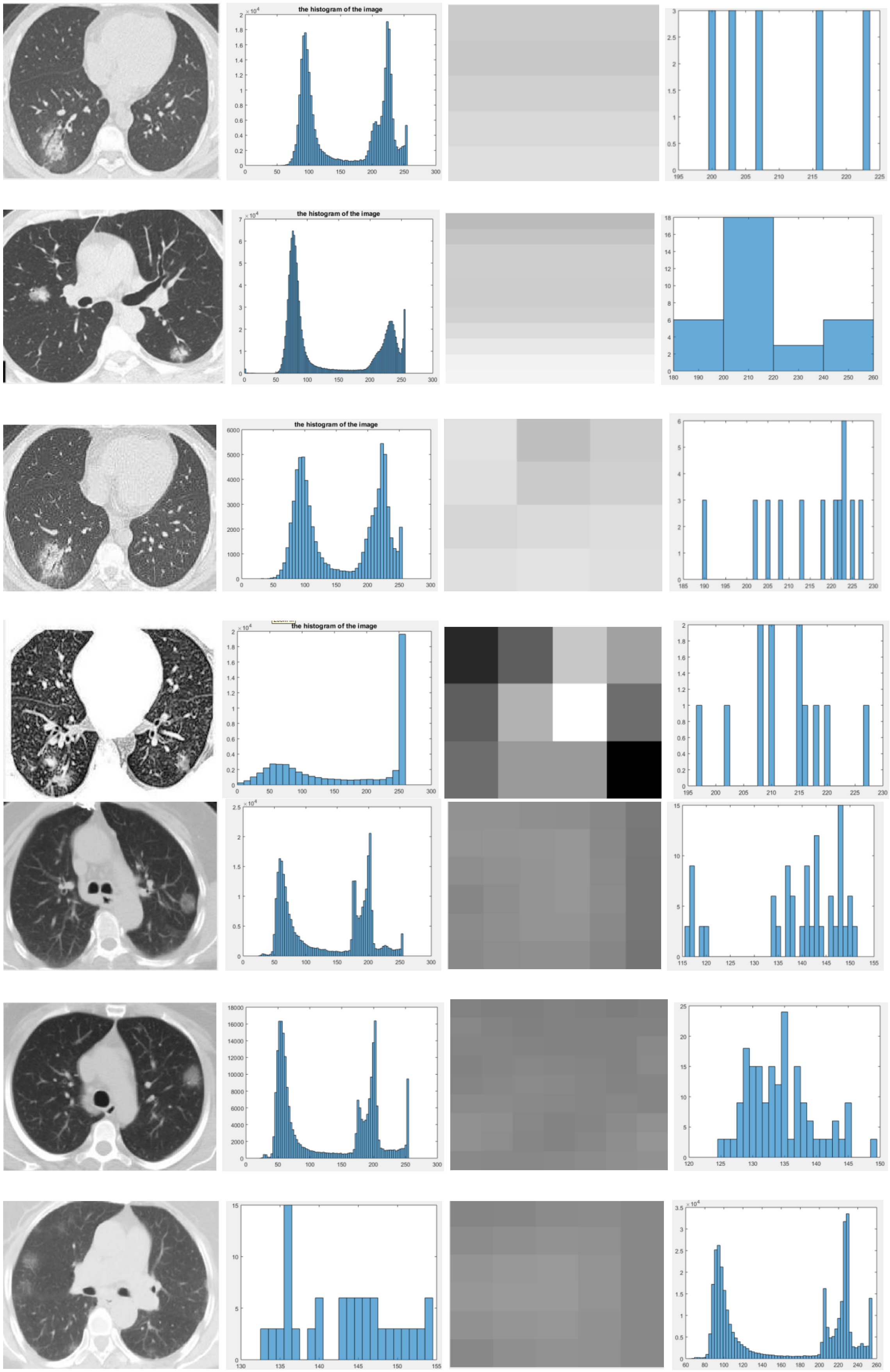
the histogram of the image
the histogram of the image
the histogram of the image
the histogram of the image
$\times 10^4$

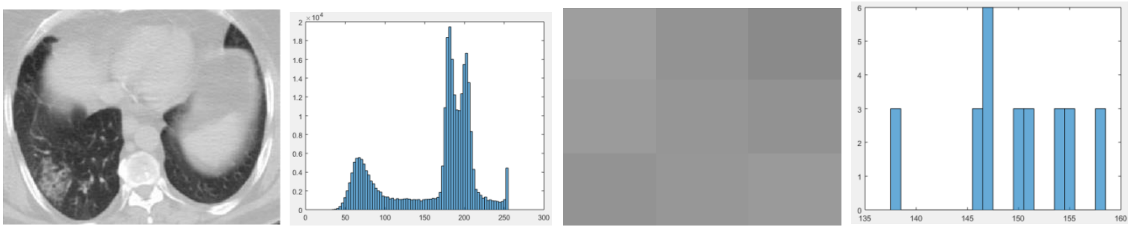

(a) **(b)**

Figure (4. 18): Histogram of the input Covid-19 lung images in (a) and of a sample of infected regions in (b).

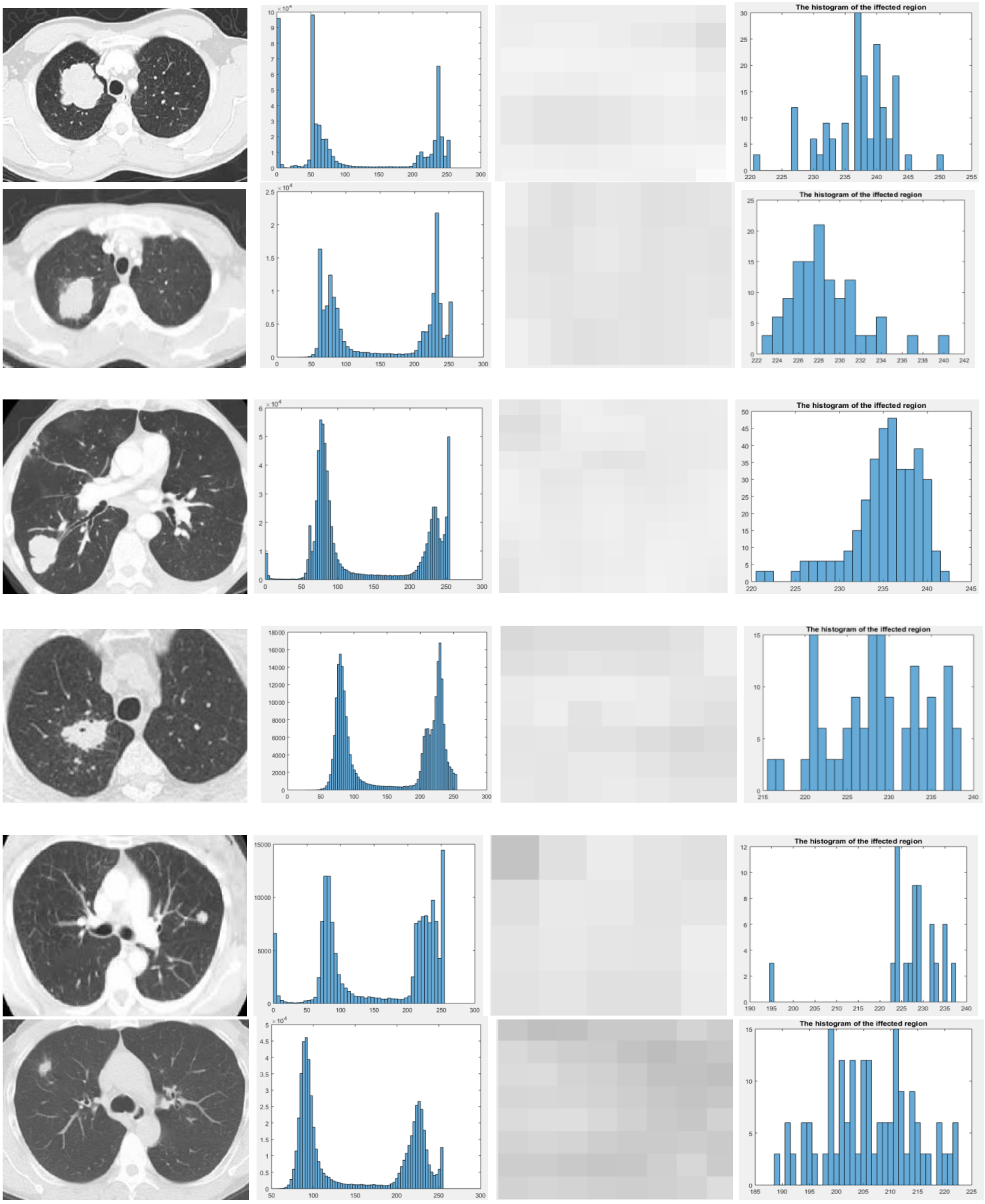

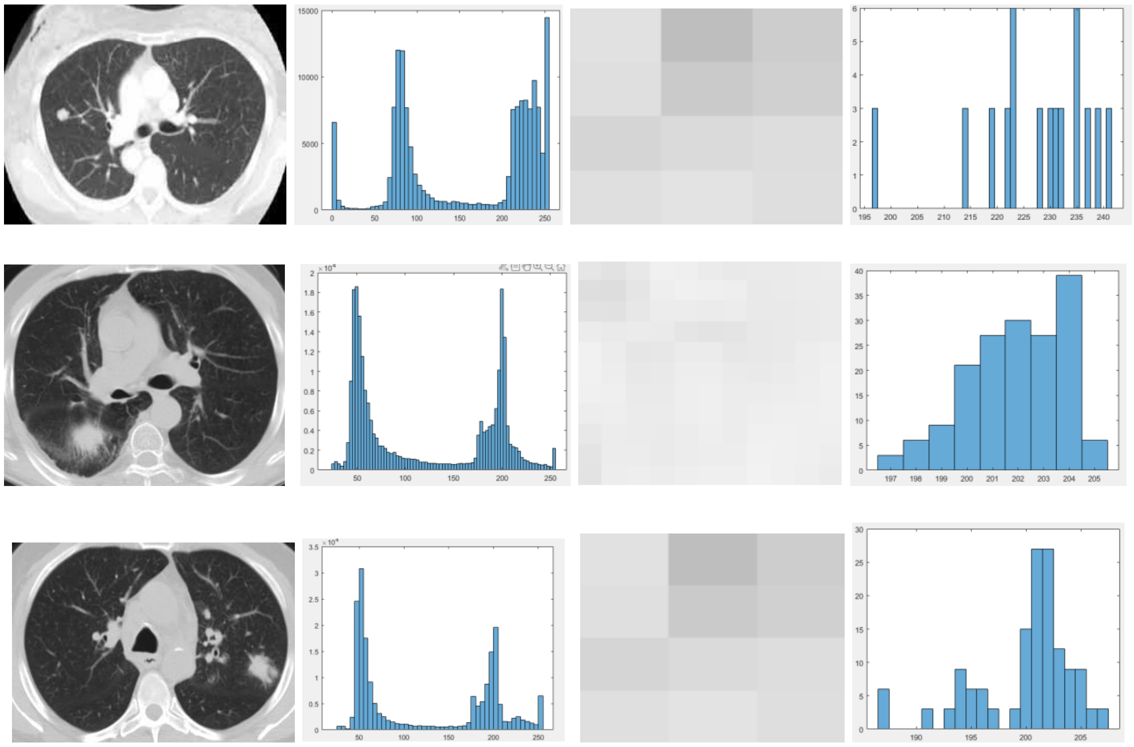

(a) **(b)**

Figure (4. 19): Histogram of the input tumor images in (a) and of a sample of infected regions in (b).

Figures (4.18) and(4.19) represent histogram plot of the whole lung and histogram of the samples of the infected region in the lung. The first and second columns (a) show the hole lung and their histograms, while the third and fourth columns (b) show the implemented sample of the infected regions and their histograms.

4.7.1.2 Contrast Adjustment

Many different interest ranges were tested to highlight the infected regions by applying contrast adjusting depending on the histogram information and Figures (4.20) and (4.21) present the results of this step for CT scan images of (Covid-19 and tumors) respectively.


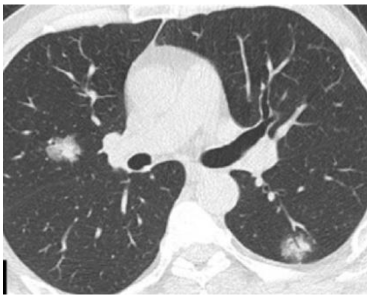


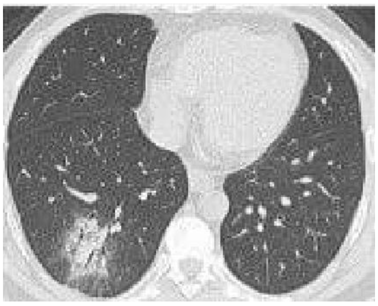
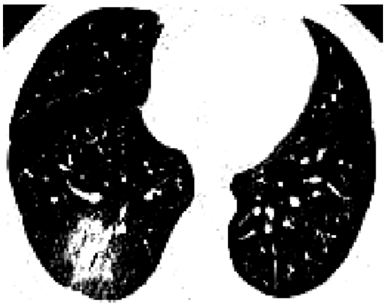

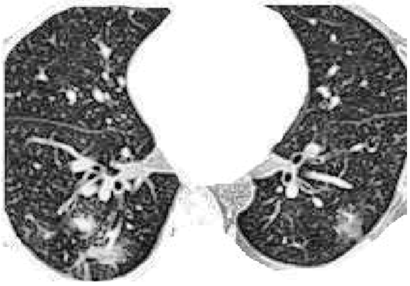


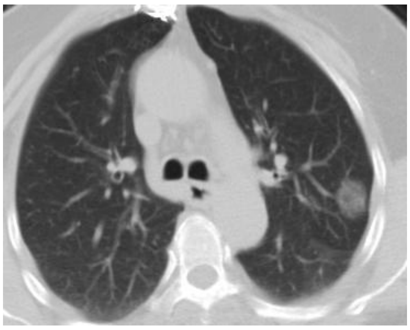
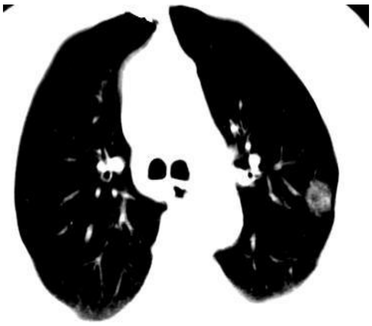

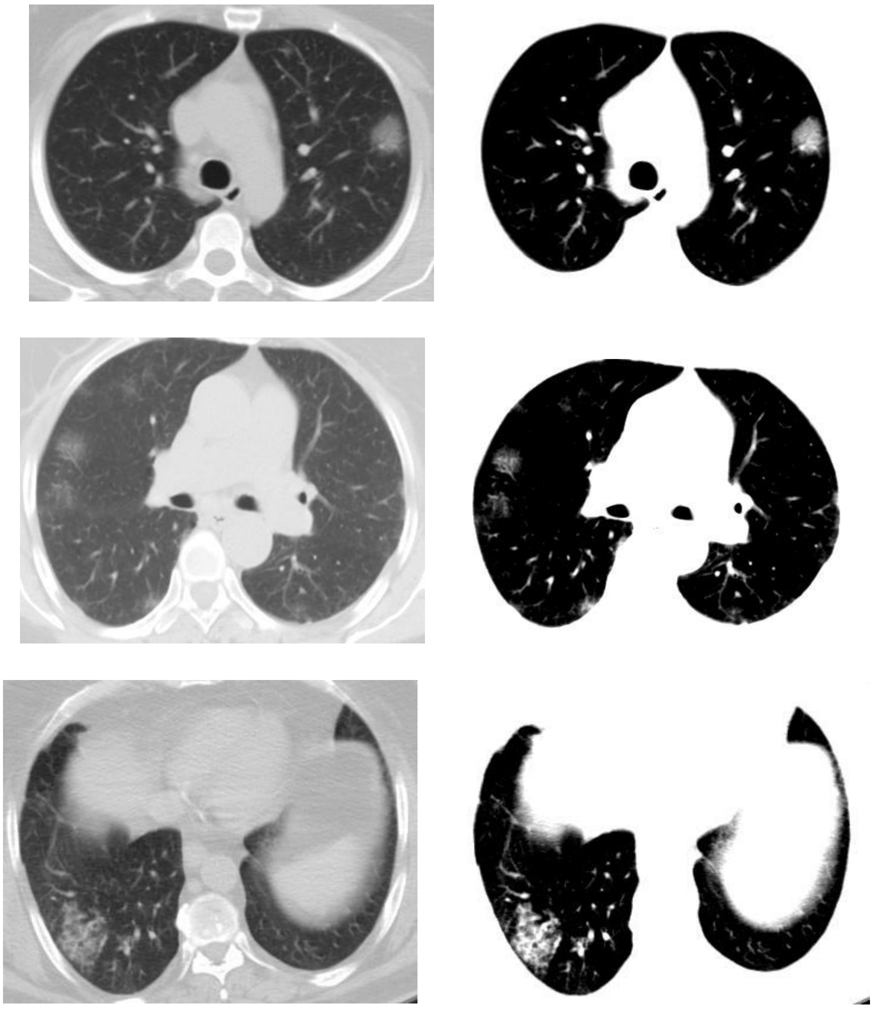

Figure (4. 20): Results of contrast adjustment for Covid-19 lung CT scan images.

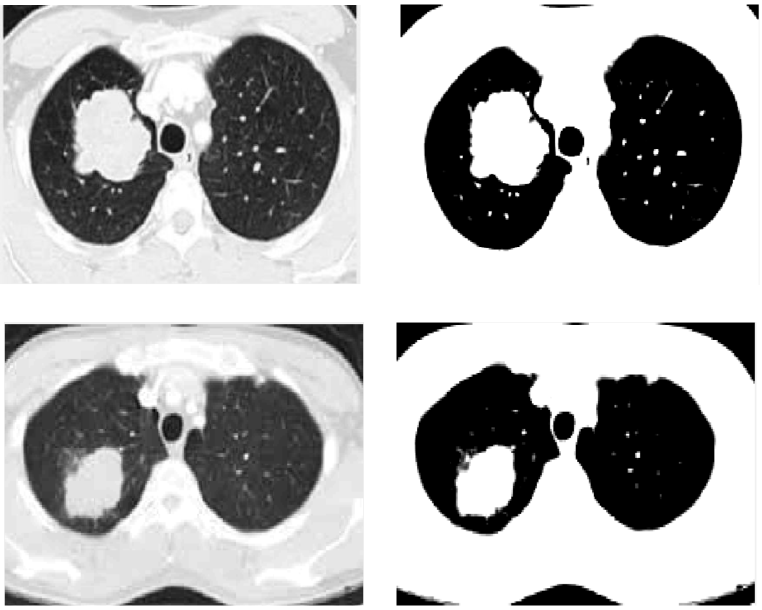



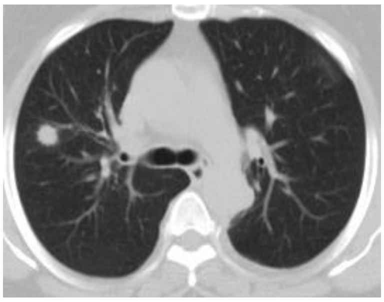
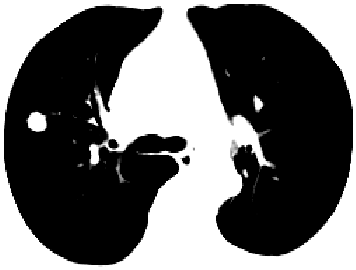

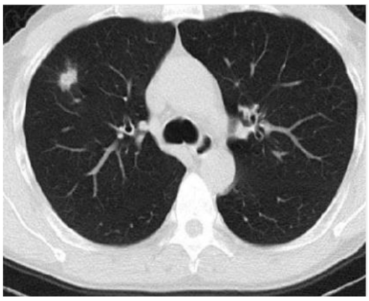
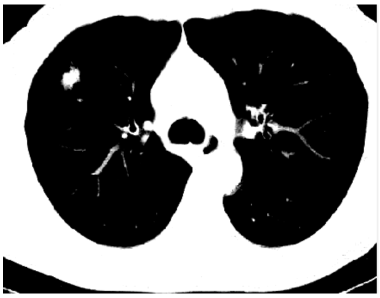

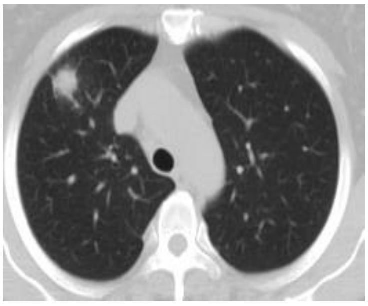
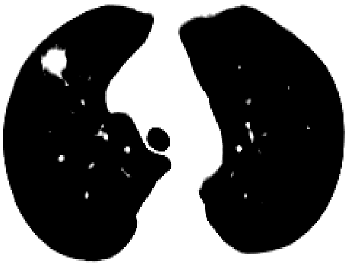

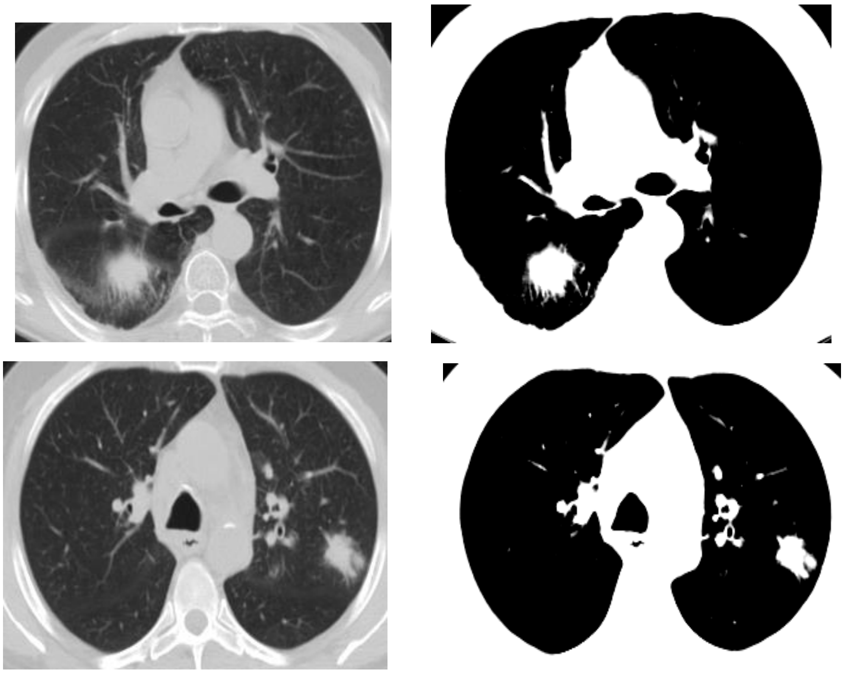

Figure (4. 21): Results of contrast adjustment for tumor lung CT-scan images.

In Figures (4.20) and (4.21) the first column shows the input images while the second column present the resultant contrast adjusted images. The background of the image in the figures has been deleted by using the various Mat lab functions. In this study the function was used get rectangle function.

4.7.2 Segmentation Methods

Four segmentation Methods were implemented to isolate and extract the infected regains. The results them presented in the following sections:

4.7.2.1 K-means Clustering Method

The following steps summarize the processes involved by this method:

1- Input image.

2- Implementing K-means with different numbers of clusturs (3, 4and 5) for (Covid-19 and tumor) CT scan lung images.

3- Selecting the cluster of the abnormality by comparing all clusters images depending on background knowledge.

4. Applying many morphological operations and selecting area function extracteing abnormality. Opening dilation with structure element of disk shaped of radius ranged (2-6) depending on the images under processing.

5- Getting the gray image of the infected regions.

6- Calculating the area of the Covid-19 and tumor infected regions.

7- Output image

1- Covid-19 Infected Lung Images

The result of clustering by K-means algorithm was implemented on lung CT images with diffrent number of clusters (3, 4 and 5) to segment the adopted images and the results are presented in Figures (4.22)-(4.24).

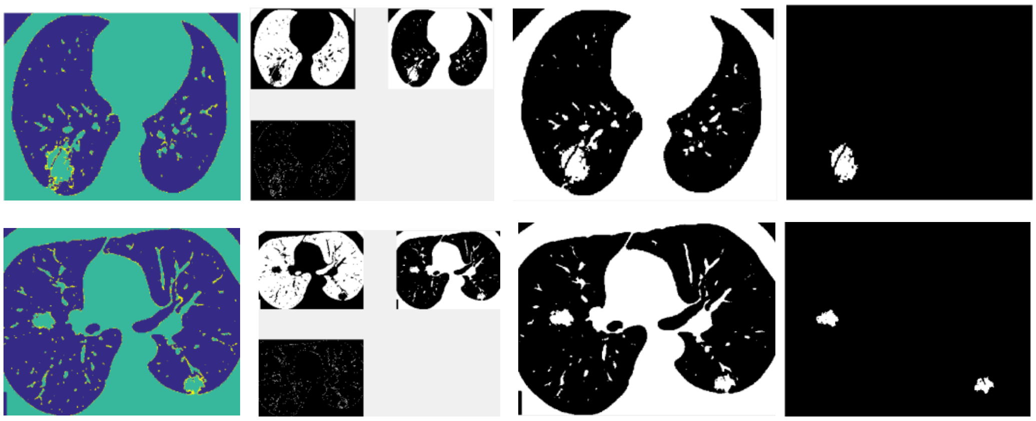

a b c d

Figure (4.22): Results of implementing K-means Clustering with three clusters. (a) segmented image, (b) the discrete clusters, (c) the cluster of the infected region and (d) the final extracted infected region.

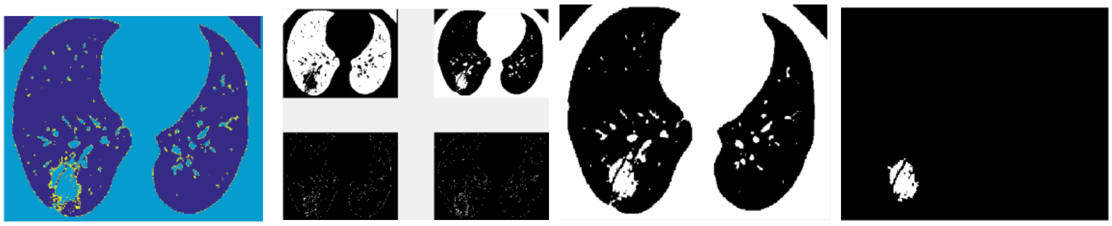

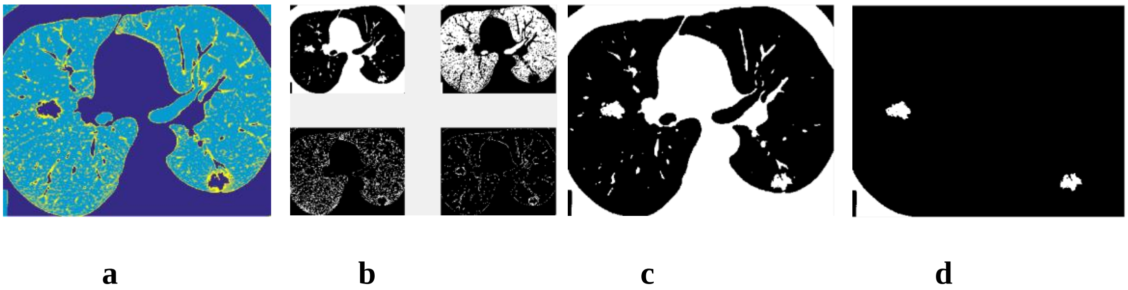

Figure (4.23): Results of implementing K-means Clustering with four clusters. (a) segmented image, (b) the discrete clusters, (c) the cluster of the infected region and (d) the final extracted infected region.

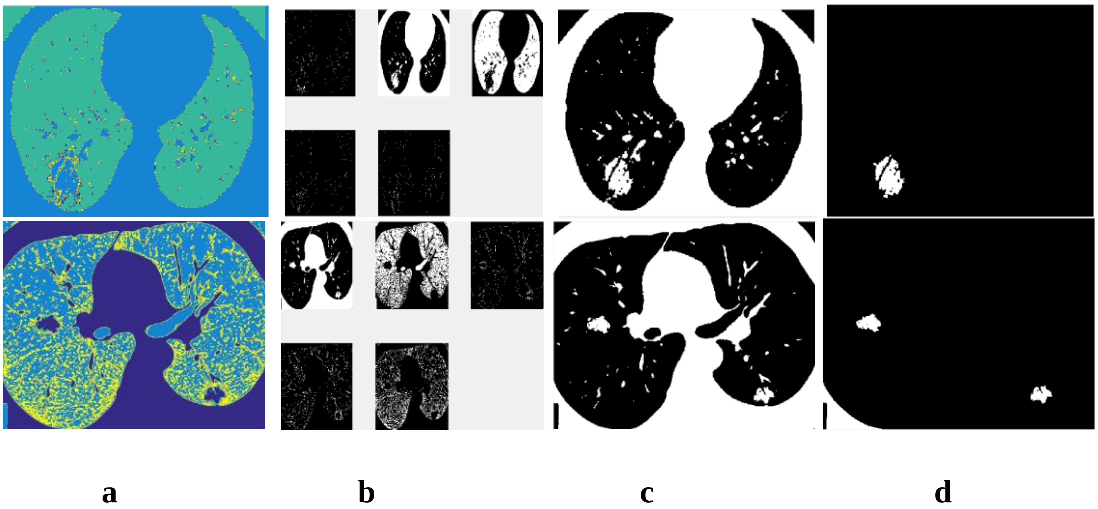

Figure (4.24): Results of implementing K-means Clustering with five clusters. (a) segmented image, (b) the discrete clusters, (c) the cluster of the infected region and (d) the final extracted infected region.

Figures (4.22)-(4.24) show the results of implementing K-means algorithm with number of clusters (3,4 and5), In Figures (4.22)-(4.24), the first column (a) represents a segmented image, the second column (b) shows the discrete clusters, the third column (c) presents the cluster of abnormal regions, and the last column (d) shows the extracted Covid-19 infected region and the results of this process for other images were presented in the appendix 1.

2- Tumors Infected Lung Images

The result of applying K-means algorithm that implemented on lung CT images with difrent number of clusters (3, 4 and 5) to segment the adopted images, are presented in Figures (4.25)-(4.27).

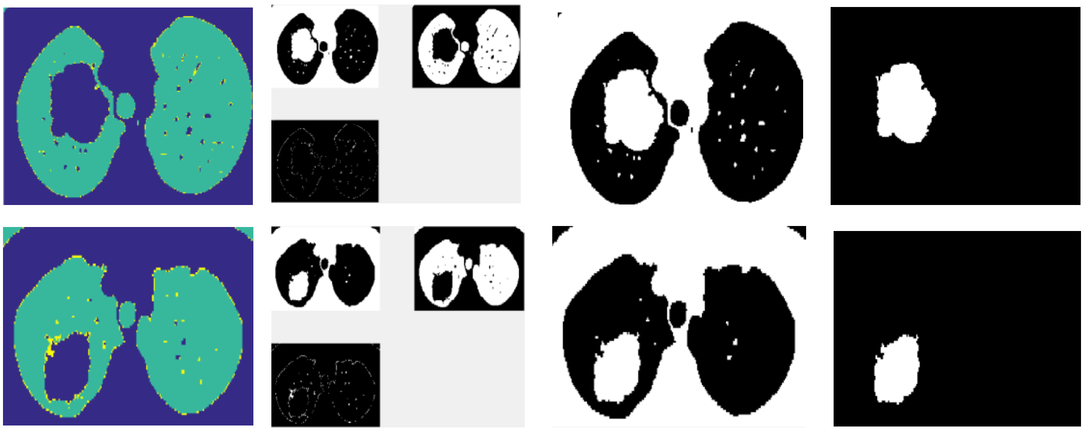

a b c d

Figure (4.25): Results of implementing K-means Clustering with three clusters. (a) segmented image, (b) the discrete clusters, (c) the cluster of the infected region and (d) the final extracted infected region.

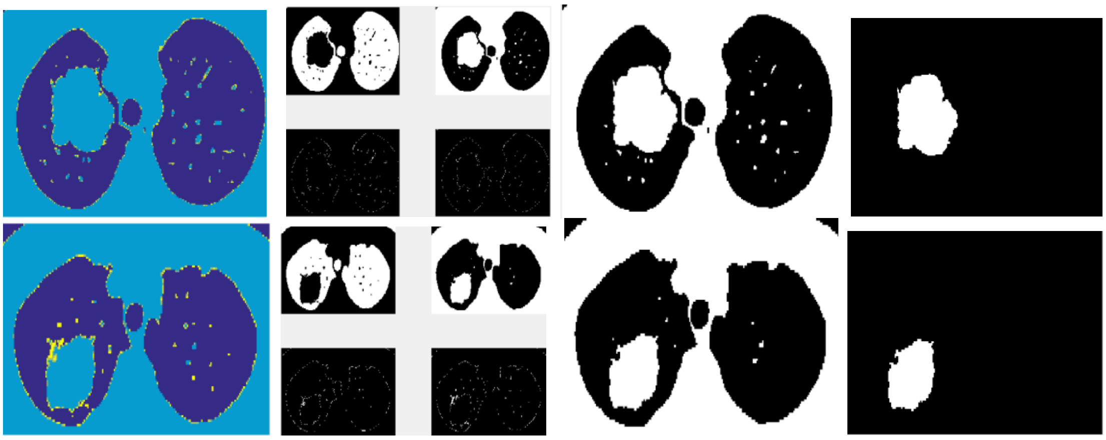

a b c d

Figure (4.26): Results of implementing K-means Clustering with four clusters. (a) segmented image, (b) the discrete clusters, (c) the cluster of the infected region and (d) the final extracted infected region.

a **b** **c** **d**

Figure (4.27): Results of implementing K-means Clustering with five clusters. (a) segmented image, (b) the discrete clusters, (c) the cluster of the infected region and (d) the final extracted infected region.

Figures (4.25)-(4.27) show the results of implementing K-means algorithm with number of clusters on images tumor. In Figures (4.25)-(4.27) the first column (a) represents segmented image, the second column (b) shows the discrete clusters, the third column (c) presents the cluster of abnormal regions, and the last column (d) shows the extracted tumor region.

Three clusters was the most proper number of clustering according to the advice of a radiologist and the results of this process for other images were presented in the appendix1.

4.7.2.2 HSOFM Unsupervised ANN

The following steps can summarize the procedure of this method:

1-Input image.

2- Once and extracting the lungs regions only without any extra objects.

3- Implementing HSOFM with numbers of nods (3, 4 and 5) nodes for (Covid-19 and tumor) CT scan tlung images.

4- Selecting the segment of the abnormality by comparing all segments images depending on background knowledge.

5- Applying many morphological operations and selecting area function to extracted abnormality. The applying morphological operations (opening, dilation) were implemented with structure element of disk shaped of different radius ranged (2-6) depending on the image under processing.

6- Calculating the area of the extracted Covid-19 and infected tumors regions.

7- Getting the gray image of the Covid-19 and infected tomors regions.

8- Output image.

1- Covid-19 Infected Lung Images

The results of implementing this method are illustrated in Figure (4.28)-(4.30).

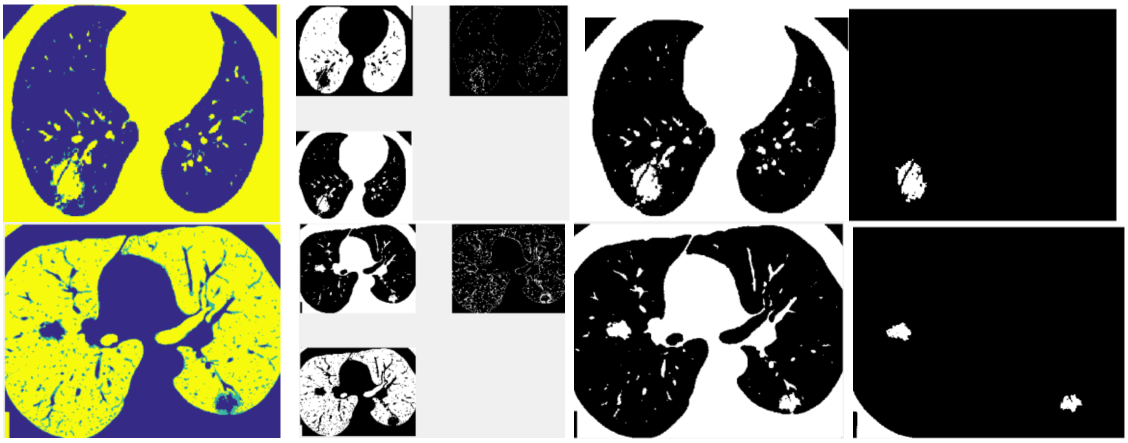

a b c d

Figure (4.28): Results of implementing HSOFM clustering with three nodes. (a) segmented image, (b) the discrete clusters, (c) the cluster of the infected region and (d) the final extracted infected region.

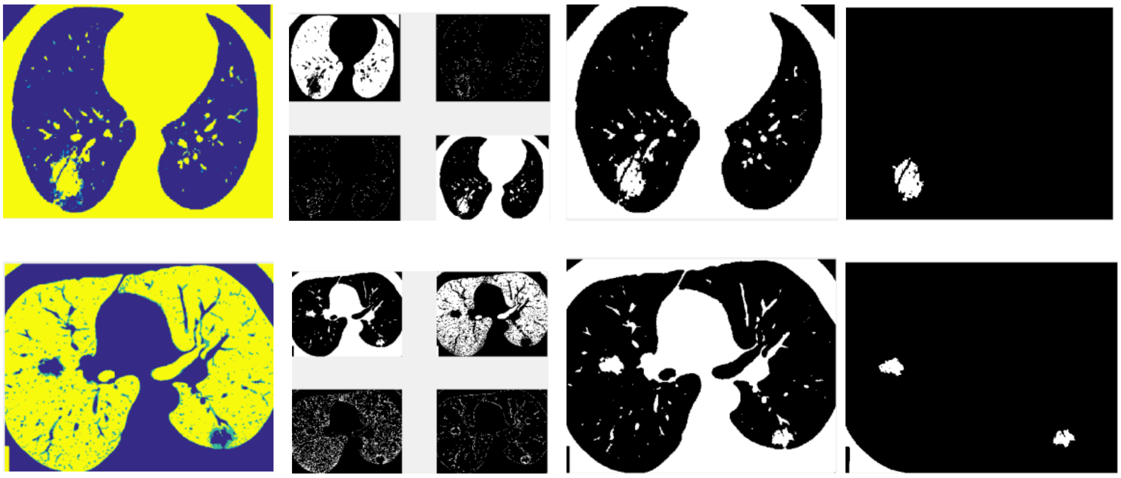

a b c d

Figure (4.29): Results of implementing HSOFM Clustering with four nodes. (a) segmented image, (b) the discrete nodes, (c) the cluster of the infected region and (d) the final extracted infected region.

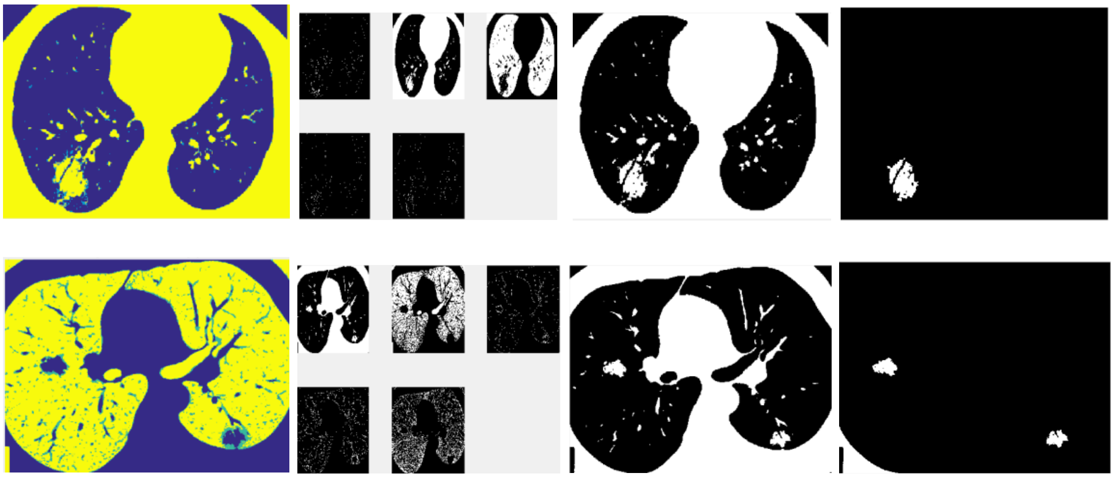

a **b** **c** **d**

Figure (4.30): Results of implementing HSOFM Clustering with five nodes. (a) segmented image, (b) the discrete nodes, (c) the cluster of the infected region and (d) the final extracted infected region.

In Figures (4.28)-(4.30) the first colume (a) presents segmented image, second one (b) illstrates the discrate segments, third one (c) indicate the segment that belong infected region to, and last column (d) presents the refined extracted infected region after applying the needed morphological operations. The results showed an adquate extraction of the infected regions according to the radiologist consultation and three nodes was is the more approporate nodes number that adeqaue for extracting of Covid-19 infected regions and the results of this process for other images were presented in the appendix2.

2- Tumors Infected Lung Images

The results of implementing this method on tumor infected lung image are illustrated in the Figures (4.31)-(4.33).

a b c d

Figure (4.31): Results of implementing HSOFM Clustering with three nodes. (a) segmented image, (b) the discrete nodes, (c) the cluster of the infected region and (d) the final extracted infected region.

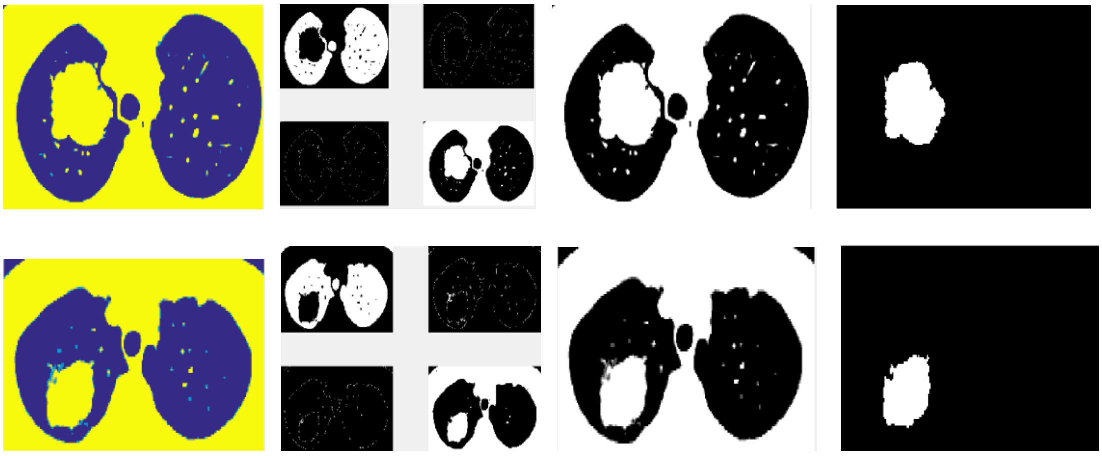

a b c d

Figure (4.32): Results of implementing HSOFM Clustering with four nodes. (a) segmented image, (b) the discrete nodes, (c) the cluster of the infected region and (d) the final extracted infected region.

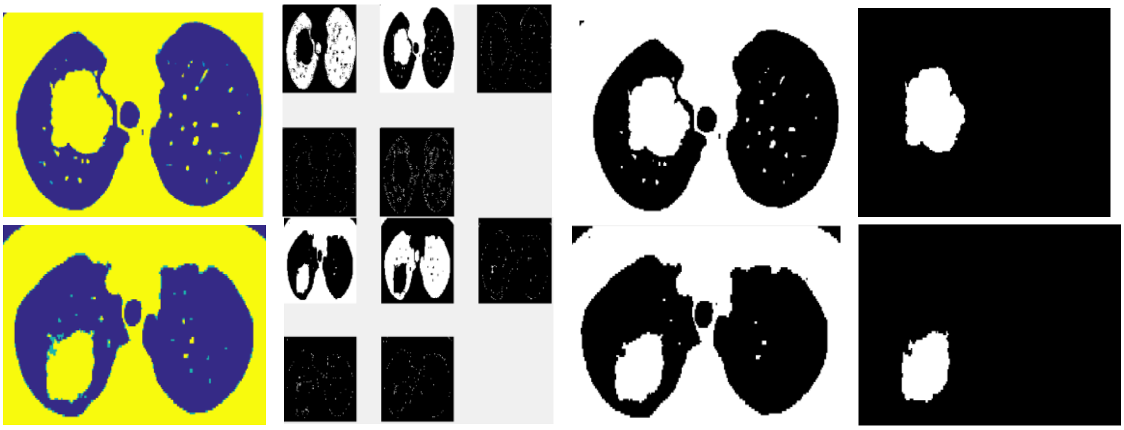

a b c d

Figure (4.33): Results of implementing HSOFM Clustering with five nodes. (a) segmented image, (b) the discrete nodes, (c) the cluster of the infected region and (d) the final extracted infected region.

In Figures (4.31)-(4.33), the first colume (a) presents the segmented image, second one (b) illstrates the discrate segments, third one (c) indicate the segment that belong infected region to, and last column (d) presents the refined extracted infected region after applying the approporate morphological operations. The results showed an adquate extraction of the infected regions according to the radiologist consultation and number three of nodes is the more approporate nodes number that adeqaue for extracting of tumor regain and the results of this process for other images were presented in the appendix2.

4.7.2.3 FCM Clustering

FCM algorithm was applied with different numbers of clusters to segment the images under study. FCM algorithm for CT scan lung images was applied with a number of clusters (3, 4 and 5). The following steps can summarize the procedure of this method:

1- Input image.

2- Implementing FCM with different cluster numbers (3, 4 and 5) clusters for (Covid-19 and tumor) CT scan lung images.

3- Selecting the cluster of the abnormality by comparing all clusters images with an image of normal cases.

4- Applying many morphological operations and selecting area function extracted abnormality. The morphological operations like opening and dilation were applied with structure element of disk shaped with different radius ranged (2-6) depending on the images under processing images.

5- Calculating the area of the extracted Covid-19 and infected tumor regions.

6- Output image.

1- Covid-19 Infected Lung Images

Figures (4.34)-(4.36) show the results of applying FCM algorithm with the number of segments (3, 4 and 5) respectively.

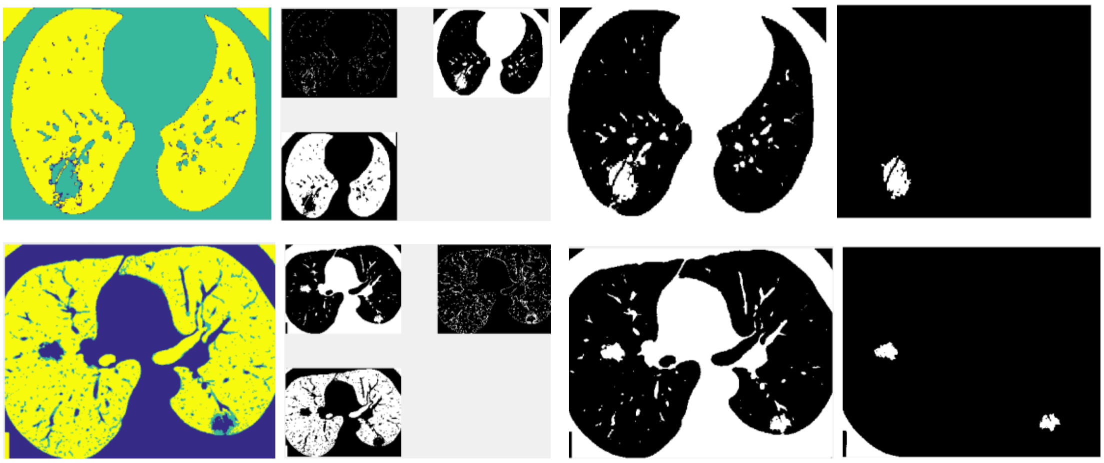

a b c d

Figure (4.34): Results of implementing FCM Clustering with three clusters. (a) segmented image, (b) the discrete clusters, (c) the cluster of the infected region and (d) the final extracted infected region.

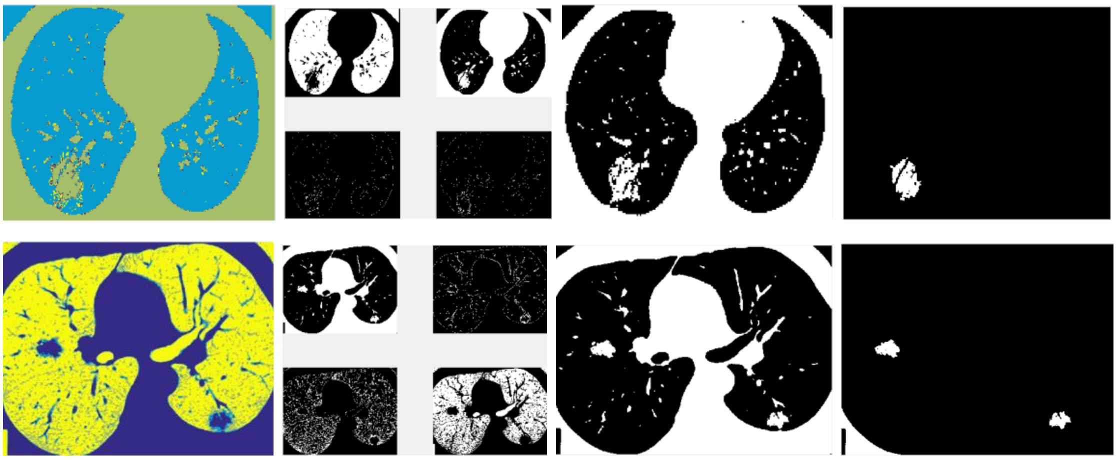

a b c d

Figure (4.35): Results of implementing FCM Clustering with four clusters. (a) segmented image, (b) the discrete clusters, (c) the cluster of the infected region and (d) the final extracted infected region.

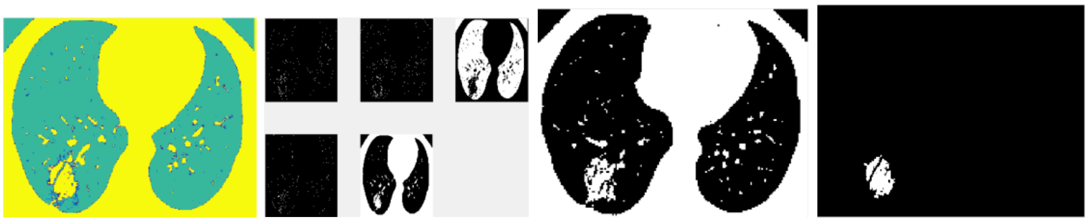

Figure (4.36): Results of implementing FCM Clustering with five clusters. (a) segmented image, (b) the discrete clusters, (c) the cluster of the infected region and (d) the final extracted infected region.

In Figures (4.34)-(4.36) the first colume (a) presents segmented image, second one (b) illstrates the discrate segments, third one (c) indicates the segment that the infected region belong to, and last column (d) presents the refined extracted infected region after applying the many morphological operations. The results showed an adquate extraction of the infected regions according to the radiologist consultation and the number three of nodes is the more approporate nodes number that adeqaue for extracting Covid-19 infected regions. [This was the first study in which the areas of infection with Covid-19 were extracted using FCM Clustering with (3, 4 and 5) cluster] and the results of this process for other images were presented in the appendix(3).

2- Tumor Infected Lung Images

Figures (4.37)-(4.39) show the results of applying FCM algorithm with the number of segments clusters (3, 4 and 5) respectively.

Figure (4.37): Results of implementing FCM Clustering with three clusters. (a) segmented image, (b) the discrete clusters, (c) the cluster of the infected region and (d) the final extracted infected region.

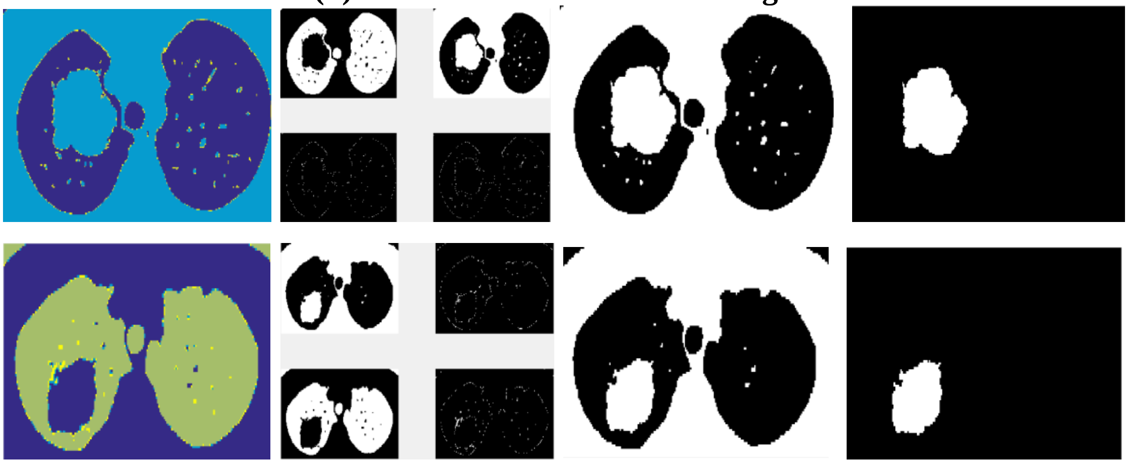

Figure (4.38): Results of implementing FCM Clustering with four clusters. (a) segmented image, (b) the discrete clusters, (c) the cluster of the infected region and (d) the final extracted infected region.

.

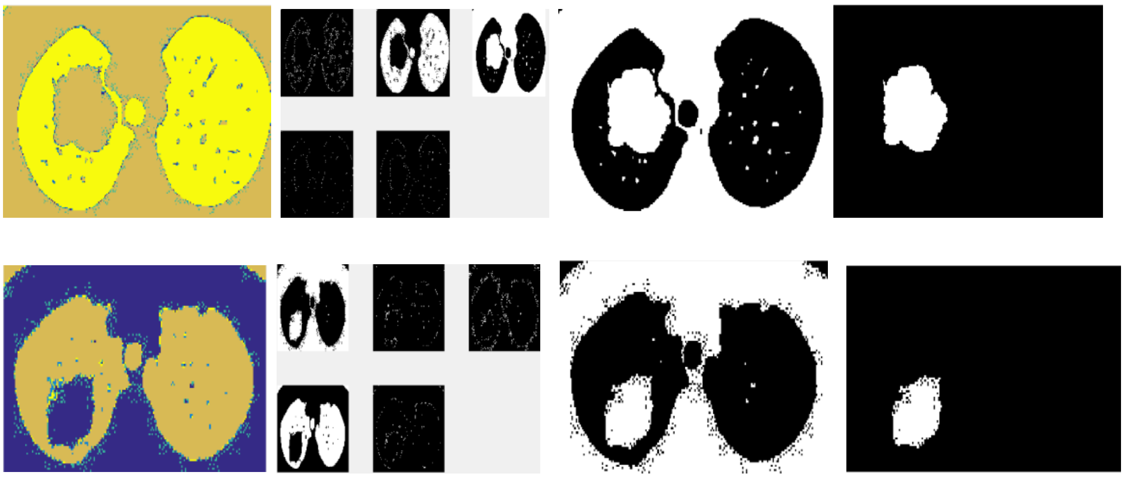

Figure (4.39): Results of implementing FCM Clustering with five clusters. (a) segmented image, (b) the discrete clusters, (c) the cluster of the infected region and (d) the final extracted infected region.

In Figures (4.37)-(4.39) the first colume (a) presents segmented image, second one (b) illstrates the discrate segments, third one (c) indicates the segment that of the infected region, and the last column (d) presents the refined extracted infected region after applying the many morphological operations. The results showed an adquate extraction of the infected regions according to the radiologist consultation and number three of nodes is the more approporate nodes number that adeqaue for extracting tumor infected regions and the results of this process for other images were presented in the appendix3.

4.7.2.4 HSOFM Hybrid Technique

In this technique the ultimate centers of k-means clusteres were adopted as first value of the nodes in HSOFM algorithm in order to reduce the long elapsed times of HSOFM and to improve the clustering process for CT scan images of (Covid-19 and tumors) respectively.

1- Covid-19 Infected Lung Images

Figures (4.40)-(4.42) show the results of this technique applied on Covid-19 infected lung images with number of nodes (3, 4 and 5) respecting.

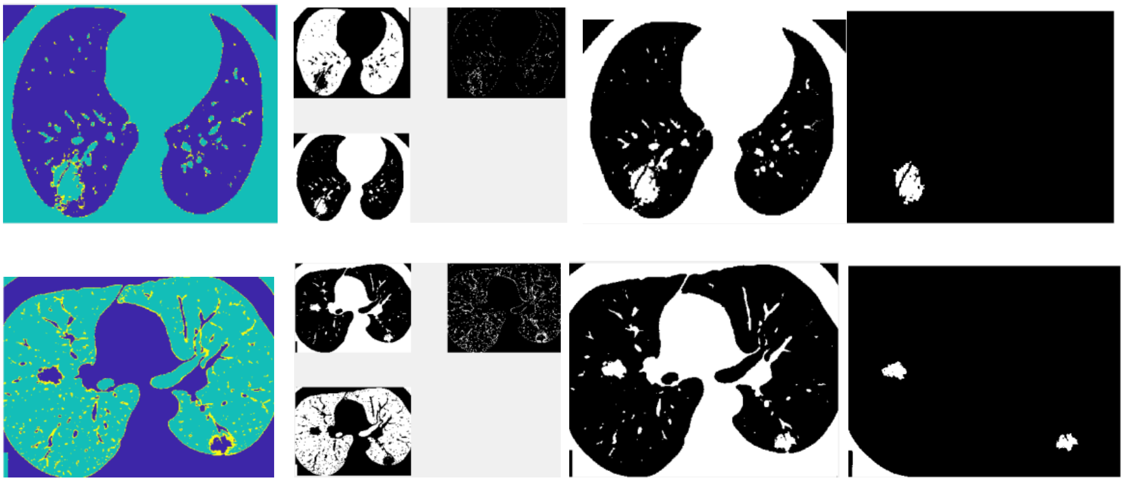

a b c d

Figure (4.40): Results of implementing the hybrid clustering technique with three clusters. (a) segmented image, (b) the discrete clusters, (c) the cluster of the infected region and (d) the final extracted infected region.

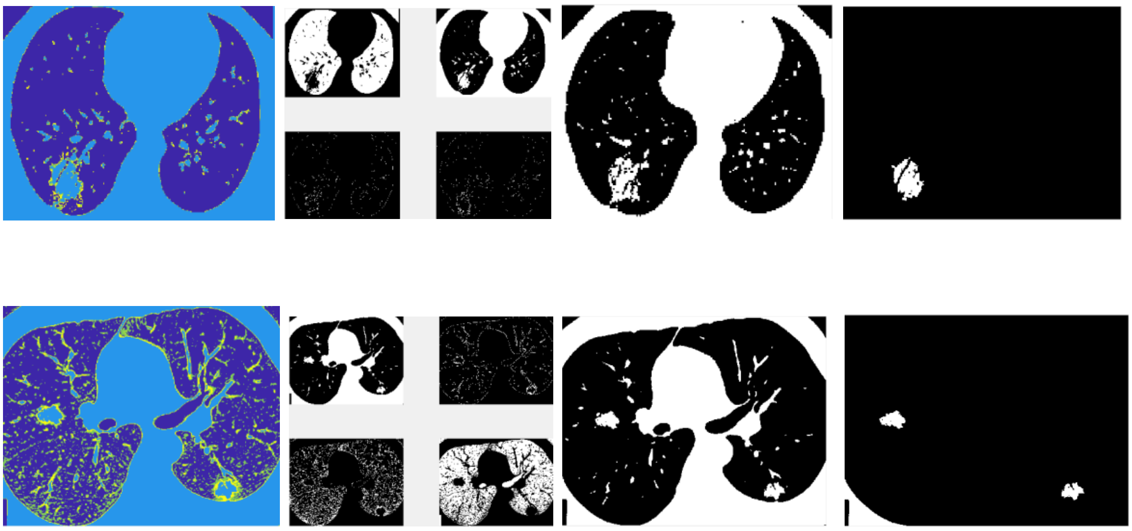

a b c d

Figure (4.41): Results of implementing the hybrid clustering technique with four clusters. (a) segmented image, (b) the discrete clusters, (c) the cluster of the infected region and (d) the final extracted infected region.

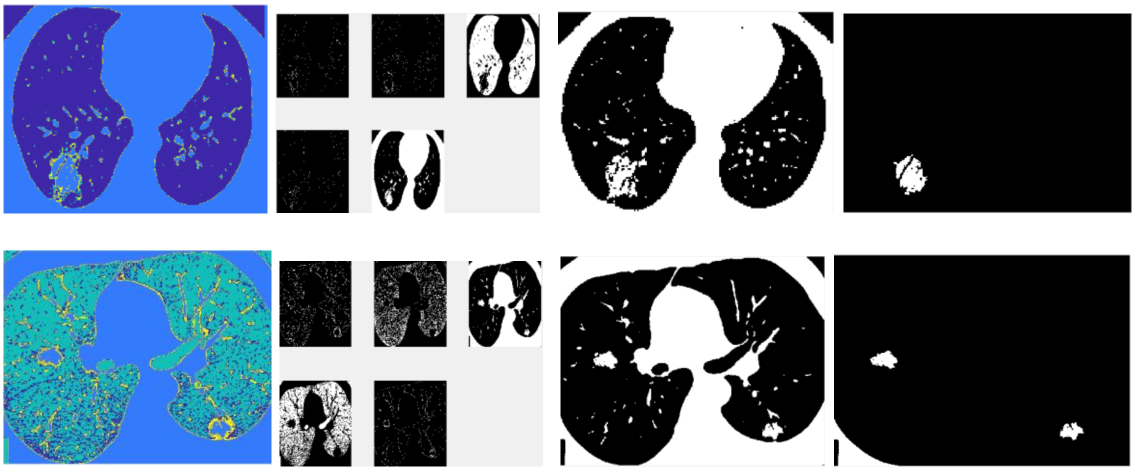

a b c d

Figure (4.42): Results of implementing the hybrid clustering technique with five clusters. (a) segmented image, (b) the discrete clusters, (c) the cluster of the infected region and (d) the final extracted infected region.

In Figures (4.40)-(4.42) the first colume (a) presents segmented image, second one (b) illstrates the discrate segments, third one (c) indicates the segment that of the infected region, and the last column (d) presents the refined extracted infected region after applying the many morphological operations. The results showed an adquate extraction of the infected regions according to the radiologist consultation and number three of nodes is the more approporate nodes number that adeqaue for extracting tumor infected regions and the results of this process for other images were presented in the appendix4.

2- Tumor Infected Lung Images

Figures (4.43)-(4.45) show the results of this technique implemented on tumor infected lung images with number of nodes (3, 4 and5) respecting.

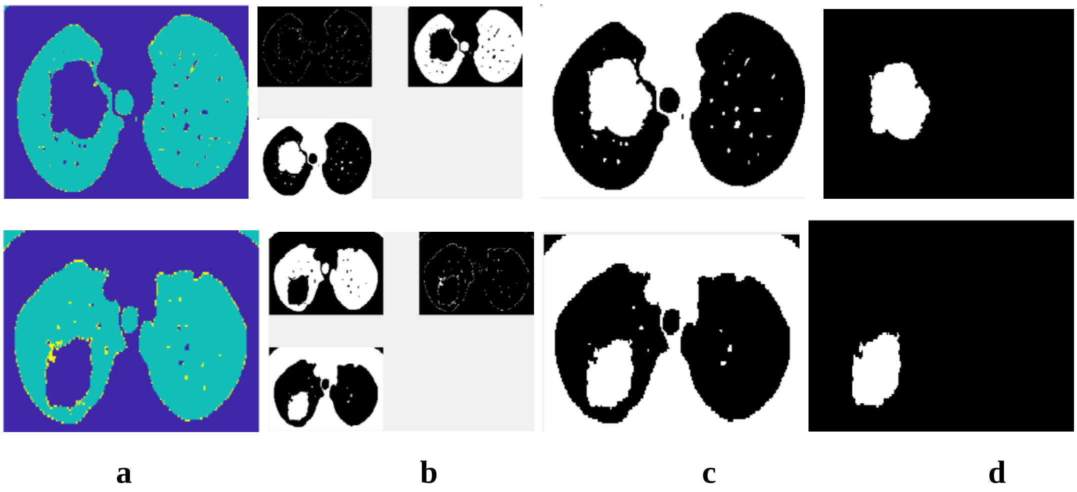

Figure (4.43): Results of implementing hybrid clustering technique with three nodes. (a) segmented image, (b) the discrete nodes, (c) the cluster of the infected region and (d) the final extracted infected region.

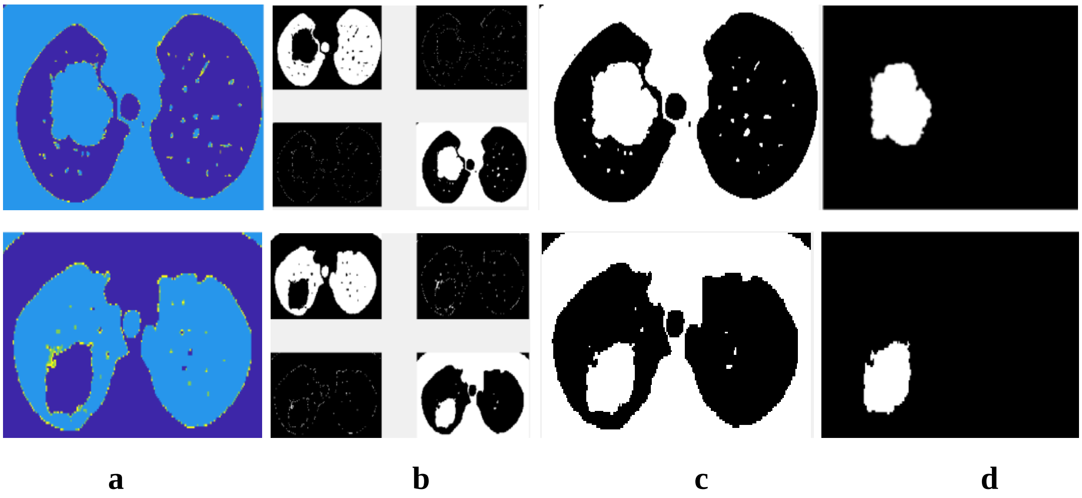

Figure (4.44): Results of implementing the hybrid clustering technique with four nodes. (a) segmented image, (b) the discrete nodes, (c) the cluster of the infected region and (d) the final extracted infected region.

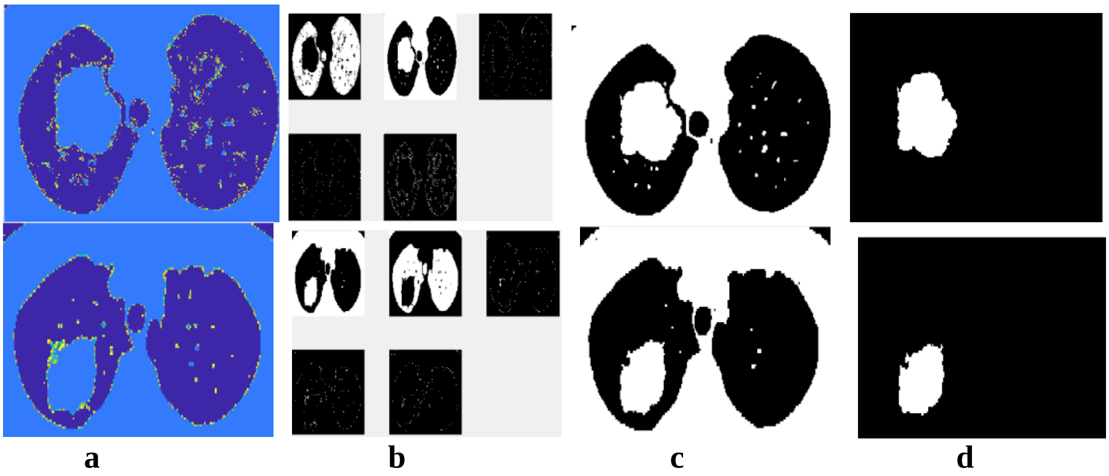

Figure (4.45): Results of implementing the hybrid clustering technique with five nodes. (a) segmented image, (b) the discrete nodes, (c) the cluster of the infected region and (d) the final extracted infected region.

In Figures (4.43)-(4.45) the first colume (a) presents segmented image, second one (b) illstrates the discrate segments, third one (c) indicates the segment that of the infected region, and the last column (d) presents the refined extracted infected region after applying the many morphological operations. The results showed an adqquate extraction of the infected regions according to the radiologist consultation and number three of nodes is the more approporate nodes number that adeqaue for extracting tumor infected regions and the results of this process for other images were presented in the appendix4..

The percent relative infected region area was calculated for each image by calculating the surface area of the whole infected lung and the surface area of extracted region. This process was achieved by extracting the whole infected lung only and then calculating its surface area.
Figures (4-46) and (4.47) illustrates the results of this step and Table (4.8) and (4.9) Presents the calculated surface area for Covid -19 and tumors lung infected image respectively.

Table (4.8): The calculated values of the surface area of the extracted infected regions for the implemented methods of the Covid-19 images.

Images	Surface Area (pixels)											
	Number of clusters											
	three				four				five			
	k-means	HSOFM	FCM Clustering	Hybrid Method	k-means	HSOFM	FCM Clustering	Hybrid Method	k-means	HSOFM	FCM Clustering	Hybrid Method
Covid-1	1238	1247	1244	1245	1212	1225	1230	1231	1201	1215	1223	1198
Covid-2	9058	9060	9057	9045	9041	9042	9039	9033	9021	9025	9027	9002
Covid-3	349	348	344	349	332	335	331	321	325	328	321	314
Covid-4	622	632	625	623	613	615	611	605	604	611	609	605
Covid-5	908	943	901	908	838	835	838	831	838	798	835	835
Covid-6	835	815	832	835	748	741	748	742	792	787	785	792
Covid-7	1452	1499	1445	1496	1022	1035	1083	1081	997	983	981	989
Covid-8	2535	2166	2525	2533	2375	2333	2343	2335	2289	2265	2318	2322

Table (4.9): The calculated values of the surface area of the extracted infected regions for the implemented methods of the tumor images.

Imaesg	Surface Area (pixels)											
	Number of clusters											
	three				four				five			
	k-means	HSOFM	FCM Clustering	Hybrid Method	k-means	HSOFM	FCM Clustering	Hybrid Method	k-means	HSOFM	FCM Clustering	Hybrid Method
Tuomer1	2947	2949	2950	2950	2932	2944	2932	2920	2920	2941	2933	2932
Tuomer2	957	956	956	957	938	939	938	938	932	940	932	933
Tuomer3	4038	4021	4028	3098	3905	4020	3848	3905	3776	3849	3776	3792
Tuomer4	1567	1563	1568	1543	1543	1559	1543	1548	1523	1555	1525	1523
Tuomer5	95	94	95	93	93	91	93	89	91	89	91	91
Tuomer6	177	178	177	172	168	168	172	168	167	171	167	165
Tuomer7	126	126	126	123	121	122	123	122	120	119	120	119
Tuomer8	949	942	943	911	911	940	898	937	889	935	880	964
Tuomer9	523	521	523	497	498	520	498	517	484	517	491	484

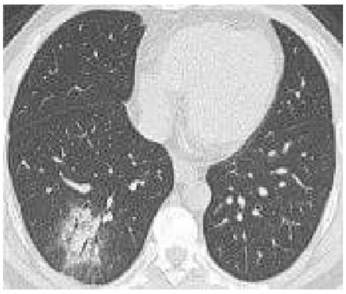

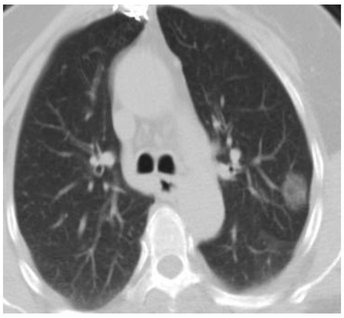

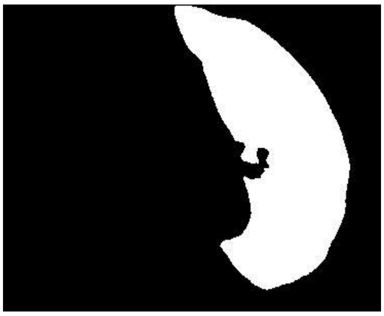

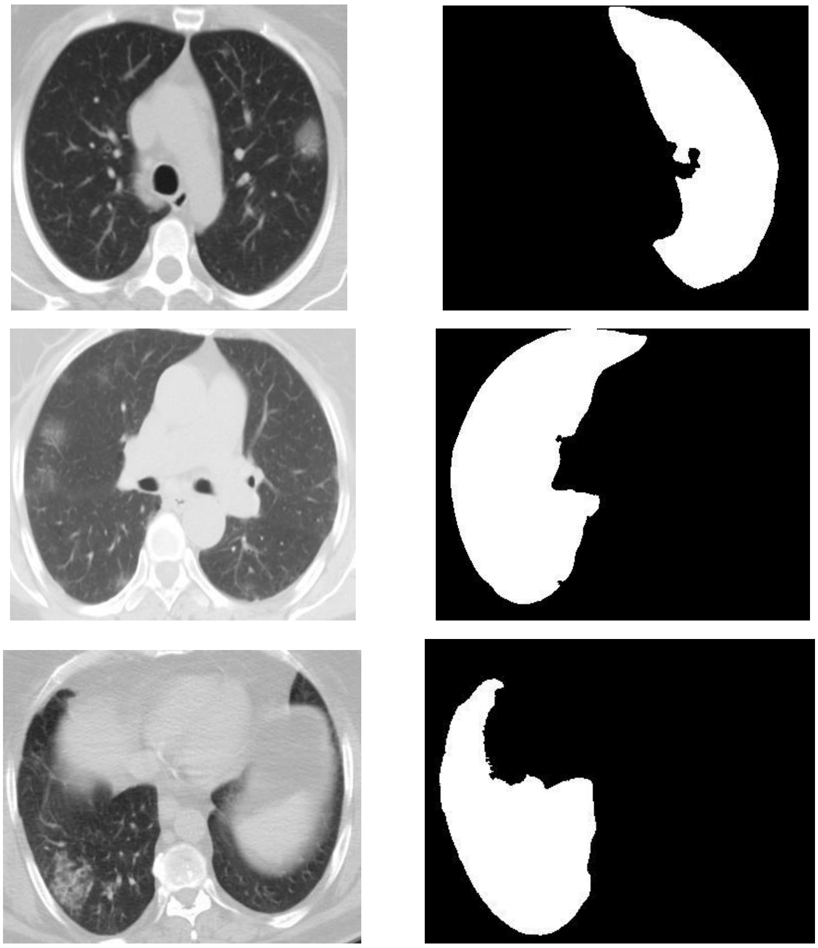

Figure (4. 46): The extracting whole infected lung images.

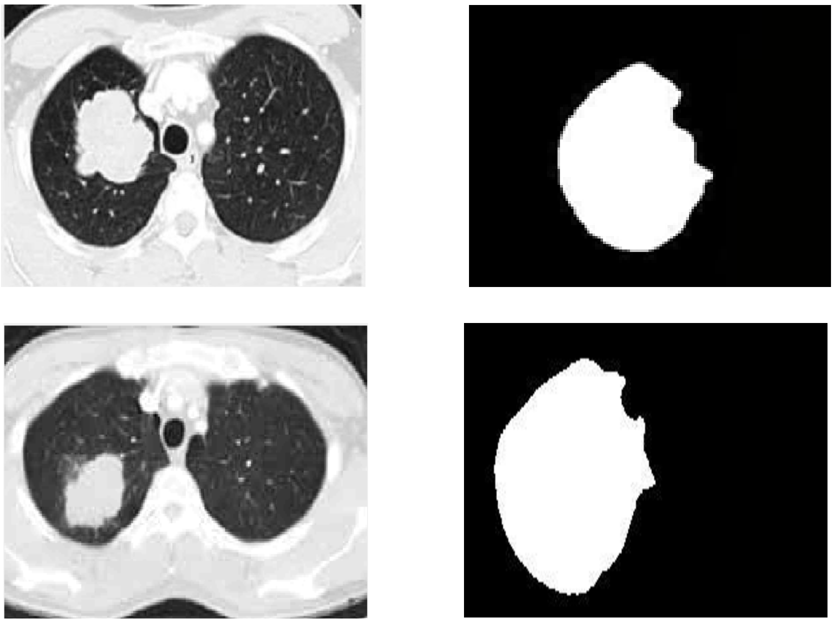



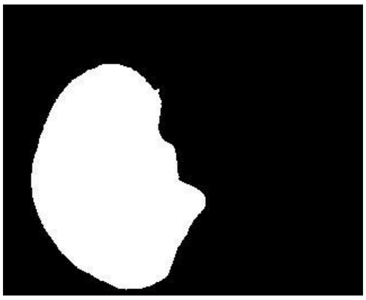

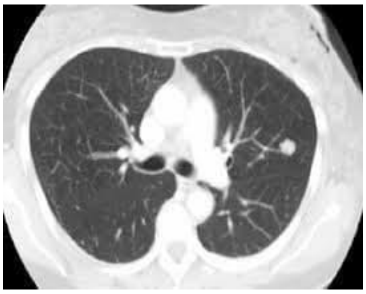


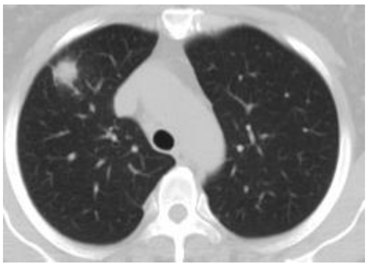


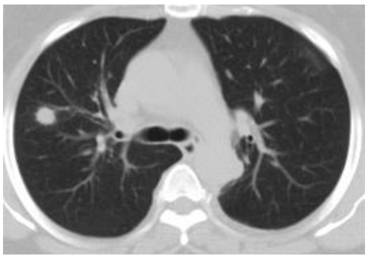
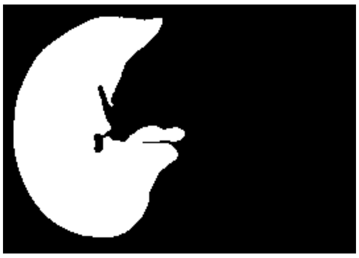

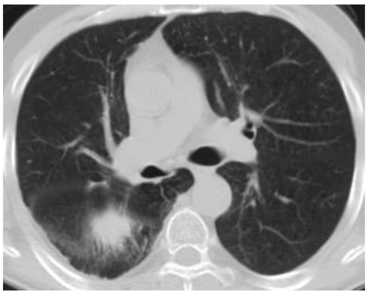


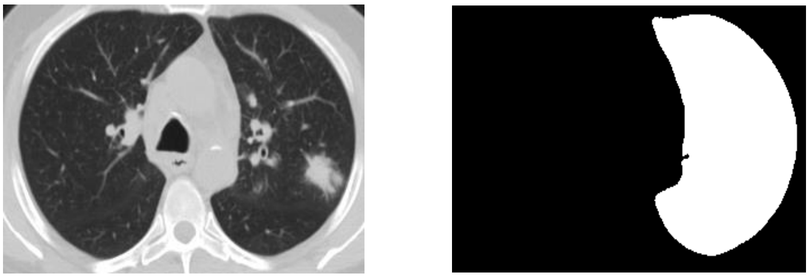

Figure (4. 47): Results of extracting infected lung images.

In Figures (4. 46) and (4.47) the first colum represents the lung image and the second colum represents the affected lung Blw images.

To calculate the percent relative surface area of the extracted infected regions with respect to the whole infected lung, the whole infected lungs regions was extracted and then calculating their surface area. Which are 7401864, 63658513, 1981949,6237368, 5389471, 5789930, 2239082, 4481881. for Covid-19 cases. For tumor cases the whole infected lungs were : 10479, 4807, 77495, 20959, 11195, 11195, 13161, 20363, 17121 respectively. The utilized related for caluclating the Precent relative surface area of the extracted infected region with respect to the whole infected lungs for Covid-19 is :

See Table (4.10) and Table (4.11).

$$\textbf{Precent Relative surface area of the infected regions} = \frac{\boldsymbol{tumor\ or\ (Covid-19)\ regaion\ areas}}{\boldsymbol{area\ of\ the\ whole\ infected\ regions}}\ \% \qquad \ldots\ldots\ldots..(\mathbf{4.1})$$

Table (4.10): Precent relative surface area of the extracted infected region with respect to the whole infected lungs for Covid-19.

Images	Precent Relative surface area of the infected regions %											
	Number of clusters											
	three				four				five			
	k-means	**HSOFM**	**FCM Clustering**	**Hybrid Method**	**k-means**	**HSOFM**	**FCM Clustering**	**Hybrid Method**	**k-means**	**HSOFM**	**FCM Clustering**	**Hybrid Method**
Covid-1	0.0167	0.0168	0.0168	0.0168	0.0163	0.0165	0.0166	0.0166	0.0162	0.0164	0.0165	0.0161
Covid-2	0.0142	0.0142	0.0142	0.0142	0.0142	0.0142	0.0141	0.0141	0.0141	0.0141	0.0141	0.0141
Covid-3	0.0176	0.0176	0.0176	0.0174	0.0167	0.0167	0.0167	0.0161	0.0163	0.0165	0,0161	0.0158
Covid-4	**0.0097**	**0.0101**	**0.0100**	**0.0099**	**0.0098**	**0.0784**	**0.0098**	**0.0096**	**0.0096**	**0.0097**	**0.0097**	**0.0096**
Covid-5	0.0168	0.01749	0.01684	0.01684	0.0155	0.0154	0.0155	0.0154	0.0155	0.0148	0.0154	0.0154
Covid-6	0.01442	0.01407	0.01443	0.0144	0.0129	0.0127	0.0129	0.0128	0.01367	0.01359	0.01355	0.01367
Covid-7	0.0648	0.06694	0.0645	0.06681	0.04562	0.0483	0.0482	0.0484	0.0445	0.0439	0.0438	0.0441
Covid-8	0.05656	0.04832	0.0563	0.0565	0.0529	0.0520	0.05107	0.05053	0.0510	0.0505	0.0517	0.0518

Table (4.11): Precent relative surface area of the extracted infected region with respect to the whole infected lungs for tumors.

Images	Precent Relative surface area of the infected regions %											
	Number of clusters											
	three				four				five			
	k-means	**HSOFM**	**FCM Clustering**	**Hybrid Method**	**k-means**	**HSOFM**	**FCM Clustering**	**Hybrid Method**	**k-means**	**HSOFM**	**FCM Clustering**	**Hybrid Method**
Tumor1	28.12	28.14	28.15	28.15	27.98	28.09	27.9	27.98	27.86	28.06	27.99	27.99
Tumor2	19.90	19.89	19.89	19.90	19.51	19.53	19.51	19.51	19.38	19.55	19.38	19.40
Tumor3	5.21	5.18	5.20	3.99	5.03	5.19	4.97	5.03	4.87	4.97	4.87	4.89
Tumor4	7.48	7.46	7.48	7.36	7.36	7.43	7.36	7.38	7.27	7.41	7.28	7.27
Tumor5	**0.85**	**0.84**	**0.85**	**0.83**	**0.83**	**0.81**	**0.83**	**0.79**	**0.81**	**0.79**	**0.81**	**0.81**
Tumor6	1.58	1.59	1.58	1.54	1.50	1.50	1.53	1.50	1.49	1.53	1.49	1.47
Tumor7	0.95	0.95	0.95	0.93	0.91	0.92	0.93	0.92	0.91	0.90	0.91	0.90
Tumor8	4.66	4.62	4.63	4.47	4.47	4.61	4.40	4.60	4.36	4.59	4.32	4.73
Tumor9	3.05	3.04	3.05	2.90	2.91	3.04	2.91	3.02	2.82	3.02	2.87	2.82

In Table (4.10) and (4.11) show the Percent relative surface area of the extracted infected region with respect to the whole infected lungs for Covid-19 and infected lungs for tumors.

4.8 Manual Radiologist Delineation

Manual delineation of all the images under study was done by a specialist of radiology. The delineated regain were extracted and then their surface area were calculated to a doped them as a ground truth in order to investigate the performance quality of the implemented segmentation methods. Figures (4.48) and (4.49) illustrate the results of this step for Covid-19 and tumor infected lung images respectively.

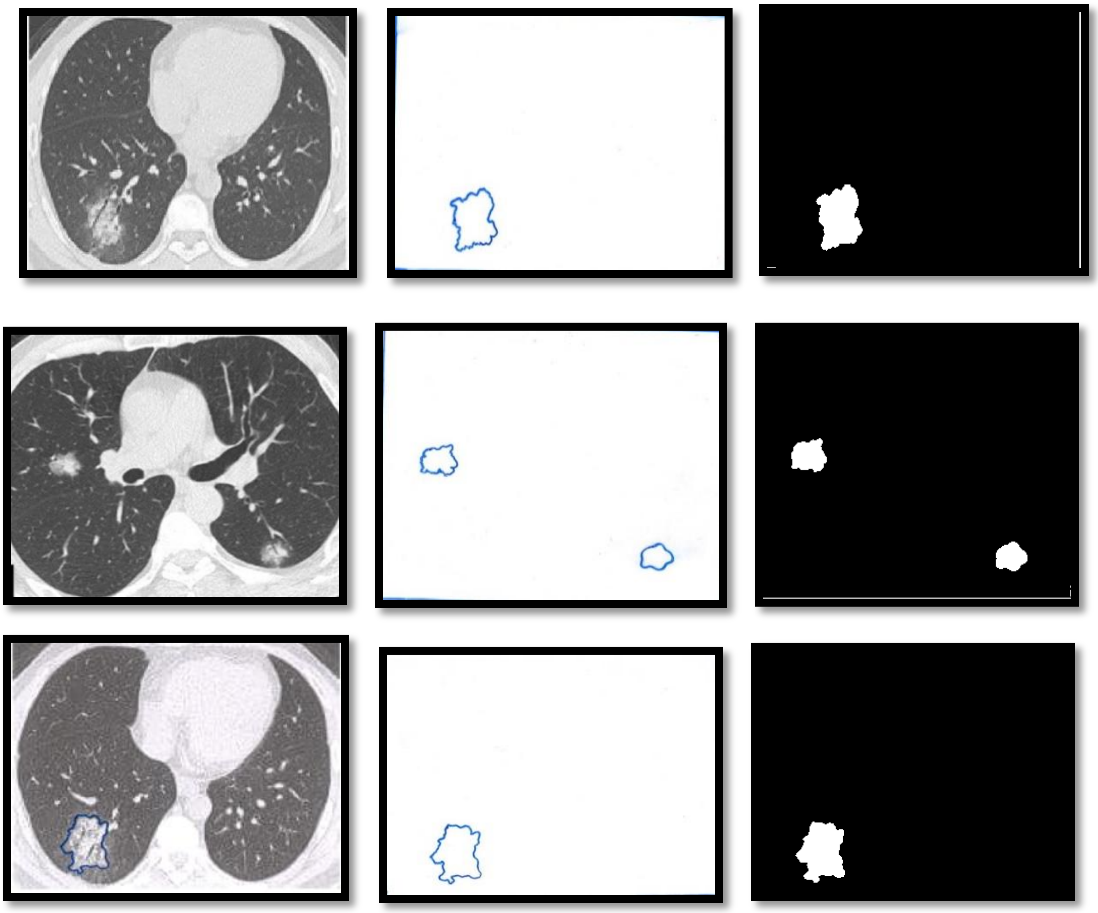

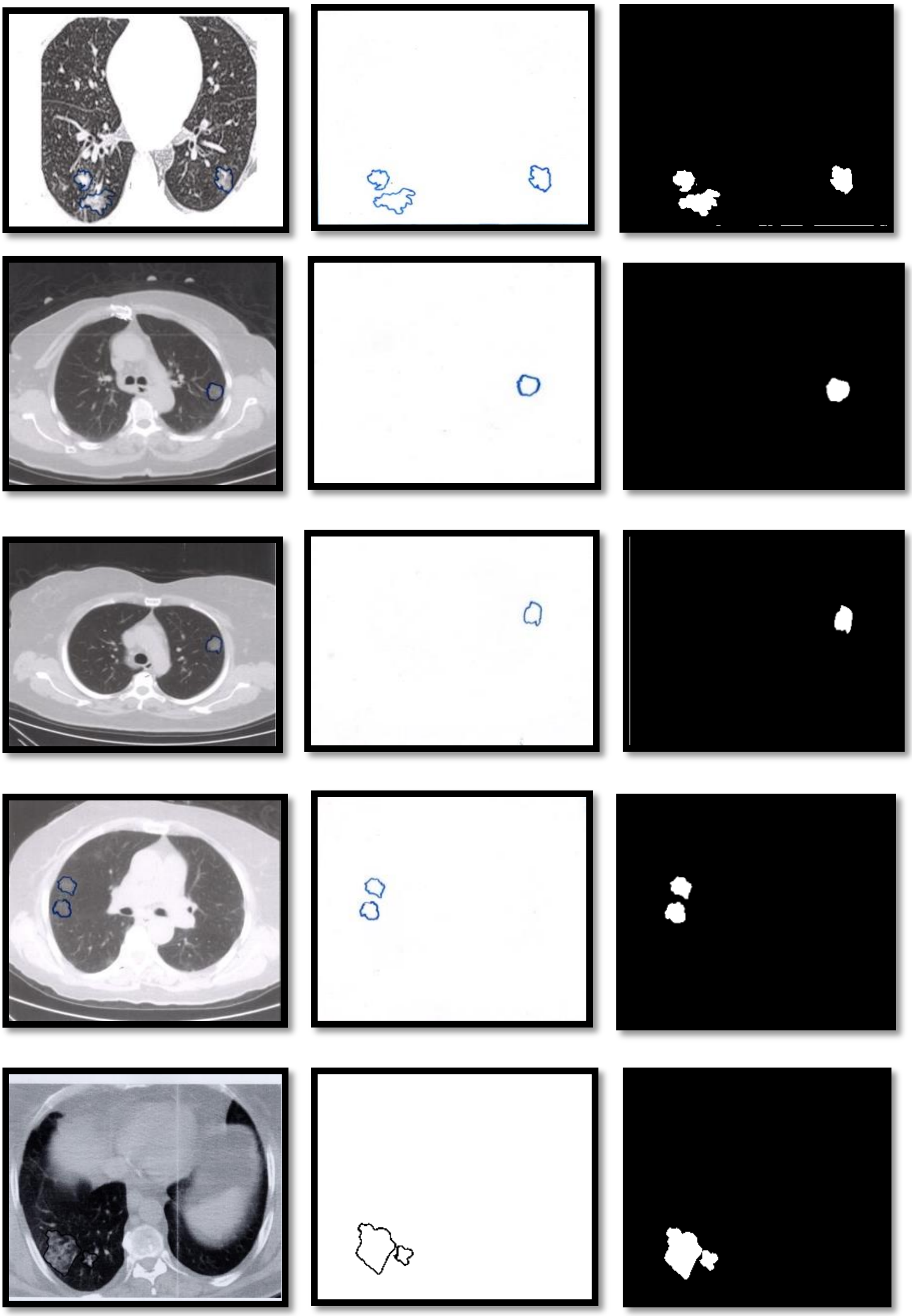

Figure (4.48): Radiologist manual delineation of abnormal area of Covid-19 images.

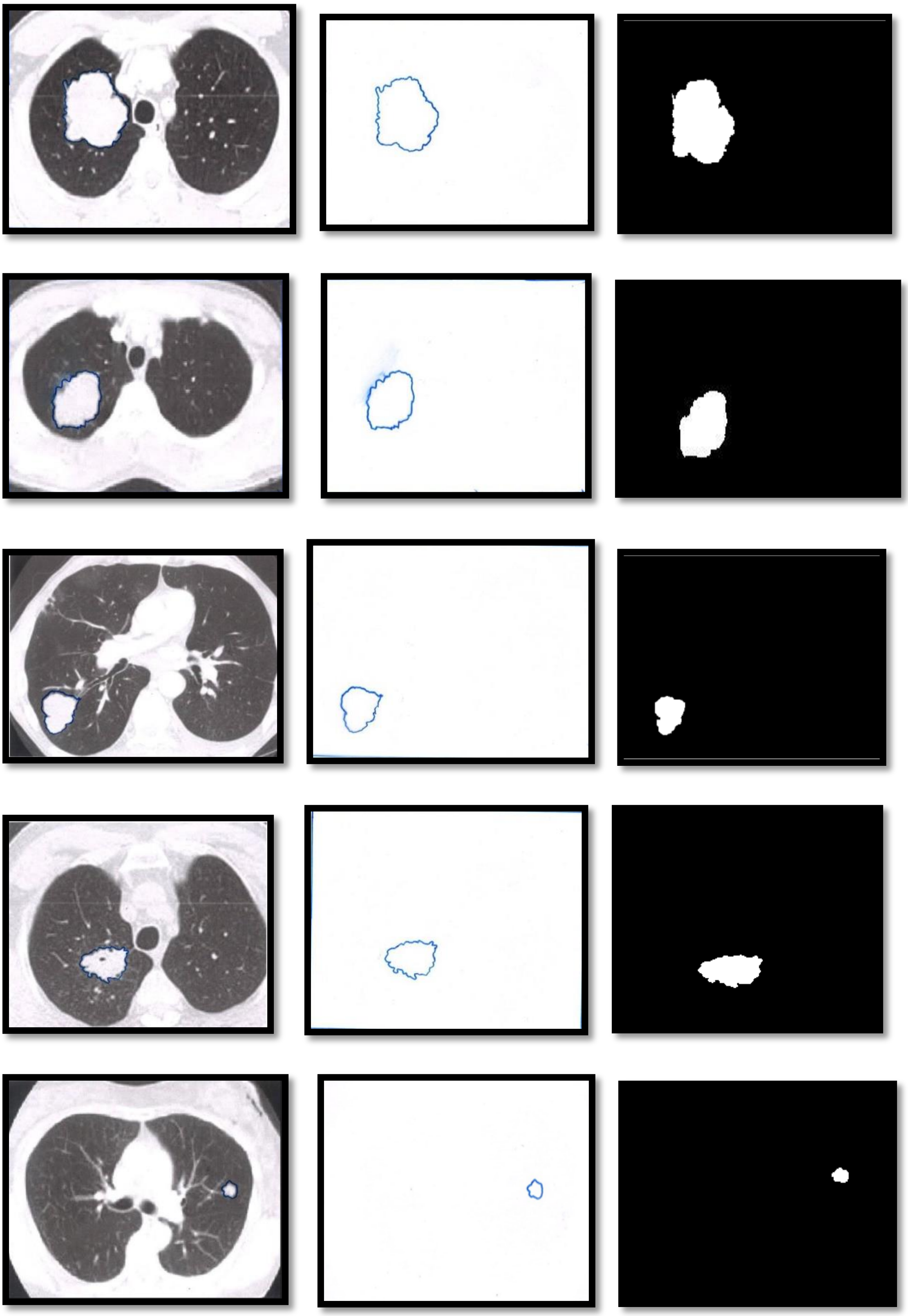

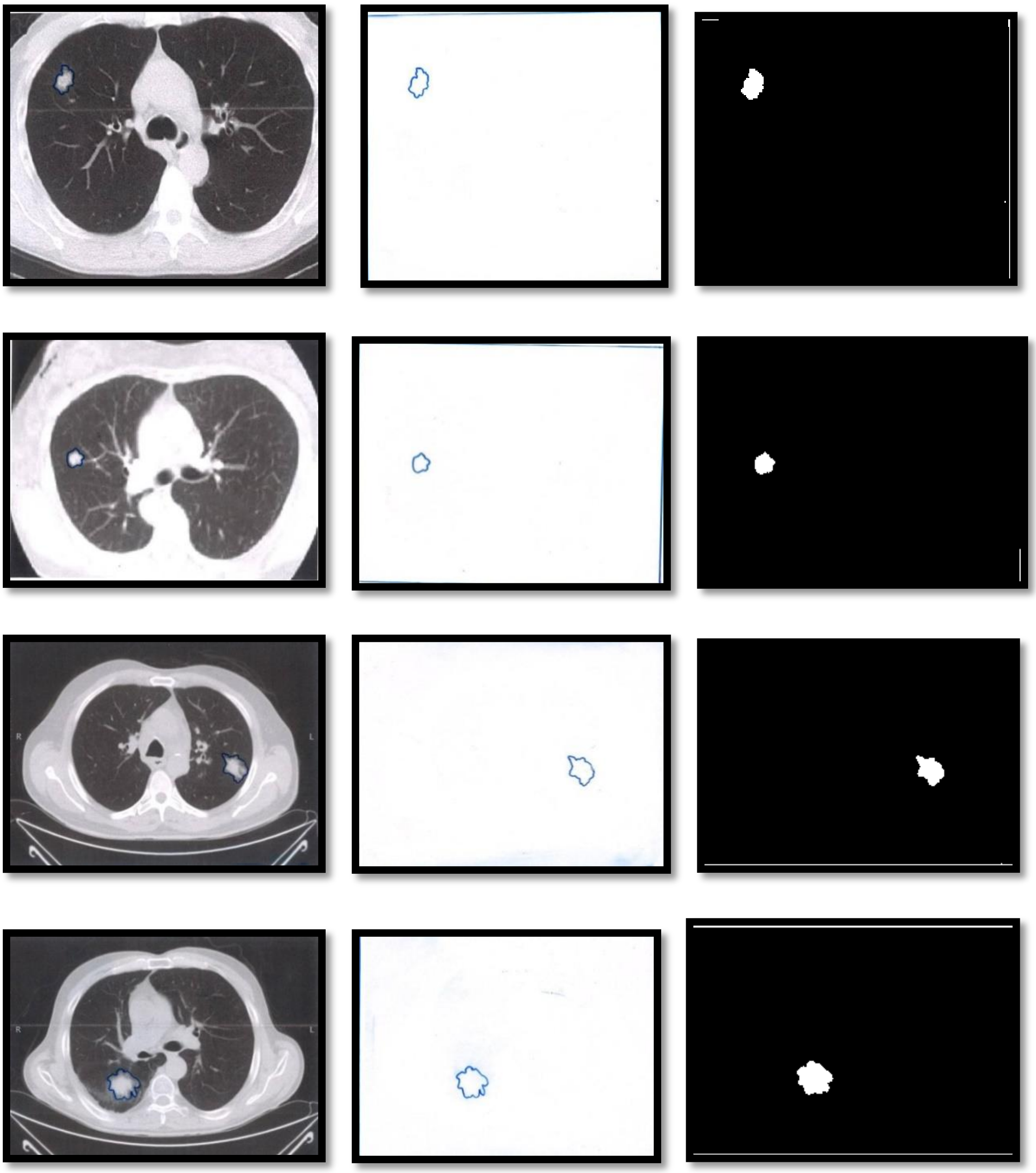

Figure (4.49): Radiologist manual delineation of abnormal area of tumor images.

In Figures (4.48) and (4.49), the first column shows the radiologist delineation of the abnormal regions, the second column represents the delineation contour only, while the last column illustrates the filled delineation abnormal regions after applying some image processing functions. The second and the third columns are resulted from applying processing operation on the images of the first column.

The calculated surface area of the radiologist delineatin regions are presented in Table (4.12).

Table (4.12): The calculated surface area of the radiologist delineatin regions.

The calculated surface area of the radiologist delineatin regions (pixsels)								
Tumor1	Tumor2	Tumor3	Tumor4	Tumor5	Tumor6	Tumor7	Tumor8	Tumor9
2894	903	3986	1642	120	171	125	1087	514

The percent relative differences of the surface area for the extracted abnormal regions for tumors concerning the radiologist delineation were calculated according to the equation:

$$present\ relative\ difference = \frac{|area\ of\ radiologist - area\ of\ implemented\ methods|}{area\ of\ radiologist} \qquad .....(4.2)$$

The results of this step are presented in Table (4.13).

Table (4.13): The percent relative differences of extracted tumor regain by implementing the proposed methods and the radiologist delineation.

Images	**Percent Relative Differences (%)**											
	Number of clusters											
	three				Four				five			
	k-means	**HSOFM**	**FCM Clustering**	**Hybrid Method**	**k-means**	**HSOFM**	**FCM Clustering**	**Hybrid Method**	**k-means**	**HSOFM**	**FCM Clustering**	**Hybrid Method**
Tuomer1	1.831	1.900	1.935	1.935	1.313	1.727	1.313	0.898	0.898	1.624	1.347	1.313
Tuomer2	5.980	5.869	5.869	5.980	3.875	3.986	3.875	3.875	3.211	4.097	3.211	3.322
Tuomer3	1.304	0.878	1.054	2.228	2.032	0.852	3.586	2.074	5.268	3.268	5.561	4.867
Tuomer4	4.567	4.811	4.506	6.029	6.029	5.054	6.029	5.724	7.247	5.298	7.125	7.247
Tuomer5	20.83	21.67	20.83	22.5	22.5	24.16	22.5	25.83	24.16	25.83	24.16	24.16

Tuomer6	3.508	4.093	3.508	0.584	1.685	1.685	0.584	1.754	2.339	0.584	2.339	3.509
Tuomer7	0.8	0.8	0.8	1.6	3.2	2.4	1.6	2.4	4	4.8	4	4.8
Tuomer8	12.69	13.33	13.24	16.19	16.19	13.52	17.38	13.79	18.21	13.98	19.04	11.31
Tuomer9	1.750	1.361	1.750	3.307	3.112	1.167	3.112	0.583	5.836	0.583	4.474	5.836

[The percent relative differences of the surface area for the Covid-19 infected, cannot be calculated because the areas infected with the Covid-19 virus spread in a tree-like shape that do not from in one place like tumors, and that the delineation of the radiologist includes the areas of Covid-19 infected with empty areas that are not infected by the virus].

The elapsed time of applying HSOFM and the hybrid technique was measured and the percent reduction of time was calcuted, see Table(4.14) and (4.15).

The equation for caluclating the present reduction time from the implementing the hyprid HSOFM techidues:

$$present\ time\ reduction = \frac{|time\ of\ HSOFM - time\ of\ hybrid\ methods|}{time\ of\ HSOFM} \quad .....(4.3)$$

Table (4.14): Elapsed time of implementing HSOFM and the hyprid HSOFM techidues and present reduction for Covid-19.

Images	**Elapsed time (sec)**								
	Number of clusters and nodes								
	three			**four**			**five**		
	HSOFM	**Hybrid Method**	**precent Relative reduction of time%**	**HSOFM**	**Hybrid Method**	**precent Relative reduction of time%**	**HSOFM**	**Hybrid Method**	**Precent Relative reduction of time%**
Covid-1	399.278892	349.231122	12.53	440.079731	331.215890	24.73	560.153120	471.865216	15.768
Covid-2	425.028270	208.110970	51.03	485.833029	389.339743	19.86	519.030622	401.073239	22.72
Covid-3	355.275672	259.906633	26.84	482.086451	308.976321	35.90	513.169056	401.226420	21.81

Covid-4	459.391472	308.454098	32.85	565.208814	397.158364	29.73	590.094702	478.014375	18.99
Covid-5	479.250293	327.697106	31.62	402.670835	307.237890	23.69	502.670835	321.762219	35.98
Covid-6	614.804659	309.769236	49.62	439.034838	301.089763	31.42	439.034838	308.772104	29.68
Covid-7	488.896515	374.203049	23.46	402.981078	301.076020	25.29	602.981078	411.335678	29.68
Covid-8	643.092421	344.017523	46.505	504.647871	309.062123	38.76	404.647871	299.407217	26.01

Table (4.15): Elapsed time of implementing HSOFM and the hyprid SOFM techidues for tumor.

Images	**Elapsed time (sec)**								
	Number of clusters and nodes								
	three			**four**			**five**		
	HSOFM	**Hybrid Method**	**precent Relative reduction of time%**	**HSOFM**	**Hybrid Method**	**precent Relative reduction of time%**	**HSOFM**	**Hybrid Method**	**Precent Relative reduction of time%**
Tumor1	422.398990	301.291136	28.67	430.689771	301.215890	30.06	512.109920	291.865216	43.00
Tumor2	433.542289	299.319243	30.95	478.107344	289.339743	39.49	489.130828	301.872539	38.28
Tumor3	402.877612	311.708329	22.62	432.786221	308.976321	28.61	462.189038	401.835272	13.06
Tumor4	489.091176	303.402117	37.98	515.208814	297.158364	42.32	560.591104	298.90175	46.68
Tumor5	654.987122	322.109275	50.8	670.811071	320.620854	52.20	671.106632	319.104229	52.45
Tumor6	514.908891	353.710418	31.30	522.982398	311.917332	40.36	530.701760	308.95443	41.78
Tumor7	416.255321	349.207719	16.10	454.101366	301.944021	33.50	460.108874	299.122091	34.99
Tumor8	405.833651	298.518513	26.4	511.901175	285.994121	44.13	524.743821	281.407217	46.37
Tumor9	490.913155	301.108217	38.66	499.019836	299.108821	40.60	502.204431	280.207761	44.20

By a close inspection on Tables (4.14) and (4.15), it is clear that the applying the hybrid method reduced the required implementing time with percent reduction ranged from (18.99 - 49.62)% for Covid-19 and reached to for (13.05- 52.2)% for tumor.

4.9 Accuracy of Segmentation Methods

The accuracy of the implemented segmentation methods was calculated according to:

$$\text{over accuracy} = \frac{\text{number succeeded segmented images}}{\text{total segmented images}} \qquad ....(4.4)$$

The results are shown in Table (4.16).

Table (4.16): Accuracy of segmentation methods.

Accuracy %			
K-means	**FCM**	**HSOFM**	**Hybrid technique**
95	**95**	**94**	**94**

4.10 Visual Comparison

A visual comparison of the extracted abnormal regions of the implementing adopted methods: K-means, FCM, HSOFM and hybrid technique compared with the radiologist's delineation are presented in Figures (4.50) and (4.51) for Covid -19 and tumors of lung CT scan images respectively.

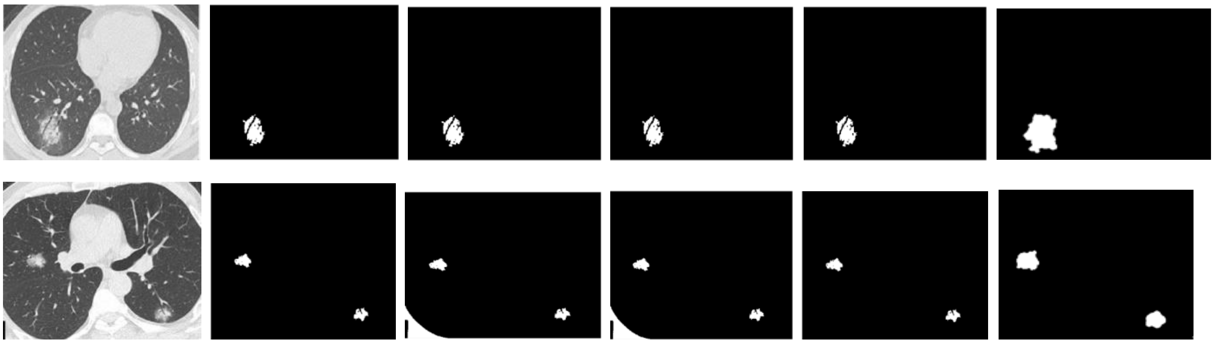

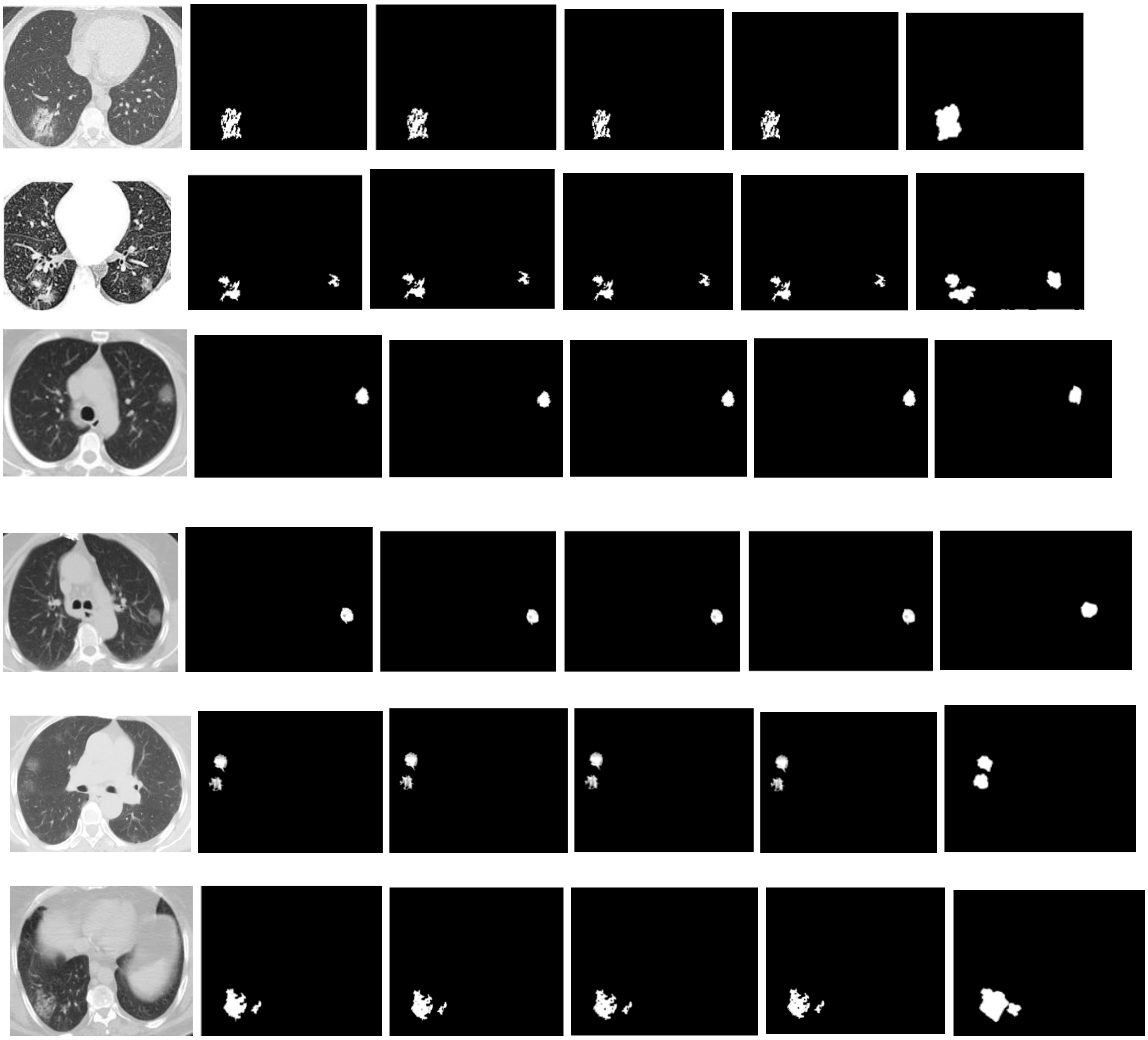

a b c d e f

Figure (4.50): Visual comparison of the results (a) input Covid-19 image of four methods (b) k-means and (c) FCM and (d) HSOFM and (e) hybrid method and (f) the radiologist delineation for Covid -19 of lung CT scan images.

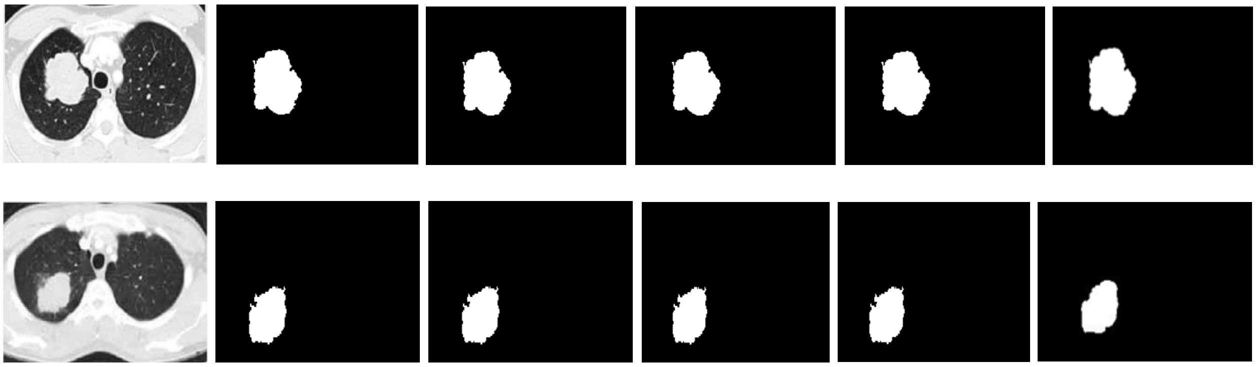

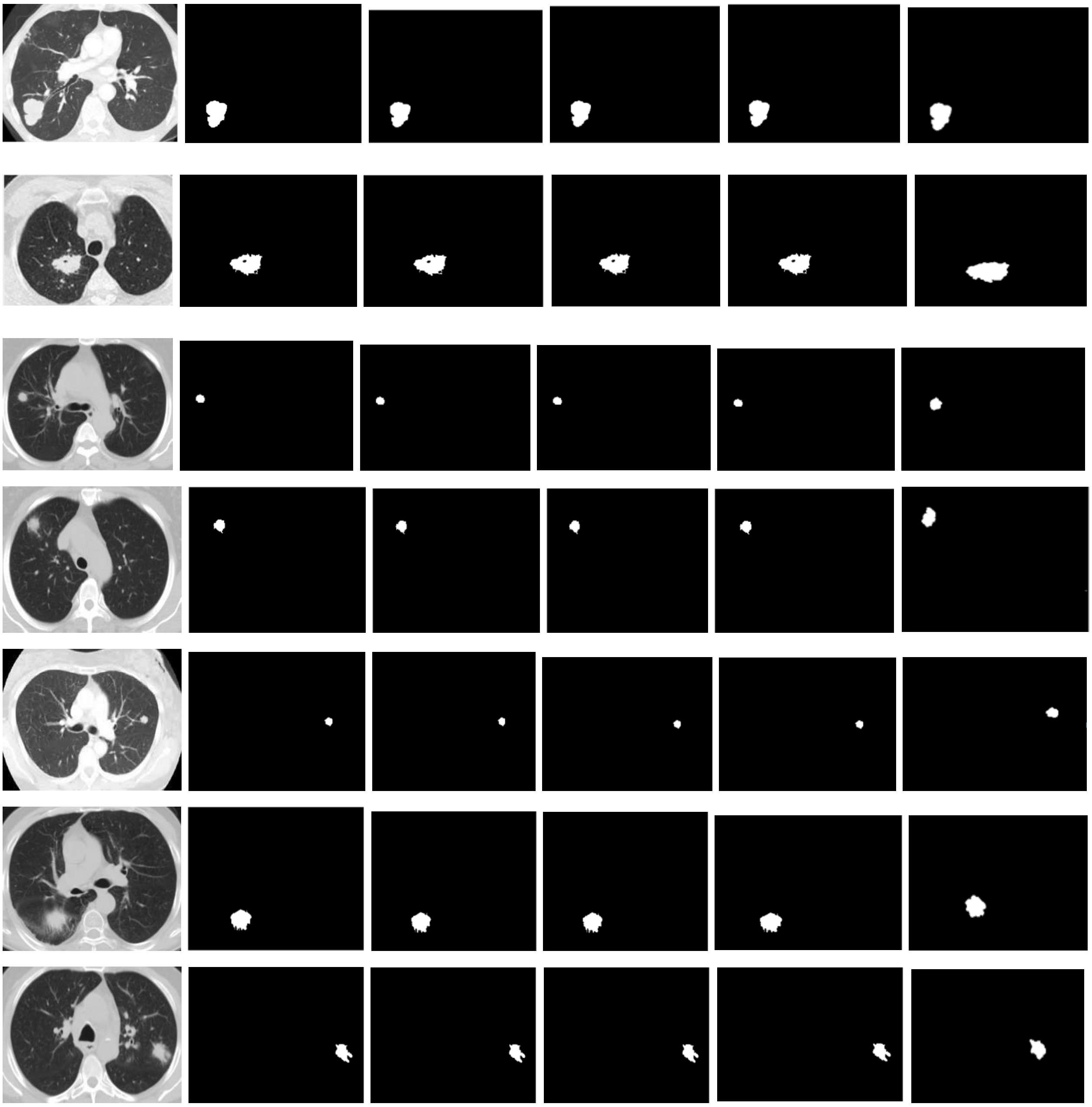

a b c d e f

Figure (4.51): Visual comparison of the results (a) input tumor image of four methods (b) k-means and (c) FCM and (d) HSOFM and (e) hybrid method and (f) the radiologist delineation for tumors of lung CT scan images.

By examining the images of the extracted abnormalities that were resulted from the implemented techniques and compare them visually with the radiologist's delineation, it turns out that all the proposed methods are capable for successful isolating and extracting and the results were in good agreement with manual delineation for tumor cases. For Covid -19 cases, some images the infection take a tree shape that the manual delineation could not determine it correctly while the applied methods could isolate these regions correctly.

Conclusion and Future Studies

5.1 Conclusions

From the results of implementing the proposed techniques : K-means, FCM, HSOFM, and HSOFM hybrid method it can be concluded that:

1- Adopting CNN is a good choice for classifying different sets of images to their different classes (normal, Covid-19, Tumor) with high accuracy (99.9) , Sensitivity (99.9)% and Specificity(99.9)%. For Covid-19 and with high accuracy (99.98) , Sensitivity (99.98)% and Specificity(99.98)% for tumor

2-The number of clusters, three is the appropriate choice for implementing K-means and FCM.

3- The number of nodes, three is the suitable nodes number to differentiate the abnormal regions from others.

4- The proposed hybrid technique succeeded to reduce the elapsed time of implement HSOFM reduction (18.99 - 49.62)% for Covid-19, reached to for (13.05- 52.2)% for tumor.

5-All the adopted segmentation methods have high quality performances with high accuracy value.

6- All the implemented segmentation methods in this study were in good agreement with the delineation of the radiologist (0.3868)% with relation difference reached.

5.2 Future Studies

1- The suggested system (CNN) is trained and tested on another data set, such as a chest x-ray.

2- The main objective of this study is to classify CT images into Covid-19 and normal and tumor using deep learning methods (CNN). Another type of network can be used for the purpose of classification.

3- Using the proposed methods to isolate and extract abnormal cells

Regions that appear in images of organs such as the kidney and the liver.

4- Using another hybrid technique to detect and isolate abnormalities in CT scan images to improve the extraction of infect areas.

5.3 Recommendations

1- Using CT lung images to diagnose people with Covid-19 to get better and more accurate results than X-ray images.

2- Using the Matlab (2020) program to process multiple medical images with various medical imaging methods, such as (x-ray, CT, MRI, PET) because it has better storage capabilities than older versions to accommodate the huge amount of data (images).

List of Abbreviations

Symbol	Definition of Abbreviations
US	Ultrasound
MRI	Magnetic Resonance Imaging
SPET	Single-Photon Emission Computed Tomography
PET	Positron Emission Tomography
CT	Computed Tomography
2D	2-Diamention
NSCLC	Non-Small Cell Lung Cancer
SCLC	Small Cell Lung Cancer
Covid-19	Coronavirus Disease-2019
ANN	Artificial Neural Network
ANS	Artificial Neural Systems
CNN	Convolution Neural Networks
Relu	Rectified Linear Units
Tanh	Hyperbolic Tangent Function
DA	Data Augmentation
TN	True Negative
TP	True Positive
FN	False Negative
FB	False Positive
Acc	Accuracy
Sen	Sensitivity
Pre	Precision
Spe	Specificity
S	softMax Function
ELU	Exponential linear unit
SOFM	Self-Organizing Feature Map
FCM	Fuzzy C-Mean
HSOFM	Hierarchical Self Organizing Feature Map

List of Figures

List of Tables

References

1. H. Zhou, J. Wu and J. Zhang," Digital Image Processing Part one", Publishing ApS, (2010).
2. G. Dougherty, "Digital Image Processing for Medical Applications", USA, New York, (2009).
3. S. Folea, " Practical Applications and Solutions Using LabVIEW™ Software", General Council of Superior Technological Education of Mexico (DGEST), p.297,(2011).
4. S. Angenent, E. Pichon, and A. Tannenbaum." Mathematical Methods in Medical Image Processing", American Mathematical Society Vol.43, No.3, pp. (365–396), (2006).
5. T. Kesavamurthy and S. SubhaRani," Pattern Classification using imaging techniques for Infarct and Hemorrhage Identification in the Human Brain", Calicut Medical Journal, Vol. 4,No. 3, p.1,(2006).
6. T M. Deserno, T Aach, K Amunts, W Hillen, T Kuhlen and I Scholl," Advances in medical image processing", Computer Science - Research and Development - Springer, Vol.26, No.1-2, pp. (1–3), (2011).
7. https://www.sciencedirect.com/topics/computer-science/image-enhancement
8. R. Maini and H. Aggarwal," A Comprehensive Review of Image Enhancement Techniques", Journal of computing, Vol. 2, Issue 3, P.6, (2010).
9. R. Rakesh, P. Chaudhuri, and C. A. Murthy, "Thresholding in Edge Detection: A Statistical Approach", IEEE Transactions on Image Processing, Vol. 13, No. 7, PP. (927-936), (2004).
10. W. K. Pratt, " Digital Image Processing", New York, (2001).
11. B. Kudayir Shukur, Nabeel H., and A. Al-Bakry, "A New Clustering Approach For Medical Brain Images", University of Babylon, Computer Science Department, (2012).

12. C. Tony, and Z. Wei, "Level Set Based Shape Prior Segmentation", IEEE Conf. on Computer Vision and Pattern Recognition, (2005).

13. K. S. Darne and S. S. Panicker," Use of Fuzzy C-Mean and Fuzzy Min-Max Neural Network in Lung Cancer Detection", International Journal of Soft Computing and Engineering, Vol.3, Issue 3, PP. (265-169), (2013).

14. A. R Kaur," Feature Extraction and Principal Component Analysis for Lung Cancer Detection in CT scan Images", International Journal of Advanced Research in Computer Science and Software Engineering, Vol. 3, Issue 3, PP.(187-190), (2013).

15. W. A. Abbas," CT-scan Lung Cancer Detection Using Image Processing Techniques", M.Sc. thesis, Baghdad University / College of Science / Department of Physics, (2014).

16. R. S. Abdoon, L. K. Abood and S. M. Ali, "Adaptive Techniques for Brain Tumor Detection in MRI", Lap LAMBERT Academic Publishing, Germany, (2015).

17. S. N. Jain and B. G. Patil," Cancer Cells Detection Using Digital Image Processing Methods", International Journal of Latest Research in Science and Technology, Vol. 3, Issue 4, PP. (45-49), (2015).

18. B. A. Miah Md. and M. A. Yousuf," Detection of Lung Cancer from CT Image Using Image Processing and Neural Network", International Journal of Latest Research in Science and Technology, Vol. 978, No. 2, p. 6, (2015).

19. E. E. Nithila and S. S. Kumar, Segmentation of Lung Nodule in CT Data Using Active Contour Model and Fuzzy C-Mean Clustering", Alexandria Engineering Journal, Vol. 55, Issue 3, PP. (2583-2588), (2016).

20. X. Fave, L. Zhang , J. Yang , D. Mackin , P. Balter , D. Gomez , D. Followill , A. Kyle Jones , F. Stingo and L. E. Court, "Impact of Image

Preprocessing on the Volume Dependence and Prognostic Potential of Radiomics Features in non-small Cell Lung Cancer ", Translational Cancer Research., Vol.5, No.4, P.15, (2016).

21. P. Sarker, M Hossain Shuvo Md., Z. Hossain and S. Hasan," Segmentation and Classification of Lung Tumor from 3D CT Image Using K-Means Clustering Algorithm", International Conference on Advances in Electrical Engineering, Dhaka, Bangladesh, Vol. 8, No.2, PP. (731-736), (2017).

22. O. S. Khudair Abboud," Utilizing Different Segmentation Methods to Detect Tumors and Abnormalities in Medical Images," M.Sc. Thesis in Medical image processing, Babylon, Iraq, (2017).

23.A. Sevani and H. Modi," Implementation of Image Processing Techniques for Identifying Different Stages of Lung Cancer", International Journal of Applied Engineering Research , Vol. 13, No. 8, PP.(6493-6499), (2018).

24. A. Chang and A. Moturu," Detecting Early Stage Lung Cancer Trained with Patches from Synthetically Generated X-Rays Using a Neural Network", University of Toronto, Ontario, Canada, P. 9, (2019).

25. S. Candemir and S. Antani," A Review on Lung Boundary Detection in Chest X-Rays", International Journal of Computer Assisted Radiology and Surgery, Vol. 14, Issue 4, PP. (563-576), (2019).

26. H. S. Kareem Rasool, “Segmenting of X-Rays based Medical Scanning Images Utilizing Image Processing Techniquesl”, M.Sc. Thesis in Medical image processing, Babylon, Iraq, (2020).

27. W. D, Kadhim and R. S, Abdoon. "Utilizing k-means clustering to extract bone tumor in CT scan and MRI images." Journal of Physics: Conference Series. Vol. 1591. No. 1. IOP Publishing, (2020).

28. B. Rohan, R. Kumar, and D. Writer. "CoronaNet: A Novel Deep Learning Model for COVID-19 Detection in CT Scans." Journal of Student Research 9.2, (2020).

29. A. K. Mishra, S. K. Das, P. Roy, and S. Bandyopadhyay, (2020). Identifying COVID19 from chest CT images: a deep convolutional neural networks based approach. Journal of Healthcare Engineering, (2020).

30. A. A. Jim, I. Rafi,M. S. Chowdhury, N. Sikder, M. P. Mahmud, S. Rubaiee ... and A. A. Nahid, "An Automatic Computer-Based Method for Fast and Accurate Covid-19 Diagnosis." medRxiv, (2020).

31. A. Talha, and S. Zakir. "Deep learning based diagnosis of COVID-19 using chest CT-scan images." , (2020).

32. L. Mohamed, G. Manogaran, and N. Eldeen M. Khalifa. "A deep transfer learning model with classical data augmentation and cgan to detect covid-19 from chest ct radiography digital images." Neural Computing and Applications, (2020).

33. J. Zhao, X. Yang, X. He, Y. Zhang, S. Zhang, and P. Xie, "Covid-ct-dataset: a ct scan dataset about covid-19." arXiv preprint arXiv:2003.13865 490, (2020).

34. Purohit, K., Kesarwani, A., Ranjan Kisku, D., and Dalui, M. "Covid-19 detection on chest x-ray and ct scan images using multi-image augmented deep learning model." BioRxiv (2020).

35. S. Yang, L. Jiang,Z. Cao, L. Wang, J. Cao, R. Feng,... and F. Shan,"Deep learning for detecting corona virus disease 2019 (COVID-19) on high-resolution computed tomography: a pilot study." Annals of Translational Medicine 8.7, (2020).

36. X. Ouyang, J. Huo, L Xia, F. Shan. J. Liu, … and D. Shen, "Dual-Sampling Attention Network for Diagnosis of COVID19 from

Community Acquired Pneumonia." IEEE Transactions on Medical Imaging , (2020).

37. N. Ali, C. Kaya, and Z. Pamuk. "Automatic detection of coronavirus disease (covid-19) using x-ray images and deep convolutional neural networks." arXiv preprint arXiv:2003.10849, (2020).

38. C. Zheng, X. Deng, Q. Fu, Q. Zhou, J. Feng, H. Ma,... and X.Wang, "Deep learning-based detection for COVID-19 from chest CT using weak label." medRxiv ,(2020).

39. R. Hu, G. Ruan, S. Xiang, M. Huang, Q. Liang, and J. Li, "Automated Diagnosis of COVID-19 Using Deep Learning and Data Augmentation on Chest CT." medRxiv (2020).

40. X. Xu, X. Jiang, C. Ma, P. Du, X. Li, S. Lv, ... and L. Li, "A deep learning system to screen novel coronavirus disease 2019 pneumonia." Engineering , pp. (1122-1129), (2020).

41. A. Amyar, R. Modzelewski, H. Li, and S. Ruan, "Multi-task deep learning based CT imaging analysis for COVID-19 pneumonia: Classification and segmentation." Computers in Biology ,(2020).

42. S. Dilbag, V. Kumar, and M. Kaur. "Classification of COVID-19 patients from chest CT images using multi-objective differential evolution– based convolutional neural networks." European Journal of Clinical Microbiology & Infectious Diseases, (2020).

43. J. F. Hernández Santa Cruz, ―An ensemble approach for multi-stage transfer learning models for COVID-19 detection from chest CT scans,‖ Intell. Med., Vol. 5, No., p. 100027, (2021).

44. A. Garain, A. Basu, F. Giampaolo, J.D. Velasquez, and R. Sarkar, Detection of COVID-19 from CT scan images: A spiking neural network-based approach." Neural Computing and Applications (2021).

45. S. H. Khan, A. Sohail, A. Khan, and Y. S. Lee, (COVID-19 detection in chest X-ray images using a new channel boosted CNN. Diagnostics, Vol. 12, No. 2, p. 267, (2020).

46. A. Drevelegas and N. Papanikolaou, "Imaging of Brain Tumors with Histological Correlations: Imaging Modalities in Brain Tumors", Springer-Verlag Berlin Heidelberg, PP.(13-33), (2011).

47. S. P. Awate, T. Tasdizen and R. T. Whitaker, "Unsupervised Texture Segmentation with Nonparametric Neighborhood Statistics", Conference, Scientific Computing and Imaging Institute, University of Utah,Salt Lake City, UT PP. (494-507), USA, (2006).

48. T. Kesavamurthy, S. Subha Rani,"Pattern Classification using Imaging Techniques for Infarct and Hemorrhage Identification in the Human Brain", Calicut Medical Journal, Vol.4, No.3, (2006).

49. URL: http//www.ge.com.

50. A. Bernheim, X. Mei, M. Huang, Y. Yang, Z. A. Fayad, N. Zhang, and M. Chung, Chest CT findings in coronavirus disease-19 (Covid-19 (2020).

51. X. Yang, X. He, J. Zhao, Y. Zhang, S. Zhang, and P. Xie, (2020). COVID-CT-dataset: a CT scan dataset about Covid-19 (2020).

52. K. M. M. Rao and V. D. P. Rao, “Medical Image Pprocessing”. At: http://www.drkmm.com/resources/MEDICAL_IMAGE_PROCESSING_25sep06.pdf .

53. A. P. Dhawan, "MEDICAL IMAGE ANALYSIS", 2nd Edition, John Wiley and Sons, Inc., Hoboken, New Jersey, (2011).

54. V. Chan, "Basics of Ultrasound Imaging", springer Science, PP. (13-19), (2011).

55. T. Kesavamurthy, R. S. Subha, "Pattern Classification using Imaging Techniques for Infarct and Hemorrhage Identification in the Human Brain", Calicut Medical Journal, Vol.4, No.3, (2006).

56. A. R. Peter, "An introduction to Magnetic Resonance in Medicine", Third edition, Oxford Blackwell scientific publications, (1993).

57. A. Alaa, “Identification of Abnormalities (Masses and Calcifications) in Digital Mammography Images”, M.Sc. Thesis in Image processing, University of Baghdad, Iraq, (2012).

58. T. M. Deserno, "Biomedical Image Processing", Springer-Verlag Berlin Heidelberg, (2011).

59. J. V. Frangioni, “New Technologies for Human Cancer Imaging”, Journal of clinical oncology by American Society of Clinical Oncology, Vol. 26, No. 24, PP. (4012-4021), (2008).

60. A. P. Dhawan, "Midical Image Analysis", 2nd Edition, John Wiley & Sons, Inc., Hoboken, New Jersey, (2011).

61. R. Pelberg, and W. Mazur "Cardiac CT Angiography Manual: Basic Principles in Computed Tomography (CT)", Springer-Verlag London, PP. (19-58), (2015).

62. http://kanvadiagnostic.com/?page_id=1395

63. L. W. Goldman, "Principles of CT and CT Technology", J. Nucl. Med. Technol., Vol. 35, No. 3, PP. (115-128), September, (2007).

64. http://crystalclearimaging.com/services-3/cat-scan-angiography-cta

65. https://www.pinterest.com/pin/323133341988878309

66. http://www.eurorad.org/eurorad/case.php?id=2832

67. A. F. Kopp , K. Klingenbeck-Regn , M. Heuschmid , A. Küttner , B. Ohnesorge, T. Flohr, S. Schaller, and C. D. Claussen,"Multislice Computed Tomography: Basic Principles and Clinical Applications", New Applications with the Assistance of Innovative Technologies, Vol. 68, No. 2, PP. (94-105), (2000).

68. K. S. Caldemeyer and K. A. Buckwalter, "The basic principles of computed tomography and magnetic resonance imaging", Journal of

The American Academy of Dermatology, Vol. 41, No. 5, PP. (768-771), (1999).

69. G. R. Aben, " CT Scanning", Department of Radiology, College of Osteopathic Medicine, Michigan state University, (2012).

70. J. G Betts, P. Desaix, E. Johnson, J. E. Johnson, D. Kruse, B. Poe, J. Wise, M. D. Womble, K. A. Young, and O. Korol, ", OpenStax College,Rice University, Houston, Texas p.1015, (2013).

71. https://images.app.goo.gl/smoMdPjznn3e35w98

72. T. M. St. John, M.D.,"With Every Breath: A Lung Cancer Guidebook", pp.(3-10), (2005).

73. V. C. Scanlon, and T. Sanders,"Essentials of Anatomy and Physiology",fifth edition, pp. (346-351), (2007).

74. www.medicalnewstoday.com › articles .

75. A. A. Liebow and B. Castleman," Benign Clear Cell ("Sugar") Tumors of the Lung", The Yale journal of biology, Vol. 79, No. 4, PP. (213-222), (1971).

76. P. Baluk, H. Hashizume, and D. M. McDonald," Cellular Abnormalities of Blood Vessels as Targets in Cancer", Current Opinion in Genetics & Development, Vol. 15, No. 743, PP. (102-111), (2005).

77. https://www.cancer.org/cancer/cancer-basics/signs-and-symptoms-ofcancer.html

78. I. Hunt, M. Muers and T. Treasure,"ABC Lung Cancer", 1nd Ed, P. 21, (2009).

79. https://images.app.goo.gl/gwZK6R2rPmvymZDU6

80. N. Gianchandani, A. Jaiswal, D. Singh, V. Kumar, V., and M. Kaur, "Rapid COVID-19 diagnosis using ensemble deep transfer learning models from chest radiographic images." Journal of ambient intelligence and humanized computing, (2020).

81. L. A. Gallagher, R. K. Shears, C. Fingleton, L. Alvarez.E. M. Waters, J. Clarke, L. Bricio-Moreno, C. Campbell, A. K. Yadav, F. Razvi, E. O’Nieil, A. J. O’Neill, F. Cava, P. D. Fey. A. Kadioglu, and J. P. O’gara, "Impaired Alanine Transport or Exposure to d-Cycloserine Increases the Susceptibility of MRSA to β-lactam Antibiotics." The Journal of infectious diseases Vol. 221, No.6, pp. (1000-1016), (2020).

82. S. S. Sharma, "A note on the Asian market volatility during the COVID-19 pandemic." Asian Economics Letters 1.2 (2020).

83. R. Rangayyan, F. Ayres, and J. Desautels, "A review of computer-aided diagnosis of breast cancer: Toward the detection of subtle signs" Journal of the Franklin Institute, Vol. 3, No. 44, PP. (312-348), (2007).

84. Y. Bizais, C. Barillot, and R. Paola, "Information Processing in Medical Imaging", Proceedings of 14th Int. Conf., Kluwer Academic, (1995).

85. I. Soesanti, A. Susanto, T.S. Widodo, and T. Measadji, "Optimized Fuzzy Logic Application for MRI Brain Images Segmentation", International Journal of Computer Science and Information Technology (IJCSIT), Vol. 3, No. 5, PP. (137-146), (2011).

86. K. Koster and M. Spann, "MIR: An Approach to Robust Clustering Application to Range Segmentation", IEEE Trans. on Pattern Analysis and Machine Intelligence, Vol. 22, No. 5, PP. (430-444), (2002).

87. D. L. Pham, C. Xu. and J. L. Prince, " A Survey of Current Methods in Medical Image Segmentation" , Annual Review of Biomedical Engineering, Vol. 2, No. 8, PP. (315-337), (2000).

88. T. Heinonena, P. Dastidarb, H. Freyc and H. Eskolaa, "Applications of MR Image Segmentation", International Journal of Bioelectromagnetism, Vol. 1, No. 1, PP. (35-46), (1999).

89. J. C. Rajapakse, J. N. Giedd, and J. L. Rapoport, "Statistical Approach to Segmentation of Single-Channel Cerebral MR Images", IEEE Transactions on Medical Imaging, Vol. 16, No. 2, PP. (176-87), (1997).

90. S. N. Kinkar, "Development and Application of Semi-automated ITK Tools for the Segmentation of Brain MR Images", Master thesis in Computer Science, Worcester Polytechnic Institute, (2005).

91. A. J. Worth, N. Makris, V. S. Caviness, Jr, and N. D. Kennedy, "Neuroanatomical Segmentation in MRI: Technological Objectives", Center for Morphometric Analysis, General Hospital-East, Charlestown, USA, Vol. 11, No. 8, P. 34, (2000).

92. M.C.J. Christ and R.M.S Parvathi, "Segmentation of Medical Image using Clustering and Watershed Algorithms", American Journal of Applied Sciences Vol. 8, No. 12, pp. (1349-1352), (2011).

93. N. H. Rajini and R. Bhavani,"Classification of MRI Brain Images using k- Nearest Neighbour and Artificial Neural Network", IEEEInternational Conference on Recent Trends in Information Technology, ICRTIT, 2011.Emerging Technology and Advanced Engineering. Vol. 3, Issue 6, June (2013).

94. A. Barley and C. Town, "Combinations of Feature Descriptors for Texture Image Classification", Journal of Data Analysis and Information Processing, Vol. 2, No. 5, pp. (67-76), (2014).

95. H. Demuth and M. Beale, "Neural Network Toolbox For Use with MATLAB", User's Guide, Version 4, Neural Network Toolbox User's Guide, COPYRIGHT by The Math Works, Inc, (2002).

96. A. Krenker, J. Beter and A. Kos, "Introduction to the Artificial Neural Networks, Artificial Neural Networks-Methodological Advances and Biomedical Applications", Prof. Kenji Suzuki (Ed.), ISBN: 978-953-307-243-2, InTech, (2011).

97. L. M. Fu, “ Neural Networks in Computer Intelligence”, Mc Graw-Hill, New York, (1994).

98. A. Zhang, Z. C. Lipton, J. S. Aston M. Li, DiveintoDeepLearning. (2020).

99. K. Yun, PhD, A. Huyen and T. Lu, ―DEEP NEURAL NETWORKS FOR PATTERN RECOGNITION,‖ California Institute of Technology, (2018).

100. Z. Y. Zu, M. D. Jiang, P.P. Xu, W. Chen, Coronavirus Disease 2019 (COVID-19): A Perspective from China,‖ Radiology, Vol. 296, No. 2. Radiological Society of North America Inc., pp. (E15–E25), Aug. 01, (2020).

101. M. Theses, M. Reports, and L. Baruah, Performance Comparison of Binarized Neural Network with Convolutional Neural Network,‖ Baruah, Lopamudra, Open Access Master’s Report, Michigan Technological University, (2017).

102. K. O’Shea and R. Nash, An Introduction to Convolutional Neural Networks,‖ arXiv Prepr. arXiv, p. 1511.08458, (2015).

103. A. Diba, M. Fayyaz, V. Sharma and A. H. Karami et al., Temporal 3D ConvNets: New Architecture and Transfer Learning for Video Classification,‖ arXiv, p. 1711.08200, (2017).

104. B. A. Krizhevsky, I. Sutskever, and G. E. Hinton, ImageNet Classification with Deep Convolutional Neural Networks,‖ Commun. ACM, Vol. 60, No. 6, pp. (84–90), (2012).

105. J. Park, H. Lee, C. Y. Park, S. Hasan, T.-Y. Heo, and W. H. Lee, Algal Morphological Identification in Watersheds for Drinking Water Supply Using Neural Architecture Search for Convolutional Neural Network,‖ Water 2019, Vol. 11, P. 1338, Vol. 11, No. 7, p. 1338, Jun. (2019).

106. M. Z. Yong Zhong, Research on deep learning in apple leaf disease recognition.‖ Computers and Electronics in Agriculture, p. 6, (2019).

107. K. Rahman and H. Ali, Face Verification Across Age Progression Using Deep Convolutional Siamese Neural Networks and Deep Aging Patterns Representation,‖ Babylon University, (2021).

108. D. Pedamonti, Comparison of non-linear activation functions for deep neural networks on MNIST classification task,‖ arXiv Prepr. arXiv, Vol. 5, p. 1, (2018).

109. A. Maneesh, RMNv2: Reduced Mobilenet V2 An Efficient Lightweight Model For Hardware Deployment, (2020).

110. K. C. Kirana, S. Wibawanto, N. Hidayah, G. P. Cahyono, and K. Asfani, Improved Neural Network using Integral-RELU based Prevention Activation for Face Detection,‖ ICEEIE 2019 - Int. Conf. Electr. Electron. Inf. Eng. Emerg. Innov. Technol. Sustain. Futur., Vol. 6, pp. (260–263), (2019).

111. B. Mandal, L. Li, G. S. Wang, and J. Lin, Towards Detection of Bus Driver Fatigue Based on Robust Visual Analysis of Eye State,‖ IEEE Trans. Intell. Transp. Syst., Vol. 18, No. 3, pp. (545–557), (2017).

112. D. Vieira and J. A. R. Paixao, Vector field neural networks,‖ Complex Syst, Vol. 6, pp. (21–30), (2018).

113. J. Li, T. Qiu, C. Wen, and K. Xie, Robust Face Recognition Using the Deep C2DCNN Model Based on Decision-Level Fusion Jing,‖ Sensors, p. 7, (2018).

114. B. A. Krizhevsky, I. Sutskever, and G. E. Hinton, ImageNet Classification with Deep Convolutional Neural Networks,‖ Commun. ACM, Vol. 60, No. 6, pp. (84–90), (2012).

115. N. S. G. Hinton, A. K. I. Sutskever, and Ruslan, Dropout: A Simple Way to Prevent Neural Networks from Overfitting,‖ J. Mach. Learn. Res., Vol. 15, pp. (1929–1958), (2014).

116. F. Schilling, The Effect of Batch Normalization on Deep Convolutional Neural Networks, (2016).

117. N. Bjorck, C. P. Gomes, B. Selman, Understanding Batch Normalization,‖ arXiv Prepr. arXiv, p. 1806.02375, (2018).

118. A. I. Shibani Santurkar, D. Tsipras, M. Aleksander „ adry, How Does Batch Normalization Help Optimization?,‖ in Proceedings of the 32nd international conference on neural information processing systems, pp. (2488–2498), (2018).

119. I. Goodfellow, Y. Bengio, and A. Courville, Deep Learning - whole book,‖ Nature, Vol. 521, No. 7553, p. 800, (2016).

120. G. Hinton, L.Deng, D. Yu and G. E. Dahi , Deep neural networks for acoustic modeling in speech recognition: The shared views of four research groups,‖ IEEE Signal Processing Magazine, Vol. 29, No. 6. pp. (82–97), (2012).

121. N. S. G. Hinton, A. K. I. Sutskever, and R. Salakhutdinov, Dropout: A Simple Way to Prevent Neural Networks from Overfitting Nitish,‖ J. Mach. Learn. Res., Vol. 15, pp. (1929–1958), (2014).

122. G. E. Hinton, N. Srivastava, A. Krizhevsky, I. Sutskever, and R. R. Salakhutdinov, Improving neural networks by preventing co-adaptation of feature detectors,‖ arXiv Prepr. arXiv, p. 1207.0580, (2012).

123. N. Srivastava, G. Hinton, A. Krizhevsky, I. Sutskever, and R. Salakhutdinov, Dropout: a simple way to prevent neural networks from overfitting. The Journal of Machine Learning Research, Vol. 15, No. (1), PP. (1929–1958)., (2014).

124. A. Narin, C. Kaya, and Z. Pamuk. "Automatic detection of coronavirus disease (covid-19) using x-ray images and deep convolutional neural networks." arXiv preprint arXiv:2003.10849 (2020).

125. S. A. Mingoti and J. O. Lima, “Comparison SOM Neural Network with Fuzzy C-Means, K-Means and Traditional Hierarchical Clustering Algorithms”, European Journal of Operational Research ,Vol. 174, No. 3, PP. (1742-1759), (2006).

126. T. Kohonen., “Self-Organization and Associative Memory”, Springer-Verlag, New York, (1989).

127. T. Kohonen., “Self-Organizing Maps”, Springer-Verlag, Berlin, (1995).

128. S. I. Gallant , “Neural Network Learning and Expert Systems”, MIT Press, Cambridge, (1993).

129. T. Logeswari , and M. Karnan , “An Improved Implementation of Brain Tumor Detection using Segmentation based on Soft Computing”, Journal of Cancer Research and Experimental Oncology Vol. 2, No. 1, PP. (006-014), (2010).

130. J. M. Mostafa, and H. Soltanian-Zadeh., “Medical Image Segmentation Using Artificial Neural Networks, Artificial Neural Networks- Methodological Advances and Biomedical Applications”, Prof. Kenji Suzuki (Ed.), ISBN: 978-953-307-243-2, InTech, (2011).

131. Y. Yang and S. Huang, "Image Segmentation By Fuzzy C- Means Clustering Algorithm With A Novel Penalty Term", Computing and Informatics, Vol. 26, PP.(17-31), (2007).

132. D. L. Pham and J. L. Prince, "Adaptive Fuzzy Segmentation of Magnetic Resonance Images", IEEE Trans. Medical Imaging Vol.18, PP. (737-752), (1999).

133. N. R. Pal, K. Pal, J. M. Keller, and J. C. Bezdek , "A Possibilistic Fuzzy c-Means Clustering Algorithm", IEEE Transactions on fuzzy systems, Vol. 13, No. 4, PP. (517-530), (2005).

134. A. Meena and R. Raja, "Spatial Fuzzy C-Means PET Image Segmentation of Neurodegenerative Disorder", Indian Journal of

Computer Science and Engineering (IJCSE), Vol. 4 No.1, PP. (50-55), (2011).

135. S. P. Hari Prasath, G. K. Sundararaj , and A. Jayachandran , "Brain Tumor Segmentation of Contrast Material Applied MRI Using Enhanced Fuzzy C-Means Clustering", International Journal of Engineering and Innovative Technology (IJEIT) Vol. 1, No. 2, (2012).

136. M. Moghbel, S. Mashohor , R. Mahmud, and M. Iqbal Bin Saripan, "Automatic Liver Tumor segmentation on Computed Tomography for Patient Treatment Planning and Monitoring", EXCLI Journal 15:406-423 – ISSN 1611-2156 Received: May 20, accepted: June 22, 2016, published: June 27, (2016).

137. W. D. Foley , " Liver: surgical planning". Eur Radiol, Vol. 15, No. 4, PP. (89-95), (2005).

138. L. Michael, F. William, D. Erik, A. Leslie, and K. Anil, "Dimensionality reduction using genetic algorithms", IEEE Transactions On Evolutionary Computation, Vol. 4, No. 2, PP. (164-172), (2000).

139. R. C. Gonzalez, and R. E. Woods R. E., “Digital Image Processing”, Prentice Hall, (2002).

140. R.C. Gonzalez , R. E. Woods , and S. L. Eddins ,“Digital Image Processing Using MATLAB”, Pearson Prentice-Hall, (2004).

141. T. Kapur, Eric W. L. Grimson, William. M. Wells, and Ron Kikinis, "Segmentation of Brain Tissue from Magnetic Resonance Images", Medical Image Analysis, Vol. 1, No.1, PP. (109-127), (1996).

142. J. W. Klingler, C. L. Vaughan, T. D. Fraker and L. T. Andrews, "Segmentation of Echocardiographic Images Using Mathematical Morphology", IEEE Transaction on Biomedical Engineering, Vol. 35, No.11, (1988).